

UNIVERSITAT AUTÒNOMA DE BARCELONA  
DOCTORAL THESIS

**Indirect Search for WIMP Dark Matter  
with the MAGIC Telescopes**

CAMILLA MAGGIO

UNIVERSITAT AUTÒNOMA DE BARCELONA  
Unitat de Física de les Radiacions

The dissertation was submitted for the defence of the degree of Doctor of Philosophy on 3 February 2021.

**Director:** Dr. Markus Gaug,  
Unitat de Física de les Radiacions & CERES-IEEC,  
Universitat Autònoma de Barcelona  
Bellaterra, Spain

**Director:** Dr. Lluís Font Guiteras,  
Unitat de Física de les Radiacions & CERES-IEEC,  
Universitat Autònoma de Barcelona  
Bellaterra, Spain

**Declaration:**

*Hereby I declare that this doctoral thesis, my original investigation and achievement, submitted for the doctoral degree at Universitat Autònoma de Barcelona, has not been submitted for any academic degree elsewhere.*



## Abstract

Albeit there is overwhelming evidence for the paradigm of dark matter (DM) in the Universe, its nature is still an enigma at present day, despite the multiple theories and models proposed, and the various experiments and astrophysical installations searching for its signatures. Among the most promising DM particle candidates beyond the Standard Model of particle physics, the Weakly Interacting Massive Particle (WIMP) is the one that has been investigated most. Predicted to have a mass between few GeV and hundreds of TeV, it fits perfectly in the energy range tested by indirect dark matter searches with Imaging Atmospheric Cherenkov Telescopes.

The Florian Göbel Major Atmospheric Gamma Imaging Cherenkov (MAGIC) telescopes, located at the Observatorio del Roque de los Muchachos, on the Canary Island of La Palma, perform indirect DM searches for WIMPs since their very beginning. Among the targets observed with the MAGIC telescopes, dwarf spheroidal satellite galaxies (dSphs) and the Galactic Center and halo are the most common, both expected to be embedded in a high DM overdensity.

In this thesis, I present the outcome of indirect WIMP annihilation searches from three different observation targets, and the results obtained by a combination of data from multiple targets. No signal has been observed in any of the four searches.

The first object analysed, the globular cluster (GC) M15, is a challenge, given its relatively low DM overdensity predicted and the large systematic uncertainties resulting from the current lack of star velocity dispersion profiles at its core. No hint of a signal was found in the analysis of a big MAGIC data set, obtained in the framework of a MAGIC key science program observation campaign. In order to get an estimate of the sensitivities achievable with this type of analyses, four different realizations of the M15 DM density profile were investigated. Statistical upper limits on the velocity-averaged WIMP annihilation cross-section have been obtained with the use of the DM profiles provided in publications by the H.E.S.S. and VERITAS experiments (compatible with the upper limits of their respective publications, once re-scaled for the larger MAGIC observation time). Further toy statistical upper limits have been obtained taking into account DM density profiles from a convolution of the M15 density profile and its expected non-baryonic matter content. The latter was retrieved from N-body simulations of the M/L ratio in the works of den Brok et al. and Baumgardt et al., and considered DM dominated. The limits retrieved with this method are better than the most promising ones from dSphs, but at the same time systematically unreliable, and provide only a minimum value of the velocity-averaged cross-section attainable in M15, awaiting more precise models on the formation and evolution of GCs, and particularly new kinematic measurements at GCs' cores.

As targets selected for a multi-year observational diversification campaign, carried out by the MAGIC collaboration on dSphs, the Draco and Coma Berenices dSphs were observed during the past years and analysed. In this case, reliable 95% CL upper limits on the velocity-averaged WIMP annihilation cross-section have been retrieved, given the absence of a signal, and are presented in this thesis.

The data of these two dSphs are also combined with the ones of two other dSphs, previously observed with the MAGIC telescopes, namely Segue 1 and Ursa Major II, in order to achieve the best sensitivity for indirect WIMP DM annihilation searches. The results obtained constitute the MAGIC Collaboration legacy in this field, and are the most constraining reached by MAGIC and the most stringent in the  $\approx 10\text{-}100$  TeV WIMP DM mass interval in gamma-ray astrophysics searches so far, reaching upper limits of the order of  $10^{-24} \text{ cm}^3\text{s}^{-1}$  for the velocity-averaged annihilation cross-section.

In the last part of this thesis, the Barcelona Raman LIDAR hardware-related activities, in which I participated, are presented. Considering the necessity of new performing systems to monitor the atmosphere above Imaging Atmospheric Cherenkov Telescopes, in the view of a fully operational Cherenkov Telescope Array, a new type of Raman LIDAR has been built. The project is explained and the outcome of a series of tests performed on its components reported.

## Resumen

Aunque haya una evidencia contundente para el paradigma de la materia oscura (DM) en el universo, la naturaleza de dicha materia sigue siendo un enigma hoy día, a pesar de las múltiples teorías y modelos propuestos, y de los numerosos experimentos e instalaciones astrofísicas que buscan sus trazas. Entre las partículas candidatas más prometedoras más allá del Modelo Estándar de la física de partículas, la Weakly Interacting Massive Particle (WIMP) es la que más se ha investigado. Las predicciones indican que la masa de la WIMP debería estar entre los pocos GeV y los cientos de TeV, encajando perfectamente en el intervalo de energías testeadas para la búsqueda indirecta de materia oscura.

Los telescopios Florian Göbel Major Atmospheric Gamma Imaging Cherenkov (MAGIC), situados en el Observatorio del Roque de los Muchachos, en la isla Canaria de La Palma, realizan búsquedas indirectas de WIMP DM desde que entraron en operación. Entre los objetos observados con los telescopios de MAGIC, las galaxias esferoidales enanas (dSphs) satélites de la Vía Láctea y el centro galáctico y su halo son los más comunes, ya que ambos se consideran envueltos en una sobredensidad de DM.

En esta tesis presento el resultado de búsquedas indirectas de aniquilación de WIMPs en tres diferentes objetos de observación y los resultados obtenidos a partir de la combinación de los datos de varias fuentes. Ninguna señal se ha encontrado en cualquiera de los cuatro estudios.

El primer objeto analizado, el cúmulo globular (GC) M15, ha sido un reto, debido al bajo contenido de DM supuesto en este tipo de objetos y las grandes incertidumbres sistemáticas encontradas a la hora de estimar los perfiles de dispersión de la velocidad de las estrellas en sus centros. Aprovechando que M15 se había observado extensamente con los telescopios MAGIC dentro del marco de uno de los programas científicos clave (*key science programs*) de la colaboración, se ha podido analizar una gran muestra de datos, pero no se han encontrado trazas de señal de DM. Para obtener una estimación de las sensibilidades que se pueden obtener con este tipo de análisis, se han considerado cuatro diferentes perfiles de densidad de DM de M15. Se han establecido límites superiores estadísticos sobre el promedio de la sección eficaz de aniquilación de WIMPs multiplicada por la velocidad (en adelante *velocity-averaged cross-section*), considerando los perfiles de densidad de DM proporcionados en los trabajos de H.E.S.S. y VERITAS (compatibles con los resultados presentados en sus respectivas publicaciones, una vez reescalados por la muestra de datos de MAGIC que presenta un tiempo de observación más grande). Se han encontrado límites superiores de prueba considerando perfiles de densidad de DM obtenidos a partir de la convolución del perfil de densidad de M15 y de su contenido de materia no bariónica. Este último se ha obtenido con simulaciones de tipo N-body del cociente M/L en los trabajos de den Brok et al. y de Baumgardt et al., el en caso del escenario de un cuerpo dominado por DM. Los límites obtenidos con este método son mejores que los límites que se obtienen con las más prometedoras dSphs, pero al mismo tiempo son poco realistas y proporcionan solamente un valor mínimo de la *velocity-averaged cross-section* alcanzable en M15, a la espera de modelos de la formación y evolución de los GCs más precisos y, en particular, de nuevas medidas cinemáticas en las partes centrales de los GCs.

Las dSphs Draco y Coma Berenices han sido observadas durante los últimos años y analizadas, ya que son objetos de observación seleccionados por una campaña de diversificación de fuentes de observación plurianual seguida por MAGIC. En este caso, dada la ausencia de señal, se han obtenido límites superiores realistas con un 95 % de nivel de confianza en la velocity-averaged cross-section de WIMPs, los cuales se presentan en este manuscrito.

Los datos de estas dos dSphs han sido también combinados con los de otras dos dSphs observadas anteriormente con los telescopios de MAGIC, en concreto Segue 1 y Ursa Major II, para obtener la mejor sensibilidad en búsquedas indirectas de aniquilación de WIMP. Los resultados obtenidos constituyen la herencia de la colaboración MAGIC en este campo, y son los más restrictivos alcanzados en MAGIC y los más estrictos en el intervalo de masa de WIMP  $\approx 10\text{-}100$  TeV por las búsquedas en astrofísica de rayos gamma, llegando a límites superiores de l'orden de  $10^{-24}$   $\text{cm}^3\text{s}^{-1}$  sobre la velocity-averaged cross-section con un nivel de confianza del 95 %.

En la última parte de la tesis se presentan las actividades en las que he participado relacionadas con el Barcelona Raman LIDAR. Este Raman LIDAR constituye un instrumento avanzado y no comercial que ha sido construido y optimizado para satisfacer las necesidades de monitorización de la atmósfera encima de los Imaging Atmospheric Cherenkov Telescopes, en vista de un Cherenkov Telescope Array completamente operativo. Se reportan el proyecto y una serie de tests realizados sobre sus componentes.

## Resum

Encara que hi hagi una evidència contundent per al paradigma de la matèria fosca (DM) en l'univers, la naturalesa d'aquesta segueix essent desconeguda a dia d'avui, malgrat la gran varietat de teories i models proposats, i dels nombrosos experiments i instal·lacions astrofísiques que busquen les seves traces. D'entre les partícules candidates més enllà del Model Estàndard (SM) de la física de partícules, l'anomenada Weakly Interacting Massive Particle (WIMP) és de les més prometedores i la que ha estat més investigada. S'espera que la seva massa estigui entre uns pocs GeV i centenars de TeV, de manera que encaixa perfectament en l'interval d'energies testejades per a la cerca indirecta de matèria fosca.

Els telescopis Florian Göbel Major Atmospheric Gamma Imaging Cherenkov (MAGIC), situats a l'observatori El Roque de los Muchachos, a l'illa canària de La Palma, realitzen cerques indirectes de WIMP DM des de les primeres observacions, essent els objectes més habitualment observats les galàxies esferoïdals nanes (dSphs) satèl·lits de la Via Làctia i el centre galàctic amb el seu halo, ja que es pensa que estan envoltats d'un excés de densitat de DM.

En aquesta tesi presento el resultat de cerques indirectes de l'anihilació de WIMPs en tres diferents tipus d'objectes observats, així com els resultats obtinguts amb la combinació de les dades de varies fonts. Cap senyal s'ha trobat en qualsevol d'aquests quatre estudis.

El primer objecte analitzat, el cúmul globular (GC) M15, ha estat un repte, degut al baix contingut de DM previst per a aquest tipus d'objectes i a les grans incerteses sistemàtiques en l'estimació dels perfils de dispersió de la velocitat de les estrelles en el seu centre. Aprofitant que M15 s'havia observat extensament amb els telescopis MAGIC dins el marc d'un dels anomenats programes científics claus (*key science programs*) de la col·laboració, s'ha pogut analitzar una gran mostra de dades, però no s'han trobat indicis de senyal de DM. Per tal d'obtenir una estimació de les sensibilitats que es poden obtenir amb aquest tipus d'anàlisis, s'han considerat quatre diferents perfils de densitat de DM en M15. S'han establert límits superiors estadístics a la mitjana de la secció eficaç d'anihilació de la WIMP multiplicada per la velocitat (en endavant *velocity-averaged cross-section*) considerant els perfils de densitat de DM proporcionats en els treballs de H.E.S.S. i VERITAS (compatibles amb els resultats presentats en les respectives publicacions, un cop re-escalats per la mostra de dades de MAGIC, que presenta un temps d'observació més gran). S'han trobat límits superiors de prova considerant perfils de densitat de DM a partir de la deconvolució del perfil de densitat de M15 i el seu contingut de matèria no bariònica. Aquesta última s'ha obtingut amb simulacions a de tipus N-body del quocient M/L en els treballs de den Brok et al i de Baumgardt et al., en l'escenari d'un cos dominat per la DM. Els límits obtinguts amb aquest mètode són millors que els que s'obtenen amb les més prometedores dSphs, però d'altra banda són poc realistes i proporcionen només un valor mínim de la *velocity-averaged cross-section* a M15, a l'espera de models de formació i evolució dels GCs que siguin més precisos, i en particular de noves mesures cinemàtiques en les parts centrals dels GCs.

Les dSphs Draco i Coma Berenices han estat seleccionades en una campanya de diversificació de fonts del tipus dSphs observades en varis cicles anuals d'observació i les seves dades analitzades. Com que tampoc s'ha obtingut un

senyal, s'han derivat uns límits superiors realistes de la velocity-averaged cross-section amb un nivell de confiança del 95%, que es presenten en aquesta tesis.

Les dades d'aquestes dues dSphs s'han combinat amb les de les altres dues dSphs que s'havien observat anteriorment amb MAGIC, concretament Segue 1 i Ursa Major II, per tal d'obtenir una millor sensibilitat en cerques indirectes d'anihilació de WIMP. Els resultats obtinguts constitueixen el llegat de la col·laboració MAGIC en aquest camp, són els més restrictius trobats amb MAGIC i els més estrictes en l'interval de massa de WIMP entre  $\approx 10$  i 100 TeV per les cerques en astrofísica de raigs gamma, arribant a límits de l'ordre de  $10^{-24} \text{ cm}^3\text{s}^{-1}$  sobre la velocity-averaged cross-section amb un nivell de confiança del 95%.

Finalment, en l'última part de la tesis es presenten les activitats en les que he participat relacionades amb el Barcelona Raman LIDAR. Aquest Raman LIDAR constitueix un instrument avançat i no comercial que ha estat desenvolupat i optimitzat per a monitoritzar l'atmosfera sobre els Imaging Atmospheric Cherenkov Telescopes, complint amb els requeriments que el futur Cherenkov Telescope Array imposa. Es presenta el projecte del Raman LIDAR i els tests sobre els seus components en els que he participat.

*A Kira, a JJM e alla straordinaria forza della Natura.*



# Contents

<b>1</b>	<b>Introduction</b>	<b>1</b>
<b>2</b>	<b>Very High Energy Gamma-astrophysics: MAGIC and CTA</b>	<b>3</b>
2.1	Very High Energy astrophysics . . . . .	3
2.1.1	IACTs and other gamma-ray detection instruments . . . . .	6
2.2	The Florian Göbel Major Atmospheric Gamma Imaging Cherenkov telescopes . . . . .	8
2.3	The Cherenkov Telescope Array . . . . .	9
<b>I</b>	<b>WIMP Dark Matter Indirect Searches with the MAGIC Telescopes</b>	<b>12</b>
<b>3</b>	<b>Dark Matter</b>	<b>13</b>
3.1	What is the Dark Matter? . . . . .	14
3.2	Weakly Interacting Massive Particle dark matter . . . . .	19
3.2.1	WIMP candidates and other dark matter candidates . . . . .	20
3.2.2	Alternative cosmology . . . . .	23
3.3	Dark matter searches . . . . .	23
	Direct detection . . . . .	23
	Production at colliders . . . . .	25
	Indirect detection . . . . .	26
3.3.1	Dark matter indirect detection through gamma-ray observations . . . . .	30
	Dark matter sources of interest . . . . .	30
3.3.2	Gamma-ray emission from dark matter annihilation/decay . . . . .	33
	Dark matter density profile . . . . .	34
<b>4</b>	<b>The MAGIC telescope system</b>	<b>37</b>
4.1	The telescopes design . . . . .	38
4.1.1	The frame . . . . .	38
4.1.2	The reflector . . . . .	39
4.1.3	The camera . . . . .	40
4.2	The MAGIC data acquisition . . . . .	42
4.2.1	The readout chain . . . . .	43
4.2.2	The trigger system . . . . .	44
4.2.3	Calibration . . . . .	46
4.3	Environmental monitoring . . . . .	46

<b>5</b>	<b>MAGIC Data Reconstruction and Dark Matter Analysis: Theory and Methods</b>	<b>48</b>
5.1	Stereo data reconstruction and quality checks . . . . .	49
5.1.1	Data quality check . . . . .	54
5.2	Gamma-initiated shower selection and event reconstruction . .	56
5.3	Extended source analysis: Donut Monte Carlo simulation . . .	58
5.4	High-level analysis: gamma-ray flux estimation . . . . .	60
5.5	Binned likelihood analysis for dark matter targets . . . . .	64
5.6	Cut optimization for improved analysis sensitivity . . . . .	66
<b>6</b>	<b>Dark Matter Searches on M15</b>	<b>68</b>
6.1	Star clusters . . . . .	69
6.1.1	Globular clusters: dynamics and dark matter content .	71
6.2	The globular cluster M15 . . . . .	72
6.3	Data sample and quality cuts . . . . .	75
6.4	Dark matter profile evaluation . . . . .	79
6.5	Results and discussion . . . . .	83
6.6	Conclusions and outlook . . . . .	87
<b>7</b>	<b>Search for WIMP Dark Matter from the Draco Dwarf Spheroidal Satellite Galaxy</b>	<b>89</b>
7.1	The Draco dwarf spheroidal satellite galaxy . . . . .	91
7.2	Draco data sample and data reduction . . . . .	91
7.3	Flux estimation and results . . . . .	96
7.4	Discussion and conclusions . . . . .	98
<b>8</b>	<b>Search for WIMP Dark Matter from the Coma Berenices Dwarf Spheroidal Satellite Galaxy</b>	<b>102</b>
8.1	The Coma Berenices dwarf spheroidal satellite galaxy . . . . .	104
8.2	Data reconstruction and results . . . . .	105
8.3	Discussion and conclusions . . . . .	109
<b>9</b>	<b>Combination of Upper Limits from Dwarf Spheroidal Satellite Galaxies</b>	<b>114</b>
9.1	Dwarf spheroidal satellite galaxy data samples . . . . .	116
9.1.1	Revised analysis of Segue 1 . . . . .	117
9.2	Results and discussion . . . . .	117
9.3	Conclusions and outlook . . . . .	120
<b>II</b>	<b>The Barcelona Raman LIDAR for the Cherenkov Telescope Array</b>	<b>134</b>
<b>10</b>	<b>Atmospheric Characterization for the Cherenkov Telescope Array</b>	<b>135</b>
10.1	LIght Detection And Remote sensing systems . . . . .	136
10.2	CTA atmospheric monitoring plans . . . . .	138
10.3	The Barcelona Raman LIDAR . . . . .	139
10.3.1	The project and its design . . . . .	139
10.3.2	The telescope structure . . . . .	142

10.3.3	The laser and used wavelengths . . . . .	143
10.3.4	The mirrors . . . . .	144
10.3.5	The Liquid Light Guide . . . . .	145
10.3.6	The polychromator . . . . .	146
10.3.7	The acquisition system: Licel modules and software . . . . .	147
<b>11</b>	<b>Component Characterization of the Barcelona Raman LI-</b>	
	<b>DAR and Concluding Remarks</b>	<b>148</b>
11.1	Laser beam divergence test . . . . .	148
11.1.1	Theoretical background . . . . .	148
11.1.2	The experimental setup and the data acquisition . . . . .	150
11.1.3	Data analysis . . . . .	152
11.1.4	Results and discussion . . . . .	155
	Sample 3 detailed results . . . . .	155
	Sample 2 detailed results . . . . .	159
	Sample 1 detailed results . . . . .	159
11.1.5	Conclusions . . . . .	163
11.2	PMT characterization . . . . .	164
11.2.1	Experimental setup . . . . .	164
11.2.2	Data analysis . . . . .	165
11.2.3	Results and conclusions . . . . .	166
11.3	Barcelona Raman LIDAR results of the commissioning phase . . . . .	168
11.4	Conclusions and future plans . . . . .	169
<b>12</b>	<b>Conclusions</b>	<b>171</b>
	References . . . . .	175
	<b>Bibliography</b>	<b>175</b>
	<b>List of Figures</b>	<b>195</b>
	<b>List of Tables</b>	<b>207</b>
	<b>Acronyms &amp; Abbreviations</b>	<b>210</b>
<b>A</b>	<b>Specifications Quantel Brilliant</b>	<b>213</b>

# Chapter 1

## Introduction

Dark Matter (DM) is one of the notorious puzzles that Physicists have tried to solve for years. At present day, 27% of what composes the Universe still remains a mystery. Our knowledge on DM is based on several properties that stem from experimental evidence and from comparison of simulated structures of the Universe with the observed ones.

The Weakly Interacting Massive Particle (WIMP) is one of the most common candidates for representing DM, given that it satisfies all the requirements imposed by observational evidence. It is weakly interacting and couples with neither the electromagnetic nor the strong sector, and it is massive. In this way, it predicts the exact relic density that we expect from the standard cosmology.

As this non-luminous matter seems not to be part of the Standard Model (SM) of particles, but more massive and with different properties, the only way of getting information about it is when it decays or annihilate to standard baryonic matter.

In this thesis, the method adopted to shed light on DM is to search for Very High Energy (VHE) gamma-photons, primary or secondary products of annihilation of two DM particles. This is done pointing the MAGIC telescopes to regions of DM over-densities of the Universe and searching for gamma-ray spectra produced by WIMP particles over a range of hypothetical DM particle masses.

In **Chapter 2**, the Imaging Atmospheric Cherenkov Telescope (IACT) technique, that is employed by the MAGIC telescopes, is presented. After an overview of the current gamma-ray detectors, the MAGIC telescopes are introduced. At the end of the chapter, a short description of the Cherenkov Telescope Array (CTA) is given.

The thesis is then divided in two parts. The first one, up to chapter 9, is related to indirect WIMP DM searches with the MAGIC telescopes, the second one describes the Barcelona Raman LIDAR for CTA.

**Chapter 3** presents a general introduction of DM. The first part of this chapter introduces the concept and gives an overview of the properties and candidates of DM, focusing on WIMPs. The second part discusses ways of searching for it, highlighting indirect searches and the observational targets of interest for IACTs.

**Chapter 4** is dedicated to a description of the hardware of the MAGIC telescopes. In addition, the data acquisition and the environmental monitoring instrumentation are presented.

**Chapter 5** gives a detailed description of how to perform a DM analysis with MAGIC data, starting from the raw data and ending with results on the investigated DM properties.

**Chapter 6** reports the DM analysis performed on the globular cluster M15, together with a description of the different astrophysical factors used to evaluate the expected DM content of the object. At the beginning of this chapter, a description of the properties of star and globular clusters is given.

**Chapter 7** and **Chapter 8** present the analyses performed, and results obtained, on the data of the Draco and Coma Berenices dwarf spheroidal satellite galaxies (dSphs). These are the latest dSphs observed with the MAGIC telescopes in the framework of a multi-year DM target diversification project, introduced in chapter 7.

**Chapter 9**, together with the previous two chapters, form the main body of the thesis. It presents the results of the combination of data from several dSphs, included the ones reported in this thesis, that lead to the MAGIC legacy results on WIMP DM for dSphs.

The second part of the thesis starts with **Chapter 10**. The chapter begins with an introduction on the LIDAR technique and describes the atmospheric monitoring foreseen for CTA. In continuation, the Barcelona Raman LIDAR is presented.

**Chapter 11** reports two test that have been performed during the commissioning phase of the Barcelona Raman LIDAR and concludes with the latest results obtained in a data taking night shift.

The thesis will end with a general conclusion of both parts.

## Chapter 2

# Very High Energy Gamma-astrophysics: MAGIC and CTA

Our knowledge of the Universe has been acquired, so far, through the observation of light, i.e. through photons. These have given us information, starting from the lowest energies in the radio band ( $10^{-11}$  eV), to the highest ones ( $> 10^{14}$  eV), with gamma rays. Gamma rays in the Very High Energy (VHE) regime ( $10^{11} - 10^{14}$  eV) are the starting point of this thesis. Imaging Atmospheric Cherenkov Telescopes (IACTs), such as MAGIC and CTA, can detect Cherenkov light produced by gamma photons reacting with the Earth's atmosphere, and these, in turn, give us insights on non-thermal processes in the Universe.

In the first part of this chapter (section 2.1), a general overview on gamma rays and *Extensive Air Showers* (EASs) will be given. At the end of the section, the Cherenkov technique will be described, and the current gamma detection experiments will be presented. In section 2.2, a detailed description of the MAGIC telescopes will follow. The chapter will end with an introduction to the Cherenkov Telescope Array. This last part will be useful for entering in the second part of the thesis, in which the Barcelona Raman LIDAR will be presented.

### 2.1 Very High Energy astrophysics

VHE gamma-rays are produced in non-thermal processes in the Universe. The latter are so-defined, as they cannot be described in terms of radiation from particles in thermal equilibrium, and are produced in the so-called *violent Universe*. The mechanisms that contribute to their creation are: synchrotron radiation, inverse Compton radiation, thick-target Bremsstrahlung, electron-positron annihilation and proton-proton interactions, among others. All these processes take place by the interaction of energetic charged particles with matter or magnetic fields. Some of these particles reach the Earth where they are detected as *Cosmic Rays* (CRs), with the highest energies observed (up to  $10^{20}$  eV). They are of fundamental importance to understand the composition and evolution of the Universe. However, their origin cannot be traced back,

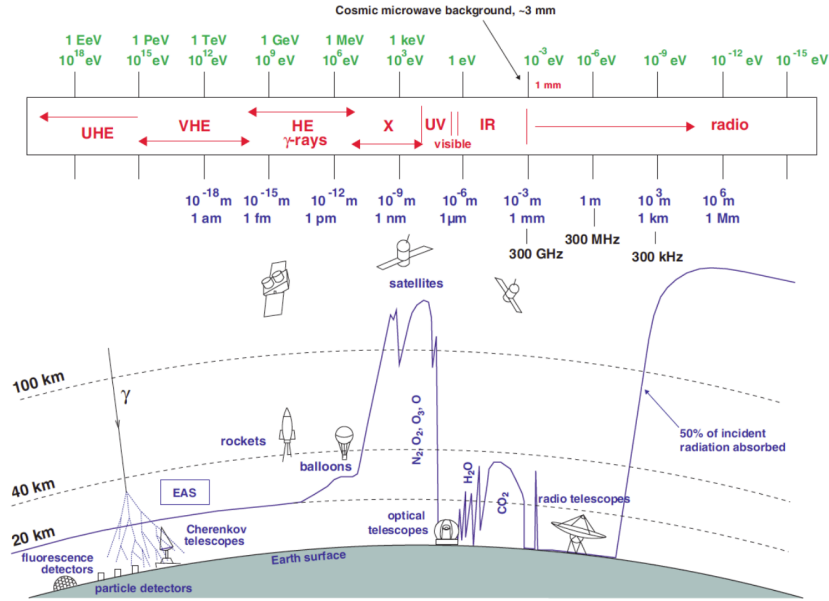


**Figure 2.1:** Electromagnetic spectrum associated to the instruments that can detect photons in a precise energy interval. Credits to [1–3].

since their interactions with the Galactic and Intergalactic magnetic fields deflect their path to the Earth. Photons, on the other hand, are neutral particles that can travel mostly undisturbed from their production point to the Earth. The energy of the photon determines its possibility of being detectable on the Earth’s surface, see Fig. 2.1.

Photons with energies between neV and  $\mu$ eV are observable with radio telescopes, and in the infrared/visible, with optical telescopes. To observe photons at different energies, one needs to go to space (e.g. with satellite telescopes), except in the case of VHE gamma-rays. In this case, the gamma photons can be detected indirectly from ground, using the atmosphere as a giant calorimeter. When gamma photons reach the atmosphere, they start to interact with the electrostatic field of the atmospheric molecules and nuclei, initiating a particle cascade called *Extensive Air Shower*. Each interaction between an energetic photon and a virtual photon of the electrostatic field generates an  $e^+e^-$  couple that, subsequently, radiates photons through bremsstrahlung. This latter radiation, if sufficiently energetic, produces another  $e^+e^-$  couple and so on, giving life to an ElectroMagnetic (EM) shower. The *radiation length* of bremsstrahlung for electrons and positrons in air and the mean free path of the gamma rays are quite similar ( $\approx 1$  km at 10 km a.s.l.). For this reason, the resulting cascade is mostly symmetric and compact, as the charged particles do not scatter too much from the shower axis. The development of an EM shower is sketched in the left part of Fig. 2.2.

The process of multiplication of the number of  $e^+e^-$  terminates when the kinetic energy of the electron/positron  $E < E_C$ , where  $E_C$  is a critical energy of  $\sim 86$  MeV in the atmosphere. At this energy, the number of shower particles has reached its maximum, and the energy loss through ionization starts

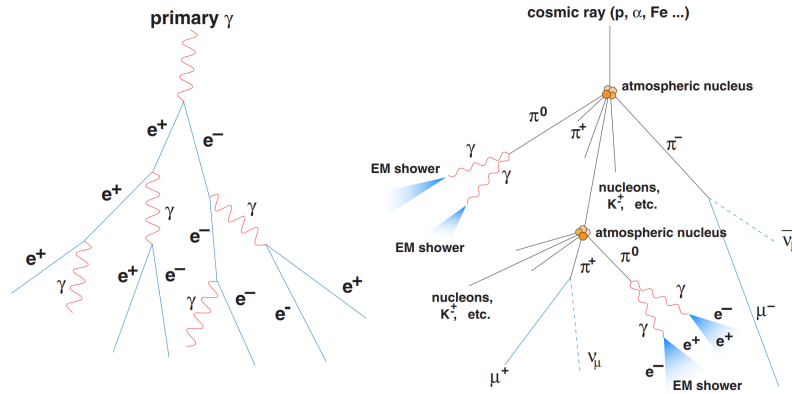


**Figure 2.2:** Comparison of the development of an EM shower (*left*) w.r.t. a hadronic shower (*right*). Image taken from [3].

to dominate. The altitude at which this happens it called *height of the shower maximum* ( $H_{max} \propto \ln(E')$ ), where  $E'$  is the energy of the primary gamma ray, and typically is found at around 10 km from the ground for a 100 GeV gamma-ray. It is worth to notice that, as the interaction length of gamma rays with the atmosphere is, in first order, independent of the energy of the primary photon, the first gamma ray interaction can be found at a similar height on average, for different gamma-ray energies. This altitude is at 20-30 km a.s.l.

Another type of EAS can be found in the atmosphere, schematically represented on the right side of Fig. 2.2. Hadronic showers are created by the interaction of nuclear CRs and atmospheric nuclei: initially a proton interacts with the atmosphere, producing pions with 90% probability, and kaons and nucleons for the remaining 10%. In this case, the cascade stops when the energy per nucleon is lower than the one needed for pion production ( $\sim 1$  GeV). The composition of these types of showers consists of hadrons (nuclei and mesons), photons, electrons and positrons, and muons.

As sketched in the figure, hadronic showers are more extended than EM ones, because of the possible large transversal momenta of kaons and pions. They are also less symmetric, and develop later than EM showers.

The charged particles produced during an EM cascade travel at a velocity greater than that of light in the medium, the Earth's atmosphere, and therefore emit *Cherenkov radiation*. This type of radiation is fundamen-

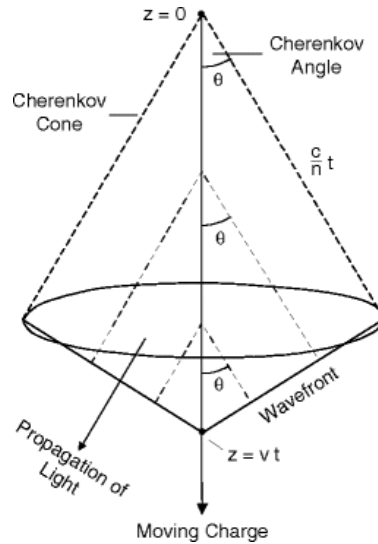


**Figure 2.3:** Schematic view of the Cherenkov radiation emitted by a charged particle when travelling in a medium. Credits to [4].

tal to allow the detection of air showers through IACTs, that base their working principle on this effect. On ground, Cherenkov light appears as a bluish radiation, peaked at around 320 nm, in the UV band. As shown in Fig. 2.3, it develops in a conic surface that presents an angle of aperture  $\theta$  with respect to the direction of flight of the charged particle travelling at a superluminal velocity. The emission angle is written as:

$$\cos(\theta) = \frac{c'}{v} = \frac{c}{vn(\lambda)} \quad (2.1)$$

where  $c' = c/n$  is the speed of light in the medium, that present a refractive index as a function of the wavelength  $n(\lambda)$ , and  $v$  is the velocity of the charged particle.

The Cherenkov rings, produced by the latter, propagate to the ground, ending up in an area called the *Cherenkov light pool*. If the gamma photon generating the EAS arrives perpendicular to the Earth's surface, and considering that the Cherenkov angle of emission is about  $1^\circ$ , the Cherenkov light pool presents a diameter of  $\sim 250$  m, and a light density proportional to the energy of the gamma-ray that initiated the shower (valid only in the case of EM showers). Inside this diameter and above gamma-ray energies of  $\sim 100$  GeV, the Cherenkov photon density can be considered approximately uniform, slightly raising up towards the outer edges of the pool. This effect is due to the increase of  $\theta$  as a function of the refraction index encountered while charged particles penetrate through the atmosphere.

Another aspect to take in consideration when looking for the extension of the Cherenkov light pool is the zenith angle of observation. For low zenith angles, as the shower is almost perpendicular to the ground, the pool is smaller, but has a higher density of photons for a given energy, while at *large zenith angles* (LZA) the shower is more distant, the light pool is larger and the photon density lower. As a consequence, at LZA the shower has a higher probability of being scattered/attenuated by the aerosols and molecules present in the atmosphere, travelling a larger path, and the EAS initiated by more energetic gamma-rays are most likely to be detected.

### 2.1.1 IACTs and other gamma-ray detection instruments

As already mentioned, the *Imaging Atmospheric Cherenkov Technique* is based on the detection of Cherenkov photons emitted in EAS (Fig. 2.4). If an EAS lies in the Field of View (FoV) of an IACT, its emitted Cherenkov light can be reflected by the receiving mirrors and collected in a fast pixelized camera (usually composed by PhotoMultiplier Tubes, PMTs, due to their velocity and efficiency in detecting the Cherenkov light flashes). The image created is, then, a projection of the EAS, and spatial and timing information can be obtained directly from it. In addition, the Cherenkov light density that reaches the ground is used to reconstruct the energy of the initial gamma photon. In this scenario, hadronic showers are not of interest for IACTs, as their provenance cannot be reconstructed properly, and they form part of the background detected by the telescopes.

Typically, IACTs are built in arrays of telescopes, in order to perform stereoscopic observations, that help to reconstruct properly the geometrical parameters of the detected EASs, improving the angular resolution and the rejection

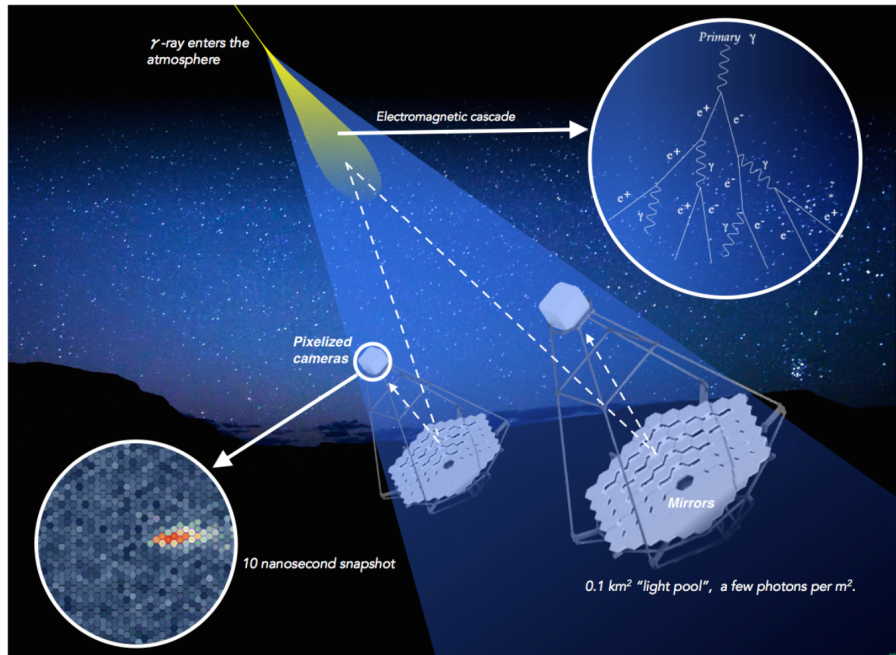


**Figure 2.4:** Representation of the IACT technique. The Cherenkov cascade is reflected by the telescopes' mirror to the camera, where the signal is collected. Image taken from CTA website [5].

of the hadronic background. Current experiments of this type are MAGIC (described in the following lines), H.E.S.S. [6] (top left of Fig. 2.5), VERITAS [7] (top right of Fig. 2.5) and CTA (introduced at the end of this chapter). To look for gamma photons at lower energies, not sufficiently energetic to create EAS, satellite detectors, such as Fermi-LAT [8] (bottom left of Fig. 2.5), are needed. These kind of experiments can directly detect gamma rays by pair conversion of the gamma photon in the detector layers. Moreover, they can benefit from a large duty cycle, a large FoV and a proper energy calibration, as they are tested with real particle beams at ground-based accelerators before being launched. The only drawback is that they are limited in size, thus the surface available for collecting the signal is several orders of magnitude smaller than the one of an IACT.

On the other extreme of the VHE interval, water Cherenkov detectors, such as HAWC [9] (bottom right of Fig. 2.5), have better performance. This is due to the extremely large duty cycle (the only dead time are due to instrumental shut off) and the wide FoV.

In the following section, more details about the MAGIC and CTA arrays of IACTs will be given.

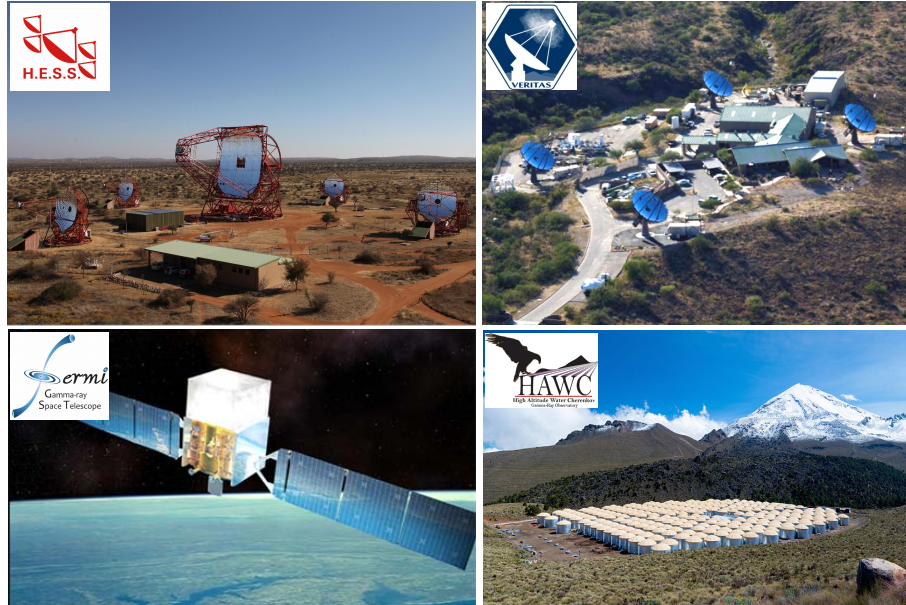


**Figure 2.5:** In order, a picture of the H.E.S.S. experiment (*top left*) [Credits to: H.E.S.S. Collaboration, Clementina Medina], a picture of the VERITAS experiment (*top right*) [Credits to: K. Gibbs & N. Galente, Whipple Observatory], an artistic representation of the Fermi-LAT experiment (*bottom left*) [Credits to: NASA E/PO, Sonoma State University, Aurore Simonnet] and a picture of the HAWC experiment (*bottom right*) [Credits to: Jordana Goodman].

## 2.2 The Florian Göbel Major Atmospheric Gamma Imaging Cherenkov telescopes

The MAGIC (Major Atmospheric Gamma Imaging Cherenkov telescope) telescopes are an experiment supported by an international collaboration consisting of more than 250 members from all over the world. After the inauguration of the first telescope MAGIC 1 (M1) in 2004, the system worked in mono-mode for five years and became, in 2009, a stereoscopic system composed of two IACTs (added M2), at a distance of  $\sim 85 \text{ m}^1$  from each other.

The MAGIC telescopes, together with the electronics and remote control building (the Counting House, CH), are located at the Observatorio del Roque de los Muchachos, on the Canary Island of La Palma (see Fig. 2.6), at an altitude of 2235 m a.s.l. ( $28.8^\circ\text{N}$ ,  $17.8^\circ\text{W}$ ). The site is renowned for harbouring numerous astronomical installations, due to the excellent weather conditions found, among the best in the world (the temperature varies from a minimum of  $-8^\circ \text{C}$ , in January/February, to a maximum of  $26^\circ \text{C}$  during the summer). A noticeable fact is that the particular microclimate of the island causes the

<sup>1</sup>The choice of the distance is not arbitrary, but due to the fact that for detecting a same EM shower with both telescopes, the maximum distance should be  $\sim 250\text{m}$ , which is the average diameter of an EM shower.



**Figure 2.6:** Location of the MAGIC telescopes. In the map on the background, some of the countries part of the MAGIC Collaboration are marked in light blue. Other member countries are not visible, because of the zoom into only a part of the world.

formation of a quasi-permanent temperature inversion layer at low altitude (between 1000 m and 2000 m) blocking clouds and aerosols from moving up to the altitude of the mountain rim, at 2420 m a.s.l., the Roque de los Muchachos. Moreover, the local laws in force, together with the specific location (the observatory is at the center of a natural reserve) reduce the light pollution almost to zero, improving the quality of the data acquired. Nevertheless, occasional strong winds (from the Northern sector of the island, but the storms come from South-East), winter snowfalls, calima<sup>2</sup> and high humidity are possible, and demand a strong technical effort to prevent damaging and ageing.

### 2.3 The Cherenkov Telescope Array

The Cherenkov Telescope Array (CTA) is the next generation of ground-based telescopes that makes use of the IACT technique [10]. The project was proposed in 2005 and is now supported by 1500 collaboration members coming from more than 200 institutes from 31 countries.

The proposal for the array foresees the construction of three different sizes of telescopes on both Earth's hemispheres (see Fig. 2.7): an array of 19 telescopes placed on the Canary Island of La Palma (CTA-N) and another array of 99 telescopes in the Atacama Desert in Chile (CTA-S). In the smaller array, the one in the northern hemisphere, 4 Large Size Telescopes (LSTs) and 15 Medium Size Telescopes (MSTs) are planned. The first ones presenting a reflective surface

<sup>2</sup>An fine Saharan sand transported by the wind from Africa which, for some days of a year, cover the entire sky.

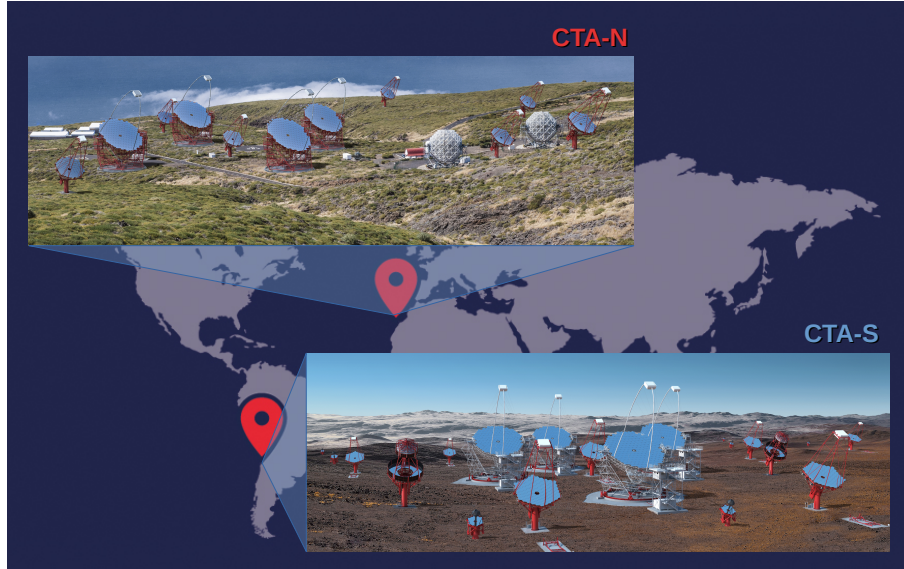


**Figure 2.7:** Artistic representations of the northern (CTA-N) and southern (CTA-S) sites approved for the construction of the Cherenkov Telescope Array. Credits to Gabriel Pérez Díaz and Marc-André Besel (Cherenkov Telescope Array Observatory, CTAO) for the two representations.

of 23 m diameter and the second ones of 12 m diameter. The energy range covered by the northern array will range from 0.02 TeV to 20 TeV. On the other hand, the southern array, in the Atacama Desert is foreseen to reach up to 300 TeV, thanks to the presence of 70 Small Size Telescopes (SSTs) of 4 m diameter each. In addition to these telescopes, 4 LSTs and 25 MSTs will be constructed, covering a total surface of 4 km<sup>2</sup>.

CTA will reach a sensitivity more than a factor 10 better than the MAGIC telescopes, as shown in Fig. 2.8 and would be the the most powerful ground-based instrument for detecting VHE gamma-rays.

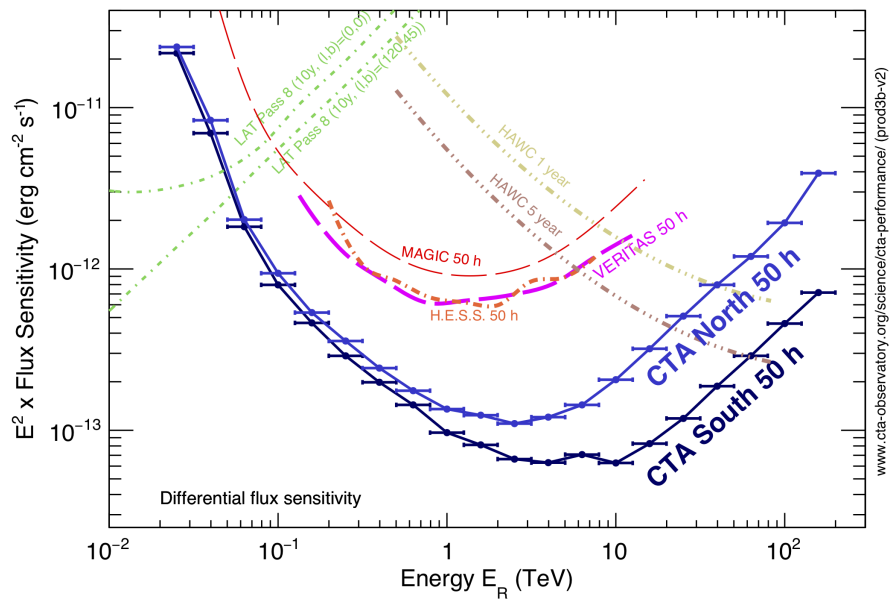


**Figure 2.8:** CTA sensitivity, for each construction site, w.r.t. the sensitivity of other gamma experiments operative at the current days.

## Part I

# WIMP Dark Matter Indirect Searches with the MAGIC Telescopes

## Chapter 3

# Dark Matter

The Dark Matter (DM) paradigm was first postulated by F. Zwicky in 1933 [11] following hints of observation of a new massive, non-luminous and gravitationally interacting type of matter. After this first evidence observed in the velocity dispersion of galaxies in the Coma galaxy cluster, several other probes followed successfully identifying this new category of matter in both galactic and extragalactic scenarios (mass estimates of galaxy clusters [12], variations in galaxies' rotation curves [13], *Cosmic Microwave Background* (CMB) anisotropies [14], gravitational lensing observations [15], the Bullet cluster galaxy collision [16,17] the Sunyáev-Zeldóvich effect in galaxy clusters observations [18], etc.). A large number of theories (particle DM, baryonic DM, MODified Newtonian Dynamics [19–21], etc.) and models (such as Lambda-Cold Dark Matter [22], warm DM and hot DM) were postulated, trying to describe the nature of this hitherto unknown phenomenon. The failure in describing DM particles with the Standard Model (SM) of particle physics alone led the community to the contemplation of numerous new classes of elementary particles. The search for these particles has, in any case, to deal with SM particles, producing DM at the colliders or looking for its effects, either directly (*direct detection*) or observing its SM particle products (*indirect detection*).

In this chapter, I will first describe the properties of DM presented currently in the literature and list the candidates that could compose this non-luminous matter (section 3.1). I will, then, focus on the different kinds of searches performed to unveil its nature and report the latest results obtained in the field (section 3.3). In section 3.3.1, I will describe the indirect DM searches using *Very High Energy* (VHE) gamma-astronomy, pointing out the sources of interest and describing quantitatively the DM content of them. This last part will link to the DM analysis described in the next chapter.

### 3.1 What is the Dark Matter?

The first adjective associated by F. Zwicky to this unknown type of matter was *dark* [11], as it was not luminous, but revealed thanks to its gravitational interaction with the luminous baryonic matter, of which stars and galaxies are composed of. Multiple definitions for DM popped up in later times, changing continuously along the years, and different candidates have been proposed to be part, or constitute the totality, of it. However, its characteristics, determined by the evidence of DM in the Universe at all scales, remained largely unaltered, or were just subject to small corrections. The properties retrieved during the years are listed in the following lines.

In general, **DM is not-luminous, neutral**, otherwise it could couple with photons and therefore would not be dark, and **gravitationally, and possibly weakly, interacting**. Strong interactions, similarly to the couplings with the electromagnetic sector, are highly suppressed if taking into account the observations<sup>1</sup> [23] (even if DM models taking into account DM candidates strongly interacting have been proposed [24,25]). In addition, DM results to be **collisionless**, as observed in the spectacular case of the Bullet cluster 1E0675-558 [16], considered one of the strongest evidence of its presence, and **stable** (discussed in the next section). If we look at DM from a cosmological point of view and consider different scales of magnitude, other properties can be inferred.

First of all, it is well established that **DM makes up  $\sim 27\%$  of the energy budget of Universe**, while the remaining  $\sim 73\%$  is composed of baryonic matter ( $\sim 5\%$ ) and *dark energy*<sup>2</sup> ( $\sim 68\%$ ) [26]. These numbers have been estimated in the benchmark of the *Lambda*<sup>3</sup> Cold Dark Matter ( $\Lambda$ CDM) cosmology [22], a model describing the cosmic structure formation and evolution. This model is based on *general relativity* and the *Cosmological Principle*<sup>4</sup>, and presents CDM, i.e. particle DM candidates with a non-relativistic behaviour at the moment of the freeze-out (epoch in the early universe in which DM drops out of the thermal equilibrium with the SM particles), as the main ingredients. The  $\Lambda$ CDM model, having the *big bang theory* as one of the pillars, contains a transition from a *radiation dominated era* of the Universe, in which an expanding very hot plasma of particles is present, and where high energetic photon radiation prevents complex structure formation, to a *matter dominated era*, in which the temperature of the Universe has cooled sufficiently down, such that the Universe has become transparent to photons and large structure could form thanks to the gravitational attraction, accreting matter from smaller structures into larger ones. The current epoch of the Universe is the last era predicted by the  $\Lambda$ CDM model, in which the expansion rate of the Universe is accelerating, under the negative pressure of an unknown form of energy, the so-called *dark energy*.

In this context, the CMB is an important means to obtain information about

<sup>1</sup>In presence of strong interaction, an electromagnetic counterpart would have been seen.

<sup>2</sup>Unknown form of energy, hypothesized to permeate all the Universe, that seems to drive its accelerated expansion.

<sup>3</sup>The cosmological constant introduced by Einstein in his general relativity equations [27] to explain the accelerated expansion phase of the Universe, in which we are nowadays.

<sup>4</sup>It states that the Universe, at large scales, is homogeneous and isotropic.

the evolution of the Universe. It is composed of a radiation at an actual temperature of 2.73 K [28] emitted during the *recombination era* (just before the *matter dominated era*), an epoch of the Universe in which the temperature was low enough to permit electrons to combine with atomic nuclei becoming electrically neutral hydrogen atoms and, therefore, allowing photons to freely propagate in the Universe with a homogeneous temperature. This relic radiation is the most precise black-body spectrum found in nature, but shows also anisotropies of the order of  $10^{-5}$  K, as visible in the top image of Fig. 3.1. Given the assumed production process of this CMB, its temperature anisotropies are directly related to the fluctuations in the primitive baryon density. Areas with high baryonic density correspond to cold spots in the CMB map (in blue) and under-densities correspond to warm ones (in red). This baryon-photon relation is of utmost importance to describe the evolution of the Universe and is quantifiable looking at the temperature power spectrum of the primary CMB, shown in the bottom image of Fig. 3.1 for the case of the Planck satellite measurements [26]. In particular, the peaks shown come from the oscillations of the baryon-photon plasma in the early Universe. The odd peaks correspond to compressions determined by radiation pressure and baryon gravitation potential (larger for large masses) while even peaks correspond to decompression driven only by pressure. From the position of the first peak and the relative amplitude of the second peak with respect to the first, one can infer the overall energy content of the Universe and constrain the baryonic density, respectively [26].

Other information on the baryon-photon relation is given by the *baryonic acoustic oscillations* (BAO) detectable nowadays. These are relativistic acoustic waves, frozen during the *photon decoupling*, resulting from the interplay between gravity and radiation pressure.

To completely define the value of the relic densities in the  $\Lambda$ CDM model, the scale factor has to be defined correctly. In order to do this, type Ia supernovae are used as standard candles for calibrating distance measurements, as at the moment of explosion they have a standard luminosity curve [30].

DM has not been mentioned in these lines regarding the CMB, but it has a leading role in describing its anisotropies and, as a consequence, the structure formation of the Universe. The fluctuations given only by baryonic matter would not have been enough to create the structures we see nowadays, thus the anisotropies in the CMB have led to add DM as a creator of the above-mentioned primordial gravitational potential wells. In fact, DM got decoupled when photons and baryons were still in thermal equilibrium and strongly interacting. In that way, the density fluctuations of DM began growing earlier than the ones of the baryonic matter. When baryonic structures collapsed, they fell into the already existing potential wells created by DM over-densities, and went on growing up following the *hierarchical structure scenario*. In the absence of DM, the baryonic perturbations would have been washed out and no characteristic correlation scale would be observed today.

In order to get structure formation leading to the correct current Universe, one needs to consider a *cold* type of DM: if the DM particle pressure due to their free-streaming velocity had not been smaller than the one associated to their mass, we would not see the present Universe, as the relativistic DM particles would not have permitted baryonic particles to aggregate into structures. Nevertheless, the CDM is not the only type of DM theorized. Depending on the

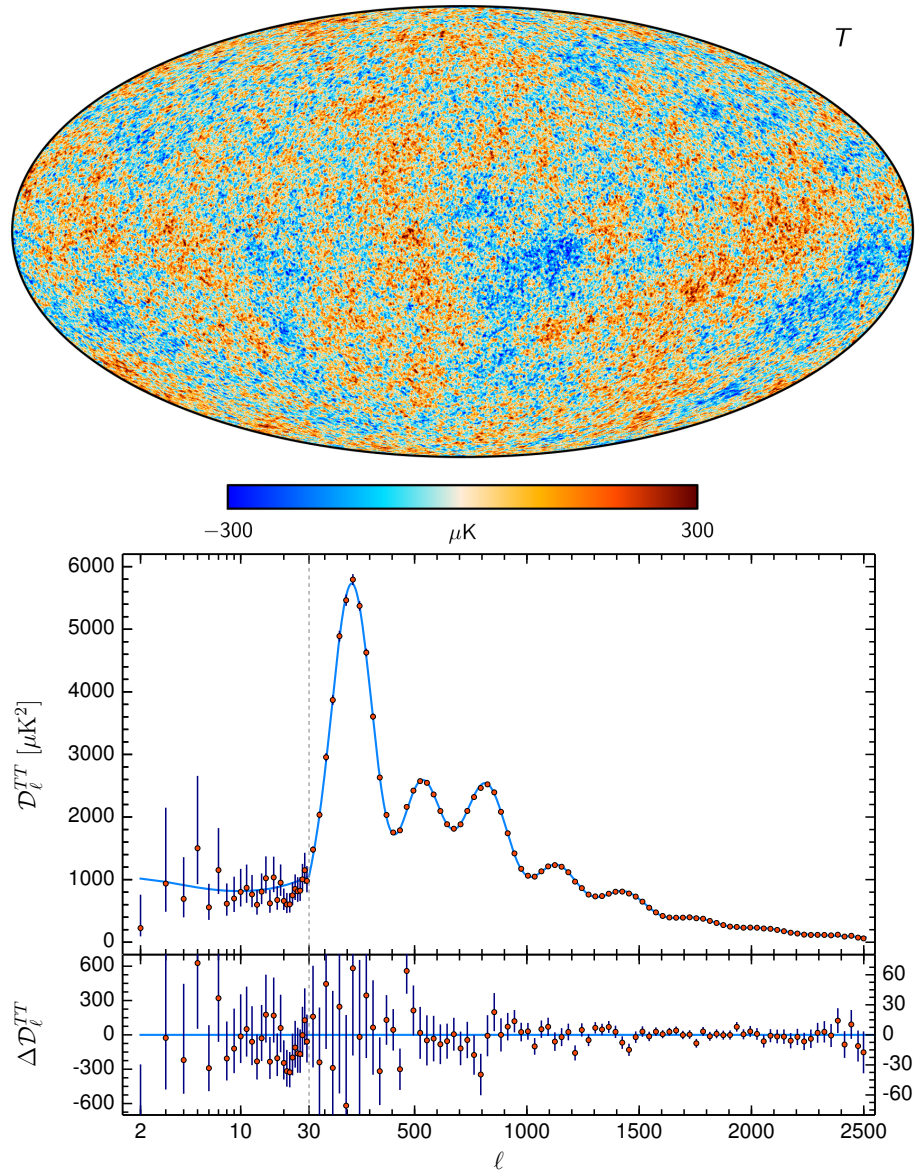


**Figure 3.1:** Planck satellite map of the temperature anisotropies of the CMB, retrieved using the SMICA method [29] (*top*) and the retrieved temperature power spectrum [26] (*bottom*). In the graphics on the bottom, the temperature power spectrum points have been fitted with a base- $\Lambda$ CDM theoretical spectrum (*light blue line*). In the bottom part of the plot, the residuals are shown. Credits to ESA and the Planck Collaboration.

DM velocity at the moment of the freeze-out, DM can be differentiated into three types:

- **hot DM (HDM)**: the particles were relativistic at the freeze-out (mass of the order of the eV or smaller). Candidates for this DM are the SM neutrinos [31, 32];
- **warm DM (WDM)**: the particles have masses around the keV and are becoming non-relativistic in this era. Their velocity at freeze-out falls somewhere in between the cases of HDM and CDM. Candidates for these are the gravitinos, the sterile neutrinos and some non-thermal Weakly Interacting Massive Particles (see next section for more details);
- **cold DM (CDM)**: the masses of these particles are in the GeV-TeV scale and these were non-relativistic at freeze-out. The most studied candidates are the neutralinos and Kaluza-Klein states (see next section for more details).

Numerical simulations, referred to as *N-body simulations*<sup>5</sup>, are used to properly model the structure formation and evolution scenario, from the initial DM density to the largest DM halos today, and provide a way to discriminate among different classes of DM candidates. In order to carry out this distinction, one has to introduce a DM initial velocity distribution as input for the simulations [33, 34] and compare the results with the observations of the actual patterns of structure found in the Universe, performed by sky surveys [35–37]. An example of this procedure is presented in Fig. 3.2.

One of the outcomes of these studies is the differentiation between a hierarchical, or *bottom-up*, process of structure formation and a *top-down* one. The former is possible only in the presence of CDM, as the growth of small scale structures is predicted to be suppressed in the case of HDM [40, 41]. On the other hand, HDM could form very low mass halos in the early Universe, that could have merged to gradually build larger and larger DM structures. If sticking to the case of the hierarchical structure scenario, as CDM accounts better for the observed patterns of large scale structure, three main issues appear when comparing DM-only simulations and observations [42]:

- **Missing satellite problem**: N-body DM-only simulations predict more satellite galaxies in orbit around the Milky Way compared to the ones actually observed [43];
- **Cusp/Core controversy**: some data of dwarf spheroidal satellite (dSph) galaxies point to a shallow central slope of the density profile, not found in the simulations [44];
- **Too big to fail problem**: observed galaxies are not as large as the ones simulated [45].

The presented issues show a failure of the  $\Lambda$ CDM model at small (galactic and sub-galactic) scales, if taking into account DM-only simulations, and have led

---

<sup>5</sup>The name comes from the fact that these simulations keep track of the many-body gravitational interactions between DM halos as they merge together to form even larger structures.

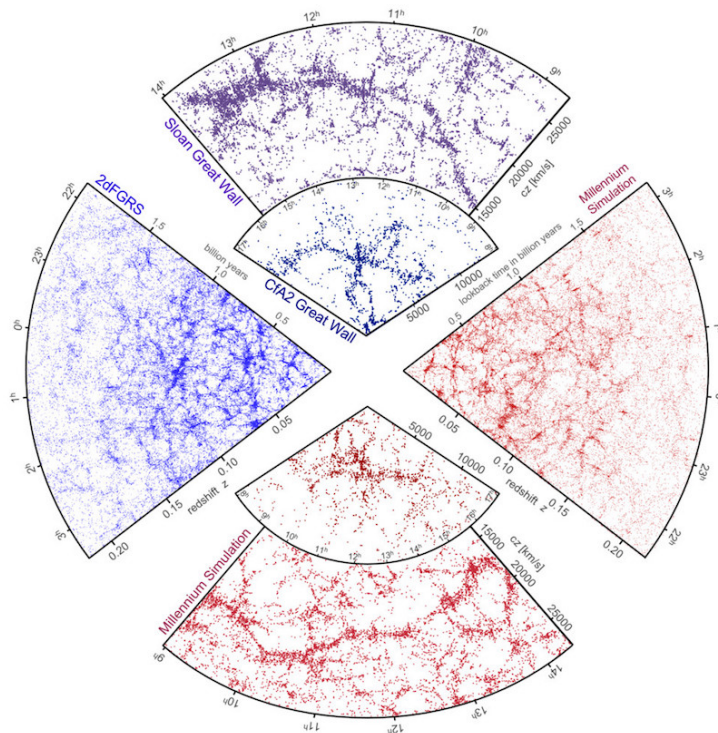


**Figure 3.2:** Large scale structure of the Universe mapped by the 2dF Galaxy Redshift Survey [37] (*left panel*) and by the Sloan Digital SkySurvey [35] (*top panel*), and obtained with the *Millennium simulations* [38] for the corresponding portions of the sky (*right and bottom panels, respectively*). Figure taken from [39].

to take into account WDM as possible solution to these problems [46, 47]. The pros in considering WDM is given by its free-streaming length, longer than the one of CDM, that washes out structures at small scales. Another possibility for solving these puzzles is the inclusion of baryons in the simulations. In fact, the presence of baryons tends to flatten the inner part of the DM halos, thus giving an answer to the core shape of the dSphs, predicted, by the previous simulations, to present very cuspy profiles. Moreover, the *Missing satellite problem* seems to disappear when taking into account tidal stripping and feedback given by the introduction of baryons in N-body simulations [48]. In this way, some of the subhalos are destroyed, pushing their number down to observed levels. Nevertheless, the *Too big to fail problem* cannot be explained just with the introduction of baryons. Self-interacting dark matter, which provides dark matter subhalo central densities lower than the ones predicted with only CDM [49], needs to be introduced. Even if this property of DM has still to be proven, analytical models appear to support its valence.

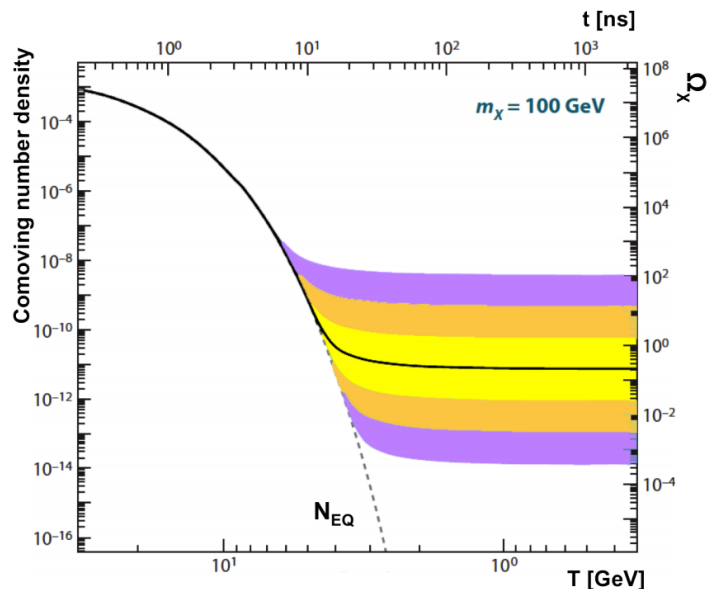


**Figure 3.3:** Comoving number density (left axis) and thermal relic density (right axis) of an annihilating DM particle of mass  $m_\chi = 100$  GeV, as a function of the inverse temperature of the Universe  $T$  and the time  $t$ . The solid black line corresponds to the annihilation cross-section that yields the correct relic density. The yellow, orange and violet regions correspond to cross-sections that differ from the central value for a factor 10, 100 and 1000, respectively. The dashed black line depicts the number density  $N_{\text{EQ}}$  of a particle that remains in thermal equilibrium. Image adapted from [52].

### 3.2 Weakly Interacting Massive Particle dark matter

Following the  $\Lambda$ CDM scenario, a Weakly Interacting Massive Particle (WIMP) has been considered the best candidate to provide a major contribution to DM so far [50], due to the fact that it presents all the properties previously listed and it naturally accounts for the present DM density (the so-called *WIMP miracle* [51]). As all other particles at the epoch, DM particles were in thermal equilibrium in the primordial plasma. The temperature of the Universe was gradually decreasing, inversely to its expansion rate. When the temperature of the Universe had dropped below the value of the DM mass  $m_\chi$ , the latter decoupled from the rest of the particles, its production ended and, consequently, its density started to decrease exponentially. At this stage, the Universe was already so expanded that the density of DM was not sufficient to give rise to the annihilation process. DM particles then *froze-out* with a number asymptotically approaching a constant, the so-called *thermal relic density*. This evolution is shown in Fig. 3.3.

The comoving number density, presented in the figure, is the ratio  $Y = n/s$  between the DM number density  $n$  and the total entropy of the Universe  $s$ . It is defined as the density in a comoving volume  $V_C$ , in which the number

densities of non-evolving objects locked into the Hubble flow are constant with redshift. Starting from the Boltzmann equation, calculating the comoving DM number density, whose evolution is governed by the cross-section thermally averaged on the velocity of the DM incident particles  $\langle\sigma v\rangle$  [53], namely *velocity-averaged cross-section*, and solving the equation for the DM abundance today, the thermal relic density results to be [46, 52]:

$$\Omega_\chi h^2 \simeq \frac{10^{-26} \text{cm}^3 \text{s}^{-1}}{\langle\sigma v\rangle} \quad (3.1)$$

where  $h$  is the scaled Hubble constant.

One of the possibilities for obtaining this value is to take into account a weakly interacting DM particle, whose temperature at freeze-out should have been  $T \sim m_\chi/10$  [54], thus, with a mass in the GeV-TeV range [55]. In addition, this particle has to be stable, or with a mean life-time  $\gg t_U$  (lifetime of the Universe), and dissipationless<sup>6</sup>, such as to exist at present day. These characteristics, together with the naturalness in producing these kind of particles in new particle physics model (see next section), makes WIMPs excellent DM candidates, making up the *WIMP miracle*.

It should be noticed that SM particles do not have the characteristics required for DM (except for the case of the neutrino). In order to find appropriate candidates for a WIMP, new theories beyond the SM had to be produced.

In the next section, a list of possible WIMP candidates, together with other DM candidates, will be presented.

### 3.2.1 WIMP candidates and other dark matter candidates

No Standard Model particle can fulfil the requirements for being a WIMP. To overcome this, new particles beyond the SM have been selected as the best candidates until now.

For this work, I will concentrate on the SuperSymmetry (SUSY) theories and the DM candidates they can provide.

These theories pair bosons with SUSY partner fermions, and vice-versa: for each SM particle, the existence of a new particle with the same set of quantum numbers and gauge interactions, and spin increased by  $+1/2$ , is conjectured. The original aim of this model was to solve several theoretical problems of the SM: the *hierarchy problem* [56], the observation of strong CP violation in experiments [57] and the imperfect unification of gauge couplings at the Planck scale ( $M_{Pl} \sim 10^{19} \text{GeV}$ )<sup>7</sup> [58].

A general supersymmetric extension of the SM (SUSY) contains many unknown parameters. The reduction of these parameters, and related particles, to a minimum number, results in the most commonly adopted Minimal SUSY model (MSSM) [59]. Nevertheless, symmetry breaking (the CP violation) leads

<sup>6</sup>Thus, being unable to cool by radiating photons during, e.g., galaxy formation.

<sup>7</sup>*I.* It questions the smallness of the Higgs boson's mass with respect to the value it would have introducing radiative corrections. The discrepancy is, then, solved by cancelling the divergences in the radiative corrections through the establishment of the SUSY theory; *II.* To avoid this problem, an ad hoc symmetry in an extension of the SUSY model has been introduced; *III.* The unification is possible if SUSY particles are included in the renormalization-group equations.

to a proton lifetime far shorter than the age of the Universe due to the different masses between particles and super-particles. Therefore, an ad-hoc discrete symmetry, the *R-parity*, has been introduced to solve this issue.

If *R-parity* is conserved, the supersymmetric particles of the MSSM can only be produced/annihilated in pairs, and, thus, the lightest SUSY particle (LSP) becomes stable. As it is expected to be heavy, neutral and, as just pointed out, stable, it fits perfectly into the  $\Lambda$ CDM prediction on the nature of DM [60].

Among the numerous new particles of the MSSM extension, the *gravitino*, the *sneutrinos* and the *neutralino* are the ones that match naturally with the characteristics of DM. The spin 3/2 fermion *gravitino* is a supersymmetric field that qualifies as DM in some particular scenarios [61, 62]. Although theoretically well motivated, it would be very difficult to detect, as interacting only gravitationally, and it is, thus, not contemplated in DM searches. In a similar way, the *sneutrinos*, spin 0 scalars, are not taken into account, as underabundant (given their large annihilation and scattering cross-sections) or still undetected in direct detection experiments. The best candidate for DM is, then, the *neutralino*. It is a spin 1/2 fermion, superposition of fermionic spartners (SUSY partners) of SM bosons (the bino  $\tilde{B}^0$ , superpartner of the weak hypercharge gauge boson, the wino  $\tilde{W}_3^0$ , superpartner of the electroweak interaction mediating boson, and the Higgsinos  $\tilde{H}_u^0, \tilde{H}_d^0$ , superpartners of the neutral Higgs bosons). It shows up in four states  $\tilde{\chi}_{1\dots 4}^0$ . The lightest of these ones (LSP) is defined as:

$$\chi \equiv \tilde{\chi}_1^0 = n_{11}\tilde{B}^0 + n_{12}\tilde{W}_3^0 + n_{13}\tilde{H}_d^0 + n_{14}\tilde{H}_u^0 \quad (3.2)$$

where  $n_{ii}$  are the respective weights of each superparticle. This is the principal DM candidate, since it is stable, if the R-parity is a conserved symmetry, and all the heavier particles can decay into it.

Being a Majorana fermion<sup>8</sup> the *neutralino* can self-annihilate into SM particles:

- *Fermions*: the leading neutralino annihilation channels are into fermion pairs at tree-level, via the *s*-channel through the exchange of *Z* or Higgs bosons, or via the *t*-channel through sfermion exchange. The dominant final states are composed by heavy particles, like  $\tau^+\tau^-$ ,  $b\bar{b}$  and  $t\bar{t}$  (for sufficiently high masses);
- *Photons*: direct annihilation into photons can occur at one loop level, as  $\chi\chi \rightarrow \gamma X$ , where  $X = \gamma, Z$  or  $h$ . Such a process is strongly suppressed, but not impossible. Photons produced in this way would be detected as sharp lines at energies  $E_\gamma = (1 - m_X^2/4m_\chi^2)$ , representing an undoubted evidence of dark matter detection. Photons can also be produced in the so-called *internal bremsstrahlung* scenario [63]: if neutralinos annihilate into leptons, the annihilation exchange particle is a charged sparticle that can emit a photon. This photon restores the helicity in the annihilation processes of type  $\chi\chi \rightarrow l^+l^-\gamma$ , thus allowing for otherwise forbidden interactions. Photons produced this way are expected to carry a significant amount of energy ( $E_\gamma > 0.6 m_\chi$ ) and to produce a characteristic bump at the end of the differential photon energy spectrum;

---

<sup>8</sup>Fermions that present the characteristic to be their own antiparticle.

- *Gauge bosons*: in the low-velocity regime, pure gaugino-like neutralinos can annihilate into  $Z$  and  $W^\pm$  bosons via the  $t$ -channel, while pure higgsino-like and mixed neutralinos would produce these particles via the  $s$ -channel;
- *Higgs boson*: neutralinos can annihilate into pairs of Higgs bosons or a Higgs and a gauge boson. The most favoured channels are the annihilation into a light neutral Higgs and a  $Z$  boson ( $\chi\chi \rightarrow h^0 Z$ ), into a heavy Higgs and a  $Z$  boson ( $\chi\chi \rightarrow H^0 Z$ ), into a charged Higgs and a  $W$  boson ( $\chi\chi \rightarrow H^\pm W^\pm$ ), and into a light Higgs and a pseudoscalar Higgs ( $\chi\chi \rightarrow h^0 A_0$ ).

In this list, only the annihilation of DM particles has been taken in consideration, as the decay process should be suppressed because of the stability of the LSP. However, this particle becomes unstable under  $R$ -parity violation. Several models have been presented to describe this process, and the decay of DM as *wino*, *sneutrino*, *gravitino* and or the *axino*<sup>9</sup> were predicted. I will skip the description of all these processes, as out of scope of this thesis.

Apart from the SUSY models and its related extensions, other models present particles that can be good WIMP DM candidates. Among all these alternative possibilities, one can find:

- *Axions (not considering their thermal production)* These new light pseudoscalar bosons, chargeless and spin-0 particles (Goldstone bosons<sup>10</sup>, come out from the spontaneous breaking of the Peccei-Quinn symmetry and present a mass of  $10^{-6} - 10^{-2}$  eV. As a good DM particle candidate, axions interact very poorly with matter and only oscillations into photons in magnetic fields or in cosmic distances may allow us to detect them;
- *Kaluza-Klein states* A substitute of SUSY are the Universal Extra Dimensions (UED) theories, in which a 4-dimensional space-time is believed to be embedded in a larger frame with flat extra dimensions where all the SM fields are allowed to propagate. In this scenario, Kaluza-Klein states for each SM particle are present and meet a symmetry (the so-called KK parity) that states that the contributions to SM arise only at loop level, in which the particles are produced in pairs, and that the lightest KK particle (the LKP) is stable. Then, the LKP is a good DM candidate;
- *Wimpzillas* Possible candidates of DM directly created at the end of the *Inflation*<sup>11</sup> era thanks to gravitational interaction. Their mass is predicted to be of the order of  $10^{13}$  GeV and it decays into SM particles through the creation of UHE (Ultra High Energy, energies in the range 30 TeV-30 PeV) or EHE (Extremely High Energy, energies  $> 30$  PeV) cosmic rays.

---

<sup>9</sup>Superpartner of the axion, introduced in the following lines.

<sup>10</sup>Goldstone's theorem states that, for each breaking of a generator of a global symmetry, one obtains a scalar boson of spin-0 and zero mass, the Goldstone boson.

<sup>11</sup>Theory starting claiming that the Universe has been subjected to a period of very rapid expansion after the Big Bang, because of a negative pressure generated by the energy of a quantic field called *inflaton*.

A lot of further particles can be listed as DM candidates, such as axion-like particles, primordial black holes, sterile neutrinos, branon DM, little higgs, mirror matter and so on, but a description of these is out of the scope of this thesis. For an overview on these alternative proposals of DM candidates, the reader is invited to have a look at [50].

### 3.2.2 Alternative cosmology

The  $\Lambda$ CDM scenario, given its good description of the large structure formation and its consistency with the Big Bang Nucleosynthesis relic abundance of light elements, is the most adopted model for a cosmology containing DM. Even if it presents the issues mentioned above and other challenging discrepancies with observations, such as the Tully-Fisher relation [64], the large scale velocity flow [65,66], the low multipoles in the CMB [67,68], etc., it is the only model that offers a consistent complete evolutionary image of the Universe.

Alternative cosmological explanations have also been proposed as possible solutions to the DM problem. Based on the fact that DM is not cold or weakly interacting, or even postulating that DM does not exist at all, the majority of these cosmologies typically provide solutions to singular problems, not taking into account the overall view of the Universe's evolution.

*MOdified Newtonian Dynamics* (MOND) [19], of which the *Tensor-Vector-Scalar* (TeVeS) *gravity* [69] is a relativistic generalization, suggests that the Newton's law of gravity should be modified. This would explain the observed flattening of the rotation curves of galaxies, and cluster of galaxies, as well as the Tully-Fisher relation, but has limitations at galaxy cluster and cosmological scales.

Many other models and theories can be listed in this section, but this goes beyond the scope of this thesis. In the following section, I will focus the attention on WIMP DM and describe the different ways of detecting it.

## 3.3 Dark matter searches

Until now, searches for dark matter have been mainly performed with the idea of looking for a Weakly Interacting Massive Particle, interplaying with the SM particles via direct interaction and/or their production. In this view, three complementary ways for its detection can be attempted: *direct detection*, *production at colliders* and *indirect detection*.

### Direct detection

WIMP particles  $\chi$  are expected to directly interact with SM particles  $X$  in elastic scattering processes of type  $\chi X \rightarrow \chi X$ . DM direct detection experiments are placed under the Earth's surface, and require a big size and cryogenic apparatus. They detect recoil of the nucleus of a dense target material, with which the galactic WIMP incident flux, due to the Earth's motion in the DM halo of the Milky Way, interacts through elastic scattering. In the non-relativistic limit, this scattering can be divided into two classes: the *spin-independent* (SI) one that couples to the mass of the detector nuclei, increasing the scattering

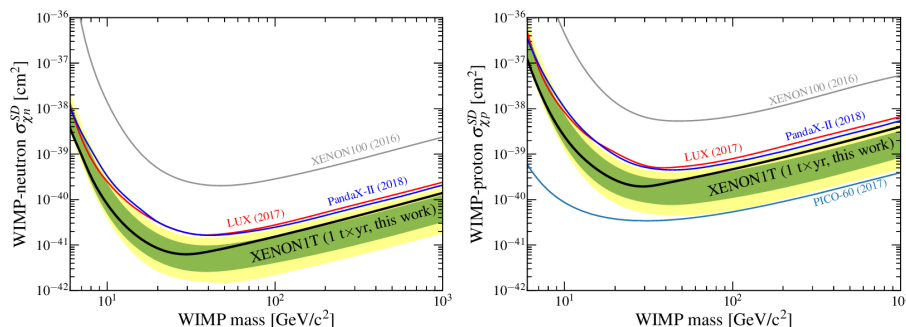


**Figure 3.4:** XENON1T upper limits on WIMP-nucleon cross section in comparison to the LUX [79] and PandaX-II [74] results for the case of spin-independent interactions (*left*), and to XENON100 [80], LUX [79], PandaX-II [74] and PICO-60 [76] for the case of spin-dependent interactions (*right*). Figures taken from [72] and [81].

rate as  $\sigma \propto A^2$ , where  $A$  is the mass number, and the *spin-dependent* (SD) one that couples to the spin of the nuclei.

The recoil of a  $10^1 - 10^3$  GeV mass WIMP, assuming a Galactic velocity of the order of  $10^{-3}c$ , is of the order of 1 – 100 keV. Since the detection rate is only  $10^0 - 10^5$  events  $\text{kg}^{-1} \text{ week}^{-1}$  for a typical expected DM cross section of the order of  $10^{-43} \text{ cm}^2$ , an important challenge for this kind of experiments is to reduce the various backgrounds and keep them under control. Cosmic rays (CRs), gamma photons and electrons due to the decay of radioactive isotopes present in the rocks and in the air around the detector and the electronic recoils induced by the detector apparatus are the main sources of such backgrounds. To cope with all these undesired signals and ensure better performance of the detector, direct detection experiments are usually made of high purity materials, surrounded by shields of lead and reinforced concrete, provided by a veto system to distinguish between electronic noise/background and the recoil signal, and located in deep underground laboratories.

The working principle of such experiments can be manifold and is based on:

- *heat and ionization signals*, i.e. revealing both charge signals from ionization, after nuclear recoil, and heat signals, thanks to crystal semiconductor materials and cryogenic cooling (an example of these detectors is CoGeNT [70]);
- *scintillation signals*, i.e. measuring the scintillation light emitted by the flux of DM through the target material (as in the case of DAMA [71]).

In addition, there are noble liquid experiments (such in the case of XENON1T [72, 73], PandaX-II [74] or LUX [75]), superheated liquid experiments (e.g. PICO-60 [76]), and other variants.

In the last two decades, hints of WIMP DM flux modulation detection were reported by DAMA [77, 78] and CoGeNT [70], but were later excluded by the results of XENON1T for spin-independent interactions (Fig. 3.4, *left*) and by the results of PICO-60 for spin-dependent ones (Fig. 3.4, *right*).

In the past years, the experiments have extended their focus to particles different from the commonly considered WIMP, and have taken into account other

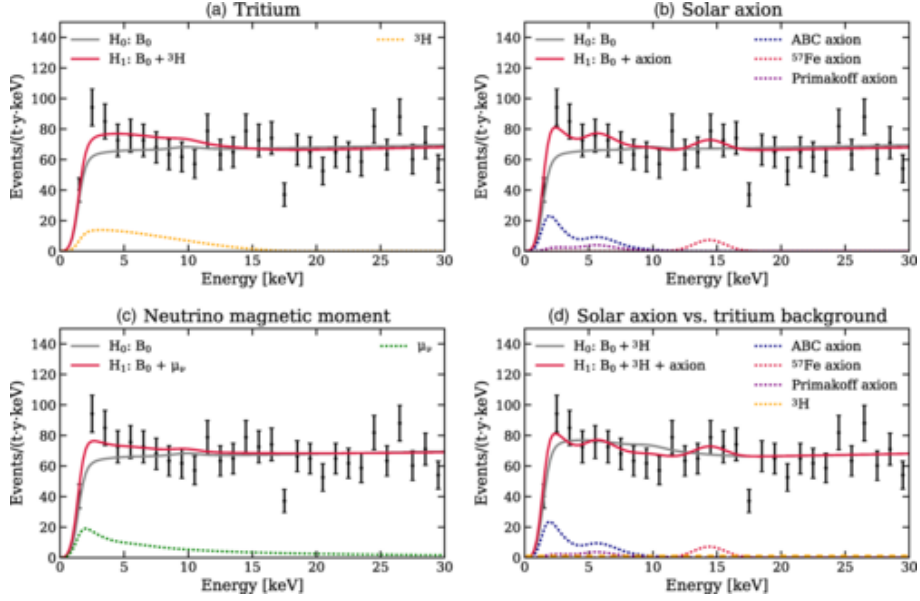


**Figure 3.5:** Fits to the data of the XENON1T experiment (black data points) under various hypotheses: tritium (a), solar axions (b), and a neutrino magnetic moment (c). The null and alternative hypotheses in each scenario, respectively, are denoted by gray (solid) and red (solid) lines. Panel (d) shows the best fits for an additional statistical test on the solar axion hypothesis, in which an unconstrained tritium component is included. Image taken from [73].

GeV and sub-GeV particles models when estimating the DM-nucleon interaction cross section. An excellent result has been obtained by the XENON1T collaboration, considering an axion particle related to the detection of an excess at around 2-3 keV. The excess obtained is presented in Fig. 3.5, associated to different models used to fit it.

The solar axion flux model (plot (b) in Fig. 3.5) is the hypothesis that provides the best fit, with a significance of  $3.5\sigma$  over the null hypothesis. Another possible explanation for the excess can be given by an anomalous magnetic moment of the neutrino (plot (c) in Fig. 3.5), favoured with a significance of  $3.2\sigma$  over the null hypothesis, or the presence of residual quantities of tritium in the water tank of the detector, which might create spurious signals through  $\beta$  decay (plot (c) in Fig. 3.5). If considering this last contribution, the significances of the solar axion and neutrino magnetic moment hypotheses decrease to  $2.1\sigma$  and  $0.9\sigma$ , respectively.

### Production at colliders

High energy colliders, such as LHC [82], have the possibility to test production a WIMP DM via hadron or lepton collisions, given that their luminosity and center-of-mass energy are sufficiently high for reaching the WIMP mass. These particles can be obtained in pairs from collisions of SM particles or, with good detection prospects, by the creation of heavier superparticles (following the SUSY model) that in turn decay into quarks, gluon jets and pairs of neutralinos.

The process in consideration is, thus,  $XX \rightarrow \chi\chi$ , where  $X$  is the SM particle and  $\chi$  the WIMP.

The presence of WIMPs in such products can be identified in two ways:

- by measuring missing transverse energy (MET): i.e. retrieving the energy carried away the particle (weakly interacting, thus not recognizable by the system) and leaving the detector, after reconstructing it from the momentum conservation law<sup>12</sup>;
- by detecting associated jets or photons. Such mono-photon or mono-jet events, from the initial state radiation (used as trigger for the event), together with the missing transversal energy, would represent striking signatures of WIMPs presence.

Lepton colliders have better possibilities to disentangle these types of signals from background, compared to hadron colliders. In the former, the energy of the leptons colliding can be controlled with high precision, whereas in the latter the energy of the gluons and the quarks that constitute the colliding hadrons are unknown and can be defined only in a probabilistic way. Moreover, in hadron colliders, these processes are affected by background, such as production of neutrinos and single tops.

No evidence of WIMPs have been found so far in experiments such as ATLAS [83] or CMS [84], located at the LHC, and very constraining upper limits have been set. In Fig. 3.6, upper limits on the nucleon-WIMP cross-section, estimated by ATLAS, are shown and compared with other direct detection experiments. In the case of spin-dependent WIMP-SM particle interactions (*bottom*) the limits obtained by ATLAS are much more constraining than the ones reached with direct detection searches.

WIMP detections at colliders would provide plenty of information about the nature of the particle produced, but even in this case, its existence as DM has to be independently confirmed by indirect detection experiments.

### Indirect detection

The characteristic way to indirectly identify the nature of DM particles and to measure their properties is to look for secondary products of their annihilation/decay into SM particles. The latter can be gamma photons, neutrinos, electrons/positrons, protons/antiprotons, antideuterons or synchrotron radiation, detectable through a variety of modern ground and space-based observatories. A schematic view of these products in an annihilation process of WIMP candidates is presented in Fig. 3.7.

However, charged particles are deflected when propagating through interstellar space, populated by magnetic fields, and consequently the source of information will get lost. On the contrary, gamma rays and neutrinos travel mostly undisturbed (if the scales are not too large as to be affected by the Extragalactic Background Light) through the Universe, allowing to trace the particle's propagation direction back its source.

<sup>12</sup>The momentum of incoming projectiles in the direction orthogonal to the beam is zero, so the final products of the collision must balance their momenta in the transverse plane. If in the final state an unbalanced contribution is found, the production of WIMPs can result as a possible explanation.

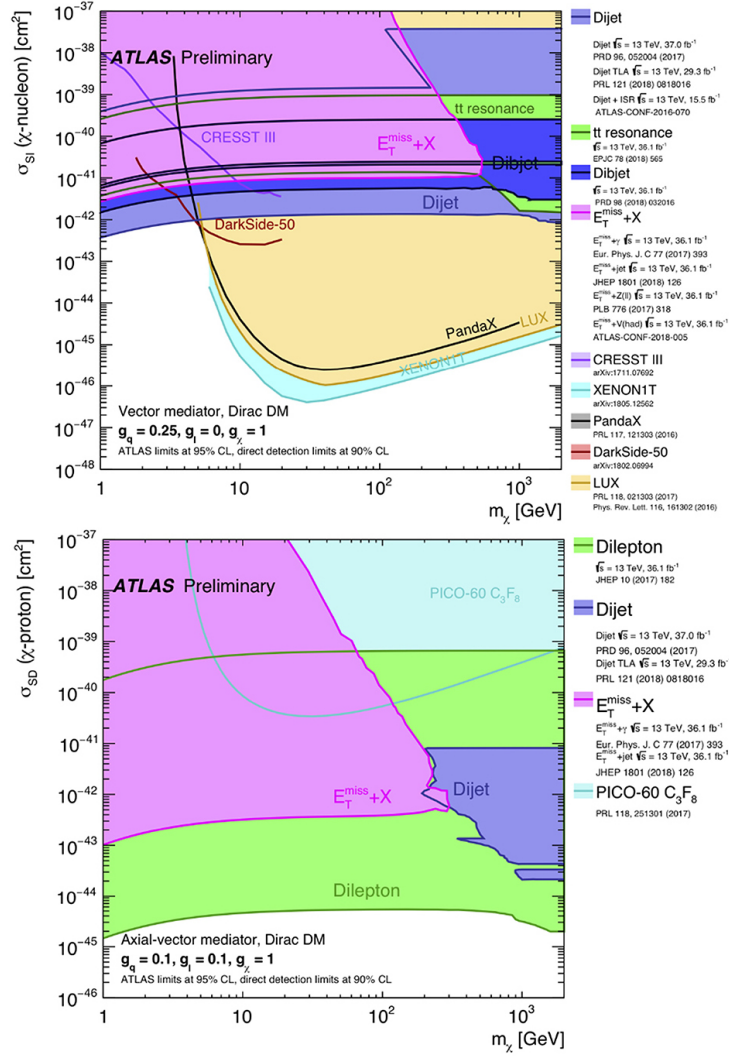


**Figure 3.6:** ATLAS results on the WIMP-nucleon cross-section compared with limits from direct detection experiments, in the case of spin-independent (*top*) and spin-dependent (*bottom*) interactions, respectively. Image taken from [85].

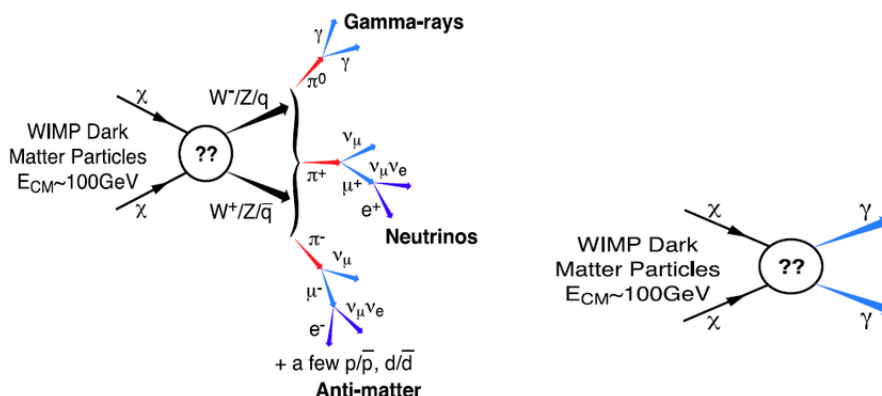


**Figure 3.7:** Schematic view of WIMPs annihilation into heavy SM particles (*left*) or directly into gamma-photons (*right*).

A way of searching for DM through the study of CRs, is to look for anomalous components in their isotropic spectrum. Satellite detectors, such as PAMELA [86], AMS [87] and the future GAPS [88], are leading experiments in this sector. Since matter and antimatter should have been formed in equal quantity in the early Universe, a measure of excesses of positrons, antiprotons or light antinuclei, with respect to those expected by standard astrophysical processes, can be a hint for DM annihilation or decay processes. The advantage of indirect DM searches through CRs, as compared to the use of other mediator particles, is the very low background and the possibility to perform measurements across a large FoV, without having to restrict itself to a particular region of the sky. In comparison, **neutrino** detectors suffer from very high background contamination. Supposedly produced in large amounts in DM annihilation/decay processes, the provenance of neutrinos can be reconstructed thanks to their limited interaction with the intergalactic medium and magnetic fields. They can also be produced by DM captured in deep gravitational wells, such as the Sun, and that annihilates at significant rates if gathered in high concentrations. As they can escape from moderately dense objects, interacting via the weak force, a neutrino detection in the direction of the Sun can indicate the presence of DM. In a similar way one can take into account neutrinos captured by the Earth, but the detection prospects are weaker. Large size detectors are usually adopted for catching neutrinos, given their very small interaction cross-sections. In addition, the experiments are built deep under the sea, as in the case of ANTARES [89], or in ice, such as IceCube [90].

The last particle used for indirect DM detection is the **photon**. The majority of the photons produced in DM annihilation/decay processes are created in cascade decays of quarks, bosons, etc., into gamma rays. A minor contribution, as the process is highly suppressed<sup>13</sup>, comes from direct annihilation/decay of DM into photons. The energy of these photons (half of the original DM particle mass for decaying DM), or a cutoff in the spectrum in the other case,

<sup>13</sup>Being DM particles neutral, to couple with photons need a loop Feynman diagram, in which DM first annihilates into two virtual charged particles and then these annihilate into two real photons.

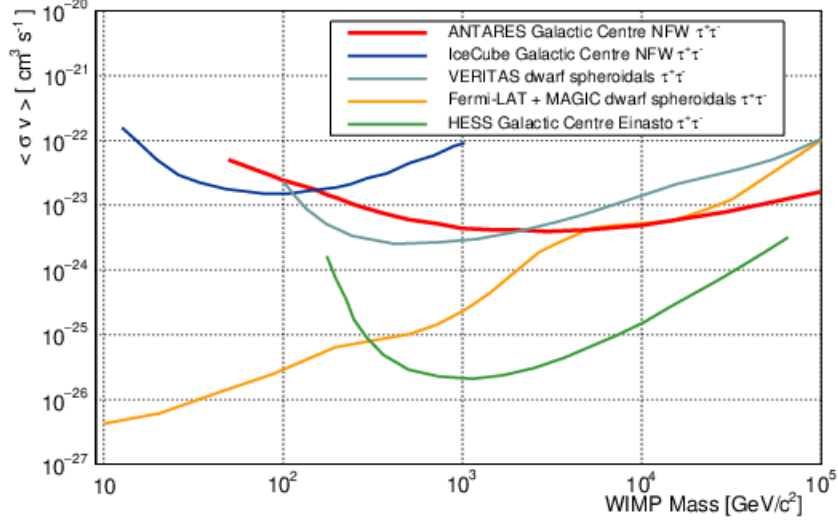


**Figure 3.8:** Limits on the velocity-averaged cross-section of WIMP DM annihilation, in the  $\tau^+\tau^-$  channel, obtained with 11 years of ANTARES data, compared with current similar searches from IceCube [91] and from the gamma-ray telescopes VERITAS [92], Fermi-LAT + MAGIC [93] and H.E.S.S. [94], for different targets of observation and different DM density profile models. Image taken from [95].

tells us the DM particle mass. Furthermore, the former can be considered a “smoking gun” for a DM signal, since no astrophysical source can produce a similar spectrum.

The experiments and astrophysical installations performing indirect DM searches through the observation of gamma-rays have already been presented in chapter 2, as all VHE gamma-ray experiments dedicate observation time to the search for DM. No hint of a signal has been found so far from these observations, and limits have been set on the velocity-averaged cross-section and for the decay lifetime of WIMPs in the case of annihilation and decay processes, respectively.

Thus, depending on the different sensitivities to the relevant DM mass ranges, current orbiting gamma-ray telescopes (e.g. Fermi-LAT), ground-based IACTs (e.g. MAGIC, H.E.S.S., VERITAS), the new-generation water Cherenkov detector (HAWC), neutrino experiments (e.g. IceCube and ANTARES) and other satellite detectors (e.g. PAMELA and AMS) provide overlapping and complementary results on DM.

In Fig. 3.8, limits obtained by different experiments on the velocity-averaged cross-section of WIMPs annihilating into the  $\tau^+\tau^-$  channel, and consequently decaying into photons, among other products, are shown as an example. Even if not representing the most recent results, this plot is illustrative to show the different sensitivities reached by each kind of experiment for DM masses in the 1 GeV-100 TeV range.

CTA is one of the new projects that will greatly improve measurement sensitivity and focus on the energy range between 100 GeV and 100 TeV. Thanks to this, it is predicted to probe the thermal relic cross-section for

WIMPs, with these masses (see Fig. 2.8).

In indirect DM searches, hence, the resulting SM products are expected to carry valuable information on the properties of DM particles. Moreover, this approach can probe the astrophysical distribution of DM, which is not possible with direct and collider searches. The main obstacle of this search method is the overwhelming abundance of astrophysical backgrounds. Disentanglement of SM particles that have a DM origin, from those of astrophysical origin, becomes, hence, a complex task.

In this subsection, we have focused our attention on WIMP DM, even if other DM particle candidates are investigated. Considering also these alternative studies, the multiplicity of DM models, theories and candidates provided in the literature, lead us to look for DM in all its variants and at all possible energy scales. This would open the possibility of discovering new classes of candidates and of designing new experiments in the hope that DM would not be secluded in the Dark Sector<sup>14</sup>. A nice overview of all these new perspectives in DM searches and theories is given in [50]. Fig. 3.9 is reproduced here to get an idea of the direction in which current research is moving.

### 3.3.1 Dark matter indirect detection through gamma-ray observations

#### Dark matter sources of interest

The most obvious sources where to search for DM are the ones with high DM overdensities in the Universe, such as: the Galactic Center and its halo (GH), dwarf spheroidal satellite galaxies (dSphs), galaxy clusters and dark subhalos. The specified sources of interest are classified in terms of their DM amount (i.e. looking at their DM halo density profile), of their distance from the observer, and of the number and types of background sources present in the area surrounding the target.

The mass-to-light (M/L) ratio of the system should also be taken into account, since a large baryonic content may have major drawbacks. Baryonic matter can disrupt the DM halo, smoothing the central high DM density, and hence, reducing the expected flux of SM messenger particles. Furthermore, baryons can act as strong background for the DM signal, as they can produce photons via conventional astrophysical processes in a more abundant number.

In Fig. 3.10, the different observational targets for gamma-ray indirect DM searches are presented, together with their characteristics and associated detectors.

The **Galactic Center** is the known region dominated by DM closest to the Earth (at a distance of  $\sim 8.5$  kpc). From theoretical arguments and numerical simulations, its DM density profile is expected to be cuspy toward the centre, thus strongly enhancing a possible annihilation signal. However, the presence of a black hole leads to a modification of the DM profile, making its density distribution highly uncertain [98].

Observations of the Galactic Center in the VHE regime, where WIMP signals are expected, have been carried out by IACTs and satellite telescopes. The non-variable signal detected does not agree with the prediction of a pure

---

<sup>14</sup>Region that does not have any interaction with the SM particles.

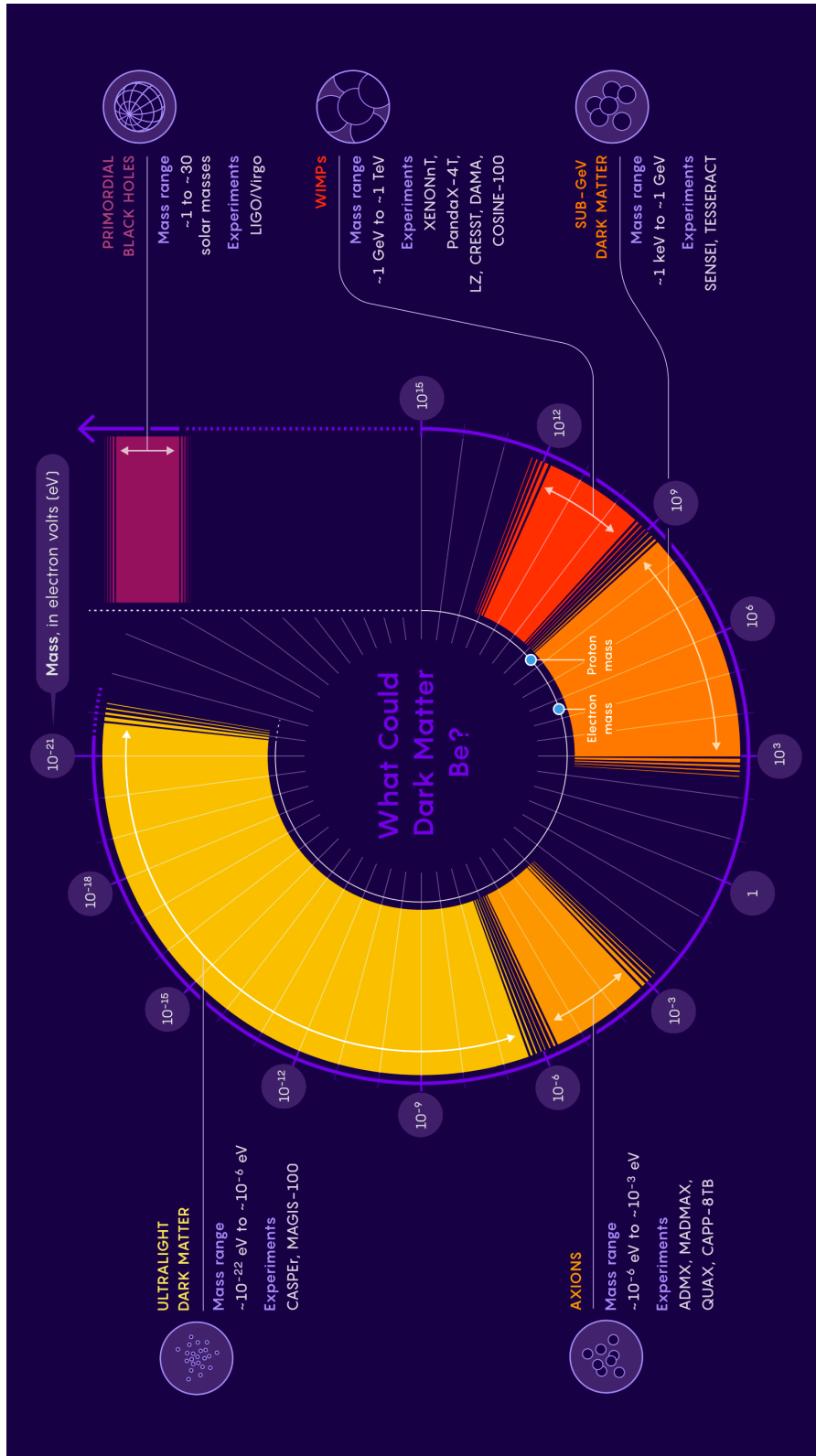


**Figure 3.9:** Scheme of the current DM candidates taken into consideration, associated to the detection systems that can observe them. Image taken from [96].

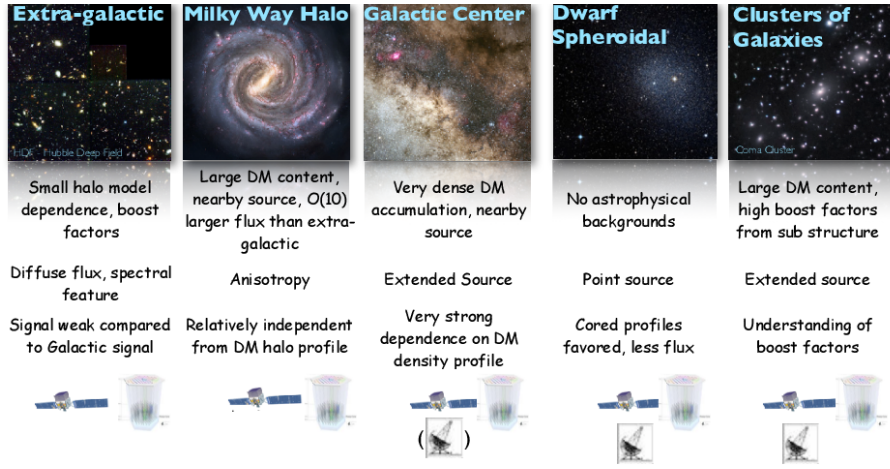


**Figure 3.10:** Representation of the targets of indirect DM searches with gamma rays. Each candidate is presented with its respective characteristics and the associated detection instrument. For the latter, the Fermi-LAT satellite and IceCube images have been used as reference for gamma-ray satellite detectors and neutrino detectors, respectively. The third type of instrument is a general IACT. Image taken from [97].

DM profile, and its origin is more likely due to radiation from conventional counterparts in the vicinity of the Galactic Center (the super-massive black hole SgrA\*, the supernova remnant SgrA\* East and the pulsar with nebula G359.09-004), which may completely hide the potential DM signal [99, 100]. It has to be noted that the Galactic Center is a densely populated region, with a large baryonic content. Source of background are present at all wavelengths. The **Galactic halo** presents a lower DM density with respect to the Centre, but it is still of interest for DM decay searches (more effective if carried out at larger galactic latitudes). This guarantee the possibility to achieve similar results as for observations close to the central region of the galaxy, with a considerably lower background level and almost no uncertainty concerning the DM profiles.

**Dwarf spheroidal satellite galaxies** are predicted by the cold DM bottom-up structure formation scenario as a part of the population of Galactic DM sub-halos. They are among the most dominated DM objects known so far [101]. These objects have M/L ratios between  $100 \div 1000 M_{\odot}/L_{\odot}$  and are relatively close to the Earth (up to  $\sim 250$  kpc). Moreover, the absence of gas and the presence of a population of old stars, provide a negligible gamma ray background. These characteristics make dSphs excellent targets for indirect DM searches with IACTs.

Currently, the most constraining limits are set by the joint analysis of the observation of 10 dSphs by Fermi-LAT and the Segue 1 result by MAGIC [93].

**Galaxy clusters** are the largest known gravitationally bound systems, with radii of several Mpc and masses of  $\sim (10^{14} \div 10^{16}) M_{\odot}$ . These objects represent the top stage of the hierarchical formation of the large scale structures. They show more than 80% of dark matter content, making them attractive objects for indirect DM searches. Their potential as DM targets is, however,

hampered by the huge background of astrophysical origin, from active galactic nuclei, to a secondary component of cosmic-ray induced radiation.

Gamma-ray observations of the Virgo, Perseus, Coma and Fornax galaxy clusters have not returned any evidence for a DM signal, as well as at the other observation wavelengths [102–104]. **Galactic and extragalactic diffuse** emission has been investigated in order to find anomalies that could give a hint of DM.

A target of interest for indirect DM searches, not shown in the image, are the **DM subhalos**. According to N-body simulations, DM evolves by creating hierarchical clusters, that results in the formation of DM clumps within halos at all scales. The larger clumps may attract enough matter to trigger stars formation, while the smaller ones do not have enough gravitational attraction and remain completely dark. Those small halos, so-called DM subhalos, are invisible in the context of the conventional mechanism, but should shine in the energy windows where the DM signal is expected, becoming gamma-ray emitters. The lack of any astrophysical background makes these subhalos excellent targets for indirect searches, with the drawback that their location is unknown so far.

Fermi-LAT has detected, until now, hundreds of Unidentified Fermi Objects (UFOs), sources that emit at very high energies, but do not have any counterpart at other wavelengths. Some of these UFOs are potential candidates for DM subhalos, if their emission is not variable.

Complementary observations of UFOs have been performed by IACTs, but no detection has been reported so far [105].

### 3.3.2 Gamma-ray emission from dark matter annihilation/decay

As reported previously, DM can annihilate or decay into SM particles, among which  $\gamma$ -rays are expected. The observational features of the photon flux can provide important information about the nature and the spatial distribution of DM.

Assuming the WIMP model, the differential gamma-ray flux of photons  $\Phi$  coming from a DM target can be written as the product of a *Particle Physics (PP) factor* and an *Astrophysical (or J-) factor* as:

$$\frac{d\Phi_\gamma}{dE} = \frac{d\Phi^{PP}}{dE} \times J(\Omega) . \quad (3.3)$$

The *PP* factor is completely determined by the nature of the DM particle considered, e.g. the WIMP, and does not depend on the properties of the target. It can be expressed as:

$$\frac{d\Phi^{PP}}{dE} = \frac{1}{4\pi} \frac{1}{m_{DM}\tau_{DM}} \frac{dN_\gamma}{dE} \quad (3.4)$$

for the case of *decaying DM*, and as:

$$\frac{d\Phi^{PP}}{dE} = \frac{1}{4\pi} \frac{\langle\sigma_{ann}v\rangle}{m_{DM}^2} \frac{dN_\gamma}{dE} \quad (3.5)$$

for the case of *annihilating DM*. The terms appearing in Eqs. 3.4 and 3.5 are the mass of the DM particle  $m_{DM}$ , the mean lifetime  $\tau_{DM}$ , the velocity-averaged

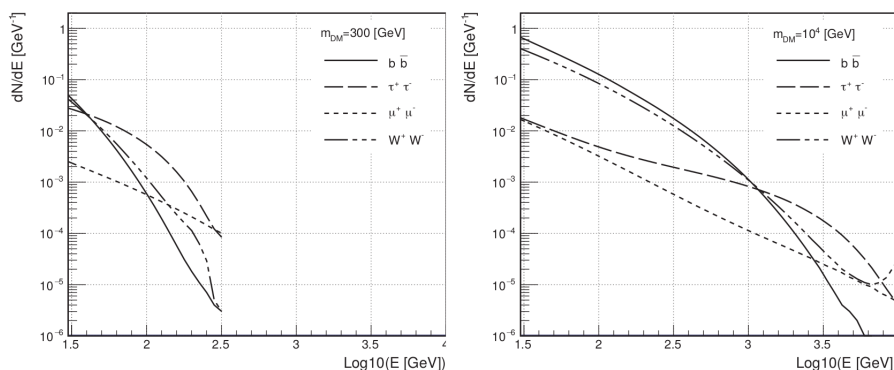


**Figure 3.11:** Differential energy spectrum of WIMP particles of mass 300 GeV (*left*) and  $10^4$  GeV (*right*) self-annihilating in the  $b\bar{b}$ ,  $\tau^+\tau^-$ ,  $\mu^+\mu^-$  and  $W^+W^-$  channels. Image taken from [106].

annihilation cross-section  $\langle\sigma_{ann}v\rangle$  and the number of photons per unit energy  $dN_\gamma/dE$  found as prompt or secondary products of the DM decay/annihilation. The latter depends on the annihilation/decay channel considered and on the spectral model. Taking into account different annihilation/decay channels, the number of gamma-photons emitted is weighted by the branching ratio  $Br$  of each of them, as:

$$\frac{dN}{dE} = \sum_{i=1}^n Br_i \frac{dN_i}{dE} \quad (3.6)$$

where  $n$  is the number of the channels considered. The *Astrophysical* factor, differently from the *PP* factor, incorporates the source's specific DM distribution and distance and is given by:

$$J(\Delta\Omega) = \int_{\Delta\Omega} d\Omega' \int_{l.o.s.} dl \rho^\beta(l, \Omega'), \quad (3.7)$$

where  $\Delta\Omega$  is the solid angle of integration,  $l$  the *line of sight*<sup>15</sup> (*l.o.s.*) parameter of integration, i.e. a considered distance along the *l.o.s.* direction, and  $\rho(l, \Omega)$  the density of DM in the source as a function of the distance  $l$  and the solid angle  $\Omega$ . The latter is a linear term,  $\beta = 1$ , in case of *decaying DM*, and quadratic  $\beta = 2$  in case of *annihilating DM*.

The differential energy spectrum expected in the case of WIMP annihilation is reported in Fig. 3.11.

### Dark matter density profile

The non-baryonic content of an astrophysical object can be evaluated by the measurement of the velocity dispersion profile of its member stars. However, the precise density profile of this matter, supposed to be DM, cannot be obtained from direct measurements. The most common way for constraining it

<sup>15</sup>The straight line of observation connecting the source to the observer. Along the line of sight, the observer is unable to distinguish gamma rays coming from the same direction but at different distances (neglecting absorption and diffraction effects). Thus, assuming the object as spherically symmetric, an integration over the solid angle is needed.

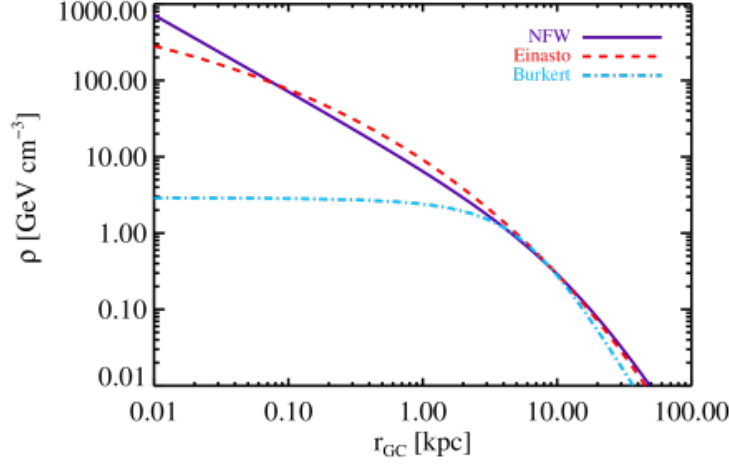


**Figure 3.12:** NFW, Einasto and Burkert profiles retrieved with Milky Way parameters. Image taken from [111].

is by fitting density profiles obtained by **N-body simulations** with kinematic data. The former aim in re-creating the current Universe following the hierarchical structure scenario and considering many-body gravitational interactions, i.e. they start with a bunch of particles in accordance to the initial DM density perturbations and end with the largest halos today.

The *universal DM density profile* considered for a spherical DM halo is the Navarro-Frenk-White (NFW) [107], obtained by DM-only N-body simulations. It is written as:

$$\rho_{\text{NFW}}(r) = \frac{\rho_0}{(r/r_s)[1 + (r/r_s)]^2} \quad (3.8)$$

where  $r$  is the radial distance from the center of the halo, and  $r_s$  and  $\rho_0$  are the scale radius and the overall normalization factor, respectively.

The *Einasto profile* [108], also obtained from DM-only N-body simulations, is expressed as:

$$\rho_{\text{Ein}}(r) = \rho_0 \exp \left[ \frac{-2}{\alpha} \left( \left( \frac{r}{r_s} \right)^\alpha - 1 \right) \right] \quad (3.9)$$

where  $\alpha \approx 0.2$  [109, 110].

Both these DM density profiles present a cusp towards the center of the halo, divergent in the former and asymptotically approaching to zero in the latter, as visible in Fig. 3.12.

This is not the case for the *Burkert profile* [112], presenting a more cored profile at the center, that can be written as:

$$\rho_{\text{Burk}}(r) = \frac{\rho_0}{\left(1 + \frac{r}{r_s}\right) \left(1 + \left(\frac{r}{r_s}\right)^2\right)} \quad (3.10)$$

where, in this case,  $r_s$  is the core radius.

If considering our Galaxy,  $r_s$  and  $\rho_0$  are similar for the first two profiles, and

present the values of 20 kpc and  $0.4 \text{ GeV/cm}^3$ , respectively. The Burkert profile exhibits constant density for radii much smaller than the scale radius and  $r_s$  is now equal to  $\sim 6$  kpc [113].

In recent years, dSphs observations [114] have shown that their DM density profiles are consistent with the DM density having a cored trend towards their centres, in contradiction with the profile modellings of NFW and Einasto. On the other hand, some others confirmed cuspy DM profiles for particular dSphs, such in the case of [115]. In order to cope with these discrepancies, and to correctly describe the DM density profile of halos and subhalos, higher resolution N-body simulations have been developed. In addition to the increased resolution, recent simulations include baryons and their interaction with DM. For example, the DM central density can be enhanced by the adiabatic condensation of gas in the center of the halo, or supernova outflows can eject DM, and so on.

A different method to retrieve the DM density profile of a source consists in fitting a relatively flexible density profile to the kinematic data, as done in [116]. The profile adopted for the fit is a *Zhao-Hernquist* density profile [117, 118] of the form:

$$\rho(r) = \frac{\rho_s}{(r/r_s)^\gamma [1 + (r/r_s)^\alpha]^{(\beta-\gamma)/\alpha}} \quad (3.11)$$

where  $\rho_s$  and  $r_s$  are the scale density and radius, respectively, and  $\alpha$ ,  $\beta$  and  $\gamma$  are the parameters to be estimated via a likelihood maximization (see [119] as an example). Note that for  $(\alpha, \beta, \gamma) = (1, 3, 1)$  we obtain the expression of the NFW profile.

A third method adopted for the estimation of the DM density profile, mainly used in the case of subhalos, is to consider kinematic data to fit for the mass<sup>16</sup> and/or the concentration<sup>17</sup>  $c$  (assumed to follow an analytic form) of the DM density profiles, as done in [120] and [121]. It has to be remarked that all the profiles mentioned in this section take into account halos or subhalos with a spherically symmetric shape.

---

<sup>16</sup>Mass of a gravitationally bound system  $m_{vir}$ , if the virial theorem applies.

<sup>17</sup>It is defined as  $c = \frac{r_{vir}}{r_s}$ , where  $r_{vir}$  and  $r_s$  are the virial and the scale radius, respectively.

## Chapter 4

# The MAGIC telescope system

The MAGIC telescopes, as IACTs, are designed to measure Cherenkov light from air showers. In particular, the purpose of the MAGIC experiment is to detect EM showers in the VHE regime, initiated by gamma rays produced by non-thermal processes in the Universe. The energy interval covered ranges from 70 GeV (with standard trigger) to 30 TeV [122], extended down to 30 GeV, if the *sum-trigger* [123] is active, and to more than 100 TeV, with very large zenith angle ( $> 70^\circ$  in zenith) observations [124]. With such a low energy threshold, limits on the distance of detectable sources have been pushed to the highest redshifts [125].

The integral sensitivity of the MAGIC telescopes (in 50 h) is of  $\sim 0.7\%$  of

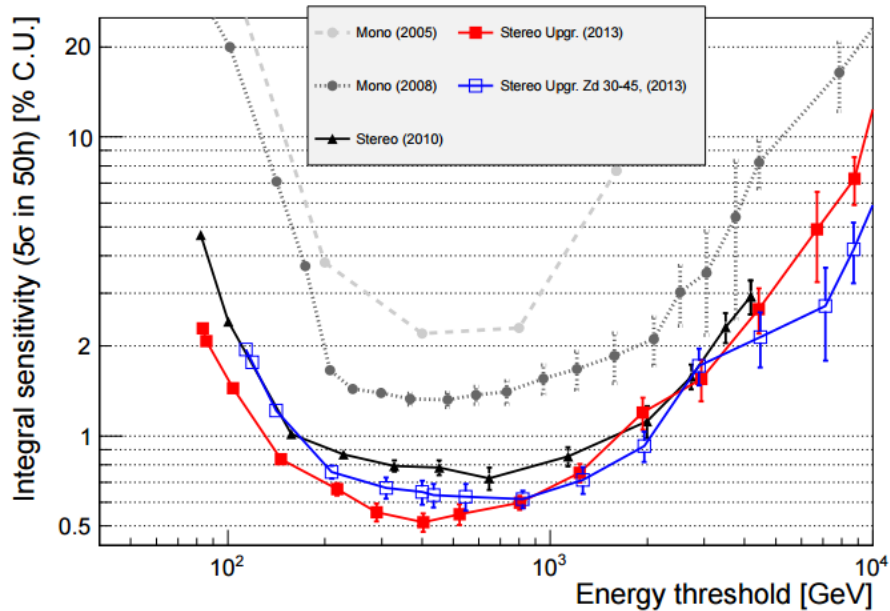


**Figure 4.1:** Evolution of the sensitivity of the MAGIC telescopes with the different upgrades. Image taken from [122].

the Crab Nebula flux above 220 GeV, as visible in Fig. 4.1. They present an energy resolution of 15% at 1 TeV (24% at 100 GeV) and an angular resolution of  $\sim 0.06^\circ$  at 1 TeV ( $0.1^\circ$  at 100 GeV) [122]. Given the characteristics of their construction, the MAGIC telescopes can also observe the, now notorious, Gamma Ray Bursts (GRBs) [126, 127], neutrinos-associated gamma-signals [128] and Gravitational Wave (GW) related ones [129], among others. The observation of these transient sources can be performed thanks to an Automatic Alert System (AAS) [130] implemented in the MAGIC control software: the signal events are promptly localized by satellite-based experiments (e.g. Fermi-GBM, Swift-BAT, AGILE) or neutrino experiments (e.g. Icecube) [131], because of their larger field of view, and communicated to, the ground-based experiments in the Gamma-ray Coordinate Network<sup>1</sup> (GCN), activating the MAGIC follow up procedure. The latter is possible only thanks to a fast repositioning technology, permitting a rotation of the telescopes of  $180^\circ$  in less than 30 s ( $7^\circ/\text{s}$  in the so-called *fast mode*).

In order to exploit at maximum the duty cycle of the telescopes, a system for observations under bright moon light conditions was implemented in 2016 [132, 133].

From the technological point of view, “Any sufficiently advanced technology is indistinguishable from *magic*” (Arthur C. Clarke) [134]: the detectors use the know-how of techniques taken from accelerator experiments that allow to economically build devices of great performance and complexity, computers and networks provide sufficient capacity to record and reconstruct large volumes of data and find their interrelations. In the next lines, the structure and the different devices of the telescopes will be described and the data acquisition will be presented in detail.

## 4.1 The telescopes design

### 4.1.1 The frame

The architecture of the two telescopes aims to reach the best mobility and the minimum weight possible and a good resistance against environmental impact. Their structure, as presented in Fig. 4.2 (*left*), consists of a very lightweight space frame made of reinforced carbon fibre tubes (Carbon Fiber Reinforced Plastic, CFRP) joined by aluminium knots, which results in a strong and light structure of a total weight of  $\sim 5.5$  tons for the mirror dish support. Thanks to its lightness, it is possible to make fast movements to follow up observations of transients, but it is necessary to have also an Active Mirror Control (AMC) system to guarantee the best possible optical *Point Spread Function*<sup>2</sup> (PSF) at different zenith angles of observations. In fact, the AMC corrects small deformations of the mirror support dish during telescope positioning and tracking, moving the panels supporting the mirrors. The alt-azimuth mount of the two telescopes (Fig. 4.2, *right*), on a circular rail of 19 m diameter, allows both movement in azimuth and in altitude thanks to three driving motors, each

<sup>1</sup><https://gcn.gsfc.nasa.gov/>

<sup>2</sup>Defined as the diameter at which the 39% of the light from a point-like source is contained.

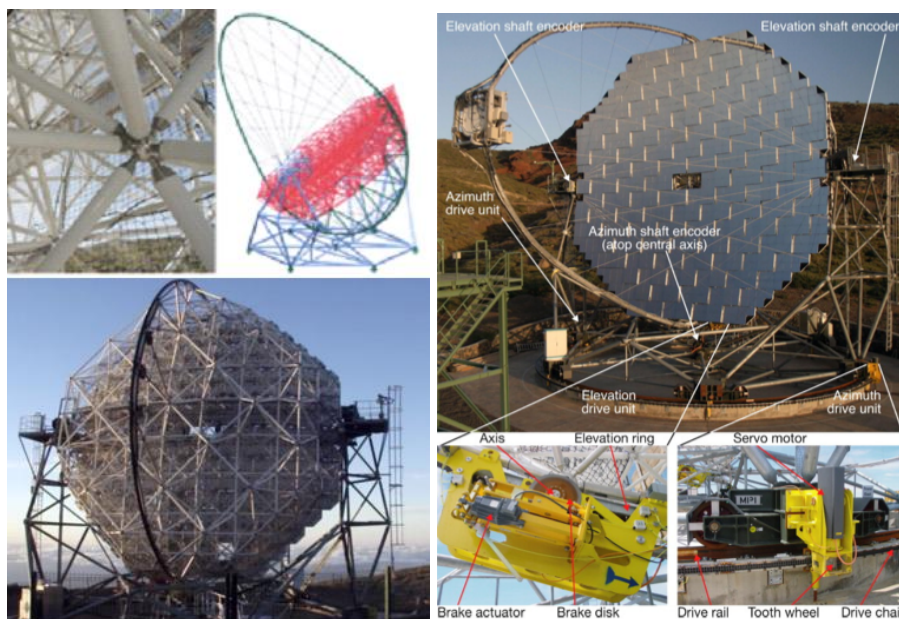


**Figure 4.2:** MAGIC telescope details of the structure frame (*left*) and of the movement system (*right*).

of a maximum power of 1 kW, moving a total weight of 64 tons in azimuth and 20 tons in altitude. The telescope can be moved from  $+99^\circ$  to  $-72^\circ$  in declination and from  $-89^\circ$  to  $+318^\circ$  in azimuth. The angular positions are controlled by absolute shaft-encoders of 14-bit precision/ $360^\circ$ . The starguider system, in addition to the encoders, monitors the exact pointing positions and correct eventual mispointings using a sensitive Charged-Coupled Device (CCD) camera, which is mounted in the center of the telescope dish and measures the differences between stellar positions by comparing the CCD images with those recorded in standard star catalogues. When not in operation, the telescope structure is secured, additionally to brakes, through the use of a series of bolts inserted all around the rail and in the elevation system arm.

#### 4.1.2 The reflector

The reflective plane of the two telescopes is a parabolic octagonal surface, with an area of  $\sim 234 \text{ m}^2$ , made of individual mirror panels of  $1 \text{ m}^2$  each (see Fig. 4.3). The dish supporting the mirrors presents a diameter of 17 m, and has an equal focal length, resulting in a focal-to-diameter ratio of  $f/D=1.03$ . Even if coma and astigmatism are prominent aberrations for this type of reflecting surface, it is the best choice for focusing light isochronically. Even if the shape of the mirrors that tessellate the telescopes is spherical, the radius of curvature increases from the center of the dish (33.9 m) to the edges (36.4 m) to approximate the overall parabolic shape. This results in an isochronicity of the signals reflected at a same angular distance from the center of the surface, that preserves the temporal structure of a Cherenkov light pulse reflected on the camera (placed at the focal distance). As a consequence of this, an improvement of the signal-



**Figure 4.3:** Reflective plane of the M1 telescope. Image taken from the MAGIC Facebook page [135].



**Figure 4.4:** Pictures of the MAGIC telescope camera from the front (*left*) and from the back (*right*).

to-noise ratio of the photon pulse in each individual camera pixel is obtained. As such, the integration windows, used to look for the signal, can be narrowed and, thus, the background from spurious night sky light or stars reduced. The goodness of the reflector is controlled each data-taking night by measuring the PSF, whose value can slightly vary as a function of the environmental conditions.

#### 4.1.3 The camera

One of the key elements of the  $\gamma$ -sensitivity of MAGIC is the camera, that is held in the focus of the reflector and is supported by a tubular arch of aluminium, stabilized by thin steel cables and counter weights. After their upgrade

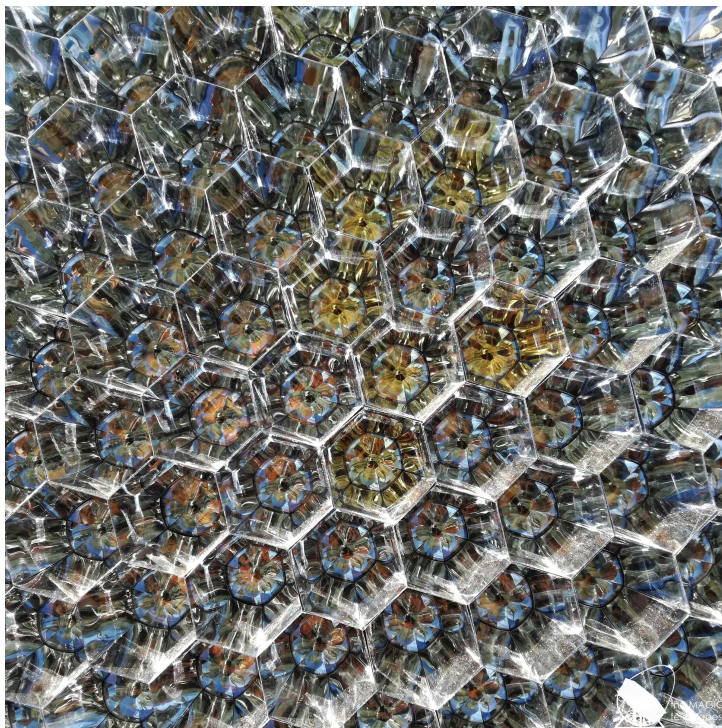


**Figure 4.5:** Detail of the front part of the camera, showing the PMTs and the Winston cones. Credits to C. Righi.

in 2012, performed to unify the stereoscopic system of the two telescopes, the cameras of both telescopes are identical and composed of 1039 PhotoMultiplier Tubes (PMTs) from Hamamatsu, presenting a hemispherical photocatode and 6 dinodes. The PMTs are grouped into 169 clusters of hexagonal shape, containing 7 pixels each. The configuration adopted permits an easy exchange of broken clusters and eases potential upgrades. Given that the photocatode of the PMTs is of spherical shape, to achieve the maximum active camera area, avoiding dead spaces between the densely packed PMTs, and rejecting background light, hexagonal light concentrators similar to Winston cones<sup>3</sup> (see Fig. 4.5) have been placed in front of the photodetector matrix.

To enhance the quantum efficiency (QE) of the PMTs, that by construction can reach a peak QE of 34% in the UV, providing a fast response of the order of  $\sim 1$  ns at Full Width Half Maximum (FWHM), a doped lacquer has been deposited on their photocatodes. Its effect is to shift the short wave UV component of the Cherenkov light into the spectral range of larger sensitivity of the PMTs. With this technique, the QE increases from  $\sim 20\%$  to  $\sim 30\%$  at short wavelengths.

An average High Voltage (HV) of  $\sim 900$  V is supplied to the PMTs during a

<sup>3</sup>Non-imaging light collectors, i.e. instruments that do not attempt to form an image of the source, but to optimize the radiative transfer from a source to the target, in the shape of an off-axis parabola of revolution. They present a reflective inner surface that maximize the collection of the incoming rays allowing off-axis rays to make multiple reflections before reaching the exit aperture.

standard data-taking night, but variations for each individual PMT are introduced following the flat-fielding procedure, needed to calibrate the signal (i.e. to have the same photon number at the entrance of each PMT).

In order to enlarge the duty cycle of MAGIC, the cameras can operate with different HV values, according to the night sky background (NSB). In particular, during moonlight conditions the PMTs operate with a relatively low gain. This reduces the amount of charge that hits the last dynode (anode) during bright observations, thus limiting the fast ageing effect. Moreover, a fixed threshold for the maximum anode current makes the PMTs to be switched off automatically, in order to not get damaged. As to protect the cameras from environmental conditions and sun light, they are covered by a plexiglass window, installed in front of the light collectors, and by movable lids (as visible in the left picture of Fig. 4.4).

In addition to the PMTs, four clusters of Silicon Photo-multipliers (SiPM) are installed for tests in the outer region of the M2 camera.

## 4.2 The MAGIC data acquisition

The MAGIC telescopes can observe during dark and twilight conditions, and recently also under bright moon conditions, summing up a total available duty cycle of about 1500 hr/year. This correspond to 18% of a year, of which only  $\sim 65\%$  ends up in effective observation time. The rest is lost because of technical problems or bad weather conditions. Data-taking is controlled by the so-called *Super Arehucas* [136], a Central Control (CC) software responsible for all the telescopes' subsystems. It works with a *LabView* interface and provides access to most of the functionalities of the telescopes.

Data-taking is performed in subruns, grouped into runs, of  $\sim 20$  min each. During this time, we can find three different kinds of events: *pedestal* events, *calibration* events and data events. The first are events (typically) recorded using a random trigger, with a fixed trigger frequency of 1 kHz, and with basically zero probability of recording atmospheric shower events. This is done with the camera lids open and triggers provided by an internal clock. Their purpose is to define the electronic noise of the readout system in order to make the mean pixel (each PMT) offset calibration, applied online by the DAQ (Data Acquisition) program (see the following paragraphs for a more detailed description). The *calibration* runs are of two different types: extensive and interleaved. The former are taken at the beginning of the observation of a new source during each night and allow the flat-fielding of the camera through the *F-factor method*<sup>4</sup> [137, 138]. The need for the correction factor comes from a residual inhomogeneous response of the camera to uniform illumination, due to different gains in the electronic chain, different electronic noise levels or different levels of the NSB. The interleaved calibration events, differently from the extensive one, are taken during data-taking, together with pedestal events, and monitor the correction factors during time, looking at the gain in the readout chain of the individual channels with a frequency of 25 Hz. Assuming that the calibration of *Domino Ring Sampler 4* (DRS4) [139] chip response is required, besides the mean pixel offset calibration, we need a readout time lapse correction and

<sup>4</sup>Method that consists in multiplying each PMT of the camera for a corrective factor, using an intrinsic PMT parameter, in order to artificially flat-field the camera.

a signal arrival time calibration to obtain optimal results as far as the noise and time resolution regard (described in chapter 5).

The MAGIC telescopes can perform observations tracking a source in (ON/OFF) mode or in *wobble* mode. In the first case, the telescopes point directly to the source, maintaining the nominal position of the target at the center of the camera. In this way, the *ON region* (where the signal from the target is expected) and the *OFF region* (from which the background is estimated) are observed separately. The latter should be taken under the most similar conditions, atmospheric and instrumental, of the signal region, in order to obtain a reliable estimation of the background. In the case of *wobble* pointing, the MAGIC telescopes track two or four different positions situated at a certain distance w.r.t. the nominal position of the target. For standard observations, the chosen offset angle is  $0.4^\circ$  (optimized for point-like sources) and the wobble position is changed every 15/20 min, in order to ensure a uniform coverage in azimuth between the two/four pointings and to avoid possible biases. The advantage of this method with respect to the (ON/OFF) mode is that the data/background acquisition time gets halved and a more reliable estimation of the background. An example of four *wobble* pointings is shown in Fig. 4.6.

A drawback of this last method is the decreased gamma observation efficiency in comparison with the ON observation mode, and the possibility of originating a *stereo blob* because of biases due to camera inhomogeneities and a broken azimuthal symmetry.

#### 4.2.1 The readout chain

The short duration of the Cherenkov light signals requires very fast readout electronics after the acquisition of the analog signals with the camera PMTs. Subsequently to the hardware upgrade mentioned previously, the analog signals, whose amplitude depend on the intensity of the Cherenkov light, are amplified by ultra-fast and low-noise preamplifiers, transformed into an optical signal by Vertical Cavity Surface Emitting Lasers (VCSELs) and transmitted to the CH ( $\sim 80$  m far away) through  $\sim 162$  m long optical fibres. These fibres are grouped into 19 bundles per telescope with 72 fibres each. This allows a better handling and ensure mechanical rigidity (they protect the fibres from breaking and from the strong sun UV radiation) being protected by a UV resistant PVC cover.

The usage of optical fibres gives a low pulse dispersion and attenuation and protect the signal inside from the external electromagnetic noise. Nevertheless, it has to be taken into account the dispersion in the arrival time for the different channels (due to different times of flight in the optical fibres). A special setup was developed to maintain more or less the same arrival times, reaching a spread in propagation time of 138 ps (RMS). The latter is corrected offline using calibration light pulses.

When the signals arrive at the electronic room of the CH, they meet the Magic Optical Nano-Second Trigger and Event Receiver (MONSTER) boards, that reconverts the signal from an optical to an electrical one, splits it into two halves, one for the digitization electronics and one for the trigger (see next subsection for more details), and generate the level-0 (L0) individual pixel trigger signal using discriminators. The analog signal from each receiver channel is then connected to a total of 48 DRS4 mezzanines installed in each readout. The latter

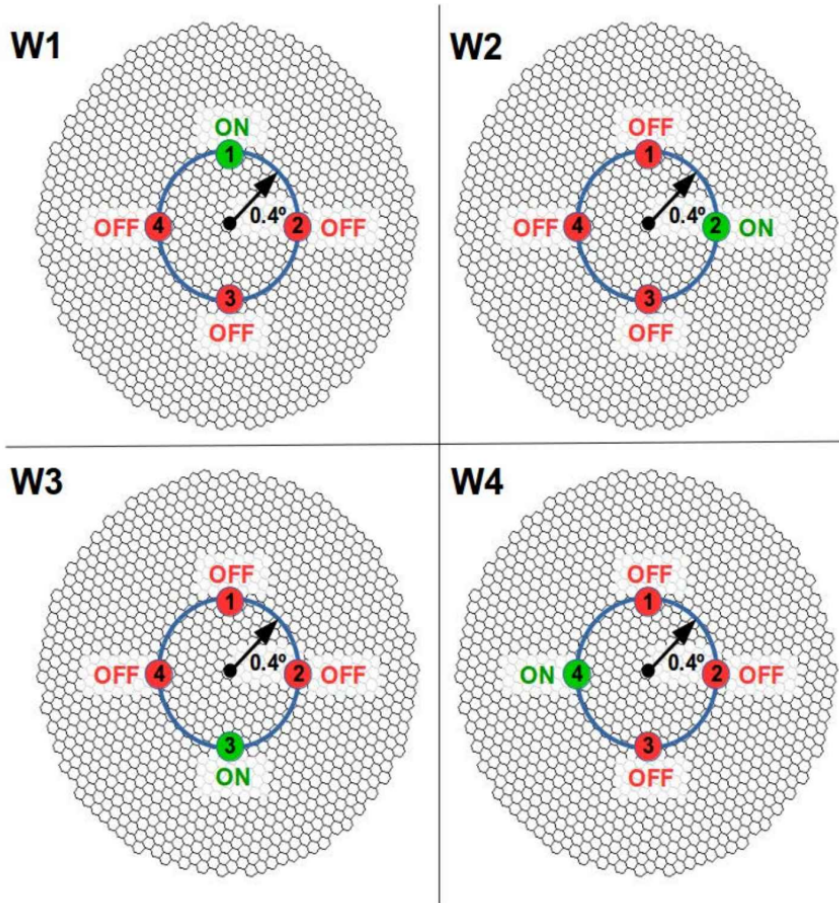


**Figure 4.6:** Scheme of the different *wobble* pointings of the MAGIC telescopes. OFF regions are marked in red, while the ON ones in green. Image taken from [133].

provide 1152 readable channels, that are sufficient to cover all the pixels of the camera. These chips are ultra-fast analog memories, read out with a sampling frequency of 1.66 GSamples/s, a linear response in an input range of 1 V and a negligible dead time of 27  $\mu$ s.

#### 4.2.2 The trigger system

Before reaching the readout system, the signals are split in two parts, of which one is sent to the trigger system. That system has been designed such that it optimizes the data acquisition rejecting background events coming from the NSB. In both telescopes, it covers 547 inner pixels of the camera, i.e. a FoV of  $2.5^\circ$  diameter (marked with a green circle in Fig. 4.7), allowing the study of extended sources with angular sizes  $\geq 0.3^\circ$ .

The trigger follows three steps:

- *Level zero (L0) trigger:* This is a simple amplitude discriminator that

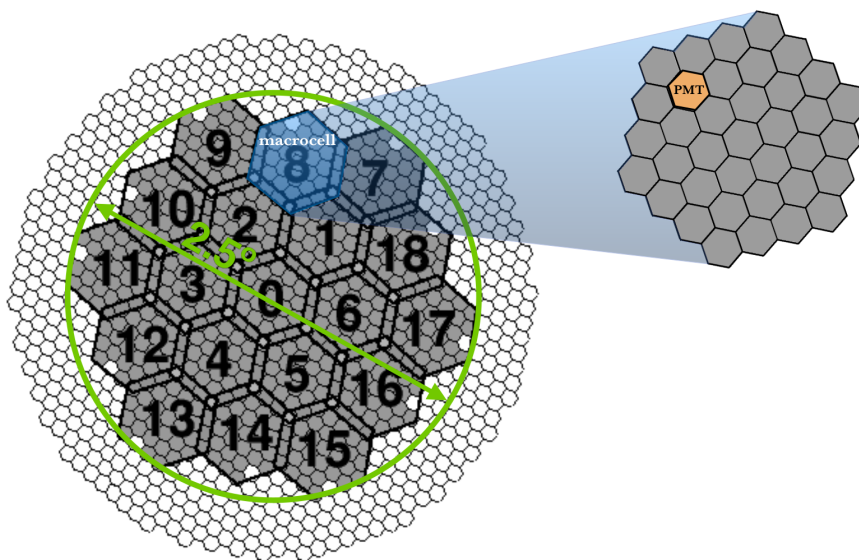


**Figure 4.7:** Scheme of the trigger regions in the MAGIC camera. The L0 trigger region is marked with a green line, the L1 trigger regions as grey areas. Image taken from [106].

operates on each pixel individually rejecting signals that do not exceed a Discriminator Threshold (DT). This is set at first at 4.25 photoelectrons (phe) in the standard mode, and, then, automatically adjusted by the Individual Pixel Rate Control (IPRC) for every pixel in the trigger region. The adjustment is made in order to provide the lowest energy threshold, while keeping the accidental rates (NSB events) at a level that can be handled by the DAQ, to prevent larger dead time periods;

- *Level one (L1) trigger:* The signals that passed the L0 arrive at this level after their widths and delays have been adjusted individually, in order to minimize the spread of arrival times for contemporaneous signals. At this step, the signal encounters a coincidence trigger arranged in 19 overlapping hexagonal macrocells of 37 pixels each (36 active and one blind), as can be seen in grey in Fig. 4.7. This individual telescope trigger is based on the next-neighbour (NN) logic, i.e. it looks for next neighbouring pixels with a signal that exceeds the DT in a tight time window in any of the cluster of channels defined previously. Several logic patterns are implemented: 2NN, 3NN, 4NN and 5NN, but for standard stereoscopic operations, 3NN is the most commonly used. When the multiplicity condition (selected remotely by software) is satisfied by any of the macrocells, a signal with a width of  $\sim 25$  ns is sent to the following trigger level. This signal has been previously corrected in width, and delayed by the multi-thread C-program HYDRA (that runs as a part of the MAGIC Integrated Readout<sup>5</sup>, MIR), to take into account the differences in arrival times of the Cherenkov light events, due to the azimuth and zenith orientation of the telescopes;

<sup>5</sup>Program that controls all the readout electronics for each telescope.

- *Level three (L3) trigger*: This last step of the trigger chain combines information of the L1 from both telescopes, searching for timing coincidence. The width of the time windows of coincidence change with the pointing directions, as the delay of the signals depends on the relative orientation of the telescopes. A maximum delay of 200 ns is possible. Overcoming this, the telescopes cannot trigger anymore.

Two other types of trigger have been implemented to improve the performance of the MAGIC telescopes at low energies. One of these is the *SumTrigger* [123], based on 55 hexagonal overlapping macrocells each containing 19 PMTs, for a total of 529 pixels. This trigger sums the analog signals of all 19 channels and compares the sum to a given DT. Once a trigger signal comes from a macrocell, the final trigger is the global OR of the local macrocells trigger. The advantages of this configuration let to relax topological constraints and to put the discriminator at the end of the sum, proving better performance in the domain below 50-60 GeV, when the events become small. The *SumTrigger* acts as a L1 trigger, while another new implemented type of trigger, the *TOPO Trigger* [140] acts as an L3. Thanks to the topological discrimination of events, it allows an order of magnitude decrease of the rate of accidental events triggering the MAGIC stereo system.

### 4.2.3 Calibration

The calibration system of the MAGIC telescopes is based on a calibration box that illuminates uniformly the PMTs of the camera with well-characterized light pulses of different intensities, in order to homogenize the PMTs' response across the whole camera. The calibration box contains a Q-switched Nd:YAG laser that produces light at 355 nm with pulses of 0.4 ns, installed at the center of the reflector, near the Starguider camera. The box contains a humidity sensor, a system that shows the laser status, a heating system to avoid water condensation and a photodiode to monitor the laser light output. The light intensity can be adjusted by means of calibrated optical filters, placed right after the laser output. To achieve a homogeneous distribution of the calibration light over all the PMTs (reaching a variation of the telescope illumination <2%), the laser beam is made diffuse through an Ulbright sphere.

## 4.3 Environmental monitoring

The atmosphere plays a fundamental role in the evolution of an EAS. The Cherenkov light emitted has to pass through several aerosol layers before reaching the telescopes, and this can affect the signal reaching the ground (a more detailed description can be found in chapter 10). For this reason, various instruments for monitoring the weather and atmospheric conditions have been installed at the MAGIC site:

- *AllSky Camera* A camera installed on the roof of the CH which provides a wide FoV optical image of the sky above the telescopes. It is used to have a qualitative estimation of the cloud coverage during data-taking;
- *Weather station* Located near the AllSky camera, it provides atmospheric pressure, humidity, temperature, and wind speed and direction

measurements. This information is processed by the telescopes CC to automatically stop observations in case of bad weather conditions;

- *Pyrometer* An instrument positioned at the center of the reflector of M1 and pointing in the same direction as the telescopes. It measures the sky temperature and provides an atmospheric monitoring through the *cloudiness* parameter ( $c = \frac{T_{ground} - T_{sky}}{T_{low} - T_{up}}$ , with  $T_{low}=250$  K,  $T_{low}=200$  K, and  $T_{ground}$  and  $T_{sky}$  temperatures measured at the ground level and in the pointing direction during the data-taking, respectively);
- *LIDAR* The Light Detection And Ranging system is the most important instrument to evaluate the density of aerosols along the line-of-sight (l.o.s.) of the telescopes [141]. It is located in a separate dome on the CH roof and is used for data selection and a-posteriori corrections of data taken with moderately-bad weather conditions. The LIDAR is an elastic system and works by emitting pulsed laser light at a position separated by  $5^\circ$  from the observed target (in order to not interfere with the regular data-taking). The light is elastically backscattered by molecules and aerosols in the atmosphere, and suffers extinction on its way to and back from the scattering point. The transmission of light can be measured as a function of the arrival time of the backscattered light.

The LIDAR operates during MAGIC regular data-taking, providing transmission profiles from 400 m to 25 km distance from ground. In case that the LIDAR is not working, the cloudiness value can be used to select data with good weather conditions.

## Chapter 5

# MAGIC Data Reconstruction and Dark Matter Analysis: Theory and Methods

In this chapter I will illustrate the steps of an indirect dark matter (DM) search analysis using data taken with the MAGIC telescopes. Together with the data reconstruction description, I will explain the theory behind it, both from a statistical and a DM physics point of view.

The chapter will begin with the explanation of the data reduction process from raw data to fully reconstructed stereo data, thus taking into account the information acquired with the two telescopes (section 5.1). In the same section, the quality check procedure, in the particular case of a DM analysis, will be explained. In section 5.2, the selection of the OFF-sample, data with no hint of a signal, and the Monte Carlo (MC) sample, Monte Carlo simulations of signal data, used to train the Random Forest (RF) decisional tree, will be presented. Section 5.3 will be devoted to the explanation of the recently developed Donut MC technique, that will lead to the flux estimation procedure, described in section 5.4. The chapter will end with the DM limits evaluation, after a theoretical explanation of the construction of the likelihood used to search for DM signals and to estimate Upper Limits (ULs), otherwise.

## 5.1 Stereo data reconstruction and quality checks

As seen in chapter 2, non-thermal processes in the universe, among which the products of DM annihilation/decay, are the possible sources of radiation detected by the MAGIC telescopes. When the Cherenkov photons, created in electromagnetic (EM) showers, arrive at the telescopes' cameras, they are recorded as short excesses of charge (in photoelectrons, phes) in a given region of the camera and at a given arrival time. Pedestal events, i.e. randomly triggered events with no signal, are used to estimate the baseline to be subtracted from the flash analog-to-digital converter (FADC) samples registered [142,143]. Once performed the subtraction, the signals are selected through a maximum search over a sliding integration window of 6 FADC times slices (3 ns) out of 60, and are converted to units of phes after being compared to the light pulses emitted by a dedicated calibration box (one for each telescope).

The associated arrival time is defined as  $t_{arrival} = \sum i s_i / \sum s_i$  where  $i$  is the time slice number and  $s_i$  is the signal in the slice  $i$ . The sum is evaluated over the time slices of the final integration window. Since different individual intrinsic delays are found on the arrival times of the photomultiplier (PMT) signals for a synchronous light pulse that illuminates all the camera, they have been previously corrected for the differences in signal delays.

To reduce the noise due to fluctuations of the Night Sky Background (NSB) or the electronics of the telescopes, an algorithm (called *image cleaning* [143]) based on the number of phes for each PMT, that takes into consideration also the arrival position in the camera and the arrival time, is used. The charge  $Q$  of a camera pixel has to be at least  $Q_{core} = 6$  phes. After removing individual pixels without any neighbour exceeding  $Q_{core} \geq 6$ , the pixels in the outer part surrounding each cluster has to be at least  $Q_{boundary} = 3.5$  phes; pixels not fulfilling any of the criteria are rejected. Selected pixels are then marked as belonging to the core region if at least one direct neighbour had been selected in a previous step. Pixels of the core area with arrival times bigger than 4.5 ns with respect to the mean arrival times of the core pixels are also rejected. This criterion is used also for boundary pixels, but with a range of time of 1.5 ns. An example of how the image cleaning behaves on the camera pixels is shown in Fig. 5.1. The image on the top left shows a detected electromagnetic shower event, the geometry of which is marked by two perpendicular red lines (one that outlines the *length* and direction, and the other one the *width*, parameters that will be explained in the following lines). On the right side, the reconstructed arrival times are shown, together with the shower image, recognizable by the red lines. On the bottom part, the image cleaning has been applied, and the shower excess is clearly visible.

In order to define the full event shower, visible as an ellipse in camera coordinates, the image parameters, labelled *Hillas* parameters [144] are determined. Referring to Fig. 5.2, the parameters of interest are:

**Size** The global number of phes of an event which, in first approximation and for fixed values of the impact parameter and zenith angle of arrival direction, is proportional to the primary particle energy;

**CoG** Center of Gravity of the image that consists of a pair of values ( $cog_X, cog_Y$ ) that determine the position in the camera of the weighted mean signal along the X and Y axis, respectively;

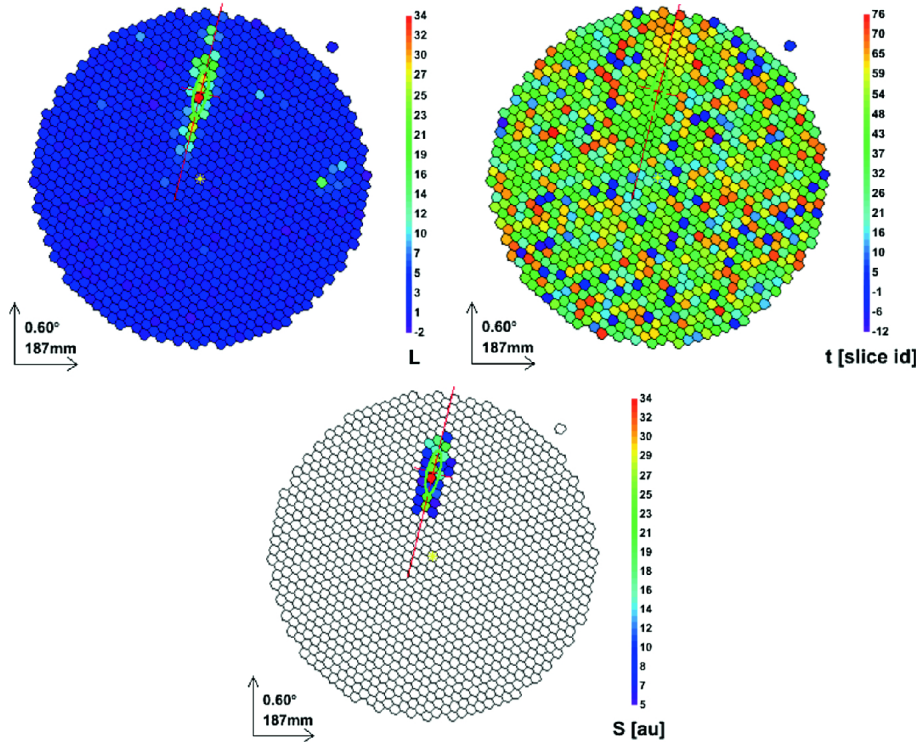


**Figure 5.1:** Image of an electromagnetic shower signal in the camera before (top left) and after (bottom) the image cleaning procedure. The image of the signal arrival times is also shown (top right).

**Width** The half width of the minor axis of the shower ellipse which, as it is correlated to the transverse development of the shower, is an important parameter for the discrimination between gamma-initiated and hadronic showers. In fact, the transverse development of the latter is larger on average than that of the former;

**Length** It consists on the half length of the major axis of the shower ellipse. Since it is correlated to the longitudinal development of the shower that is larger for hadronic showers than for gamma-initiated ones, as in the previous case, it is used for their discrimination;

**Conc-n** It is the fraction of phes contained in the  $n$  brightest pixels, that are the ones of the core of the shower. Also the Conc-n parameter can be helpful for the gamma/hadron separation, since for gamma-ray induced showers this region ought to be very compact;

**Leakage Parameter** It represents a fraction of signal distributed in the outermost camera ring with respect to the total size of the image. It can be used to reject images that cannot be reconstructed correctly, as it estimates the fractions of signal loss because of too large impact parameters;

**M3long** It is the third longitudinal momentum of the image along the major axis of the ellipse and measures the asymmetry of the signal along this axis. For this reason it is used to determine the propagation direction along the major axis (head-tail discrimination) of the shower. In fact, the head of a shower (imaging the shower maximum) is supposed to be more charge-concentrated than its tail;

**Number-of-Islands** As the name reminds, it is the number of distinct islands in the shower image and, consequently, it tells us the degree of fragmentation of the shower. Also this parameter allows the discrimination of hadronic showers, which are usually more fragmented, than the gamma-induced ones.

If taking into account observations in stereo mode, two other parameters can be listed:

**Alpha** Angle between the major axis of the ellipse and the direction from the image CoG to the reference point. It is the best parameter to distinguish hadronic showers from gamma-initiated showers, since the latter point directly to the source position in the camera and are hence characterized by small Alpha angles, on the contrary of hadronic showers. These have a rather flat Alpha distribution, as their distribution over the camera is isotropic;

**Dist** It is the distance of the image CoG to the reference point in the camera.

The parameters *Length*, *Width*, *Dist*, *CoG* and *Alpha* are presented in Fig. 5.2 for an electromagnetic shower event.

The definition of these parameters helps in distinguishing a gamma-initiated shower from a hadronic shower or a muon event. Even if the difference among these events is sometimes visible by eye during data-taking, see Fig 5.3, one way of discarding non-gamma showers is to fix a range of Hillas parameter, e.g. in *Width* and *Length*. In Fig. 5.4 the difference between a gamma-initiated shower and a cosmic-ray (hadronic) shower is shown through the different distributions of *Width* and *Length* Hillas parameters.

The fully parametrized data signals for each telescope are saved in root format [148] and called *Star data*, following the nomenclature used in the MAGIC Analysis and ReconStruction Software (MARS) [149]. Information on the atmospheric transmission [150] is also recorded in the same root file, together with the data.

The stereoscopic reconstruction of the shower parameters is, then, performed in the so-called Superstar program, obtained from the merging of the two Star files, one for each telescope.

This procedure permits to evaluate further geometrical parameters of the Extensive Air Shower (EAS), in order to better characterize them. These are:

**Shower axis direction** It is estimated from the intersection of the directions of the shower axes seen by each telescope;

**Shower core impact on ground** It is the area on the ground in which the shower impacts and comes numerically from the intersection between

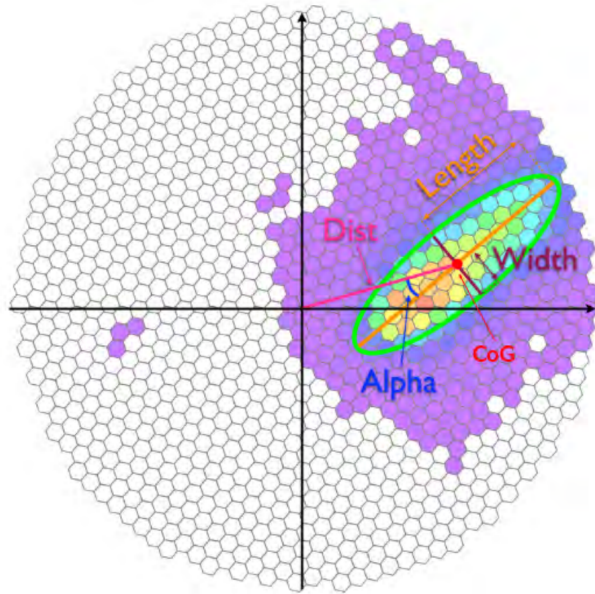


**Figure 5.2:** View of an electromagnetic shower in camera coordinates, marked with the respective Hillas parameters. Image taken from [145].

the projection on the ground of the two plans that contain the shower axis and the telescopes positions;

**Impact parameter** It is defined by the distance between the shower axis and the telescope position;

**Height of the shower maximum** It refers to the position at which the shower is brightest, and is calculated as the altitude that minimizes the distance between the shower axis and the two lines connecting the telescope position and the direction of the image centroid.

A schematic view of the stereo reconstruction is presented in Fig. 5.5.

Fundamental for the correct reconstruction of the shower axis direction and of its core impact on ground is the angular distance between the two image axes, that should be large enough to safely calculate the intersection point.

A further estimation of the incident direction in the sky of the primary gamma-ray, related to the geometrical stereo parameters, is performed in a following step of the analysis, with the aim of improving the value calculated at this step. I will talk about the adopted method in the next section.

The data reconstruction up to this step is automatically carried out by the On-Site Analysis (OSA) [152], a MAGIC on-line tool to analyse the data during data-taking nights, and Star and Superstar files can be directly downloaded from the MAGIC data center <sup>1</sup> at PIC (Port d'Informaciò Científica) <sup>2</sup>.

<sup>1</sup><http://magic.pic.es/>

<sup>2</sup><https://www.pic.es/>

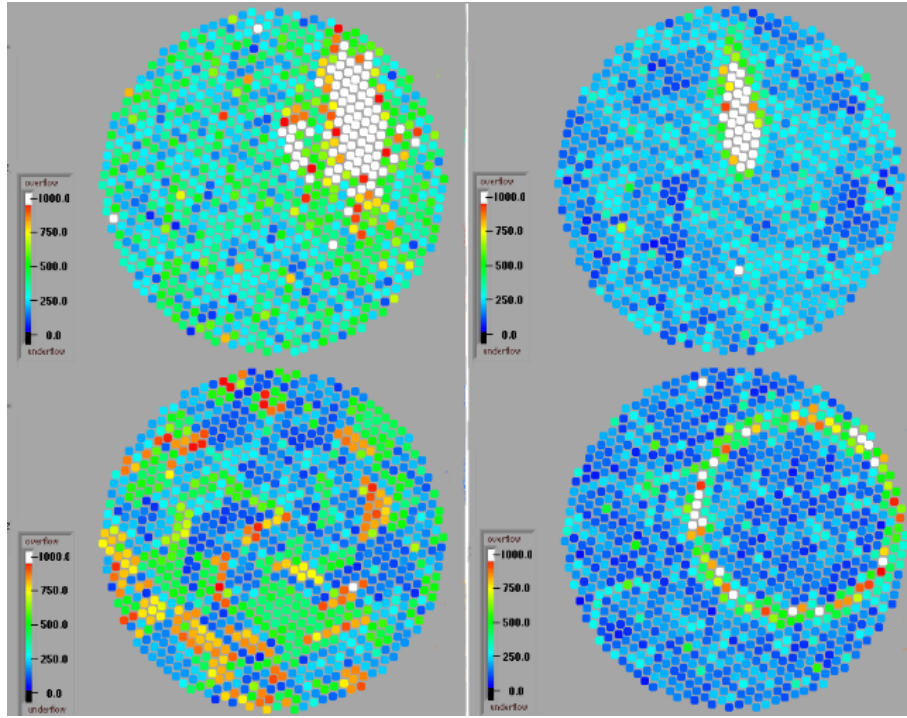


**Figure 5.3:** Excess events in the M1 camera. The image on the top left shows a hadronic-initiated shower, while the one on the top right a gamma-initiated one. On the bottom part, the NSB (on the left) and a muon ring (on the right), created by a high-energy muon [146], are presented.

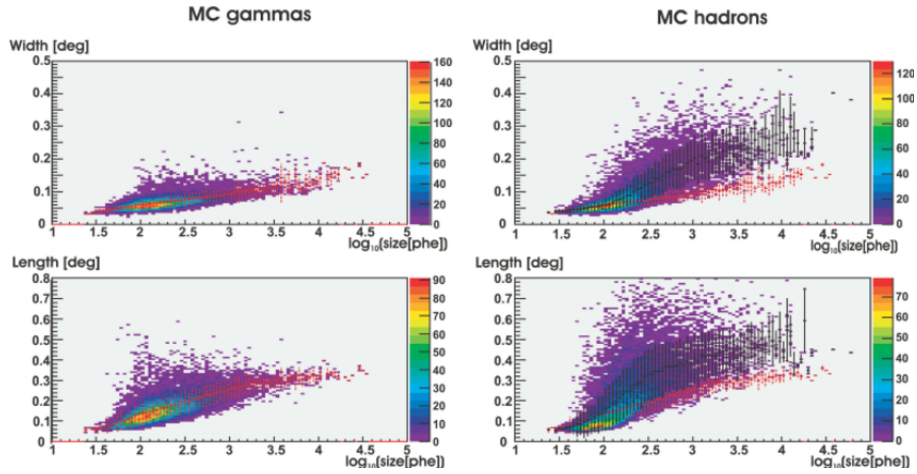


**Figure 5.4:** Simulated distributions of *Width* and *Length* Hillas parameters as a function of the shower *size* for gamma-initiated (left) and hadrons-initiated (right) showers [147].

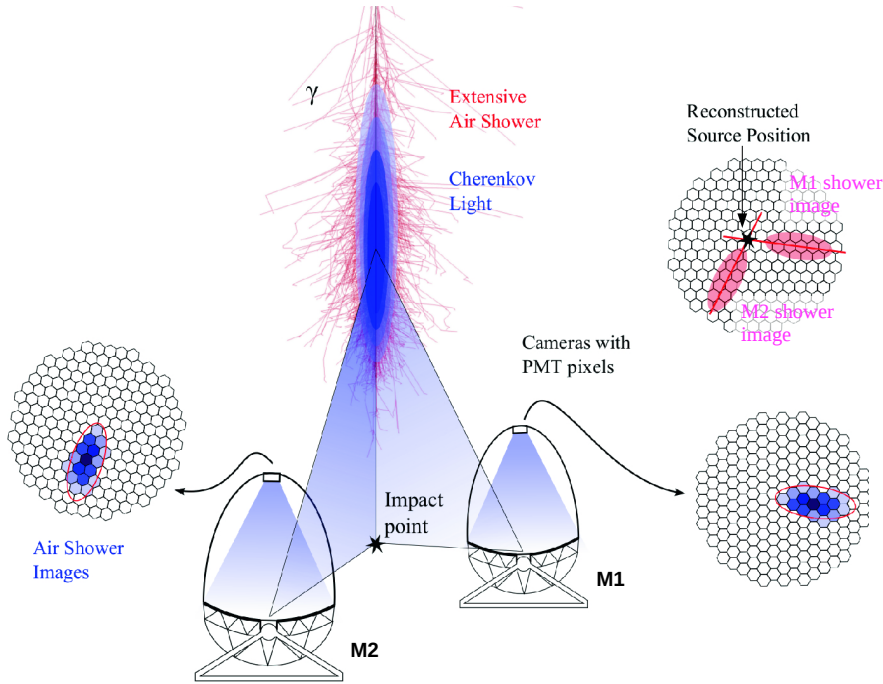


**Figure 5.5:** View of the stereo parameters reconstruction starting from a gamma-initiated shower. On the top right side of the figure, the *shower core impact on ground* evaluation, starting from the shower image of each telescope, is shown. Modified figure from [151].

### 5.1.1 Data quality check

The first action performed on the downloaded Superstar data (one can also decide to start with Star data, or even raw data, if a particular type of analysis has to be conducted, e.g. moon analysis [153]) is the data quality check. This is done using the *quate* tool, where cuts on geometrical parameters, energy, arrival times, Hillas parameters, parameters related to the hardware (e.g. PMT DC currents) and atmospheric parameters can be applied. The cuts can be made on entire runs, thus removing 20 min of data for each cut, or on time-slices. In this second case, the data-taking time of each observation night is divided in slices of two minutes, that can be removed from the overall data sample depending on the cut criteria being fulfilled or not.

For a typical DM analysis, the cut that needs to be set in all cases is the one on the aerosol transmission from 9 km altitude to ground, that should be always greater than 80%. This value has been chosen because it reflects one standard deviation of the MAGIC systematic uncertainty on energy scale [122], to which the aerosol transmission is directly proportional. Differently from other analyses, DM analyses need to start from the best data quality. An example of the cuts applied is given in Fig. 5.6 for the case of the M15 data quality check (described in the next chapter).

In the overview panel, most of the parameters are presented as a function of the Modified Julian Date (MJD) [154], just the last two ones are plotted as a function of the altitude above the MAGIC site, as they are the ones presenting

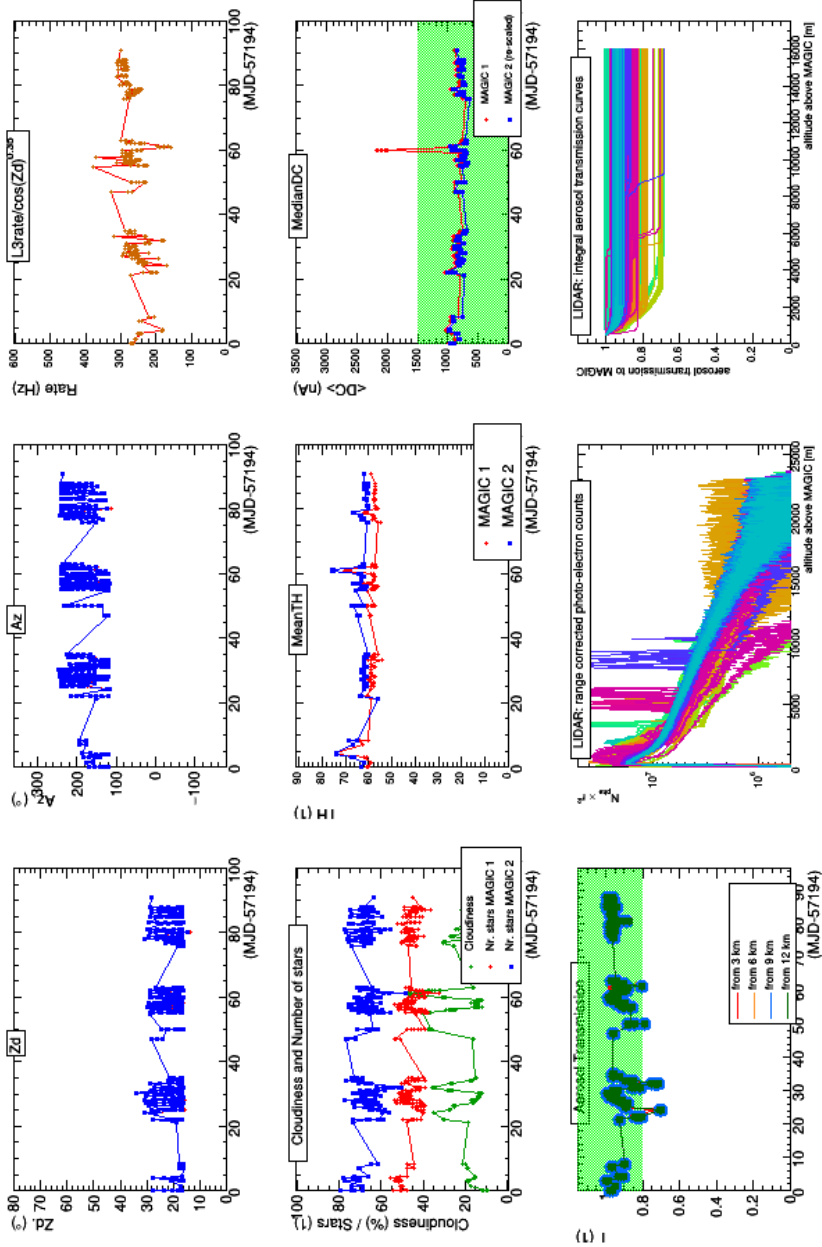


Figure 5.6: Overview panel of the quality cut procedure. See the main text for the explanation of each single plot.

LIDAR measurements. The first two plots on the top refer to the zenith (zd) and azimuth (az) cuts, cuts usually applied in case of particular needs, such as e.g. to divide the overall sample in subsample matching particular Monte Carlo (MC) samples, simulated using precise angular ranges. The third plot on the top row presents the rates of stereo triggered (L3) events, divided by  $\cos(\text{zd})^{0.35}$  to make them flat in zenith. This cut was used in the past when there was not the possibility of actively measuring aerosol transmission, but now it is not used anymore. The first plot in the central row is an indicator of the status of the atmosphere per observation night. It shows the cloudiness, measured by the pyrometer installed at the center of the M1 mirror, and the number of stars visible, measured by the starguider camera. The central plot reports the median (the "mean" is a typo in the code) discrimination threshold (TH), set by the Individual Pixel Rate Control (IPRC) [143]. In the same row, the last plot presents the median DC PMTs current for each telescope. The M2 median DC current has been rescaled, in order to be comparable with the one of M1, as the two cameras present different PMT DC currents even with the same Night Sky Background (NSB). For this parameter, a cut at  $1500 \mu\text{A}$  (green band) was applied to remove the outlier event in M1's median DC current. In general, cuts on the DC currents are used to remove moon data (presenting higher DC currents) from data taken during dark time or twilight. Finally, the first plot in the bottom row presents the aerosol transmission from different altitudes. As the 100 GeV Cherenkov shower shows its maximum at around 10 km a.s.l. on average, the transmission from 9 km above ground is the one we are interested in. In this particular plot, the cut on the aerosol transmission was set to 80%. The next plot shows the measurements performed with the LIDAR, from which the aerosol transmission is calculated.

In addition to the presented quality cuts, a selection of the data can be made also on the main Hillas parameters. This is done by taking the median over the entire data sample under consideration and excluding runs that show run-wise means beyond a certain number of standard deviations (fixed by the user) from the overall sample median.

## 5.2 Gamma-initiated shower selection and event reconstruction

At this point of the analysis, the data sample consists of a bunch of shower events, fully characterized by Hillas and stereo parameters, and by the event parameters, such as the arrival time and energy. From now on, we don't take into account anymore information about the atmosphere, as we selected the data with optimal sky conditions (if this would not have been the case, corrections on the event parameters could have been performed [155]).

The following step of the analysis consists of discriminating between hadronic showers and gamma-induced ones, and subtract events coming from gamma-ray emitting sources in the background.

As seen previously in Fig. 5.3, events coming from accidental triggers, e.g. NSB light, electronic noise etc., and from muons, that hit near the telescopes at ultra-relativistic velocities and generate rings, or sections of rings, on the cameras, can be detected together with EAS events. Once the first classes of signals are rejected in the quality check procedure, or directly by the triggering

system, EAS can be differentiated looking at the *hadronness* classification parameter. It describes the hadronic behaviour of the data taken, basing itself on the image parameter distributions, and varies in the range  $[0, 1]$ . It is defined by decision trees<sup>3</sup>, called Random Forests (RFs) [147], that are algorithms trained with events of known nature: MC simulated gamma-ray events and hadron events, extracted from an *OFF-sample*. The latter has to be formed by targets already observed with the MAGIC telescopes and in which analyses have encountered no signal excesses, at least for the data-taking period considered for the *OFF-sample*. Thus, the sources selected should be heavily dominated by hadronic events. Moreover, observation of these targets should belong to the same MAGIC analysis period, i.e. with same or equivalent characteristics of hardware and software<sup>4</sup>. Finally, in order to avoid artefacts in the training of the RF, *OFF-data* should cover the same zenith angles as the *ON-data* that we are analysing, and the total *OFF-sample* should provide sufficient statistics. Monte Carlo simulations are directly related to the MAGIC analysis period, as gamma-events should be simulated trying to follow the instrumental characteristics of the observations of our data sample. Depending on the extension of the object we are interested in analysing, we have *ringwobble MCs*, i.e. gamma-ray events simulated along a ring of radius 0.4 deg, whose core coincides with the center of the camera, and *diffuse MCs*, i.e. events simulated uniformly in a circle of radius 1.5 deg and similarly centred on the camera. The first type of MC simulations is used for the case of pointlike targets, defined as objects visible from the MAGIC site with an extension smaller than the MAGIC Point Spread Function (PSF) and typically observed in Wobble mode. This parameter depends on the detection energy and presents a maximum value of  $0.129^{+0.009}_{-0.021}$  deg for observations between  $30 - 45^\circ$  in zenith and at an energy of 95 GeV, if considering the 68% signal containment from Crab Nebula data [122]. For the sake of simplicity, we consider an average value of 0.1 deg. Thus, if the extension of the targets is smaller than this number, their gamma-emission is seen as a point that can be found around the source position in the camera, at a distance equal to the wobble distance of 0.4 deg. For this reason, if taking into account all the possible wobble and zenith/azimuth combinations, the gamma-events are simulated with the MC technique along the mentioned ring. On the other hand, if the source has a radius larger than the MAGIC PSF, the gamma-emission is more extended, and the source position cannot be uniquely defined. Although the wobbling procedure is still applied, the most general way to take into account the emission of the source consists of simulating gamma-events uniformly distributed up to the radius of 1.5 deg in the camera. In this case, depending on the effective extension of the target, the simulated events circle can be cut or re-weighted for the real size/shape of the source. The exact procedure will be explained in the following section. An example of the two types of MC simulation distributions is given in Fig. 5.7.

In addition to the consideration of the extension of the source, the zenith angle of observation of the target is taken into account when carrying out the simulations, as the MAGIC telescopes have a different resolution depending on the zenith angle. For this reason, simulations are divided into subsamples with

<sup>3</sup>A problem solving technique that is used to approximate the probability of certain outcomes by running multiple trial runs, the simulations, using random variables.

<sup>4</sup>If no OFF-data of the same period are available, data taken from periods with similar instrumental settings are allowed to be used.

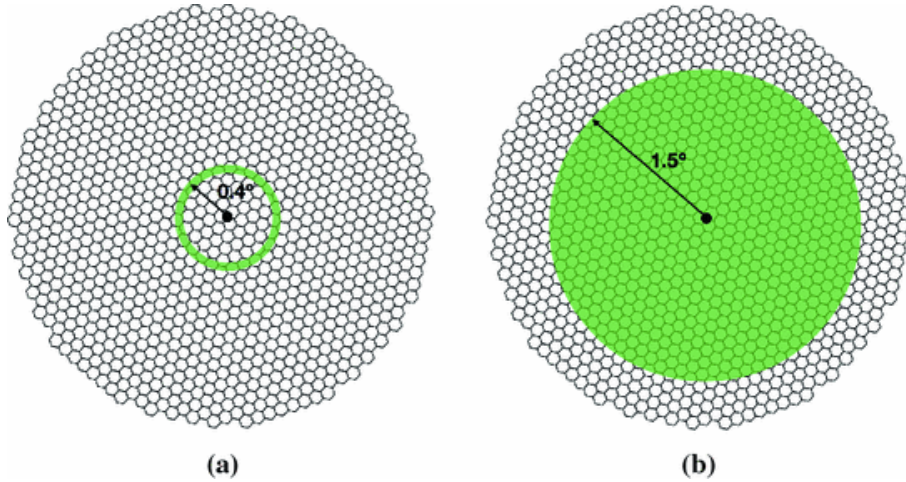


**Figure 5.7:** Schematic view of the MC simulations in the MAGIC camera, marked in green, for the case of pointlike targets (a) and extended targets (b). Image taken from [156].

different zenith ranges ( $[05^\circ-35^\circ]$ ,  $[35^\circ-50^\circ]$ ,  $[50^\circ-65^\circ]$ , etc.), and we consider only the ones covering the zenith angles of the ON-sample for our analysis.

Of the MC sample considered, half of it is used as input for the RF, while the other half is used in a following step of the analysis to estimate the spectrum and light curve of the target.

The RF method permits also to perform an energy reconstruction and to improve the calculation of the showers stereo parameter through the Distance between the Image centroid and the Source Position (DISP) method. This can be made thanks to the use of the *OFF-sample* and the MC sample to estimate the energy and the position of each event, respectively. Consequently, this fact is used to improve angular resolution.

At this step, once the RFs are created, they can be applied to the data in order to assign the hadronness estimator and the energy to the events. So, from parametrized stereo files, we obtain fully analysed event files.

The RFs are also applied to the MC sample (the half left from the previous splitting) in order to define the conversion energy and the direction of the gamma-showers, useful for the evaluation of the Instrument Response Function (IRF), performed in a following step of the analysis.

### 5.3 Extended source analysis: Donut Monte Carlo simulation

For Cherenkov telescopes, IRFs depend in general on the relative arrival direction of the gamma ray with respect to the telescope pointing direction. As mentioned, these IRFs are evaluated by means of MC simulations, thus, it is of utmost importance to correctly reconstruct, in them, the emission morphology of the target, also called *source brightness profile*. For many practical purposes, in most of the MAGIC analyses it is sufficient to evaluate IRFs for point-like gamma-ray sources, as many of the targets present an extension smaller than

the MAGIC PSF. However, in the case of DM searches, but not only, most of the objects observed are quite extended, due to their vicinity or their effective DM halo size, as for example in the case of dwarf spheroidal satellite (dSph) galaxies and galaxy clusters, and their emission morphology varies for each of them.

In order to compute the IRFs applicable to the study of these sources, to make an efficient use of the computing resources devoted to MC simulations, a method dubbed *Donut MC* has been developed [106, 157].

The natural procedure one would apply to simulate events for extended sources, through the MC method, consists in simulating gamma rays with true directions following the source morphology around the source center, and the source centres uniformly distributed in a ring centred at the telescope pointing direction and at a radius equal to the wobble distance adopted. This kind of MC production would demand at least as much computer resources as the point-like production, but would only be applicable for the study of a very specific source morphology. On the contrary, if taking into account MC productions consisting of gamma rays with true directions uniformly distributed over a 1.5 deg radius Field of View (FoV) and selecting events specifically for the study of a given source morphology, would only add a negligible overhead to the computing-intensive process of the full diffuse MC production, which is common for all possible source morphologies.

For the typical case of moderately-extended radially symmetric sources, the MC sample obtained with the *Donut MC* method shows a distribution of true gamma-ray directions with a shape resembling that of a donut, where the name of the method comes from, that maximizes the number of selected events, while keeping them statistically uncorrelated.

In order to understand the procedure followed, let us first consider a simplified version of it. We take into account only one fixed orientation between the pointing direction and the source center, and we select events from the diffuse MC based on the source morphology (see the top left plot in Fig. 5.8). If we now increase the number of orientations to  $n$ , for example equal to 100 (see the top right and bottom plots of Fig. 5.8), using the same technique, we would obtain a shaped ring in which the probability of having an event from a certain direction would increase with the number  $n$  of iterations of the procedure, thus overestimating its probability.

To avoid this artefact, the solution adopted in the *Donut MC* method is to first convolute the probability density functions (PDFs) of events with different source center/pointing direction orientation (as shown in the bottom right plot of Fig. 5.8 as a generic example and in Fig. 5.9 for the case of Coma Berenices dSph, presented in chapter 8), selected from the original MC simulations of diffuse events, and second to rescale what obtained following the source brightness profile (Fig. 5.10, for the case of Coma Berenices dSph). In this second step, a bunch of events are associated to source centres randomly selected in the expected ring, obtained in the first step, and then, after selecting the one with the same source center, they are distributed following the source brightness profile.

The application of this MC technique with particular source brightness profiles will be presented in detail in chapters 7 and 8.

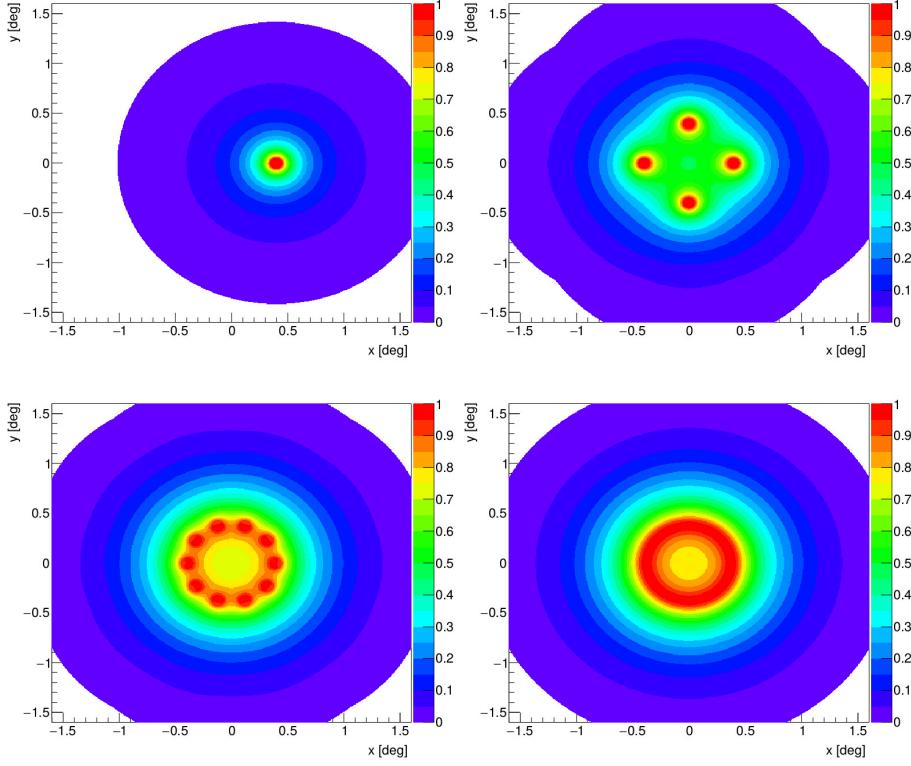


**Figure 5.8:** Probability density function simulations of true directions of gamma-events for 1 source center/pointing direction orientation (*top left*), and 4 (*top right*), 10 (*bottom left*) and 100 (*bottom right*) source center/pointing direction orientations. The last plot is the convoluted one used for the *Donut MC* method, as explained in the text. Credits [106].

#### 5.4 High-level analysis: gamma-ray flux estimation

Once rescaled the MC files through the Donut MC technique, we are ready to compute the spectrum and the light curve of the source, together with its IRF. The estimation of these quantities depends on the number of gamma-rays  $N_\gamma$  detected, emitted by the observed object and whose reconstructed directions are within a given angular distance from the nominal source position in the sky. The region defined by this angular distance is called ON region.

Given that in the ON region we measure also background events produced by cosmic rays (the case of background events emitted by the same source, but with a process we are not interested in, will be discriminated by looking at the expected spectrum), we need to define a threshold for the *hadronness* parameter in order to select a highly enriched signal event sample. An optimized selection of the *hadronness* and  $\theta^2$  parameter values is important to reach the maximum sensitivity for our analysis, and will be treated at the end of the chapter.

With the applied  $\theta^2$  and *haddronnes* cuts, we can subtract the background, estimated in the background (OFF) region, from the signal (ON) region. As

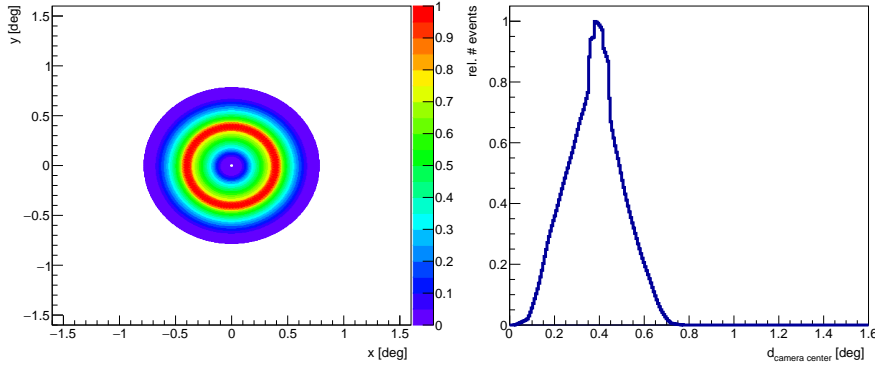


**Figure 5.9:** Example of the convolution of events' PDF for the case of MC simulated diffuse events considered in the analysis of Coma Berenices dSph in 2 dimensions (*left*) and 1 dimension (*right*). In this case, the maximum event true direction considered is found at a smaller angular distance with respect to Fig. 5.8, as in this case the extension of the source is smaller.

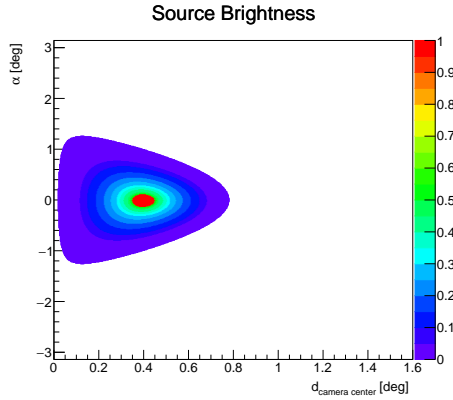


**Figure 5.10:** Source brightness profile, in the case of Coma Berenices dSph analysis, convoluted with the *Donut* ring obtained in the first step of the *Donut MC* procedure.

explained in the previous lines the ON region is defined as a circle of radius  $\theta$  around the expected source position. On the other hand, the OFF region is also a circle of the same radius, but centred on a mirrored position of the source in the camera. In the case the *simultaneous background* method is used, the mirror position is considered symmetric to the ON region, with respect to the center of the camera, during the same data taking slot. In the case of the *OffFromWobblePartner* method, the OFF region is taken from an area of the opposite wobble pointing and in a position symmetric to the signal area with respect to the center of the camera. The difference in adopting one or the other method lies in the uncertainties introduced. For the *simultaneous background* method, the influence of changes in the atmospheric conditions is minimized, as data in the OFF region are taken at the same moment as the ones in the ON region, thus presenting the very same atmospheric characteristics. Nevertheless, the data are more affected by camera inhomogeneities, if compared

with the ones considered with the *OffFromWobblePartner* method, for which signal and background are taken at the same camera position. The choice of one method or the other is, thus, based on which uncertainty is affecting less the analysis we are performing.

Several OFF regions can be used to estimate the background, but, in the case of the analyses presented in this thesis, only three or one background regions are taken into account.

After subtraction of the background, the number of gamma photons  $N_\gamma$  detected is, then, calculated as number of excess events  $N_{ex}$  in the signal region through the formula:

$$N_{ex} = N_{ON} - \frac{N_{OFF}}{\tau}, \quad (5.1)$$

where  $N_{ON}$  is the number of events in the signal region,  $N_{OFF}$  the number of events in the background region and  $\tau$  is number of background regions considered. The significance of the result obtained, as commonly done in very high energy (VHE) astronomy, is computed using Eq. 17 of [158]. The outcome of this subtraction is shown in Fig. 5.11, in which the excess events calculated for the case of the Crab Nebula are presented as an example.

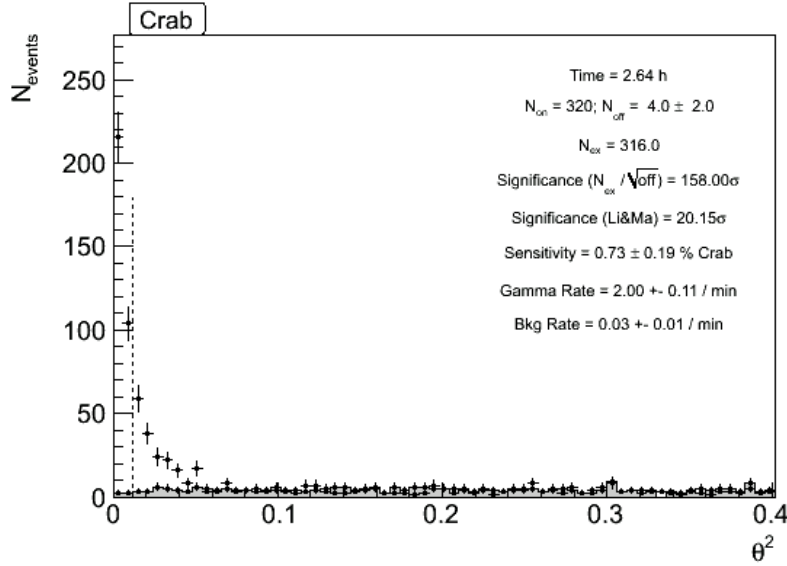


**Figure 5.11:**  $\theta^2$  plot of 2.64 h of Crab Nebula data. The signal excess is visible at the center of the source, around  $\theta^2 = 0$ . The data of the OFF region are marked with a grey area. All numerical and statistical details about the data are presented in the upper right corner.

Another way of looking for excess events is through the use of skymaps, which are two-dimensional representations of the of the number of photons arriving from each direction in the FoV, registered during the observations. An example of a skymap produced in the MAGIC analysis is given in Fig. 5.12.

Once determined the excess event in our data, the gamma-ray differential spectrum per unit of energy  $dE$ , area  $dA$  and time  $dt$  is defined as:

$$\frac{d\Phi}{dE} = \frac{d^3 N_\gamma(E)}{dE dA dt} \quad (5.2)$$

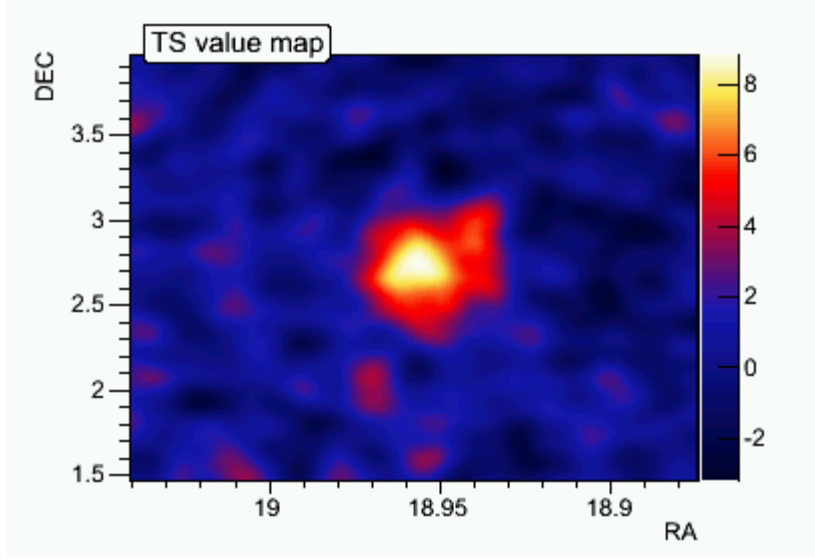


**Figure 5.12:** Example of a (smoothed) significance skymap. The excess events are marked following the color code presented in the vertical band on the right side of the figure.

where  $\Phi$  is the gamma-ray flux and  $N_\gamma$  is the number of observed excess gamma events, for a given energy  $E$  bin, after applying cuts in  $\theta^2$  and *hadronness*. The time  $t$  is the effective time of observation of the target (after the cuts applied on the data), to which the dead time of the detector (period of time typically following the recording of an event, during which the data acquisition system is busy and cannot accept any new event) has been subtracted.

The area  $A$  is the *effective collection area*  $A_{eff}$  of the telescopes, i.e. the area of an equivalent detector that would detect with 100% efficiency the same rate of gamma rays as the real instrument, calculated using the formula:

$$A_{eff} = A_{simulated} \times \frac{N_{\gamma,final}}{N_{\gamma,simulated}}, \quad (5.3)$$

thus making use of the MC simulations for estimating the primary collection area  $A_{simulated}$ <sup>5</sup>, depending mainly on the energy and incoming direction of the gamma rays, and the number of detected gamma-photons  $N_{\gamma,simulated}$  (including also those that do not trigger the telescopes).  $N_{\gamma,final}$  is the final number of photons, after the application of the analysis cuts.

The collection area, such as the number of excesses  $N_\gamma$ , is expressed as a function of the energy. This energy is named *estimated energy*  $E_{est}$  and stems from the reconstruction of the energy of the gamma ray detected. Due to the finite energy resolution and bias of the detector,  $E_{est}$  is different from the true energy  $E_{true}$  of the gamma ray. In order to get a physical meaning for the spectrum, it has to be unfolded through the use of a so-called *energy migration matrix*. This procedure is done in a final step for the case of DM analysis, thus, I will

<sup>5</sup>Assuming an intrinsic spectral shape in the MC sample, which in principle should not be too different from the real spectrum of the source

talk about this in the following section.

In the event of no signal excess, upper limits on the gamma-flux, as a function of a single or multiple energy bins, are calculated using the likelihood method described in [159]. As we are still in a general step of the analysis (not focused on DM), a generic spectrum of the source, following a power-law, is considered.

In order to take into account the proper DM spectrum, a further full-likelihood analysis, described in the following section, is performed.

## 5.5 Binned likelihood analysis for dark matter targets

As stated multiple times in the manuscript, the flux of gamma rays produced by a DM annihilation/decay process is directly related to the nature of the DM particle, and to the morphology of the source observed with the VHE experiment.

Reconsidering Eq. 3.3:

$$\frac{d\Phi_\gamma}{dE} = \frac{d\Phi^{PP}}{dE} \times J(\Omega) . \quad (5.4)$$

and introducing the gamma-ray spectra and  $J$ -factor values (see chapter 3 for detailed explanations), the spectral and morphological templates for the gamma-emission of our targets are estimated. Nevertheless, there is a quantity still undefined and that characterizes the DM particle we are looking for. In the case of WIMP DM annihilation, process considered for the analyses in the analysis presented in the following chapters, this quantity is the velocity-averaged cross-section of WIMP DM. In order to evaluate it, an ad-hoc full likelihood analysis [160] was implemented within the MAGIC collaboration, now publicly available for the use in other IACT experiments [161]. The benefit of this likelihood with respect to the one used for standard MAGIC analyses [159] is the introduction of the DM spectrum in the likelihood equation, leading to an increase of sensitivity for DM searches, and the binning in energy. This last change improves the treatment of the systematic uncertainties related to the background with respect to a full unbinned likelihood [157].

The likelihood function  $\mathcal{L}$  is expressed in terms of the weighted-averaged annihilation cross-section  $\langle\sigma_{ann}v\rangle$ , for each data set  $\mathcal{D}$  (presenting different IRFs), each target  $t$  and each wobble pointing  $i$  (equal to 1 or 3, as mentioned in the previous section). It is written for each  $j$ -th bin of energy as follows:

$$\begin{aligned} \mathcal{L}_{ti}(\langle\sigma_{ann}v\rangle; \nu_{ti} | \mathcal{D}_{ti}) = \\ \mathcal{L}(g_t(\langle\sigma_{ann}v\rangle, J_t); \{b_{tij}\}_{j=1, \dots, N_{bins}}, \tau_{ti} | (N_{ON,tij}, N_{OFF,tij})_{j=1, \dots, N_{bins}}) = \\ \prod_{j=1}^{N_{bins}} \left[ \frac{(g_{tij}(\langle\sigma_{ann}v\rangle) + b_{tij})^{N_{ON,tij}}}{N_{ON,tij}!} e^{-(g_{tij}(\langle\sigma_{ann}v\rangle) + b_{tij})} \times \frac{(\tau_{ti} b_{tij})^{N_{OFF,tij}}}{N_{OFF,tij}!} e^{-\tau_{ti} b_{tij}} \right] \times \\ \mathcal{T}_{ti}(\tau_{ti} | \tau_{obs,ti}, \sigma_{\tau,ti}) \times \mathcal{J}(J_t | J_{obs,t}, \sigma_{J,t}) . \end{aligned} \quad (5.5)$$

As one can notice, it is the product of a Poissonian function of the signal  $g_{tij}$  and background  $b_{tij}$  events, as function of the number of observed events in the ON and OFF regions ( $N_{ON,tij}$  and  $N_{OFF,tij}$ , respectively), multiplied by a likelihood for the OFF/ON acceptance ratio<sup>6</sup>  $\mathcal{T}_{ti}$ , parametrized by a Gaussian

<sup>6</sup>Computed as the ratio of the number of the observed events in the OFF and ON regions.

function with mean  $\tau_{obs,ti}$  and variance  $\sigma_{\tau,ti}$  (that includes both statistical and systematic uncertainties as  $\sigma_{\tau,ti} = \sqrt{\sigma_{\tau,stat,ti}^2 + (\tau_{ti} \cdot \sigma_{\tau,syst})^2}$ , where the  $\sigma_{\tau,syst} = 1.5\%$  as estimated in [122]), and by a likelihood for the logarithm of the  $J$ -factor  $\log(\mathcal{J})$ , also parametrized by a Gaussian function with mean  $J_{obs,t}$  and variance  $\sigma_{J,t}$ . The  $J$ -factor value  $J$  (estimated for the computation of the expected number of gamma rays  $g$ ), the expected number of background events  $b_{tij}$  and the OFF/ON acceptance ratio  $\tau_{ti}$  are considered as nuisance parameters  $\nu_{ti}$ .

The expected number of gamma-rays  $g_{tij}$  is a function of the free parameter  $\langle\sigma_{ann}v\rangle$ , the parameter of interest in our analysis, and of the  $J$ -factor nuisance parameter as follows:

$$g_{tij}(\langle\sigma_{ann}v\rangle, J_t) = T_{obs,ti} \int_{E'_{min,j}}^{E'_{max,j}} dE' \int_0^\infty dE \frac{d\phi(\langle\sigma_{ann}v\rangle, J_t)}{dE} A_{eff,t}(E) G_t(E'|E) \quad (5.6)$$

where  $T_{obs,ti}$  is the total observation time for each wobble position, the extremes of the integral  $E'_{min,j}$  and  $E'_{max,j}$  are respectively the minimum and the maximum energies in the  $j$ -th energy bin,  $A_{eff}$  is the effective collection area and  $G$  is the probability density function for the energy estimator  $E'$ , given the true energy  $E$ . The latter is called *energy migration matrix* and provides the probability of migration from the estimated energy  $E_{est}$ , in this case called  $E$  to the true energy  $E_{true}$ , here called  $E'$ . It is evaluated starting from a Gaussian fit of the  $(E - E')/E'$  distribution for each bin in  $E$  and  $E'$ . This Gaussian function presents a width given by the energy resolution  $E_{RES}$  of the telescopes and a mean given by their bias  $E_{BIAS}$ . An example of this fit is presented in Fig. 5.13.

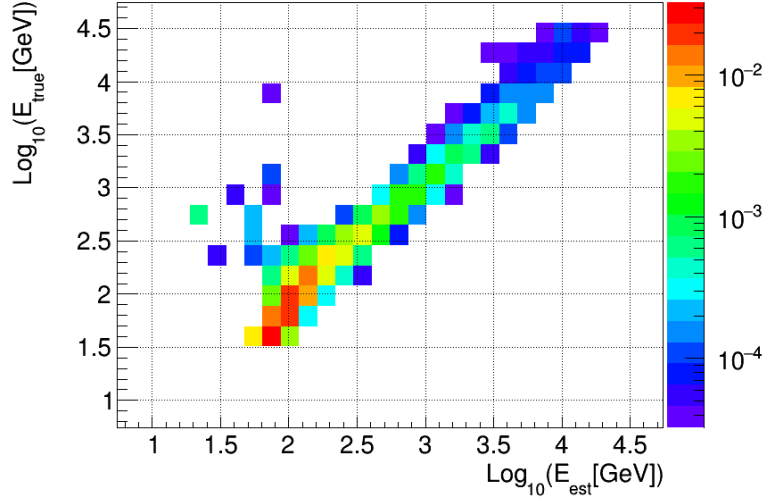


**Figure 5.13:** Migration matrix obtained for the Draco dSph data analysis.

The effective collection area  $A_{eff}$  and the migration matrix  $G(E'|E)$  represent the IRF, that is computed starting from a Monte Carlo simulated gamma-ray data-set and following the spatial distribution expected from the DM-

induced signal of the object studied.

To obtain an estimate of the velocity-averaged cross-section  $\langle\sigma_{ann}v\rangle$  per DM mass considered<sup>7</sup>, the number of gamma-events in the ON  $N_{ON}$  and OFF  $N_{OFF}$  regions for the different bins of estimated energy (after the analysis cuts), the WIMP DM mass and spectrum [162], the IRF and the mean  $J$ -factor, with its respective uncertainty, have to be introduced. The  $\langle\sigma_{ann}v\rangle$  values obtained exclude, at the 95% CL, velocity-averaged cross-sections higher than those values (from which the nomenclature *upper limits on the velocity-averaged cross-section*), thanks to the application of a *profile likelihood ratio* test statistics  $\lambda_p$ . This can be written as:

$$\lambda_p(\langle\sigma_{ann}v\rangle|\mathcal{D}) = \frac{\mathcal{L}(\langle\sigma_{ann}v\rangle; \boldsymbol{\nu}^*|\mathcal{D})}{\mathcal{L}(\langle\sigma_{ann}v\rangle'; \boldsymbol{\nu}'|\mathcal{D})} \quad (5.7)$$

where  $\boldsymbol{\nu}^*$  is the sample of nuisance parameters that maximize the likelihood for a fixed value of  $\langle\sigma_{ann}v\rangle$ , while  $\langle\sigma_{ann}v\rangle'$  and  $\boldsymbol{\nu}'$  are the values that maximize the overall  $\mathcal{L}$ , thus without doing any assumption on  $\langle\sigma_{ann}v\rangle$ .

As to obtain upper limits (*UL*) on the velocity-averaged cross-section at the 95% CL, then, following Wilk's theorem [163], the *profile likelihood ratio* should fulfil the constraint:

$$-2 \ln \lambda_p(\langle\sigma_{ann}v\rangle^{UL}|\mathcal{D}) = 2.71 \quad (5.8)$$

where 2.71 is the value assumed by the  $\chi^2$  distribution for 1 degree of freedom, as we leave  $\langle\sigma_{ann}v\rangle$  as the only free parameter, in the case of a one-sided distribution interval.

In order to obtain physical values of the event estimator  $g$ , as the number of gamma-photons cannot be negative, only positive values of it are taken into account.

For more details on the full-likelihood method application, see [160].

## 5.6 Cut optimization for improved analysis sensitivity

For DM searches, given the fact that no hint of signal has been found until now, we want to have the best sensitivity in the energy interval at which the MAGIC telescopes are optimized, i.e. around 1 TeV [122]. In order to achieve that, an optimization of the  $\theta^2$  and *hadronness* analysis cuts, mentioned in section 5.4, is applied blindly to the data. This procedure consists of finding the best sensitivity for our analysis among the ones obtained by the combination of different cuts.

The sensitivity of the DM analysis performed is defined as the average limit of  $\langle\sigma_{ann}v\rangle$  obtained for a given CL under the assumption of the null hypothesis. The values of the sensitivity for the DM masses considered can, thus, be retrieved in two ways:

- taking the value of the  $\langle\sigma_{ann}v\rangle$  at the 95% CL, subtracting the value that this same parameter assumes when minimizing  $-2 \ln \lambda_p(\langle\sigma_{ann}v\rangle^{UL}|\mathcal{D})$ , as reported in [164];

---

<sup>7</sup>The value of the DM particle mass is evaluated from the reconstructed energy of the gamma-photon.

- producing a sample of independent Monte Carlo simulations, from which estimating the  $\langle\sigma_{ann}v\rangle$  accomplishing with the null hypothesis, and taking the median of the values obtained.

As the first method is faster than the second one, but also less precise, it is used for the cuts optimization, while the Monte Carlo simulations are adopted at the moment of presenting the final results of the analysis. A description of this cuts optimization method can be found in [157], and it is presented in chapters 7 and 8.

## Chapter 6

# Dark Matter Searches on M15

Globular clusters (GCs) are the oldest objects in the Universe, having ages similar to their host galaxies, and present elevated densities of stars, in particular at their centres. Around 160 GCs have been detected in the Milky Way (MW) and more of them may still be discovered. Being relatively close to the Earth, embedded in the MW dark matter (DM) halo, and assumed to present their own DM subhalo, following the hierarchical structure scenario, they had been proposed as promising targets for indirect DM searches. After multiple studies on GCs' internal dynamics and no evidence of DM found, nowadays they are disregarded as interesting DM targets, preferring other sources, such as dwarf spheroidal satellite (dSph) galaxies, clusters of galaxies and the Galactic Center.

Imaging atmospheric Cherenkov telescopes (IACTs) keep observing this type of objects to study gamma-ray emissions, but this time coming from other astrophysical processes, in particular from populations of millisecond pulsars (MSPs), thus not counting on any possible DM signal. Nevertheless, even in this unfavourable situation, the presence of DM is still under debate.

Messier 15 (from now on M15) was observed by MAGIC in 2015-2016 for a Key Science Project (KSP) on MSPs [165]. Thanks to the large data sample available and given the possibility of detecting a WIMP annihilation signal, as the high density of baryonic matter in the core of the cluster does not yet absorb gamma-rays and enhance DM observation, it has been decided to study M15 also from a DM point of view. At the beginning, a standard MAGIC analysis was performed on the data, as described in section 6.3. Once no hint of a signal has been found, three different  $J$ -factors have been used to evaluate the  $\langle\sigma_{ann}v\rangle$  upper limits (ULs) on WIMPs DM annihilation, as described in sections 6.4 and 6.5. In section 6.6, the conclusions of the study are presented. Together with the description of future DM modelling methods that can be applied to improve this work, the use of new telescopes that can give more precise kinematic measurements on the cluster's stars is suggested.

The chapter begins with an introduction on GCs, in particular referring to their DM content, and will then move to the GC M15.

## 6.1 Star clusters

Gravitationally bound concentrations of stars are quite common in the MW and in the other galaxies of the Local Group. They show up in multiple ways and can be grouped in three main categories: *open star clusters*, called also *galactic clusters* (because of their confinement inside the galactic disk); *globular clusters* (that have obtained this name from their sphericity) and *dark star clusters*, mainly composed of non-luminous objects [166]. This latter type of clusters will not be taken into account in the following lines, as they are quite different from the other two types and they are not of interest for the research described in this chapter.

If we focus on our Galaxy, open clusters can be found in the Galactic disk (as

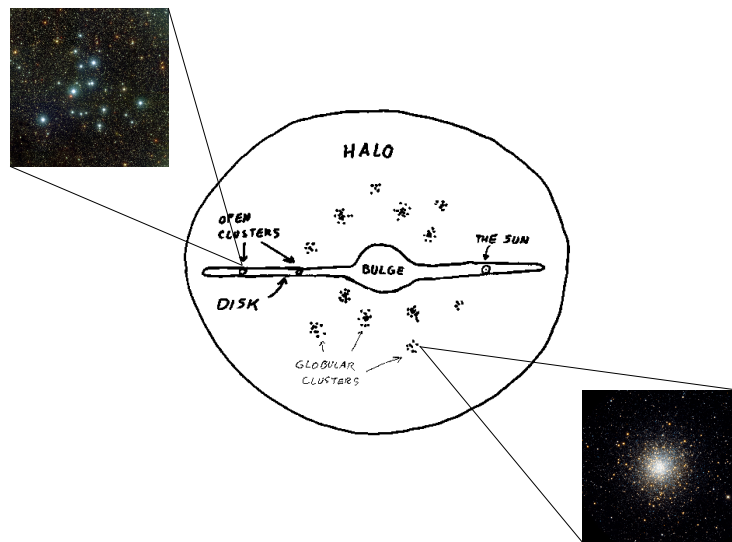


**Figure 6.1:** Schematic painting of the location of star clusters in the MW, together with the image of an open star cluster (M39) on the upper left corner, and of a globular cluster (M10) on the bottom right corner. The M39 image has been taken from APOD website [167], the central image from The University of Iowa website [168], and the bottom right one from Michael Richmond's classes [169].

mentioned in the previous lines), while GCs are concentrated in the Galactic Center, as shown in Fig. 6.1, or spread around the halo, thus not participating in the Galaxy's disk rotation. Worth to notice is that GCs present highly eccentric elliptical orbits and a distance of several thousand light years from the Galaxy, reaching relative velocities of hundreds kilometres per second. Moreover, lying out of the central plane of obscuring dust clouds, GCs suffer much less interstellar extinction than the stars in the disk [170].

Apart from their position in the MW, one can distinguish these two types of clusters looking at the number of stars contained in them and at their metallicities. Open star clusters present  $\sim 10^3$  stars and have heavy-element abundances characteristic of Population I stars. On the other hand, GCs typically

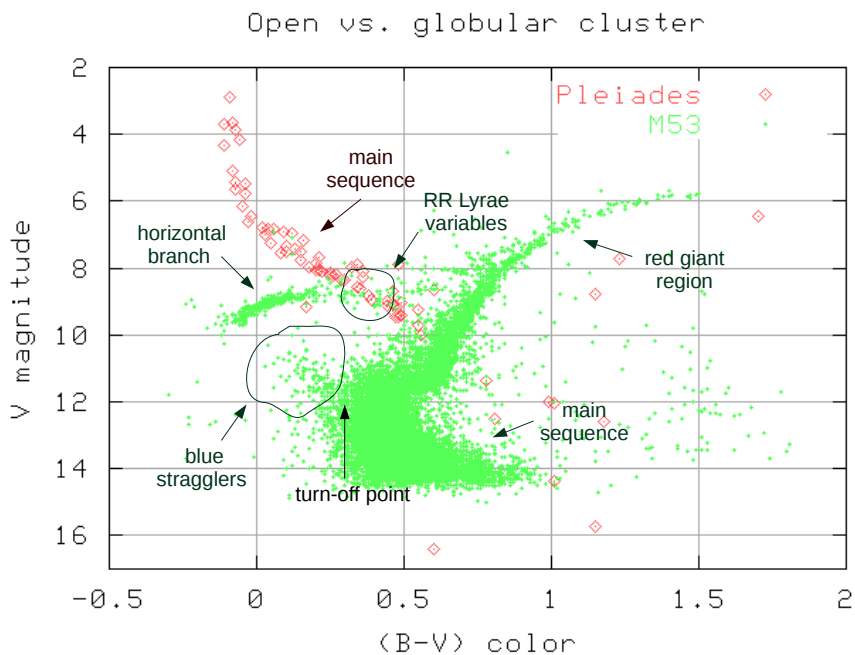


**Figure 6.2:** HR diagram of apparent magnitudes of the Pleiades open star cluster (in red) in comparison with the one of M53 globular cluster (in green), taken from [169] (the V-band magnitudes of the stars in M53 have been shifted upwards by 8 in order to fit nicely on the same graph with the Pleiades). The stars belonging to the Pleiades are reported in dark red, the ones belonging to M53 are in dark green. The turn-off point of the GC is also indicated.

contain  $\sim 10^6$  stars and present metal-poor stars of Population II, or multiple star populations [171]. This difference is clearly visible with a look at the Hertzsprung-Russel (HR) diagram of typical MW clusters, such like the ones shown in Fig. 6.2. In the figure, an open star cluster, the Pleiades, is compared to a GC, M53. The Pleiades are mainly composed of stars belonging to the main sequence. In fact, open star clusters are very young systems and metal-rich, contain Population I stars and are still full active in star formation. When comparing the HR diagram of Pleiades with the one of a typical GC, M53, a wide-spread difference can be seen. The latter, like all other GCs, is a very old gravitationally bound system, formed by Population II stars, thus with much less metal content than the Sun, and do not present any active star formation. Variable stars, white dwarfs and neutron stars (some of them showing up as pulsars) are the typical objects that can be found in a GC. A noticeable aspect of GCs' HR diagram is the presence of a further star type, namely hot brilliant stars called *blue stragglers*, situated in the upper left corner of the main sequence. Having great masses (mostly twice of the mass of a common star in the GC) and high rotation rates, it is supposed that these blue stars are the result of a merger of two red stars.

Another important aspect when looking at the HR diagram of a GC is the *turn-off point*, a point on the main sequence distribution in which the stars

turn away from it. As all the stars in the GCs have been formed mostly at the same time, the turn-off point depicts the age of the GC, and the luminosity and temperature related to it highlight the old age of the stars contained in the cluster.

It is possible that some of the GCs in our MW present multiple stellar populations. This fact appears to be a common feature in old GCs, given the possibility of having been subjected to multiple dynamical processes and the possible presence of binary systems. A more detailed explanation about this point will be given in the next section.

### 6.1.1 Globular clusters: dynamics and dark matter content

The first discovery of a GC, named Messier 22 (M22), took place 1665, and up to 160 GCs more have been detected until nowadays in our MW <sup>1</sup>. At least tens further GCs have still to be observed [172, 173], but our Galaxy might have contained substantially more globular clusters in the past, tidally destroyed because of their orbits crossing the Galactic plane and the central regions of the Galaxy [174].

GCs can be divided into two sub-populations as a function of their metallicities. Even though all show low values of metallicity, as a consequence of their old ages, there can be blue GCs, *metal-poor* (MP) GCs with distribution peaks at  $[\text{Fe}/\text{H}] \approx -1.5$  for the MW, and red, *metal-rich* (MR), GCs with a peak at  $[\text{Fe}/\text{H}] \approx -0.5$  [175]. This metallicity bimodality is naturally predicted by the hierarchical clustering scenario. MR-GCs are (1–1.5) Gyr younger than the MP ones and more spatially concentrated. They were formed in the galaxy progenitor around redshift  $z \sim 2$ , contrary to MR-GCs that are clusters accreted, either via merging satellite galaxies or by tidal capture of the clusters themselves, and formed at redshifts  $z \sim (3-4)$  [176].

GC formation has, then, occurred around the time of, or continuing after, the epoch of reionisation [177]. Nevertheless, determining the correct ages and the physical origin of GCs is still an observational challenge.

The uncertainty on the GCs' formation epoch comes together with the uncertainty on the presence of a DM halo surrounding these objects and the question if GCs were formed at the center of their own DM halo, as suggested by Peebles [178]. If we assume that this is the case, then taking into account primordial GCs, and not considering the ones merged in a second moment with the MW, there is still disagreement on the presence of DM in them at current times.

The presence or absence of DM is settled by the dynamical processes influencing the clusters evolution. First of all, due to their position in the Galaxy, GCs are subject to

textittidal shocks because of their crossing of the bulge or disk of the Galaxy. These collisions affect both baryons and DM, by, e.g., changing the velocity distribution of stars and tidally truncating the cluster, *stripping* the outer part of the assumed DM halo [179] too. Moreover, since the relaxation time of GCs (of the order of  $\sim 100$  Myr) is smaller than their age ( $\sim$ Gyr), they must have passed through a *mass segregation* process, in which larger mass stars in a gravitational encounter tend to lose kinetic energy and fall deeper into

<sup>1</sup>[https://www.messier.seds.org/xtra/supp/mw\\_gc.html](https://www.messier.seds.org/xtra/supp/mw_gc.html)

the potential well of the cluster, while, at the same time, stars of lower mass are driven out, thanks to an equipartition of kinetic energy [170,180]. If this had happened before the tidal stripping process, stars and DM (also gravitationally segregated) in the outer parts of the cluster would have been swept away [181,182]. Mass segregation can also lead to a *collapse of the cluster's core*, if the cluster does not *evaporate* before reaching that stage, reflected in a rising of the mass-to-light ratio (M/L) towards the center of the cluster, as pointed out in [183].

As GCs are very old systems and the mean time for a core to collapse is typically less than the age of the host galaxy, many GCs may be in the *post core-collapse phase*, thus re-expanding [184]. In addition to that, a consequence of the collapse, that leads to an *adiabatic condensation* of baryons in the core of the clusters, is a high concentration of DM in the center, as demonstrated in [185]. In this case, the increase of M/L tends to be more cuspy than in the case of the collapse alone, but a similar trend can show up also in the presence of an Intermediate Mass Black Hole (IMBH). Thus, an accurate evaluation of the velocity dispersion profile of the stars in the cluster's center is needed to discard one or the other option.

In this scenario, if no IMBHs can be accounted as dark mass, GCs appear to be DM dominated and very promising targets for DM detection. Unfortunately, the addition of the kinetic heating of DM by stars process in the center of the cluster, as described in [186], leads to a depletion of the core, thus reducing the DM amount.

In the next section, one of the prototypes of post core-collapsed clusters will be presented, and all the processes described here will be taken into account to characterize its dynamical evolution.

## 6.2 The globular cluster M15

The Messier 15 (M15) globular cluster (also called NGC7078) was discovered on September 1746 by the Italian astronomer Giovanni Domenico Maraldi (also known as Jean-Dominique Maraldi). As written in Charles Messier's catalogue [187], in which the object was incorporated, it appeared like a *'Nebula without a star, between the head of Pegasus and that of Equuleus; it is round, in the center it is brilliant, its position was determined by comparison with Delta Equulei'* [188].

This spectacular bunch of stars, centered at right ascension  $RA = 21^{\text{h}}28^{\text{m}}58.3^{\text{s}}$  and at declination  $Dec = 12^{\circ}10'00.6''$  in the J2000 coordinate system [189], is located at a distance of  $10.4 \pm 0.8$  kpc from the Sun [190], shows a total stellar luminosity of  $7 \times 10^5 L_{\odot}$ , and is visible from the Earth with an apparent magnitude



**Figure 6.3:** M15 GC captured by the Hubble telescope.  
Credits: ESA/Hubble & NASA

of 6.2 [191].

With its  $\sim 12$  Gyr it is one of the three oldest GCs in the MW [192]. This is demonstrated by the fact that M15 is one of the only four GCs hosting a planetary nebula, Pease 1, visible as a glowing light-blue spot in the bottom left center zone of the cluster in Fig. 6.3. Apart from the nebula, at least 112 variable stars and 9 known pulsars compose the cluster, adding up to a total mass of  $5.6 \times 10^5 M_\odot$  [193].

M15 is also one of the densest clusters ever discovered, with a stellar mass density of  $\sim 10^7 M_\odot \text{pc}^{-3}$  in its core [194], where stellar-mass compact objects, such as neutron stars and/or massive white dwarfs, become more concentrated. Given its age, elevated density and rising luminosity all the way to the center, it belongs to the class of *post-core collapse clusters* [195]. This type of clusters is often associated with the presence of an IMBH [196] of the order of thousands of solar masses in their centres. In the case of M15, it has been demonstrated that kinematic data can also be explained without the gravitational attraction of the IMBH, even if its presence is not completely excluded [197, 198].

The post-core collapse cluster scenario implies also very poor metallicity of the stars in the cluster, classifying it a *blue* GC with  $[\text{Fe}/\text{H}] = -2.37$  [199]. This brings the attention to the fact that M15 could be an excellent primordial GC candidate that, following the standard paradigm of hierarchical structure formation, formed within a DM halo [178]. The presence of, at least, a fraction of the primordial halo around the cluster is, however, still not confirmed at the present day. The extremely high stellar density in the core can minimize the gravitational effects of the halo, thus not permitting its observation with kinematic measurements.

In 2008, the Whipple collaboration performed a study on self-annihilating WIMP DM in M15 [200]. Even if models for the M/L of the cluster were consistent with a purely baryonic mass profile [201] at that time, implying a quantity of DM lower than the stellar component, the authors argued about the possibility of detecting a potential DM annihilation signal without any major limitation.

A standard NFW profile, with the virial mass and concentration parameter of the cluster, in the range  $m_{\text{vir}} = 5 \times 10^6 M_\odot - 5 \times 10^7 M_\odot$  and  $c = 32 - 82$ , respectively, was used to calculate a first estimate of the J-factor. A second J-factor was estimated taking into account the adiabatic contraction (AC) of DM in the core of the cluster, a process that could have enhanced the annihilation signal by several orders of magnitude. The AC model of Blumenthal [202], together with the assumption of circular orbits for the DM particles was used for this second estimation. The values of J presented in [200] have been converted to units of  $\text{GeV}^2 \text{cm}^{-5}$ , multiplying the exponential of the numbers in [200] with the square critical density  $\rho_c^2 = (9.74 \times 10^{30})^2 \text{g}^2 \text{cm}^{-6}$  and the Hubble radius  $R_H = 4.16$  Gpc, and are reported in Tab. 6.1.

In 2011, the H.E.S.S. collaboration performed a similar study, this time taking into account further astrophysical processes that have taken place in the source [203]. The kinetic heating of DM by baryons [186] was added to the mass segregation and the AC processes. The heating affects both the DM and baryon distribution, yielding a decrease of DM in the center of the cluster. The possible presence of an IMBH of mass  $< 10^3 M_\odot$  was also considered, even if not used for the analysis. In Tab. 6.2 their initial NFW J-factor, the one with the AC boosting and the final NFW, in which DM has been swept out by ki-

**Table 6.1:** M15  $J$ -factor values used by the Whipple collaboration for the indirect detection of self-annihilating DM [200]. Both their minimum and maximum values of the  $J$ -factor are reported for the NFW and AC NFW models.

Whipple $J$ -factors		
Model	$J$ -factor <sub>min</sub> [GeV <sup>2</sup> cm <sup>-5</sup> ]	$J$ -factor <sub>max</sub> [GeV <sup>2</sup> cm <sup>-5</sup> ]
NFW	$2.7 \times 10^{18}$	$5.8 \times 10^{19}$
AC NFW	$3.1 \times 10^{21}$	$7.7 \times 10^{21}$

netic heating, are presented. The IMBH NFW  $J$ -factor, even if not estimated in their work, has been left in the table to highlight a possible contribution of it. All the  $J$ -factors in the table have been calculated by multiplying the exponential of the values presented in [203] with the factor  $10^{24}$  GeV<sup>2</sup>cm<sup>-5</sup>.

**Table 6.2:** M15  $J$ -factor values used by the H.E.S.S. collaboration for the indirect detection of self-annihilating DM [203]. The values reported for each model are averaged over the solid angle of integration. The  $J$ -factor estimate for the IMBH model is missing, because it was not considered in the H.E.S.S. analysis. The other  $J$ -factors are estimated, in order, for a generic NFW profile (Initial NFW), for a NFW profile affected by AC (AC NFW) and for a AC NFW profile affected also by the kinetic heating by baryons (Final NFW). The latter has been used by the H.E.S.S. collaboration to calculate the upper limits on the  $\langle\sigma_{ann}v\rangle$  for WIMP DM annihilation.

H.E.S.S. $J$ -factors	
Model	$J$ -factor [GeV <sup>2</sup> cm <sup>-5</sup> ]
Initial NFW	$1.5 \times 10^{24}$
AC NFW	$4.3 \times 10^{27}$
IMBH NFW	/
Final NFW	$1.4 \times 10^{25}$

No signal was found in either of the two analyses carried out, and only upper limits (UL) on WIMP  $\langle\sigma_{ann}v\rangle$  were set. In Tab. 6.3, the 95% confidence level (CL) limits obtained by the Whipple and the H.E.S.S. collaborations in the  $b\bar{b}$  and  $\tau^+\tau^-$  channels are reported. In the case of Whipple, the  $J$ -factor presented does not fit into the AC NFW interval, as visible in Tab. 6.1, but fits into the NFW  $J$ -factor interval<sup>2</sup>. In the Whipple paper, the reason for the use of this particular  $J$ -factor value is not specified.

In the second and third line of Tab. 6.3, the results, obtained by H.E.S.S., for the initial NFW model (for which the  $J$ -factor has been estimated only considering the initial  $m_{vir} = 10^7 M_\odot$  and  $c = 50$  [200]), and the final NFW model (that takes into account also the AC and the kinetic heating by stars) are presented. The UL on  $\langle\sigma_{ann}v\rangle$ , taken from [203] has been associated to the  $b\bar{b}$  channel, as the annihilation channel considered is not specified in the paper, and the results are compatible with other limits on that annihilation channel. Given these limits, but also the available observations of stellar kinematics, there is currently no hint of a hypothesized primordial DM halo surrounding

<sup>2</sup>Contrary to expectations, it is not the average value of the interval.

**Table 6.3:** 95% CL ULs on the  $\langle\sigma_{ann}v\rangle$  of WIMP DM candidate of  $m_\chi = 1$  TeV in the case of Whipple [200] and of  $m_\chi = 2$  TeV in the case of H.E.S.S. [203], associated to the  $J$ -factors used for the estimation of the limits. The average  $J$ -factor values of H.E.S.S., presented in Tab. 6.2, have been multiplied for the solid angle  $5 \times 10^{-6}$  sr in order to get the cumulative  $J$ -factors presented in this table.

95%CL UL on WIMP $\langle\sigma_{ann}v\rangle$			
Experiment - Model	$J$ -factor [GeV <sup>2</sup> cm <sup>-5</sup> ]	$\langle\sigma_{ann}v\rangle_{b\bar{b}}^{\text{UL}}$ [cm <sup>3</sup> s <sup>-1</sup> ]	$\langle\sigma_{ann}v\rangle_{\tau^+\tau^-}^{\text{UL}}$ [cm <sup>3</sup> s <sup>-1</sup> ]
Whipple - AC NFW	$1.2 \times 10^{19}$	$5.1 \times 10^{-21}$	$3.3 \times 10^{-22}$
H.E.S.S. - Initial NFW	$2.1 \times 10^{22}$	$\sim 5 \times 10^{-23}$	/
H.E.S.S. - Final NFW	$7.0 \times 10^{19}$	$\sim 5 \times 10^{-24}$	/

M15. Moreover, from a theoretical and phenomenological point of view, a good description of the astrophysical processes that influenced the evolution of the GC is still missing, and this comes together with a lack of knowledge of its possible DM density. A further difficulty consists of the very poor kinematic measurements of stars in the cluster core, that are still not possible with the present telescopes, because of the high stellar density. From this point of view, M15 could still be a perfect primordial GC candidate and have born in a DM halo. Then, mass segregation and consequent AC of DM may have occurred, possibly enhancing the DM signal. In a second step, the kinetic heating of DM particles produced by stars could have washed out the adiabatic effect, thus reducing the DM density in the core [186]. Possible tidal stripping could then have occurred, diminishing the DM in the outer part of the halo, but still, even if the M/L ratio is small, there is a possibility of containing a DM component, that might be boosted by the presence of a possible IMBH.

These were the factors that brought Whipple and H.E.S.S. collaborations to study the GC M15 in terms of WIMP DM. In addition to that, the MAGIC collaboration carried out a long-term KSP observation of M15 searching for combined gamma-ray emission from the pulsars in its center. No signal has been found, though [165], but the availability of a such sizeable sample of data led also the MAGIC collaboration to perform an indirect DM search on this target. In the following, the data sample used and the different steps of the analysis performed in this work will be described. The results obtained from the Whipple and H.E.S.S. analyses have been validated with MAGIC data, applying the same  $J$ -factors. Upper bounds on  $J$ -factor values have also been estimated following the more recent simulations of [198] and the outcome of the N-body simulations of [183]. The results obtained using these new  $J$ -factors will also be presented.

### 6.3 Data sample and quality cuts

The GC M15 was observed in 2015 and 2016 as target of a MAGIC KSP on the joint emission of millisecond pulsars (MSPs) [165]. The datataking started at the end of June 2015 and finished at the end of September of the same year (corresponding time interval in the MAGIC analysis period ST.03.06) and then started again at the beginning of September 2016 until the end of the month

(in the MAGIC analysis period ST.03.07). A total amount of 173 h of data were collected with the two MAGIC telescopes, in stereo mode and in dark time. To optimize the signal to background ratio [204] and given the absence of peculiar sky features (e.g. gamma-ray emitting sources or bright stars in the vicinity of the target), four MAGIC standard wobble pointings were employed. The pointing positions are shown schematically in Fig. 6.4.

The zenith angles of the observations range from  $\sim 16^\circ$  to  $\sim 35^\circ$ , within the

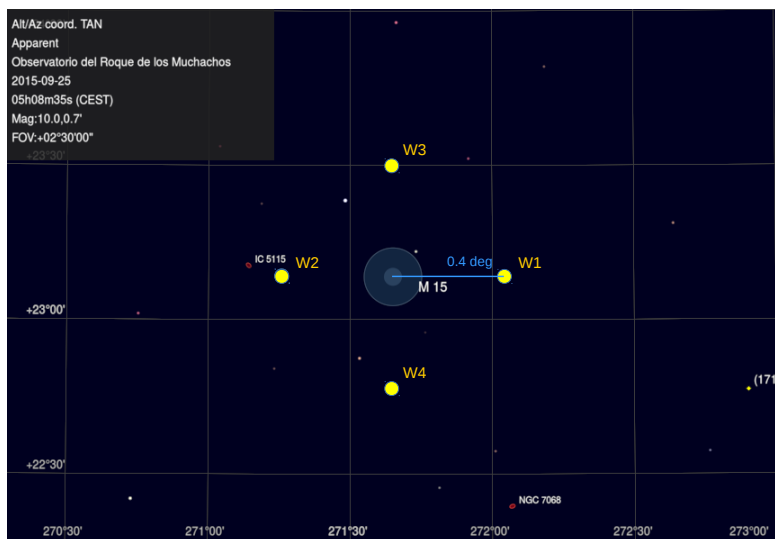


**Figure 6.4:** Schematic view of the four MAGIC wobble pointings for the case of M15 observation during the data-taking night of 2015-09-25 at 5 a.m. The image was produced using the SkyChart software [205] and setting a threshold of 10 for the apparent magnitude of the sky objects.

zenith interval where the telescopes are optimized to reach the lowest energy threshold.

The reconstructed data have been taken directly, in this case, from the analysis carried out in [165]. Up to the energy reconstruction step, the only difference between a DM optimized analysis and a standard MAGIC analysis consists in the data quality cuts used. In our case, we decided to apply quality cuts directly on reconstructed data, setting a lower threshold of 0.8 for the aerosol transmission from 9 km a.s.l. to ground and cutting on Hillas parameters. Only in the case of the data sample taken in the analysis period ST.03.07, additional quality cuts on the Hillas parameters *Width*, *Length*, and the *Number-of-Islands* were used. The quite constant presence of calima without intermediate rains, which normally wash the dust from the mirrors, during the datataking period ST.03.06, and the consequently degraded mirror reflectivity, affected the entire sample of data, but no ad hoc MC simulations had been produced for this case. For this reason, in order to not eliminate a big quantity of good quality data, the cut on the three Hillas parameters above mentioned was avoided. A cut on the maximum median pixel DC current of  $1500\mu\text{A}$  was also applied, as there was an outlier in the camera-wise DC currents, probably due to a car flash or

to scattering of light because of the presence of clouds. On the other side, the data with LIDAR issues in the period ST.03.07 were discarded.

As an example of how the cutting procedure works, the cuts on aerosol transmission for the two periods of datataking are shown in Figs. 6.5 and 6.6.

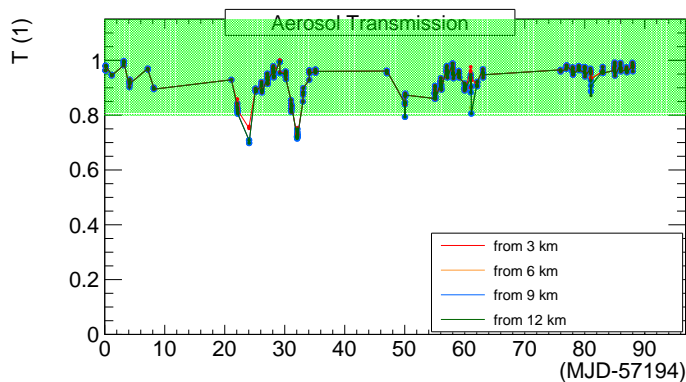


**Figure 6.5:** The aerosol transmission as a function of time at different altitudes for the data-taking cycle ST.03.06. In semi-transparent green the area that marks the data kept for the analysis is shown.

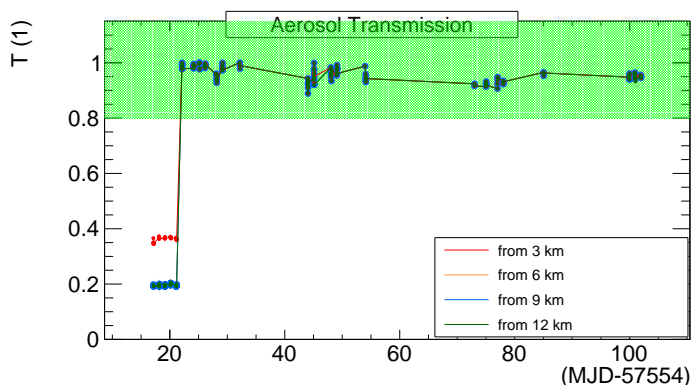


**Figure 6.6:** The aerosol transmission as a function of time at different altitudes for the data-taking cycle ST.03.07. In semi-transparent green the area that marks the data kept for the analysis is shown.

After the application of the cuts and the removal of data discarded because of the LIDAR problems, the effective exposure time got reduced by  $\sim 21\%$ , resulting in a total effective time of  $t_{\text{eff}} = 136.45\text{h}$  of data. From these remaining event files, the true energy of the events and the instrument response functions (IRFs) were estimated.

A different approach with respect to a usual DM analysis was also used for the background estimation, avoiding the OffFromWobblePartner method (background taken from an area of the opposite wobble pointing and in a position

symmetric to the signal area respect to the center of the camera) to preferring the simultaneous background method (background taken in the "non-signal" area of the camera during the same wobble position). The systematic uncertainties introduced by the two methods have been compared in order to find the most suitable one, as in our case the systematic uncertainty prevails over the statistic one due to the big amount of data available. In the case of the simultaneous background method, the uncertainty on the acceptance of the camera, because of its inhomogeneity, is considered lower than the uncertainty given by the rapid atmospheric changes in the case of the OffFromWobblePartner method. This is visible, in particular, in the case of the ST0306 period. As shown in Fig. 6.5, the atmospheric changes can be of the order of  $\sim 10\%$  on short timescales, surely higher than small camera inhomogeneities. For uniformity, the same method has been applied also to the data of the period ST0307. No signal was found in this analysis, and 95% CL upper limits were set on the gamma-ray flux for different energies. In Fig 6.7 the excesses with respect to the background for different squared angular distances from the nominal position of the target are shown. The significance of these excesses was calculated using equation 17 of the Li&Ma method [158] and is presented in the figure. In Fig. 6.8 the significance skymap is shown. Given the absence of detected

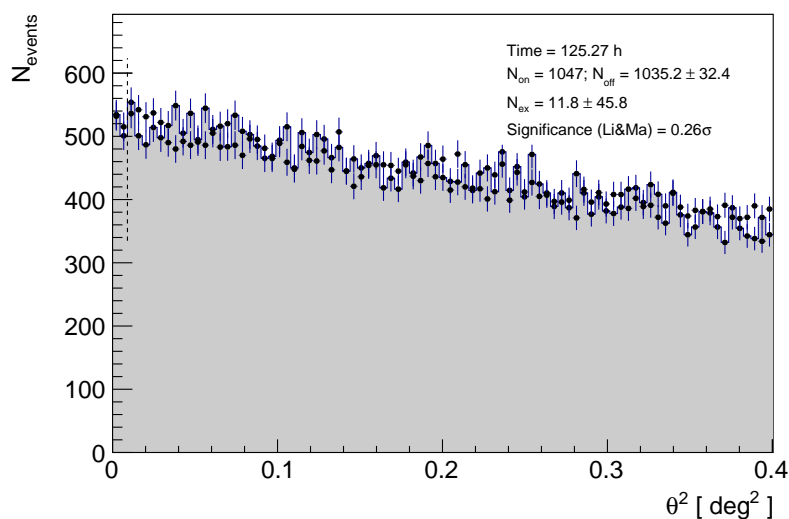


**Figure 6.7:**  $\theta^2$  plot representing the excess events with respect to the background in the signal region, delimited by a dashed vertical line. The significance obtained is reported in the upper right corner of the figure.

excess events, the ULs at 95% CL were calculated on the photon flux measured. In order to do so, the method of Rolke et al. [159], implemented in the MAGIC analysis chain, has been used. The resulting ULs, the migration matrix, and the IRFs have then been kept as input for the estimation of the ULs on the  $\langle \sigma_{ann} v \rangle$  of WIMP DM particles, performed with the gLike tool [161]. The full likelihood method compares the observed number of ON and OFF events, as a function of energy, obtained from the data, with the expected spectrum of the target, reconstructed from the DM profile of the source and

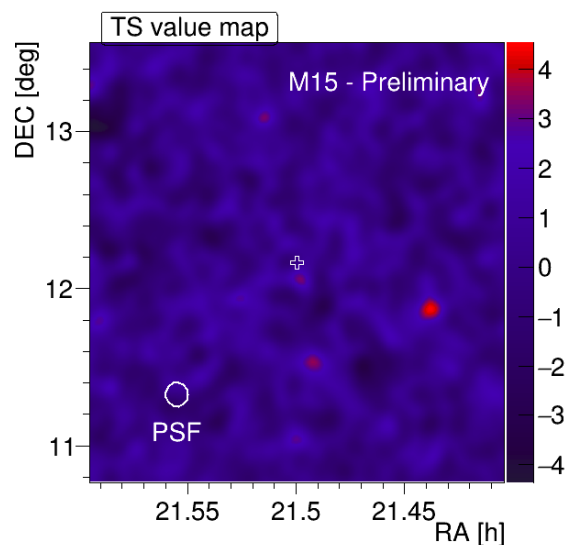


**Figure 6.8:** Smoothed significance skymap of M15 FoV for an extension of  $2.4^\circ$ . The white cross indicates the center of M15, the white solid circle the extension of MAGIC telescopes point spread function (PDF).

the annihilation model of Cirelli [162]. This latter is well established in the literature, but the  $J$ -factor has still to be well estimated, given the absence of kinematic measurements at the core of M15. In the next section, the evaluation of the DM profile and the consequently obtained  $J$ -factors used for the analysis are reported.

## 6.4 Dark matter profile evaluation

The detection of a DM target through indirect searches with IACTs is based on the measurements of gamma-ray fluxes coming from the source of interest. Those fluxes of photons are supposed to originate from the annihilation or decay of WIMPs, and can be expressed as the product of a particle physics factor (in our case taken from the model of [162]) and a  $J$ -factor, as described in Section 3.3.1. While the particle physics models are well established in the literature and do not depend on the target, the  $J$ -factor varies from target to target, as it is directly connected to the assumed DM profile of the source and its distance to Earth. Hence, we are interested in modelling the DM density and distribution in M15, in particular because of the poor kinematic measurements available in literature, especially concerning the core of the cluster.

The first approach I followed for my analysis was to consider the  $J$ -factors estimated in the Whipple and H.E.S.S. papers [200,203] and use them to convert my limits on the gamma-ray fluxes to those on  $\langle\sigma_{ann}v\rangle$ . Being aware of the large systematic uncertainties in the calculation of the M15  $J$ -factors at the time, due to a not precise description of the dynamical evolution of the cluster, it has been decided to undertake a different way for estimating the DM profile.

As one of the main experts in GCs, I contacted Dr. J. Read<sup>3</sup> with which help I defined different strategies to follow, in order to obtain reliable estimates based on current knowledge. A first attempt to find a  $J$ -factor for M15, and the only one we used for the current analysis, has been retrieving the DM profile from the work of den Brok et al. [198]. In this paper, one of the most recent on the topic, the dynamics of M15 has been studied in a more rigorous way thanks to the analyses of line-of-sight (l.o.s.) velocities and proper motion data of stars using a new method of fitting. Dynamical models have been fit to discrete kinematic data by maximizing the likelihood for individual stars, instead of working on spatially binned data or measuring velocity moments. In this way, the results are less affected from the loss of spatial and velocity information. Even if the presence of an IMBH cannot be excluded yet, because of the impossibility of getting kinematic measurements at few Schwarzschild radii from the very center of the cluster, the M/L ratio profile and the total mass-density profile as a function of the radial distance could be retrieved. In Fig. 6.9, the two resulting plots presented in [198] have been reproduced. In the case of the M/L ratio, both the projected<sup>4</sup> and deprojected profiles are shown. For

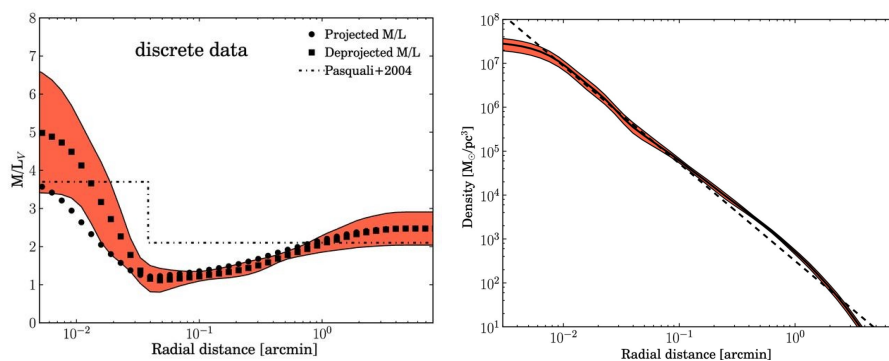


**Figure 6.9:** *Left:* Mass-to-light profile (deprojected-squares and projected-circles) of M15 from the fitting of discrete velocity data as a function of the radial distance from the center. The  $1\sigma$  band for the deprojected profile (in red) and the earlier measurements of [207] (dashed line) are also presented. *Right:* M15 inferred mass-density profile, with  $1 - \sigma$  error band (red region), as a function of the radius. The expected power-law mass-density profile for dark remnants from [197] is also presented. Both plots have been adopted from [198].

my analysis I decided to derive a most optimistic best case scenario, in which all the contributions to a M/L value higher than 1 are considered to be due to DM, discarding any contribution of other massive objects like BH, white dwarfs, etc. To do so, I convoluted the excess M/L above 1 of the deprojected M/L profile on the left of Fig. 6.9 with the solid curve of the density profile plot on the right, in order to get the DM density profile as a function of the radial distance from the center of the cluster. In Fig. 6.10 the DM density profile, in light blue, is compared to the total density profile. Fig. 6.11 shows that profile together with the density profiles modelled by the Whipple and the H.E.S.S.

<sup>3</sup>Researcher and Head of Physics at the University of Surrey, and author of multiple papers on DM and its gravitational probes, in particular of [206]

<sup>4</sup>M/L profile integrated along the l.o.s.

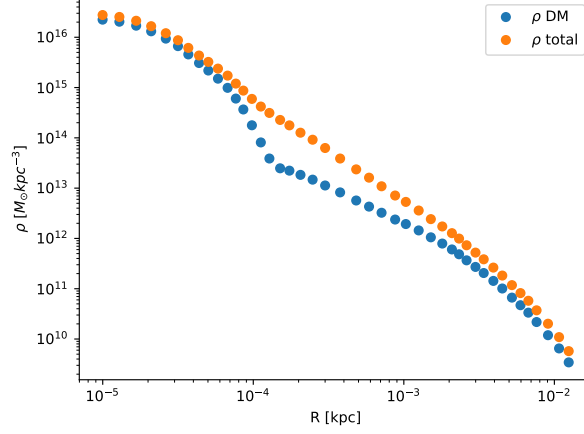


**Figure 6.10:** DM density profile (light-blue circles) in comparison to the total density profile (orange circles) as a function of the radial distance from the cluster center.

collaborations. The density profiles, from which the final  $J$ -factors have been derived, are presented in light-blue for this work, in violet for Whipple work and in green the H.E.S.S. one. Even if not used for the  $J$ -factors considered in this section, the AC NFW profiles of Whipple (in red) and H.E.S.S. (in orange) are reported. It can be noticed that these two latter differ by a very small factor, thus showing a compatibility between the two dynamical modellings. In both cases, the kinetic heating of DM by stars was taken into account at the moment of the final density calculation, adding its contribution to the AC profile. The convoluted density, being the most optimistic case for a DM content in M15, is higher than the AC NFW ones by at least one order of magnitude, as expected.

The  $J$ -factor value for the convoluted density has, then, been calculated integrating the square DM density over the solid angle and over the l.o.s., following the formula 6.1, with a procedure similar to [208].

$$J = \int_0^{2\pi} d\phi \int_0^{\theta_{max}} \sin(\theta) \int_{s_1}^{s_2} \rho^2(s, \theta) ds d\theta \quad (6.1)$$

where  $\rho$  is the DM density,  $\phi$  and  $\theta$  delineate the solid angle  $\Delta\Omega$ ,  $\theta$  is the angle defining the direction of observation and  $s$  is the variable of the l.o.s., as shown in Fig. 6.12.

Specifying  $y = 1 - \cos(\theta)$ , and  $y_{min} = 1 - \cos(\theta_{max})$ , and hence  $dy = -d(\cos\theta)$ , Eq. 6.1 can be re-written as:

$$J = 4\pi \int_0^{y_{min}} \int_0^{s_2} \rho^2(s, y) ds dy . \quad (6.2)$$

After the change of coordinates, from  $s$  to  $r$ , the Jacobian results to be  $\frac{ds}{dr} = \frac{r}{\sqrt{r^2 - D^2(2y - y^2)}}$ , where  $r$  is the radial distance of observation and  $D$

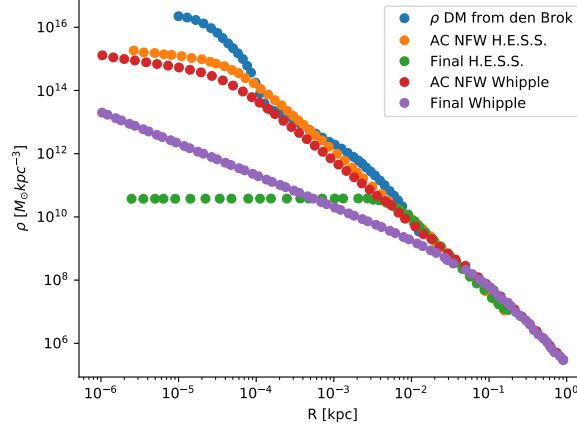


**Figure 6.11:** DM density profiles retrieved from Whipple (in red and violet), H.E.S.S. (in orange and green) and this work (in light-blue).

the distance to the target. Then, the final integration equation is:

$$J = 4\pi \int_0^{y_{min}} \int_D^R \frac{\rho^2(r) \cdot r}{\sqrt{r^2 - D^2(2y - y^2)}} dr dy \quad (6.3)$$

where  $R$  is the radius related to the maximum angle  $\theta_{max}$  considered in the work of [198].

The value of the  $J$ -factor obtained integrating Eq. 6.3 is:

$$J = 1.19 \times 10^{24} \text{ GeV}^2 \text{ cm}^{-5} .$$

The cumulative  $J$ -factor as function of the radial distance is presented in Fig. 6.14.

Given the improbable high value obtained, I decided to evaluate the  $J$ -factor with another M/L profile. The one presented in [183], based on the average of 900 N-body simulations of 50 GCs of our Galaxy, and rescaled for the M15 parameters reported in the paper (see Fig. 6.13), has been convoluted with the density profile of [198] to obtain a second DM density profile estimate and hence a new  $J$ -factor. A  $J$ -factor of just a factor 2 smaller than the previous one was obtained, as visible in Fig. 6.14, thus it was not further considered for the upper limits evaluation. In the following section,

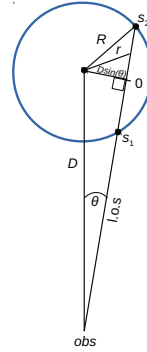


**Figure 6.12:** Geometry of the integral used to calculate the  $J$ -factor.  $D$  is the distance of the target from the observer *obs*,  $\theta$  the direction angle of observation,  $R$  the maximum radius of integration,  $r$  the variable radius of integration and  $s$  the l.o.s. at the lower ( $s_1$ ) and higher ( $s_2$ ) extremes of integration.

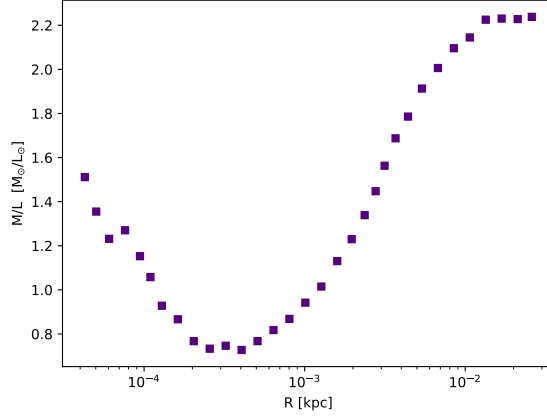


**Figure 6.13:** M15 M/L profile obtained by rescaling the averaged M/L profile of [183].

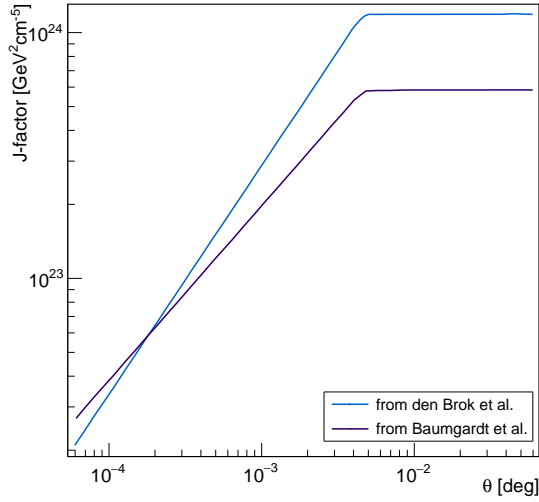


**Figure 6.14:** Cumulative  $J$ -factors with respect to the angular distance from the cluster center in the case of the estimation from [198] (in light-blue) and from [183] (in dark-blue).

the ULs obtained on the velocity-averaged cross-section using the different  $J$ -factors will be presented.

## 6.5 Results and discussion

A statistical UL at the 95% CL on the  $\langle \sigma_{ann} v \rangle$  of the annihilation of WIMP DM was obtained for three different  $J$ -factors, putting aside the uncertainties of  $J$ -factors themselves: the one used by the Whipple collaboration for their

ULs, the Final one used by the H.E.S.S. collaboration and the one I estimated in the previous section.

In Fig. 6.15, the limits in the  $b\bar{b}$  and  $\tau^+\tau^-$  annihilation channels, calculated using Whipple's  $J$ -factor  $\log(J_{\text{Whipple}}) = 19.1 \text{ GeV}^2\text{cm}^{-5}$ , are shown. The

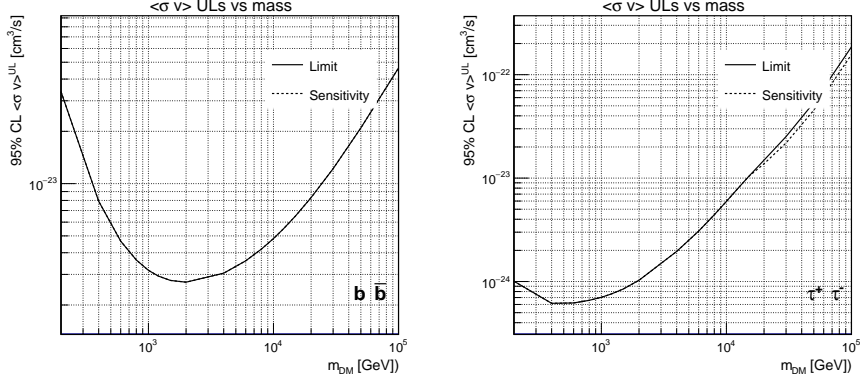


**Figure 6.15:** 95% CL ULs on  $\langle\sigma_{ann}v\rangle$  for the annihilation of WIMP DM in the  $b\bar{b}$  (left) and  $\tau^+\tau^-$  channels (right) using MAGIC M15 data and Whipple's  $J$ -factor.

95% CL ULs for the same annihilation channels using H.E.S.S. final  $J$ -factor  $\log(J_{\text{H.E.S.S.}}) = 22.3 \text{ GeV}^2\text{cm}^{-5}$  are presented in Fig. 6.16. Using the more

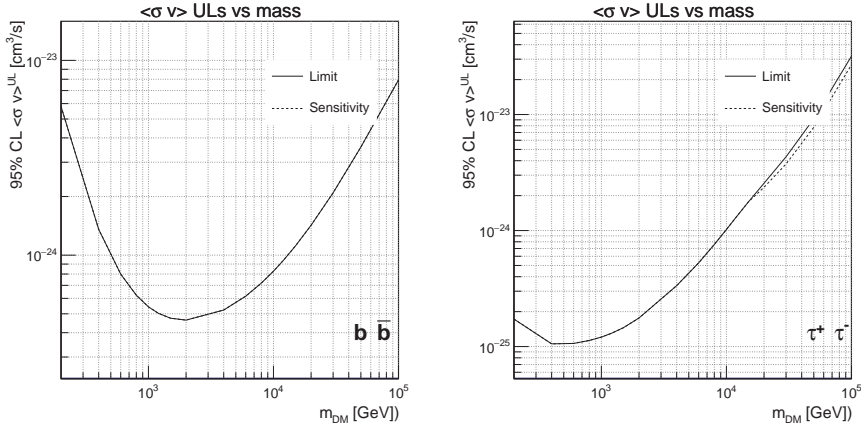


**Figure 6.16:** 95% CL ULs on  $\langle\sigma_{ann}v\rangle$  for the annihilation of WIMP DM in the  $b\bar{b}$  (left) and  $\tau^+\tau^-$  channels (right) using MAGIC M15 data and H.E.S.S.'s  $J$ -factor.

recent modelling of the dynamical evolution of [198], from which the  $J$ -factor  $\log(J_{\text{this work}}) = 24.1 \text{ GeV}^2\text{cm}^{-5}$  of this work was estimated, the ULs of Fig. 6.17 have been obtained. In Tab. 6.4, the ULs obtained for the  $\langle\sigma_{ann}v\rangle$  of WIMP annihilation are presented.

The limits obtained using Whipple's and H.E.S.S.'s  $J$ -factors are compatible with the ones calculated by the respective collaborations, once rescaled for the effective observation time of the MAGIC data sample, and among themselves. On the other hand, a difference of  $\sim 4$  orders of magnitude can be noticed between the results in the second and third row of the table, and of a difference

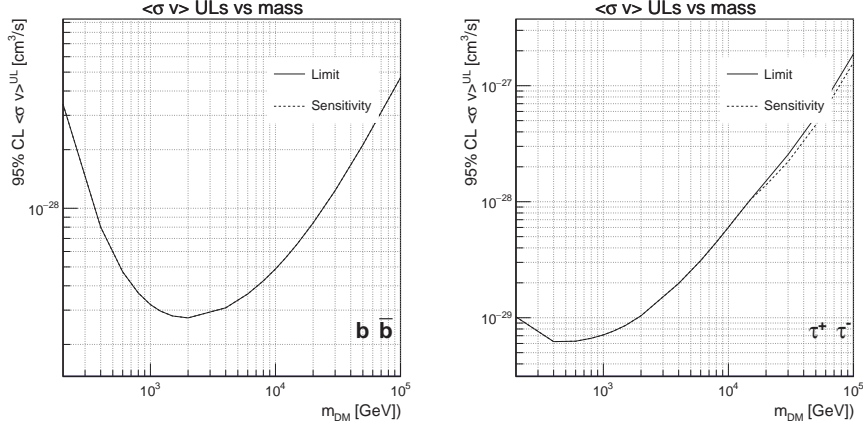


**Figure 6.17:** Toy ULs on  $\langle\sigma_{ann}v\rangle$  for the annihilation of WIMP DM in the  $b\bar{b}$  (left) and  $\tau^+\tau^-$  channels (right) using MAGIC M15 data and the optimistic  $J$ -factor calculated in this work.

**Table 6.4:** 95% CL ULs on the  $\langle\sigma_{ann}v\rangle$  of WIMP DM candidate obtained by using Whipple and H.E.S.S.  $J$ -factors in association to a MAGIC data sample and toy ULs estimated using the  $J$ -factor evaluated in this work, with the respective DM masses for the most constraining limit.

ULs on WIMP $\langle\sigma_{ann}v\rangle$				
Experiment - Model	$\langle\sigma_{ann}v\rangle_{b\bar{b}}^{UL}$ [cm $^3$ s $^{-1}$ ]	$m_{DM}^{b\bar{b}}$ [TeV]	$\langle\sigma_{ann}v\rangle_{\tau^+\tau^-}^{UL}$ [cm $^3$ s $^{-1}$ ]	$m_{DM}^{\tau^+\tau^-}$ [GeV]
Whipple - Final	$2.71 \times 10^{-24}$	2	$6.16 \times 10^{-25}$	0.4
H.E.S.S. - Final	$4.64 \times 10^{-25}$	2	$1.06 \times 10^{-25}$	0.4
this work	$2.74 \times 10^{-29}$	2	$6.23 \times 10^{-30}$	0.4

of  $\sim 5$  orders between the third and the first. This is a wide gap at first sight, but the choice to consider, in my analysis, M15 as DM dominated in its core may well explain this difference.

Both Whipple and H.E.S.S.  $J$ -factors have been calculated following different, but at the same time similar, models of the dynamic evolution of the cluster, thus starting from a parametrized NFW DM profile, increasing the central density thanks to the AC and then ending up with a quite cored central density because of the kinematic heating of DM by stars. The ULs on the  $\langle\sigma_{ann}v\rangle$  of WIMPs were thus obtained following theoretical modelling of M15 and result in numbers of the same order of magnitude as the limits obtained with the combination of the single ULs calculated from the dSphs observed by MAGIC (see the results of Chapter 9), as visible in Fig. 6.18 for the case of the  $b\bar{b}$  annihilation channel. The thermal relic cross-section is also plotted in the figure, as a reference. It is evident that the presence of a DM halo around M15 cannot be discarded by the limits obtained using Whipple and H.E.S.S.  $J$ -factors, but in any case has been confirmed the absence of a gamma-ray signal. As a consequence, the target can be still considered as DM dominated and this is exactly what have been done in my analysis, this time starting from a cluster

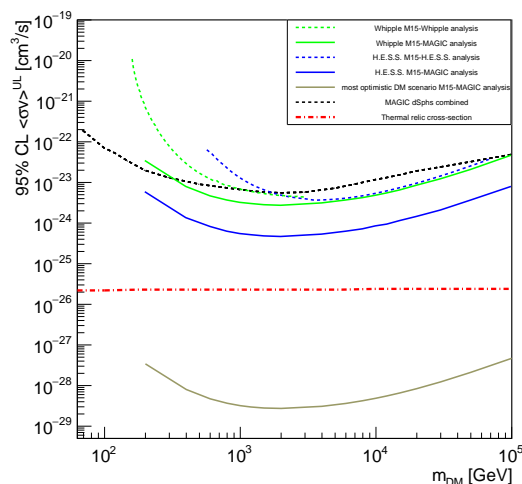


**Figure 6.18:** ULs on  $\langle\sigma_{ann}v\rangle$  of WIMPs annihilation in the  $b\bar{b}$  channel for M15 compared to the limits obtained by the combination of the single ULs, in the  $b\bar{b}$  channel, of the dSphs observed by the MAGIC collaboration (dotted black line). The ULs obtained considering the most optimistic DM scenario for M15 are showed as a solid grey line. The 95% CL limits obtained using Whipple and H.E.S.S. estimated  $J$ -factors are showed in green and blue, as a dotted line for the analyses done by the respective collaborations (extracted from [200] and [203]) and as a solid line for the analyses performed in this work. The thermal relic cross section is presented as a red dashed line.

description based more on the phenomenology of the cluster than on theoretical modelling. In particular, the dynamical models considered were fit to discrete kinematic data by maximizing the likelihood for individual stars, thus obtaining more information on the dynamics of the single star and a bit more insights about the cluster core. Considering most of the matter content as DM, a very unrealistic assumption and disfavoured in the literature, leads to ULs below the thermal relic cross-section threshold and excluding completely the presence of DM formed by WIMPs in that interval of energies.

The ample margin between the first couple of ULs and the latter reflects clearly the unquantifiable systematic uncertainties introduced when modelling the M15 DM density profile. As mentioned in the lines above, the primary reason for these uncertainties is the absence of detailed information on the dynamics of the cluster, in particular at its core, where the high density of material impedes proper stellar kinematic measurements with current instruments. The lack of sufficient angular resolution of the current telescopes does not permit to define a precise M/L profile at the center of the cluster and the only way to obtain more information on it consists of an extrapolation from simulations, as, e.g., in the case of [198] and [183].

The future generation of extremely large telescopes (ELTs), such as the Extremely Large Telescope<sup>5</sup> (ELT) [209, 210] or the Thirty Meter Telescope<sup>6</sup>

<sup>5</sup><https://www.eso.org/sci/facilities/eelt/>

<sup>6</sup><https://www.tmt.org/>

(TMT) [211] match perfectly the requirements for the high resolution measurements needed for the studies. The ELT, under construction at Cerro Armazones (Chile) since 2017, will see first light in 2025. With its 39.3 m diameter of primary mirror and a collection area of 978 m<sup>2</sup>, it will observe the Universe taking images 15 times sharper than the Hubble Space Telescope (HST)<sup>7</sup> and with an angular resolution of only 0.005 arcsec, under ideal conditions. The TMT, with a smaller primary mirror diameter of 30 m, will present a better sensitivity with respect to the ELT at smaller wavelengths [212] and will take images of the Universe 12 times sharper than the HST. Its location site is still under debate, between Maunakea, in Hawaii, and the Roque de los Muchachos Observatory, at La Palma (Spain). It will see first light in 2027. Both telescopes will make use of adaptive optics systems and will allow detailed studies of multiple subjects, such as planets around other stars, the first objects in the Universe, supermassive black holes, and the nature and distribution of the dark matter and dark energy which dominate the Universe<sup>8</sup>. Thanks to their superb angular resolution, the DM content of M15 will finally get properly assessed.

## 6.6 Conclusions and outlook

GCs are spherical agglomerations of stars presenting very high densities at their centres. Given this fact and their old ages, they are supposed to have born in a DM halo, but, at the present time, instruments and dynamical models to properly evaluate the precise DM profile of these sources are still missing. Because of its very old age and its vicinity to the Earth, M15 is one of the GCs observed with the MAGIC telescopes for a large amount of hours, and has been studied in the past by the Whipple and H.E.S.S. collaborations. In MAGIC, it was observed with the goal of searching a gamma-ray signal from a population of MSPs, but the same data sample can also be used for the indirect DM detection study presented in this work. Given the absence of any gamma-ray signal from the target, ULs on  $\langle\sigma_{ann}v\rangle$  of WIMP DM were estimated using four different realizations of the M15 DM density profile. As a first approach, the  $J$ -factors presented in Whipple's and H.E.S.S.'s publications have been used in the maximum likelihood estimation to get 95% CL ULs for the  $b\bar{b}$  and  $\tau^+\tau^-$  annihilation channels. The limits obtained, once rescaled for the effective observation time of MAGIC data sample, are compatible with the results presented by the two collaborations. The weakness of these results, affected by large systematic uncertainties introduced by the lack of information on the M/L profile at the core of the cluster, have led to face the DM density profile estimation in a different way. The M/L and total density profiles presented in the work of den Brok et al. [198] have been convoluted to obtain a DM-only density profile, taking into account the most optimistic scenario of a DM dominated source. This approach is the one that can set a most robust UL for a  $J$ -factor for M15. Taking this  $J$ -factor for real, the most constraining values  $2.7 \times 10^{-29} \text{ cm}^3\text{s}^{-1}$  and  $6.2 \times 10^{-30} \text{ cm}^3\text{s}^{-1}$  have been obtained for the  $b\bar{b}$ , at a DM mass of 2 TeV, and  $\tau^+\tau^-$ , at a DM mass of 0.4 TeV, annihilation channels, respectively. Another way of looking at the problem of the rather un-constrained  $J$ -factor consists of using the baryonic M/L profile of Baum-

<sup>7</sup><https://hubblesite.org/>

<sup>8</sup><https://www.eso.org/public/italy/teles-instr/elt/>

gardt [183], rescaled to the M15 parameters. The convolution of this profile with the total density profile of den Brok et al. resulted in a DM density profile, and a  $J$ -factor, similar to the one obtained with den Brok's M/L profile. Both approaches have, nevertheless, big uncertainties in the used M/L, and, moreover, the assumed fraction of baryons contributing to it.

The big uncertainty in the estimation of the DM profile is, then, still present at current times, given the absence of high angular resolution telescopes that can provide more precise measurements of stellar kinematics in the core of the clusters. The development of the new extremely large telescopes ELT and TMT will help in defining accurately the M/L profiles of these objects and will certainly boost DM indirect detection searches in this field.

The toy UL achieved in this work can be, then, a rapid starting point for setting the most constraining limits on WIMP DM annihilation from the M15 GC, once the DM profile of the source is well established. The likelihood method used and the big data sample will ensure the best achievable limits, once the uncertainty on the  $J$ -factor will be reduced. Then, the limits of Fig. 6.17 can be readily re-scaled with a more accurate  $J$ -factor.

At the moment, in the absence of new high resolution telescopes, other approaches can be followed to improve the M15  $J$ -factor estimation and set more accurate ULs on the WIMP velocity-averaged cross section. One way is based on revising the H.E.S.S.  $J$ -factor, that was calculated on a DM profile as the sum of a NFW profile, AC and the kinematic heating by stars. A first change on it consists in using a coreNFW profile [206], that conserves the virial mass after the scattering of DM by stars, in addition to the profile considered by the H.E.S.S. study. A second improvement is the use of the formalism of Young [213, 214], that considers a stellar orbit distribution closer to isotropic with respect to the AC model of [202], in which stars are considered to rotate in circular orbits. A further, and last, advance is to use more than just one DM halo mass.

Together with these changes, or in a separate analysis, too, the use of a virial mass and compression parameter, taken from the expressions presented in [215], in the initial NFW profile would improve the  $J$ -factor estimation.

All these methods, though, will make a lot of sense with the advent of new kinematic measurements by ELT and TMT. Meanwhile, this thesis concentrates on targets with much better determined  $J$ -factors, namely dwarf spheroidal galaxies.

## Chapter 7

# Search for WIMP Dark Matter from the Draco Dwarf Spheroidal Satellite Galaxy

DSphs are one of the best targets for WIMP annihilation studies with IACTs, and in particular for the MAGIC telescopes, given their vicinity and the absence of VHE emitting sources in the foreground. However, the uncertainty introduced when estimating their distances and the difficulty on the evaluation of their DM densities, calculated starting from kinematic measurements of their stars' velocity dispersion profiles, may introduce some bias in the results obtained. For this reason, after the studies of the two most promising dSphs candidates for DM searches, namely Segue 1 [164] and Ursa Major II (UMaII) [157] dSphs, the MAGIC collaboration decided to start a multi-year program on dSphs following an observational diversification strategy (described in more detail in chapter 9), already adopted before, to distribute the target-related systematic uncertainties.

Draco dSph was the first target proposed for this project, being one of the most promising in the northern hemisphere, after Segue 1 and UMaII. Just before starting its data taking, however, Triangulum II (TriII) was observed with the MAGIC telescopes [216], but not in the framework of the multi-year program. The mentioned object was proposed as one of the best dSph targets at the epoch [217], given its high  $J$ -factor value [218], but was discredited in a later time [219], after the analysis of new stars' kinematic measurements. With these last results, TriII was marked as star cluster or, better, tidally stripped dSph. Thus, due to the large uncertainties in the velocity dispersion profile evaluation, TriII has to be treated differently with respect to the other dSphs observed by MAGIC.

In this chapter, after an introduction on the Draco dSph (section 7.1), I will present the data sample acquired and the data check I performed during the data-taking nights (section 7.2). In the same section, I will also describe the analysis I carried out, focusing on the *Donut Monte Carlo method*, used to take into account the extension of the source. In section 7.3, the results of my analysis, cross-checked in [145], and approved by the MAGIC collaboration for the publication, will be presented. The chapter will end with a discussion of those results and a brief conclusion, that will link to the next chapter.

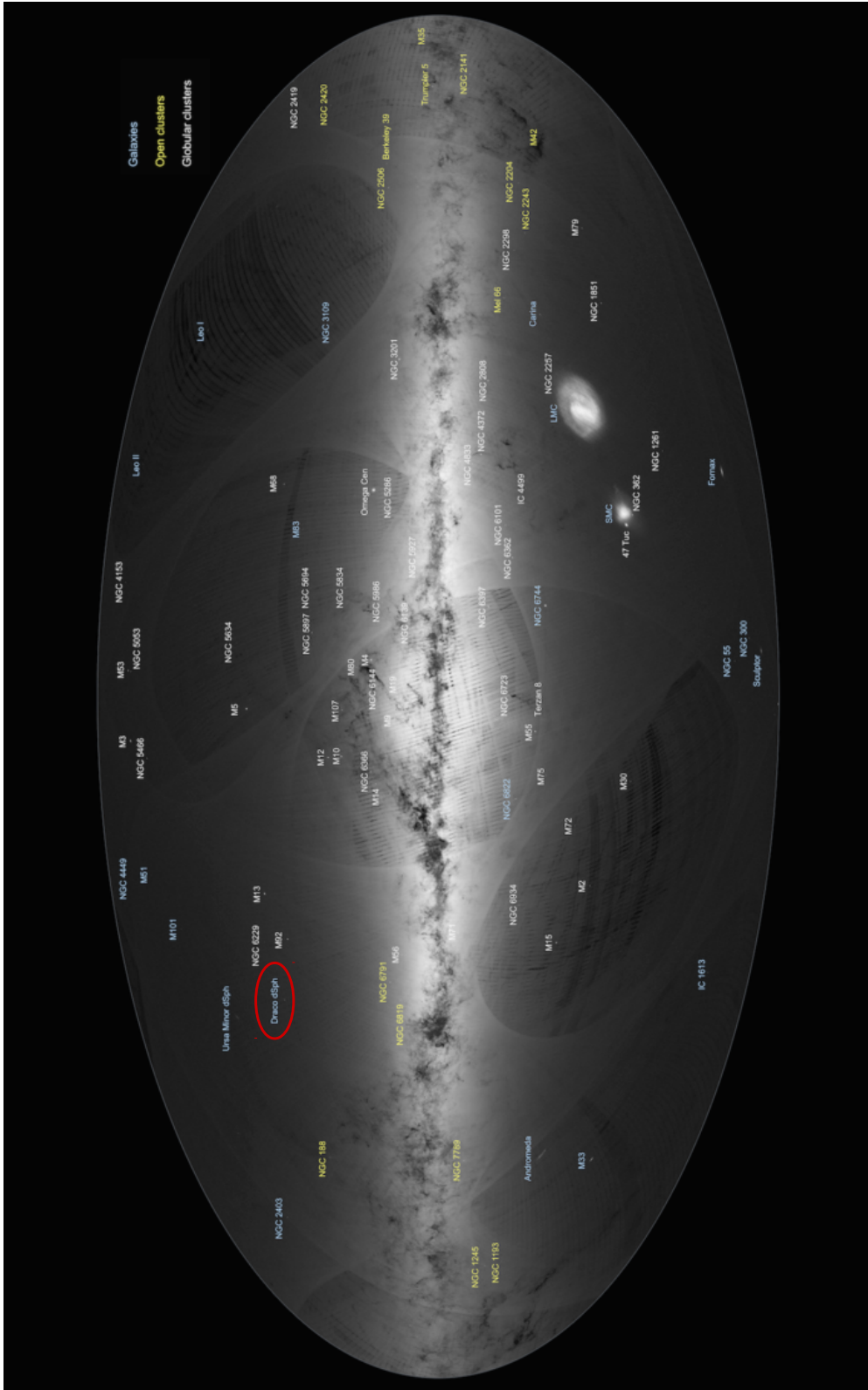


Figure 7.1: Position of Draco dSph in the MW (red circle). Image taken from the ESA website [220].

## 7.1 The Draco dwarf spheroidal satellite galaxy

Dwarf spheroidal satellite galaxies (dSphs) are the least luminous galaxies present in the Universe and the most numerous in the Local Group. They do not present gas or recent star formation, have a low baryonic content and are the most DM dominated sources in the vicinity. The work of Aaronson [221] on Draco was a pioneer one that triggered the interest in searching for DM in dSphs.

Draco was first detected in 1954 by A.G. Wilson in the Palomar Observatory Sky Survey (POSS) [222] and, before the detection of further dSphs in 2006, it was thought to be the most DM dominated object in the sky. It is located at RA = 17h20m12.4s and Dec = 57°54'55", in the J2000 coordinate system [189], in the direction of the Draco constellation, at 34.6° above the Galactic plane (the location of Draco dSph is shown in Fig. 7.1). It is visible at a visual apparent magnitude of 10.9 and it is found at a distance of  $76 \pm 6$  kpc [223]. It is a quite old galaxy and does not present any star formation for the past  $\sim 10$  Gyr [224]. Its stellar mass is  $2.9 \times 10^7 M_\odot$  [223] and it presents a M/L  $\approx 500 M_\odot/L_\odot$  [225].

The long time passed from the last star formed and the M/L ratio show that Draco must be a strong DM dominated object, hosting a DM halo, cusped and unaffected by stellar feedback at the time of the galaxy formation [115]. Starting from a stellar sample of 292 stars, truncating the DM halo at the distance of  $\theta_{max} = 1.3^\circ$  of the outermost member star, A. Geringer-Sameth et al. found the  $J$ -factor value of Draco, for DM annihilation, to be  $\log J(\theta_{max}) = 19.05^{+0.22}_{-0.21} \text{ GeV}^2 \text{ cm}^{-5}$  [119].

Showing this high DM content, and thanks to its vicinity and its low background, the Draco dSph is an optimal target for indirect DM searches with IACTs.

## 7.2 Draco data sample and data reduction

The Draco dSph culminates at La Palma at  $\sim 29^\circ$  and is observable below  $45^\circ$  in zenith from April to August. During the MAGIC observation cycle XIII, in 2018, it was observed for a total amount of 66.5 h in dark time, starting from March and ending in September 2018. Differently from the case of M15, due to luminous stars in the FoV and to the extension of the target, only the two wobbles  $W1$  and  $W3$  were adopted for these observations. Having single-wobble-pair observations (thus with only 2 OFF regions considered) permits to always reach the highest distance of  $0.8^\circ$  between the ON and OFF regions in camera coordinates, thus allowing to take into account an emission region up to  $0.4^\circ$ , summed quadratically with the angular resolution of MAGIC telescopes, without interfering with the OFF region. This is particularly suitable for extended DM profiles, for which the emission region is larger than MAGIC PSF for pointlike objects [122].

A check of the similarity of the azimuthal distributions between the two wobble pointings was performed during the whole datataking period, as visible in Fig. 7.2, in order to limitate the systematic errors coming from the different acceptance of the telescopes' cameras as a function of the distance from their centres.

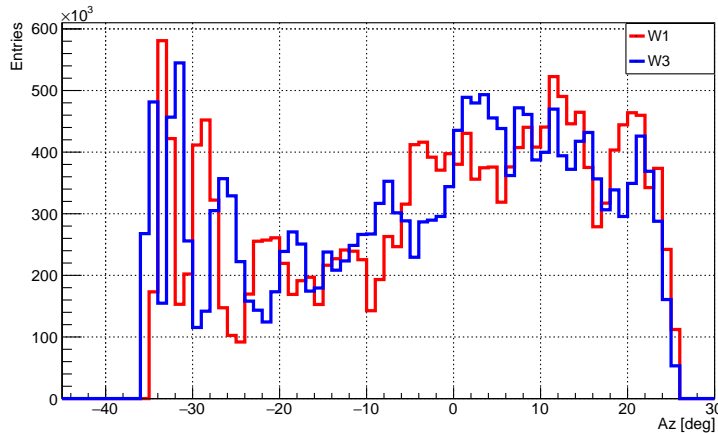


**Figure 7.2:** Distribution of the observations as a function of the azimuth telescope pointing angles for the two wobbles. *W1* observations are presented in red, while *W3* ones in blue.

The sample of data acquired has been divided into two subsamples, from now on S09 and S10, each one related to a different status of the instrumentation and paired to special Monte Carlo (MC) simulations. The sample S09, in the time interval 17/03-20/06 has been acquired during the MAGIC analysis period ST.03.09. This period, ranging from the October 10, 2017 to June 29, 2018, contains data affected by rain that cleaned the dust from the mirrors (thus improving its reflectivity with respect to the previous period) and part of the data affected by a bad point spread function (PSF) of the telescopes (presenting a double-spot). Starting from June 30, in the new MAGIC analysis period ST.03.10 (ranging from that date to October 30), the reflectance of the mirrors decreased gradually, and new MC simulations have been created in order to match better with the status of the instrumentation. During that second period, in the time interval 04/07-02/09, the data sample S10 was acquired.

In each of the two data samples, a few hours of observations were performed using wrong wobble settings, for this reason 3.7 h and 1.1 h were removed from S09 and S10, respectively. With this cut, 33.6 h in S09 and 28.1 h in S10, summing up in 61.7 h in total, were, then, used for the analysis.

The two subsamples have been treated in parallel for the *standard MAGIC data reconstruction* [226], starting from the *quality cuts*. The latter are very strict in the case of DM studies, in particular regarding the atmospheric conditions, that can largely affect the data, especially compared with the tiny signals searched for in DM analyses. For this reason, and due to the fact that with a lower aerosol transmission one should apply LIDAR corrections to estimate the energy of the gamma rays (only in the case of their detection), a minimum aerosol transmission of 85% at 9 km distance from ground [141] has been set as threshold. Cuts on the median photomultipliers (PMTs) DC currents have also been applied, fixing the acceptance for dark and twilight conditions at 0 – 3000  $\mu\text{A}$  (usual values presented by the PMTs in those conditions) [227]. Differently from other DM MAGIC analyses, cuts on the Hillas parameters

(see Sec. 5.1) have been applied. A maximum standard deviation cut of 3.5 standard deviations with respect to the median of the *Number-of-Islands* (NumIsland) in the shower image, sensitive to the night sky background (NSB) and to the atmospheric conditions, has been required, but cuts on *Width* and *Length* have been avoided. For the case of S09, the bad PSF was not visibly affecting the data, thus cuts on *Width*, sensitive to the optical PSF, and *Length*, were not needed. For the other subsample, as proper MC simulations have been created, the acceptance of bad quality data for the *Width* and *Length* parameters would have been recovered at the moment of comparing the data with the MC simulations. Thus, also in this case the cuts in *Width* and *Length* were not needed. The rejected data of both subsamples have been cut out in time slices, instead of per runs, in order not to remove entire subruns containing bad quality data, as to keep as much good quality time of observation as possible. A total sample of 52.6 hours of good quality data, summing the S09 and S10 samples, remained after the cuts. All the details about the quality selection for the two subsamples can be found in Tab. 7.1.

**Table 7.1:** The details of the Draco observation and the data selection parameters are reported in the table. In order, the time intervals, the observation conditions, the wobble pointings and the cuts applied (in percentage) are shown for each subsample. The effective times before and after the cuts (indicated with an arrow) are also presented. The total time of observation after cuts is reported at the end of the table.

<b>Sample S09</b> (2018_03_17 - 2018_06_20)	<b>Sample S10</b> (2018_07_04 - 2018_09_02)
dark time W0.40+000 - 180 deg	dark time W0.40+000 - 180 deg
2% cut in NumIsland 2% cut in transmission @ 9 km	2% cut in NumIsland 27% cut in transmission @ 9 km
33.6 h → 32.0 h	28.1 h → 20.6 h
<b>Tot. obs. time (after cuts): 52.6 h</b>	

For each subsample, an *OFF-sample* (data with no hints of a signal) and a *MC sample* have been chosen to train the *Random Forest* (RF) [228], in order to perform a data selection based on the *hadronness*, a selection parameter for the gamma/hadronic origin of a detected event.

For the subsample S09, data acquired for a dark patch and for the radio source 3C371 (when non-emitting in gamma rays) for a total of 5.7 h, were used as *OFF-sample*. The same quality cuts applied on the S09 data sample were employed for the *OFF-sample*, but no data were cut out. For the subsample S10, OFF-data from the BL Lac 1ES2037+521 observations were used. From an initial total effective time of 6.8 h, 5.7 h were left after applying the cuts.

The MC samples associated to each subsample, as described in the above lines, depend on the extension of the target. Given its  $1.3^\circ$  of radius, if taking into account the outermost member star used to evaluate the velocity dispersion profile for the estimation of the *J-factor* considered subsequently in this work, MC simulations for a diffuse uniform flux of gamma rays up to a radius of  $1.5^\circ$ ,

namely *diffuse MC simulations*, were adopted. The two diffuse MC samples, MC\_S09 and MC\_S10, were then split in halves, one part used to train the RF, and the other part for producing a spectrum and a light curve of the source. Fully analysed event files are obtained by converting the initial stereo parameters data file and assigning an energy and hadronness estimator to each event. Once reached this step, the gamma-ray flux, with respective spectrum and light-curve of the source, could be evaluated, in parallel to the *Instrument Response Function (IRF)*. As to obtain a flux reflecting properly the emission profile of the source (important aspect when analysing an extended target), the MC event reconstructed samples (the half part mentioned) were re-weighted through the *Donut MC tool* [157],.

At this step, the DM contribution to the gamma-ray flux of the source comes into play. As already mentioned, the DM density profile, and the respective *J-factor*, of Draco dSph has been taken from the work of Geringer-Sameth et al. [119]. From this publication, the *source brightness profile*, presented in Fig. 7.3, has been derived and normalized. For the re-weighting process, this

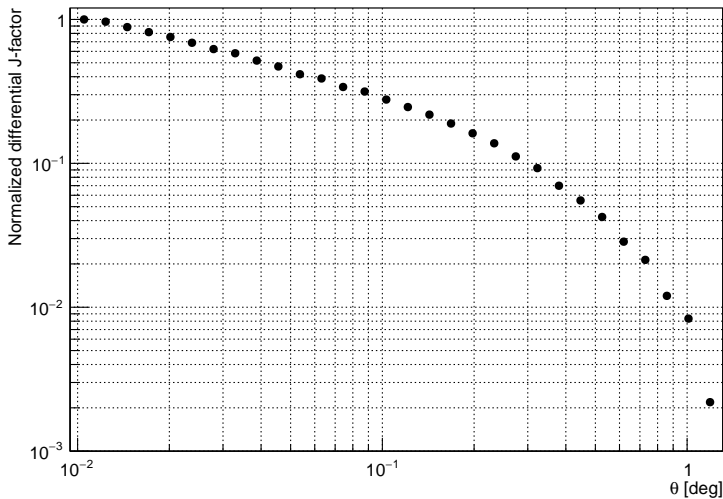


**Figure 7.3:** Source brightness profile of Draco dSph taken from the DM profile in [119] and normalized.

profile has been simulated as probability density function over the angular extension of the source, as visible in Fig. 7.4. The resulting profile has, then, been used to scale the MC simulations of diffuse  $\gamma$ -rays in order to follow the morphology of the source, obtaining the so-called *Donut MC* samples (hereafter D-MC). In Fig. 7.5, the transformation from MC simulations of diffuse  $\gamma$ -rays to D-MCs is shown for the MC simulations associated to the S09 data subsample (the same procedure has been applied to the MC sample associated to S10). The *Diffuse MC*, differently from what expected, presents a ring on the border of the camera position for which the gamma events simulated are not uniform with the rest. This is just an artefact of the histogram in the utmost parts of the camera. Looking carefully, one can also appreciate the fluctuations in the central region. As clearly visible in the *Donut MC* plot, the maximum of

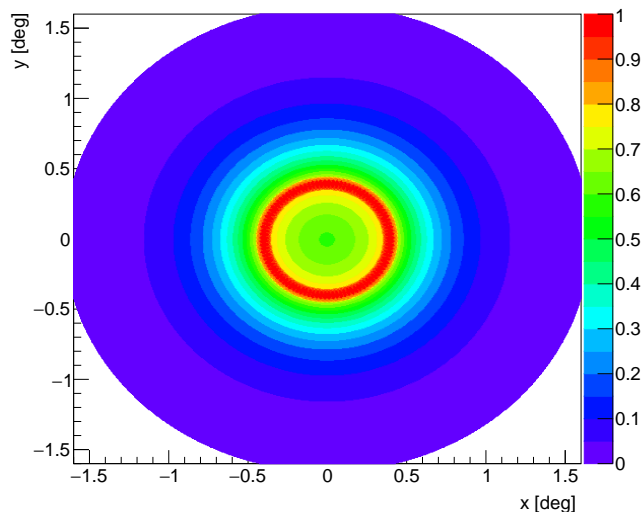


**Figure 7.4:** Source brightness profile of Draco dSph simulated as probability density functions around the camera center, in the case of 100 simulations.

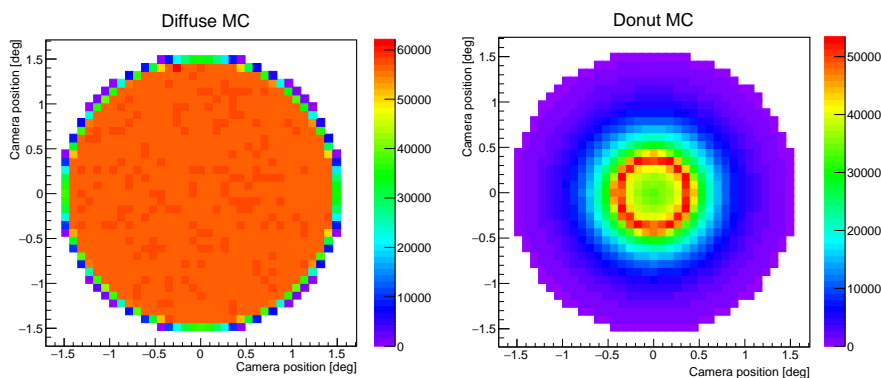


**Figure 7.5:** Example of transformation from MC simulations of diffuse  $\gamma$ -rays around the center of the camera up to an angle of  $1.5^\circ$  (*left plot*) to Donut MC simulations around the center of the camera, re-weighted for the source brightness profile of Draco dSph (*right plot*), for the case of the MCs associated to the data subsample S09.

the observed flux is given, in this case, by MC events coming from the central region of the source, i.e. located in a ring with a radius corresponding to the wobble angle in camera-wise coordinates, and the flux decreases moving to the inner and outer parts of the camera. Given the extension of the target, the simulated flux of gamma-photon in the center of the camera is not compatible with 0, but its contribution as leakage for the flux estimate is negligible, being of the order of the  $\sim 5\%$ , smaller than the  $J$ -factor uncertainty. Thus, I decided not to take into account this bias for the calculations.

Another important procedure to take into account is the background evaluation. For this analysis, the *OffFromWobblePartner* method has been applied,

being the background estimation method that limits the systematic errors due to the non-uniform acceptance of the telescopes' cameras. In Fig. 7.6, a schematic view of the considered OFF positions, marked as light-blue dots, is presented. Since Draco dSph was observed only with two wobbles, thus, the only OFF position available is the *OFF 3,1* marked in the figure.

Other two important parameters to select are the cuts in  $\theta^2$  and *hadronness*, in order to optimize for sensitivity the search for gamma photons coming from the object of interest. In the case of DM searches, and particularly for extended targets, an optimization of these cuts is performed blindly [157], checking the sensitivity of the analysis, before estimating the flux from real data. For this task, I started with the optimization of the  $\theta^2$  cut, selecting values in the range  $[0.02, 0.5]$   $\text{deg}^2$ , that translate in cuts of  $[0.14, 0.49]$  deg of angular distance between the nominal position of the target and the reconstructed event direction. Fig. 7.7 shows the normalized sensitivities obtained for different  $\theta^2$  cuts for each DM mass value

considered in the analysis. The optimal cut selected was the one providing the better sensitivity around the mass range to which the MAGIC telescopes are most sensitive, namely 1 TeV. As a consequence of this requirement, a cut at  $0.05 \text{ deg}^2$  has been chosen. A similar procedure was adopted for the case of the hadronness cut, this time considering values in the range  $[0.05, 0.3]$ . Together with this set of cuts, as the hadronness probability is largely dependent on the energy, a procedure based on a fixed  $\gamma$ -ray cut efficiency for all energy bins has been adopted. Hadronness efficiencies going from 60% to 90% have been tested (cuts in efficiency have been performed also for the  $\theta^2$ , but, as that parameter does not depend much on the energy, they have been discarded). In Fig. 7.8 the expected sensitivity curves for different hadronness cuts, as a function of the DM masses, are displayed. Also in this case, the cut has been selected for which the sensitivity is best at around 1 TeV DM mass, i.e. a cut in efficiency of 70%. Even if in the zoomed image one might opine that the fixed hadronness cut of 0.2 would be the one with the best sensitivity, considering smaller and bigger DM masses, the black dashed line of the 70% hadronness cut presents best overall sensitivities.

### 7.3 Flux estimation and results

Once defined the  $\theta^2$  and *hadronness* cut values, the flux estimation was performed through the use of a *full-likelihood method*, as described in [160]. No gamma-ray flux was detected from the target, and only the upper limits (ULs) of  $1.11 \times 10^{-11} \text{ cm}^{-2}\text{s}^{-1}$  and  $1.89 \times 10^{-12} \text{ cm}^{-2}\text{s}^{-1}$  on the photon flux (for

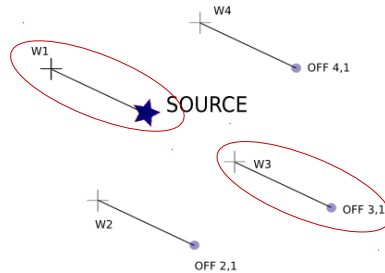


**Figure 7.6:** Geometry of the Off-FromWobblePartner background estimation method. The red ellipses indicate the wobble positions, with the respective ON and OFF positions, considered in this analysis.

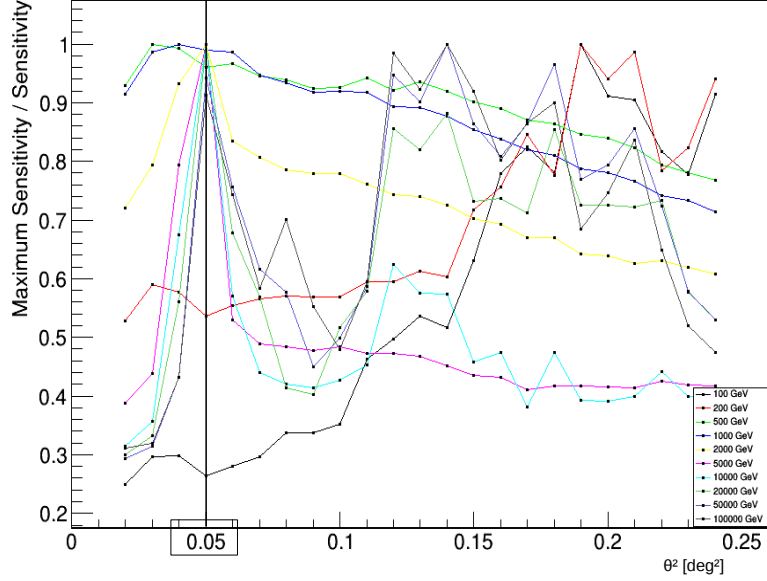


**Figure 7.7:** Normalized sensitivity of the analysis performed with respect to different  $\theta^2$  cuts. Each sensitivity curve is associated to a DM mass. The black vertical line indicates the chosen  $\theta^2$  cut value.

$E > 300$  GeV) could be set, for the S09 and S10, respectively.

The absence of hints of a signal is also visible in the *significance skymap* and the  $\theta^2$  *plot*, presented in Figs. 7.9 and 7.10, respectively. In Fig. 7.10, the gray area represents the totality of the estimated events, and the black vertical dashed line delimits the  $\theta^2$  zone, in which the excess has been searched for, once the background subtracted. On the upper right part of the figure, the number of excess events and the significance following [158] are reported. As the former is compatible with zero, only ULs on the flux could be set.

The ULs on the photon flux and the IRF obtained, together with the  $J$ -factor value, were, then, used to look for DM signatures from the target. A *binned full-likelihood function*, implemented in the *gLike* tool [161], was used to estimate the  $\langle\sigma v\rangle$  of WIMPs annihilation, as described in Sec. 5.5. An uncertainty on the  $J$ -factor of  $\log(\sigma_J) = 0.21 \text{ GeV}^2\text{cm}^{-5}$ , associated to  $\log J = 19.05 \text{ GeV}^2\text{cm}^{-5}$ , taken from [119], has been introduced as nuisance parameter in the likelihood. The diversity of the camera-wise acceptance in different regions of the camera has also been taken into account in the ON/OFF normalization parameter  $\tau$ , introducing a systematic uncertainty of width  $\sigma_{\tau, syst} = 0.015$  [122]. Only positive values of the expected number of gamma-rays estimator  $g$  have been considered, as the negative ones are non-physical.

95% confidence level (CL) ULs on the four WIMP annihilation channels  $b\bar{b}$ ,  $\tau^+\tau^-$ ,  $\mu^+\mu^-$  and  $W^+W^-$  have been estimated and are shown in Fig. 7.11. In order to evaluate the 68% and 95% containment bands, 300 simulations were performed for each annihilation channel. The most constraining exclusion limits up to  $\sim 10^{-24} \text{ cm}^3/\text{s}$  have been set for the  $\tau^+\tau^-$  channels for DM masses around the order of the TeV. In Tab. 7.2, the ULs for each annihilation channel

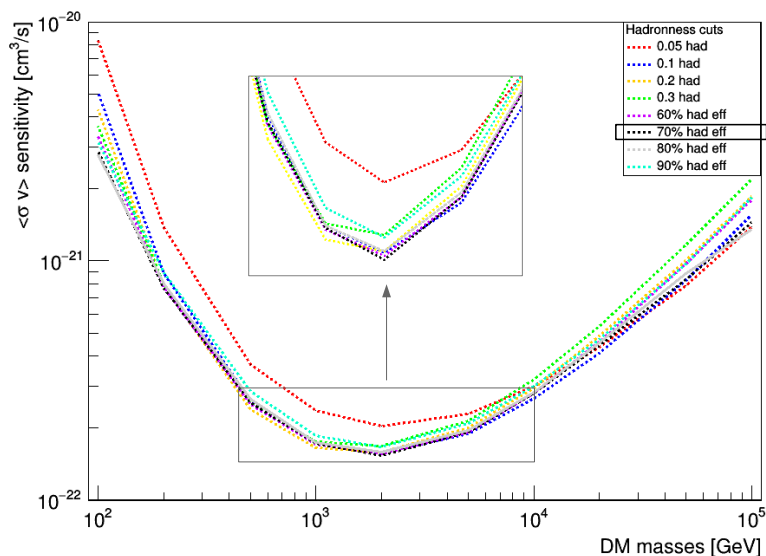


**Figure 7.8:** Sensitivities of the analysis for the different hadronness cuts (fixed for each energy bin or depending on the cut efficiency) at different DM masses. The black rectangle on the legend indicates the chosen hadronness cut value. The curves inside the rectangle, on the bottom central part of the figure, have been zoomed in, in order to let the reader appreciate the trends of the sensitivities in the central part of the covered energy range.

considered in the analysis, at the most sensitive DM mass value, are reported.

**Table 7.2:** List of the most constraining ULs on  $\langle\sigma_{ann}v\rangle$  for the four annihilation channels considered in the work. Each UL is associated to the respective WIMP mass.

Channel	DM particle mass [GeV]	$\langle\sigma_{ann}v\rangle^{UL}$ [ $\text{cm}^3/\text{s}$ ]
$b\bar{b}$	5000	$5.08 \times 10^{-23}$
$\mu^+\mu^-$	700	$2.16 \times 10^{-23}$
$\tau^+\tau^-$	1200	$7.37 \times 10^{-24}$
$W^+W^-$	1200	$3.45 \times 10^{-23}$

## 7.4 Discussion and conclusions

The 95% CL ULs obtained in this analysis are in line with the ones presented in the literature, but still not sufficient to exclude further  $\langle\sigma v\rangle$  values for WIMP annihilation. A comparison of these limits with those obtained by the analyses of Segue 1 (taken from a revised analysis of [164], not published yet), UMaII [157] and TriII [216] data is presented in Fig. 7.12 for the case of the  $b\bar{b}$  and  $\tau^+\tau^-$  annihilation channels. In either of the two figures, the Draco dSph

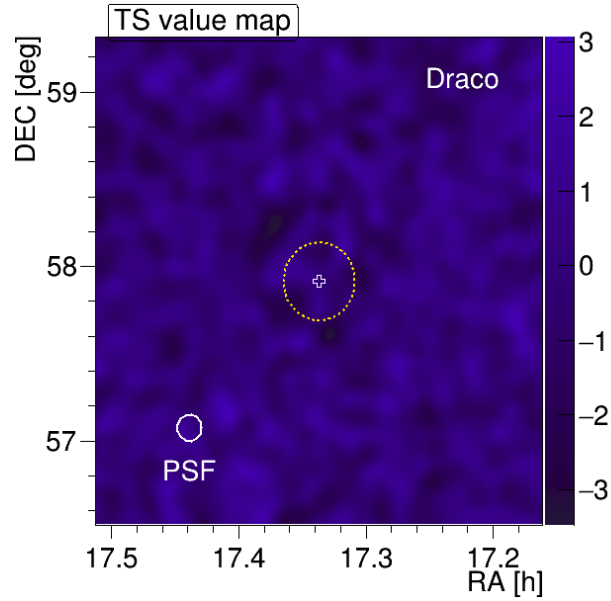


**Figure 7.9:** Significance skymap of Draco dSph for a FoV of  $2.4^\circ$ . The position of the source, in equatorial coordinates, is marked as a white cross. The orange dashed circle delimits the expected signal region. For comparing the extension of the optimized emission region of the source (defined by the square root of the  $\theta^2$  cut value), the PSF reached by the MAGIC telescope is also shown as a white solid circle.

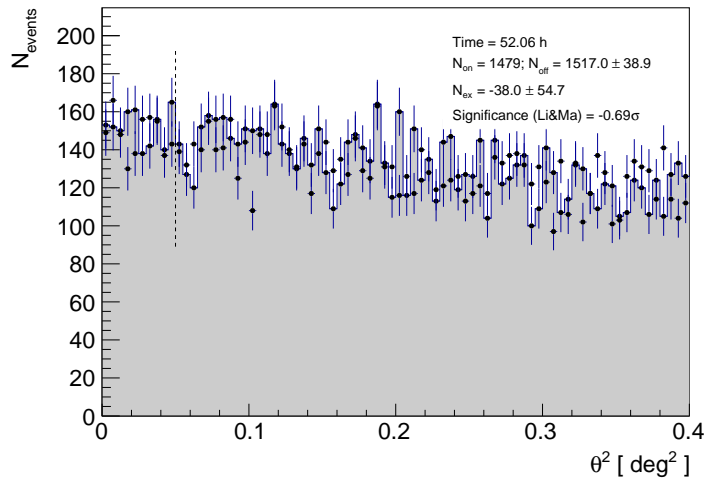


**Figure 7.10:** Squared distances of reconstructed shower directions w.r.t. source ( $\theta^2$  plot) of Draco dSph. The black vertical dashed line delimits the signal region at  $\theta^2 = 0.05 \text{ deg}^2$ .

analysis provides limits more constraining than the ones already published by the MAGIC collaboration. This result was foreseen, in case of no detection,

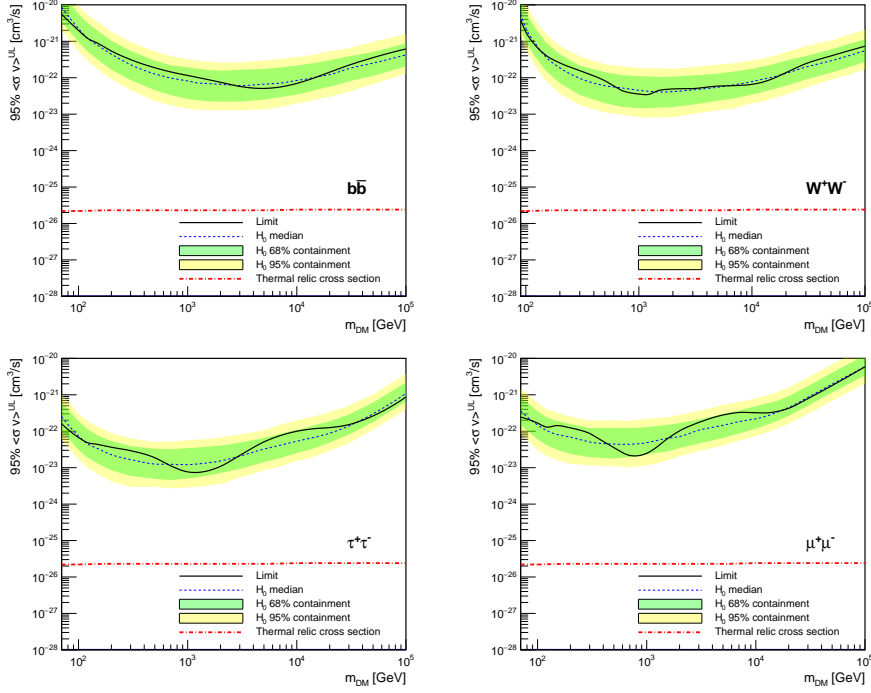


**Figure 7.11:** Draco  $\langle\sigma v\rangle$  ULs for the annihilation channels  $b\bar{b}$ ,  $W^+W^-$ ,  $\tau^+\tau^-$  and  $\mu^+\mu^-$ . The black line indicates the evaluated limit, with the respective 68% (green) and 95% (yellow) containment bands, while the dashed line is the median of the simulations. The red dashed line is present in all the plots for the comparison of the limits obtained with the thermal relic cross-section [51].

due to the  $J$ -factor reported in [119], that presents a value lower than the ones of Segue 1 and UMaII. Looking at the uncertainties of the  $J$ -factors mentioned, the larger robustness of the Draco dSph limit was also expected.

Even with its lower  $J$ -factor, and predicted higher UL, Draco dSph was decided to be observed in order to follow the observational diversification strategy adopted by the MAGIC collaboration. In this view, Segue 1 and UMaII were the first two dSphs in the list, to which Draco and Coma Berenices, presented in the next chapter, have been added. The case of TriII is not part of this discussion, as mentioned in the introduction of this chapter, and it has to be handled separately.

The effectiveness of this diversification of the targets, and hence distribution of the target-related systematic uncertainties, will become visible in chapter 9. A combination of the data of the four dSphs mentioned, excluding TriII, has been performed and the results will be presented, together with their comparison to the ULs obtained by other experiments.

Before passing to the combination of multiple dSphs data in chapter 9, Coma Berenices data taking and analysis, together with the results obtained, will be reported.

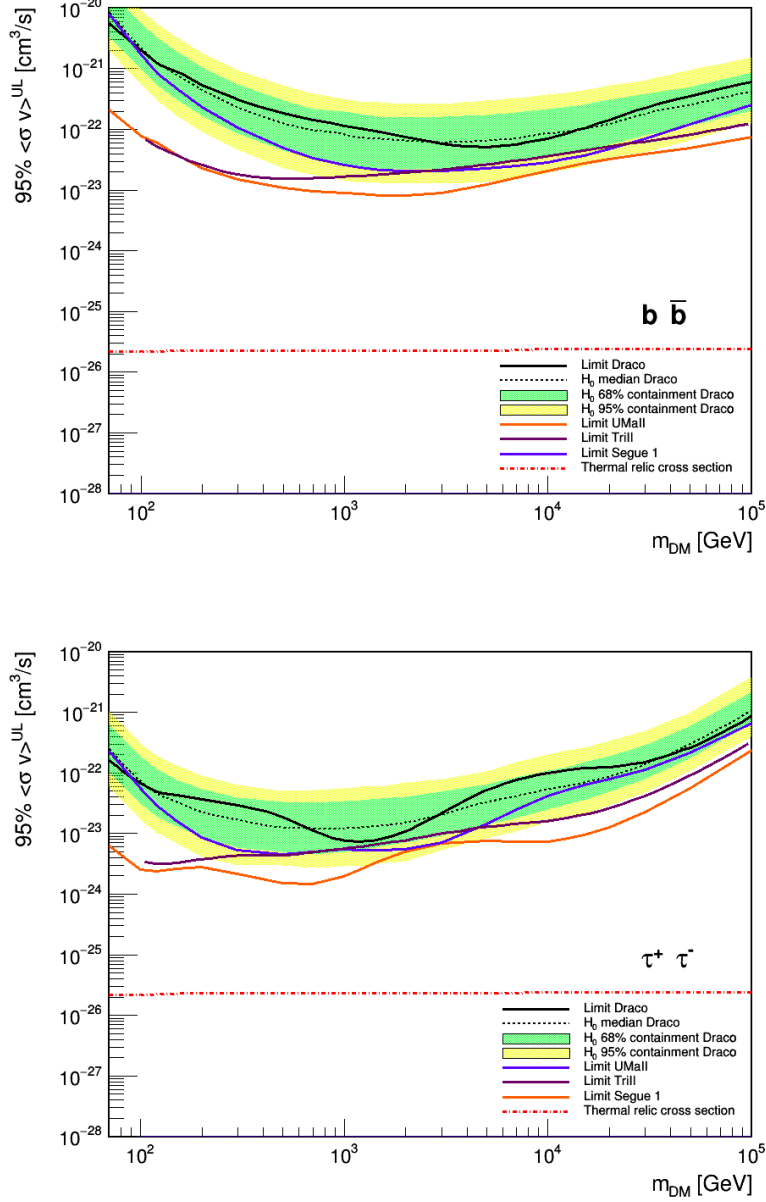


**Figure 7.12:** 95% CL ULs on the  $\langle\sigma v\rangle$  for WIMP annihilation, as a function of the DM mass, in the  $b\bar{b}$  (*up*) and  $\tau^+\tau^-$  (*down*) channels. Draco dSph ULs have been compared to the ULs obtained by the MAGIC collaboration analysing other dSphs. The limits obtained in this work are presented in black, the ones obtained from 157.9 h of Segue 1 data, in orange, the ones obtained from 94.8 h of UMaII data, in blue, and the ones obtained from 62.4 h of Trill data, in purple. For the ULs, only DM masses in the range  $10^2 - 10^5$  GeV have been considered.

## Chapter 8

# Search for WIMP Dark Matter from the Coma Berenices Dwarf Spheroidal Satellite Galaxy

The Coma Berenices dwarf spheroidal satellite (dSph) galaxy has been included in the list of dSphs for the observational diversification strategy after Draco dSph. The dSphs proposed for the observations were chosen on the basis of a raking of the objects presented in [119], [229] and [230], looking for the highest and most robust  $J$ -factors. Excluding the dSphs in the southern hemisphere, and the ones already observed, Coma Berenices dSph came out as the best candidate for the next observation.

The addition of this new target to the MAGIC dSphs sample was meant to help in reducing the possible biases in the target selection criteria, and maximizing the chances of discovery of a DM signal. Moreover, the aim of a joint analysis with other dSphs would provide potentially the best sensitivity to DM models at TeV scale.

In this chapter, I will introduce the Coma Berenices dSph and its datataking (section 8.1), for which I had the opportunity to be Principal Investigator (PI) of the observation, being responsible for drafting and presenting the observation proposal to the collaboration, and acting as data checker and main analyser. I will continue the chapter with the description of the data reduction in section 8.2 and I will present the results obtained. Finally, I will discuss the results and reach the conclusions of this analysis in section 8.3, starting to present the combined limits that will be reported in the next chapter.

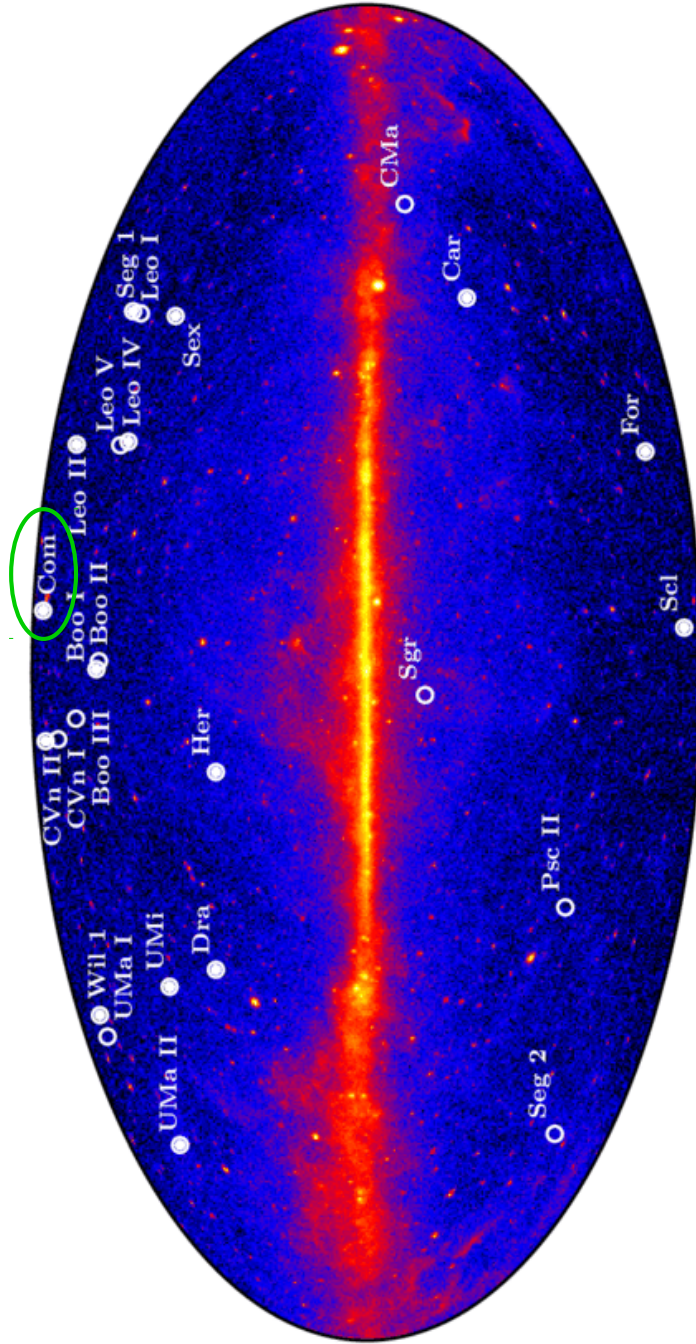


**Figure 8.1:** Position of Coma Berenices dSph in galactic coordinates. Image taken from [231]. The difference between filled and unfilled circles is given by the dSphs respectively considered or not for the analysis in [231].

## 8.1 The Coma Berenices dwarf spheroidal satellite galaxy

Coma Berenices dSph is a dwarf spheroidal satellite galaxy of the MW, observable in the constellation of Coma Berenices at RA = 12h26m59s and Dec = 23°55′09″, in the J2000 coordinate system [189] (its location is shown in Fig. 8.1). It was first detected by the Sloan Digital Sky Survey [232] in 2006, and it is one of the most appealing dSphs to be observed from the northern hemisphere, supposed to be highly DM dominated [101].

It presents an extreme low luminosity  $L \approx 3700L_{\odot}$  but a large mass value  $M \approx 1.2 \times 10^6 M_{\odot}$ , that assigns a mass-to-light (M/L) ratio of  $\sim 450$  [233]. Its star formation stopped billions years ago, and the star population presents very poor metallicity, of the order of  $[\text{Fe}/\text{H}] \approx -2.53 \pm 0.45$  to this ultra-faint dSph (UFD) [234].

Coma Berenices dSph (Com) culminates at La Palma at  $\sim 6^{\circ}$  and is observable below  $35^{\circ}$  in zenith from February to May. With the MAGIC telescopes, Com was observed for 51.4 h, from the end of January to the beginning of June 2019, in dark time and pointing only to *W1* and *W3* wobble positions, due to stars in the field of view (FoV). Given the non-uniform acceptance of the telescopes' cameras in all the receiving area, also for Com a check of the compatibility between the two azimuth distributions has been performed, shown in Fig. 8.2.

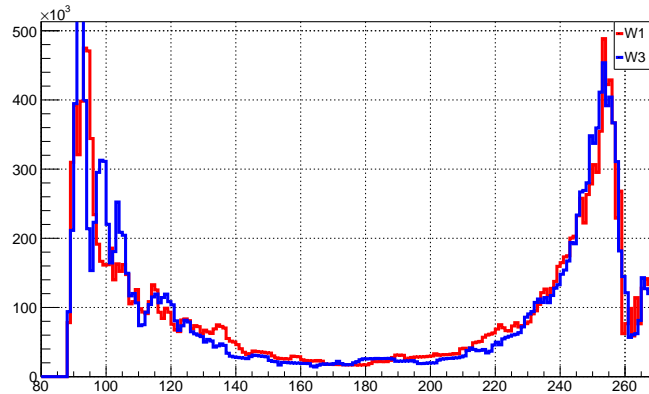


**Figure 8.2:** Distribution of the observations as a function of the azimuth telescope pointing angles for the two wobbles. *W1* observations are presented in red, while *W3* ones in blue.

No LIDAR measurements were available for mostly all the data taking period, thus auxiliary measurements of the cloudiness parameter with the pyrometer [235], mounted on the MAGIC 1 (M1) telescope, had to be used for estimating the atmospheric aerosol transmission. Moreover, a lot of triggering noisy signals, dubbed *banana shapes*, in one, or more, receiver boards of M1's camera, disturbed the data taking. All these degradations of data quality, together with the night of 2019/02/04 with wrong wobble settings, have been taken into account during the quality check procedure, as explained in next section.

## 8.2 Data reconstruction and results

The data taken for Coma Berenices were linked to only one Monte Carlo (MC) MAGIC analysis period, called ST.03.11, characterized by data associated to a gradual recovery of the mirror reflectivity.

This time, only one sample of data was considered, and stringent quality checks were applied, starting from stereo reconstructed data. In the absence of LIDAR data, a cut on the pyrometer *cloudiness* value of 30, equivalent to a cut in LIDAR aerosol transmission at 0.85 [236], was applied. Cut on the *Hillas parameters* were also performed. Moreover, given an unexplained outlier in the median DC PMT current in the 2019/04/25 data, the acceptable interval for dark time and twilight current was reduced to [200 – 800]  $\mu\text{A}$ .

The data were cut in timeslices, instead of runs, and around 2% of the total was rejected, leaving a total effective time after cuts of 50.1 h.

The training of the *Random Forest (RF)* was carried out using Monte Carlo (MC) simulations of a diffuse gamma-ray emission, given the extension of the object, for which the outermost member star used to evaluate the velocity dispersion had been found at a distance of  $0.31^\circ$  from the center of Com. The sample of *OFF data*, used for the training, too, is composed of data taken from the observation of the quasar 3c 264 and the blazar B2-1811+31, when non emitting in gamma rays, and for the Galactic halo in the OFF zone (GH-OFF-2019), i.e. a sky region where neither astrophysical sources nor DM are supposed to emit in the gamma energy range, providing a total of 21.7 h of data. The same quality cuts used for the ON data sample were used for the OFF sample, this time cutting per runs, and removing 2.4 h of data. Once trained the RF, the decision tree was applied to the data in order to assign a *hadronness* parameter to each event reconstructed.

In order to take into account the extension of the emission region of Com at the moment of the flux evaluation, the *Donut Monte Carlo* procedure was applied to the MC sample for the diffuse gamma-ray emission. The source brightness profile in Fig. 8.3, obtained from the data in [119], was applied to re-weight the MC simulations for the diffuse gamma-ray emission. The rescaled overall Donut-MC sample is presented in Fig. 8.4, together with the original overall MC sample. Comparing the two figures, it is worth to note that the positions of the simulated events after the rescaling show a smaller angular distribution. The transition from a total extension of  $5^\circ$  to  $1.6^\circ$  is due to the steep emission profile of Com.

With the Donut-MC simulations, the flux and the light curve of Com were calculated. No signal excess was found from the region of interest using the standard MAGIC analysis settings. This result was already expected, after having had a look at the significance skymap, reported in Fig. 8.5.

In order to maximize the effectiveness of the search for the signal in the MAGIC best sensitivity energy detection region, at around 1 TeV, the cuts on  $\theta^2$  and *hadronness* were optimized blindly. First, the  $\theta^2$  interval [0.02, 0.05]  $\text{deg}^2$  was tested, in steps of 0.01  $\text{deg}^2$ , together with  $\theta^2 = 0.1, 0.15$  and  $0.2 \text{ deg}^2$ , as visible in Fig.8.6, and then the *hadronness* cut was optimized.

At a first time, fixed hadronness values were used for the cut, searching for the best sensitivity in the hadronness range [0.05, 0.4], following steps of 0.05. Secondly, cuts depending on the energy bin considered, namely efficiency cuts, were applied in the interval [60%, 90%]. In Figs. 8.7 and 8.8 the splines of the

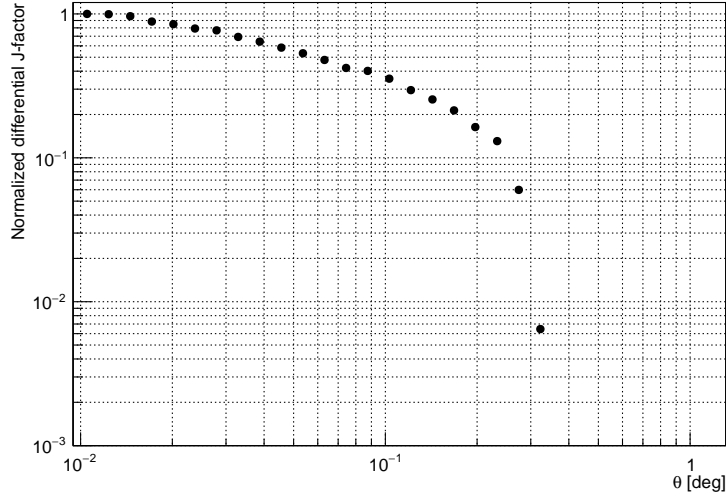


**Figure 8.3:** Source brightness profile of Coma Berenices dSph taken from the DM profile in [119] and normalized.

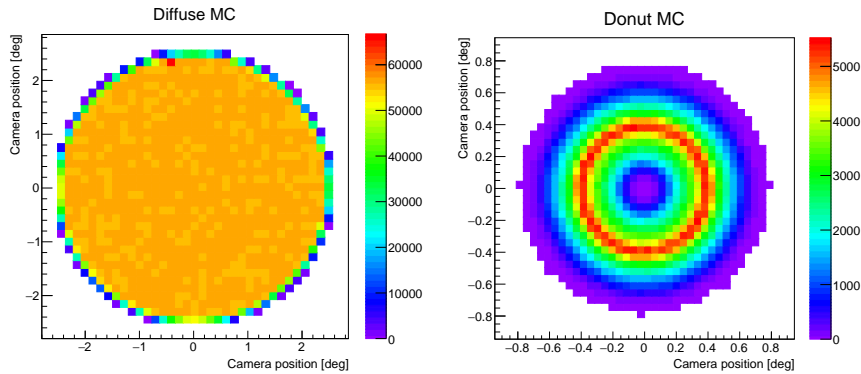


**Figure 8.4:** Example of transformation from MC simulations of diffuse  $\gamma$ -rays around the center of the camera up to an angle of  $2.5^\circ$  (*left* plot) to Donut MC simulations around the center of the camera, re-weighted for the source brightness profile of Coma Berenices dSph (*right* plot).

normalized sensitivities for the different WIMP DM masses, as a function of the hadronness cuts, are presented. With a black vertical line, the cut selected for the analysis is presented.

To decide the best hadronness cut between the selected ones in each of the method (fixed or energy bin-dependent), a further plot comparing the sensitivities was created, and it is shown in Fig. 8.9. The circle on the legend marks the selected optimal value for each hadronness cut selection method.

The best sensitivity was obtained for a  $\theta^2$  cut of  $0.03 \text{ deg}^2$  and a *hadronness* cut of 0.25, both fixed for each energy bin.

With these two cuts, the flux of gamma rays was calculated again, giving an

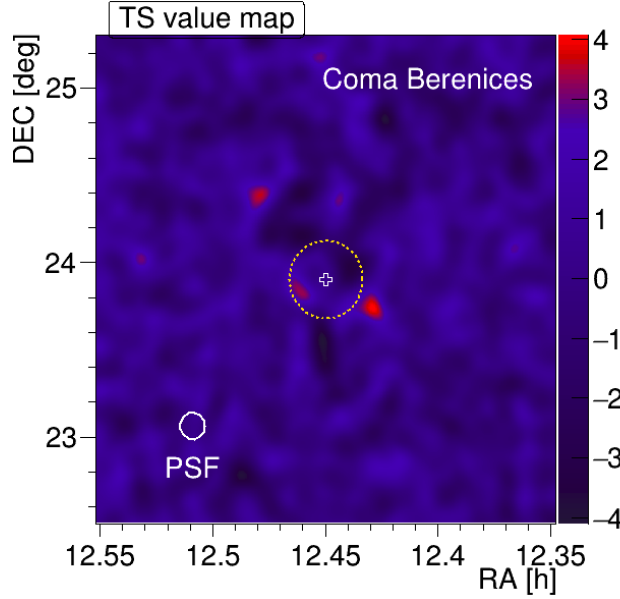


**Figure 8.5:** Significance skymap of Coma Berenices dSph for a FoV of  $2.4^\circ$ . The position of the source, in equatorial coordinates, is marked as a white cross. The orange dashed circle delimits the expected signal region. For comparing the extension of the optimized emission region of the source (defined by the square root of the  $\theta^2$  cut value), the PSF reached by the MAGIC telescope is also shown as a white solid circle.

UL of  $1.25 \times 10^{-12} \text{ cm}^{-2} \text{ s}^{-1}$  ( $E > 300 \text{ GeV}$ ). If checking for excesses in the ON data, as a function of the  $\theta^2$  distance from the nominal position of the source, an excess compatible with no signal and a Li&Ma significance [158] of  $0.76\sigma$  were obtained (see Fig. 8.10).

A binned full-likelihood method was, then, used to search for DM signals from Coma Berenices dSph. The theoretical model adopted to describe the annihilation process of WIMPs is the one by Cirelli et al. [162].

A value of  $\log J = 19.02$  with its respective uncertainty  $\log(\sigma_J) = 0.41$  (taken from [119]), considered as nuisance parameter in the likelihood, were used to define the DM content of Com. In the same way of Draco dSph analysis, also in this case, only positive values of the event estimator were taken into account. No hint of a signal was found in the analysis and only ULs could be set. In Fig. 8.11, the limits obtained for the four annihilation channels  $b\bar{b}$ ,  $W^+W^-$ ,  $\tau^+\tau^-$  and  $\mu^+\mu^-$ , at the 95% CL are reported. For each of them, the 68% and 95% containment bands have been estimated running 300 simulations. The dashed line in the center of the bands is the median of the simulations.

For each annihilation channel, the most constraining ULs obtained are reported in Tab. 8.1.

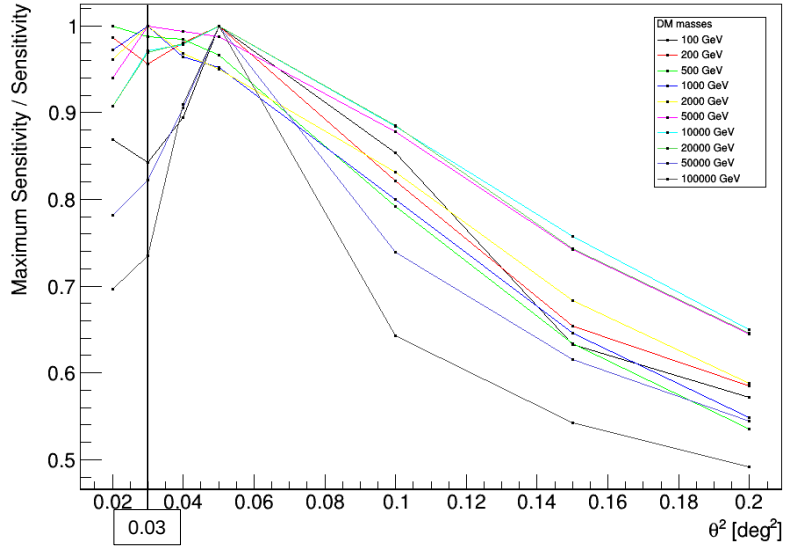


**Figure 8.6:** Normalized sensitivity of the analysis performed with respect to different  $\theta^2$  cuts. Each sensitivity curve is associated to a DM mass. The black vertical line indicates the chosen  $\theta^2$  cut value.

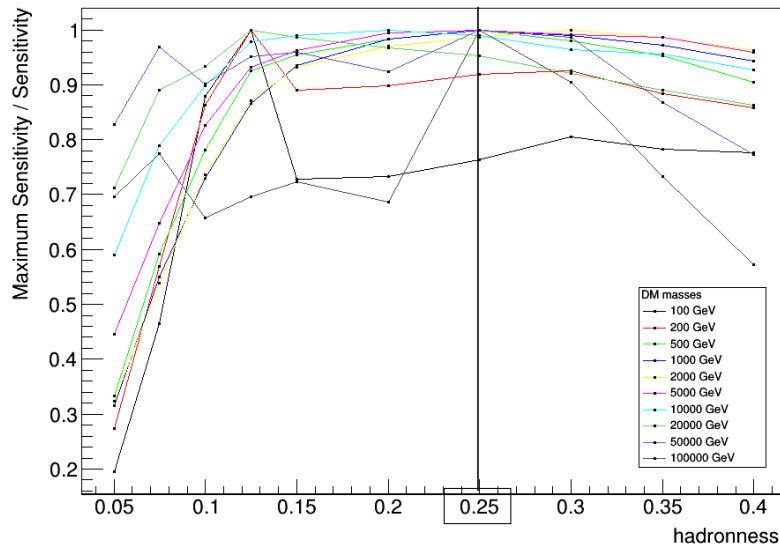


**Figure 8.7:** Normalized sensitivities of the analysis performed with respect to different hadronness cuts, per each WIMP DM mass considered. The black vertical line indicates the chosen hadronness cut value.

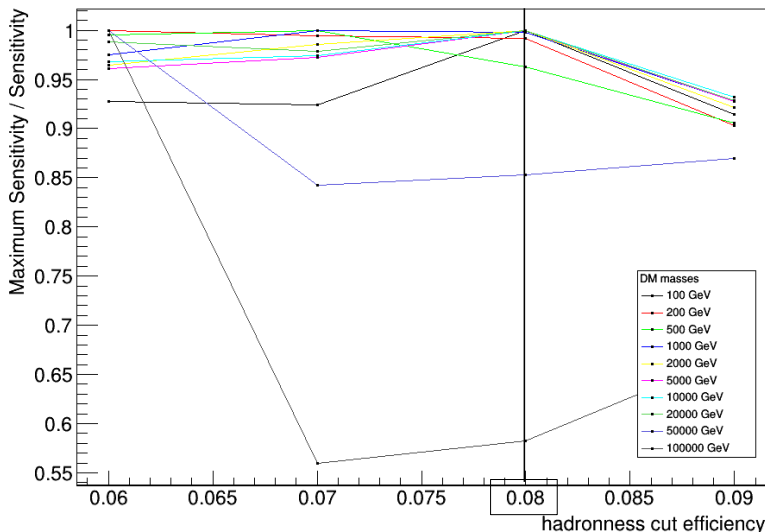


**Figure 8.8:** Normalized sensitivities of the analysis performed with respect to different hadronness cuts in efficiency, per each WIMP DM mass considered. The black vertical line indicates the chosen hadronness cut value.

**Table 8.1:** List of the most constraining ULs on  $\langle\sigma_{ann}v\rangle$  for the four annihilation channels considered in the work. Each UL is associated to the respective WIMP mass.

Channel	DM particle mass [GeV]	$\langle\sigma_{ann}v\rangle^{UL}$ [ $\text{cm}^3/\text{s}$ ]
$b\bar{b}$	2000	$5.57 \times 10^{-23}$
$\mu^+\mu^-$	1500	$6.14 \times 10^{-23}$
$\tau^+\tau^-$	500	$1.09 \times 10^{-23}$
$W^+W^-$	1500	$3.48 \times 10^{-23}$

### 8.3 Discussion and conclusions

DSphs are very compact objects and present high M/L ratios, making them typical targets to look for WIMP DM annihilation in the MW. The MAGIC collaboration decided to observe the most promising dSphs in the northern hemisphere, namely Segue 1 and Ursa Major II, for which the most constraining ULs at TeV DM masses have been obtained.

Draco dSph, presented in the previous chapter, and Coma Berenices dSph, were observed later, as targets of a multi-year observation diversification proposal. The campaign started officially in 2018, even if some diversification of the observational targets for DM searches was already attempted in earlier times.

The choice of covering different DM dominated objects was made in order to distribute the systematic uncertainties related to the particular targets, that stem from the limited capability of making accurate stars' kinematic measurements and/or precise determination of the targets' distance. One example of

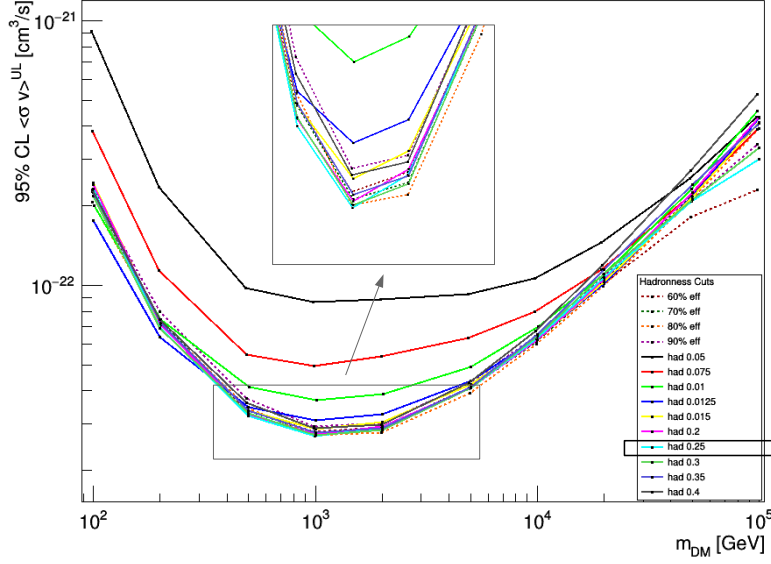


**Figure 8.9:** Sensitivities of the analysis for the different hadronness cuts, fixed for each energy bin (*had* in the legend) or depending on the cut efficiency (*eff* in the legend), at different DM masses. The black rectangle on the legend indicates the chosen hadronness cut value. The curves inside the rectangle, on the bottom central part of the figure, have been zoomed in, in order to let the reader appreciate the trends of the sensitivities in the central part of the covered energy range.

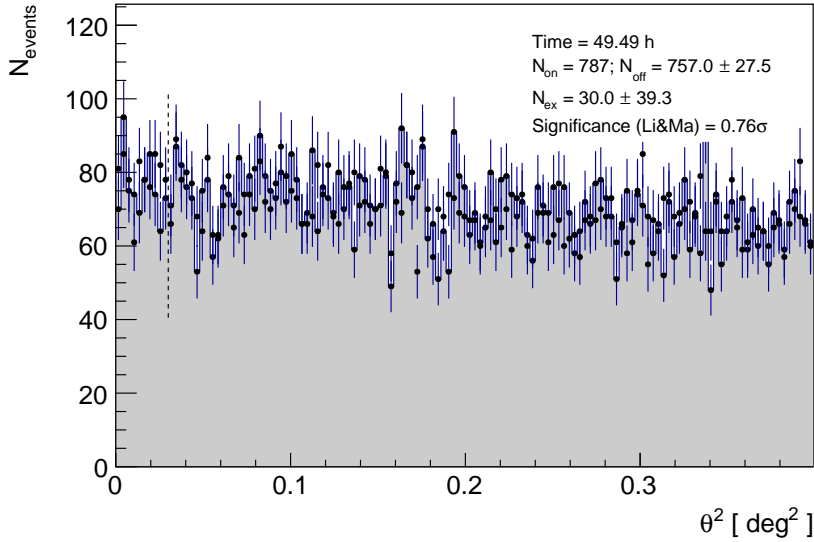


**Figure 8.10:** Squared distances of reconstructed shower directions w.r.t. source ( $\theta^2$  plot) of Coma Berenices dSph. The black vertical dashed line delimits the signal region at  $\theta^2 = 0.03 \text{ deg}^2$ .

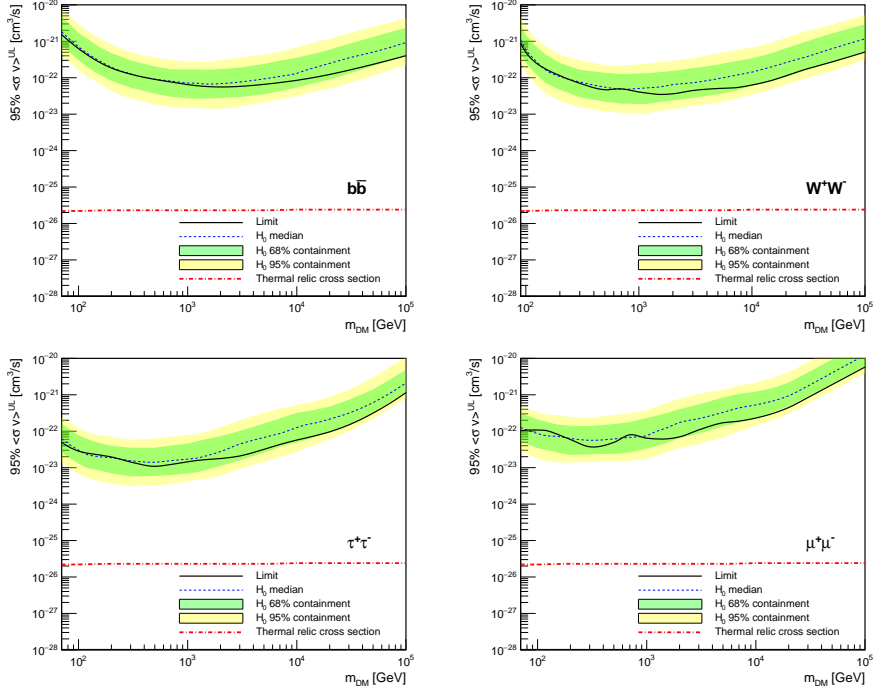


**Figure 8.11:** Coma Berenices  $\langle\sigma_{ann}v\rangle$  95% CL ULs for the annihilation channels  $b\bar{b}$ ,  $W^+W^-$ ,  $\tau^+\tau^-$  and  $\mu^+\mu^-$ . The black line indicates the evaluated limit, with the respective 68% (green) and 95% (yellow) containment bands, while the dashed line is the median of the simulations. The red dashed line is present in all the figures, for comparison, and indicates the thermal relic cross-section [51].

what mentioned here is the case of Triangulum II, thought to be one of the most promising dSphs candidate for DM discovery, if not the most promising one, in the northern hemisphere [218]. It was realized, later, to have a considerably smaller  $J$ -factor than previously estimated [219]. The correction paper was published just because of the detection of new stars, pertaining to the star sample used for the velocity dispersion profile evaluation, of which one is part of a binary system, thus affecting the kinematic measurement performed.

The study of DM velocity-averaged cross sections of WIMPs across different DM targets can, then, help in reducing the possible bias given by the result obtained from just one dSph.

Coma Berenice dSph, as already said, was the second dSph observed in the ground of the diversification project. The choice of this dSph was made after a ranking of the most DM dominated dSphs in the northern hemisphere, following the  $J$ -factor values reported in [119]. As expected from its slightly lower  $J$ -factor, but compatible within the uncertainty range with the one on Draco dSph, Coma Berenices dSph observation did not provide any hint of a signal, and only ULs on  $\langle\sigma_{ann}v\rangle$  could be set.

In Fig. 8.12, the ULs obtained for Com in the  $b\bar{b}$  and  $\tau^+\tau^-$  channel are compared to the ULs obtained looking for WIMP DM annihilation in Segue 1, Ursa Major II, Triangulum II (the latter not directly comparable, as already

mentioned) and Draco dSphs. The thermal relic cross section is also reported in the figure.

For DM masses higher than 1 TeV, the limits obtained from Com are compatible, unless fluctuations, to the ones of Draco, thus not providing any further constraint on the DM velocity-averaged cross-section. But, even if not improving the previously published MAGIC ULs, the combination of Com data with the other dSphs data can give the most constraining UL in the range of TeV DM masses, and reduce the bias possibly created by the target-related uncertainties. The combined analysis and the results obtained will be presented in the next chapter.

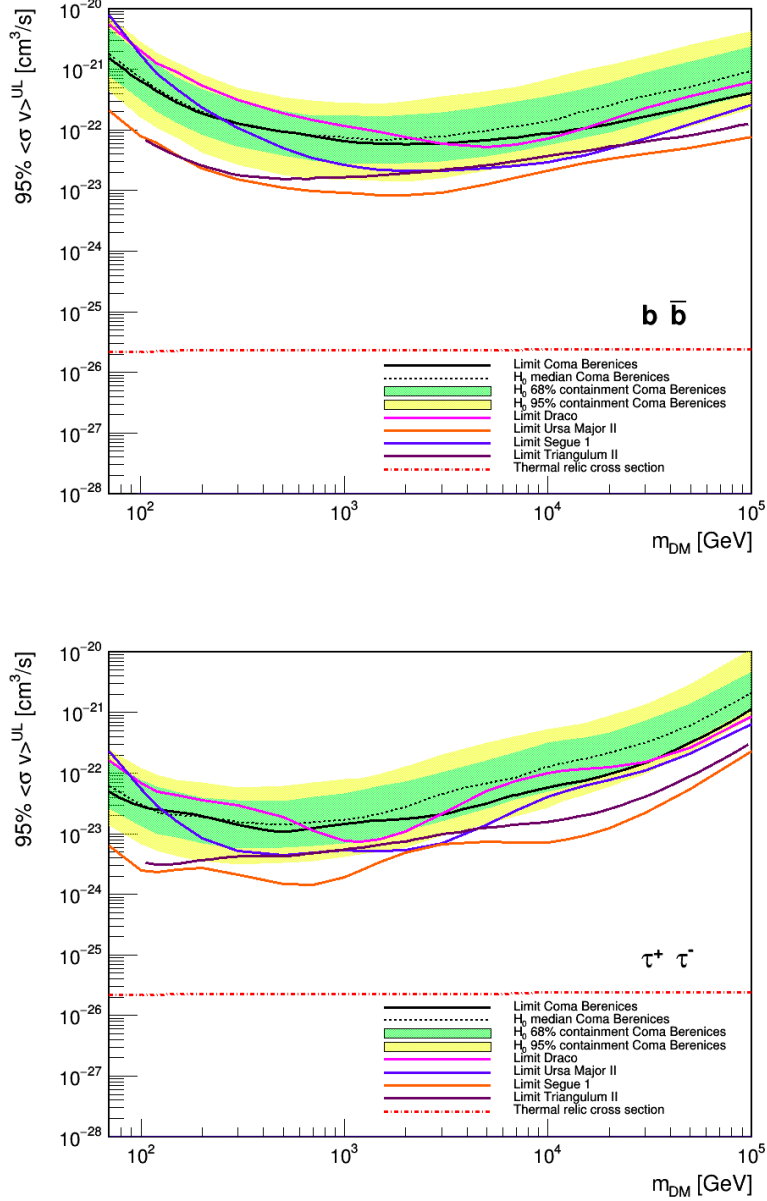


**Figure 8.12:** 95% CL ULs on the  $\langle \sigma_{ann} v \rangle$  for WIMP annihilation, as a function of the DM mass, in the  $b\bar{b}$  (top) and  $\tau^+\tau^-$  (bottom) channels. Coma Berenices dSph ULs have been compared to the ULs obtained by the MAGIC collaboration analysing other dSphs. The limits obtained in this work are presented in black, the ones obtained from the Draco dSphs analysis, presented in the previous chapter, in pink, the ones obtained from 157.9 h of Segue 1 data, in orange, the ones obtained from 94.8 h of UMaII data, in blue, and the ones obtained from 62.4 h of TriII data, in purple. For the ULs, only DM masses in the range  $10^2 - 10^5$  GeV have been considered.

## Chapter 9

# Combination of Upper Limits from Dwarf Spheroidal Satellite Galaxies

The dwarf spheroidal (dSph) galaxies satellite of the Milky Way are a target of relevance for indirect dark matter (DM) searches with Imaging Atmospheric Cherenkov Telescopes (IACTs), given their peculiar characteristics. In particular, being located at latitudes well beyond the galactic disk (i.e.  $> 20^\circ$ ), they represent the best trade-off between remarkable values of their  $J$ -factors and affordable amounts of uncertainties associated to DM profiles and gamma-ray background contamination [237].

The typical uncertainties associated to their DM estimated content, namely the  $J$ -factor, can reach up to  $O(10)$  or more, and affect largely the results of DM studies. Furthermore, together with those uncertainties related to the velocity dispersion measurements, target-related uncertainties can also be present, like the ones given by the unknown presence of a binary star system, that affect the kinematic measurements, or the possibly not stable dynamical equilibrium of the object. Therefore, a *diversification of the observational targets* represents the optimal strategy for indirect DM searches in order to reduce possible biases in target selection and to maximize the chances of discovery of DM signals. In addition, DM particle physics constraints from the observation of different targets can be easily combined *a posteriori* to the already existing ones [160].

The first study of WIMP DM in dSphs, after the upgrade of the MAGIC telescopes in 2009, was the one on Segue 1 in 2013 [164], that was the most promising target at that time, and the one that provided the best upper limits (ULs). The results from Ursa Major II dSph observations followed in 2016 [157], confirming, even if not improving, the constraints set previously by the MAGIC collaboration [238], and from then on, the observational diversification strategy started to gain ground (in a similar way to [239]). In this context, a multi-year proposal of observation was submitted to the MAGIC collaboration and approved in 2018. Draco dSph was the first in the schedule, and it was observed for  $\sim 60$  h in 2018, as presented in chapter 7. Coma Berenices dSph followed in 2019, with  $\sim 50$  h of data (chapter 8). In addition to these two, but coming from a last-minute request of observation, given a then very recent new and exciting  $J$ -factor [218], Triangulum II (TriII) was observed in 2018.

Excluding the latter, because of large uncertainties on its star sample, discovered posterior to the MAGIC observation, the data of the four dSphs mentioned have been combined, in order to achieve the most sensitive search for DM signals from dSphs of the Milky Way in the mass range above  $\sim 1$  TeV, see section 9.1. Given the newly adopted *Donut Monte Carlo* procedure, presented for the first time in [157], the analysis carried out for Segue 1 in [164] has been revised, and is reported in section 9.1.1. The results of the data combination, together with a comparison of the estimated ULs on  $\langle \sigma_{ann} v \rangle$  with the ones of other experiments are reported in section 9.2. To conclude this chapter, a summary of the study will be presented, and the next foreseen steps within the MAGIC DM observation program will be described.

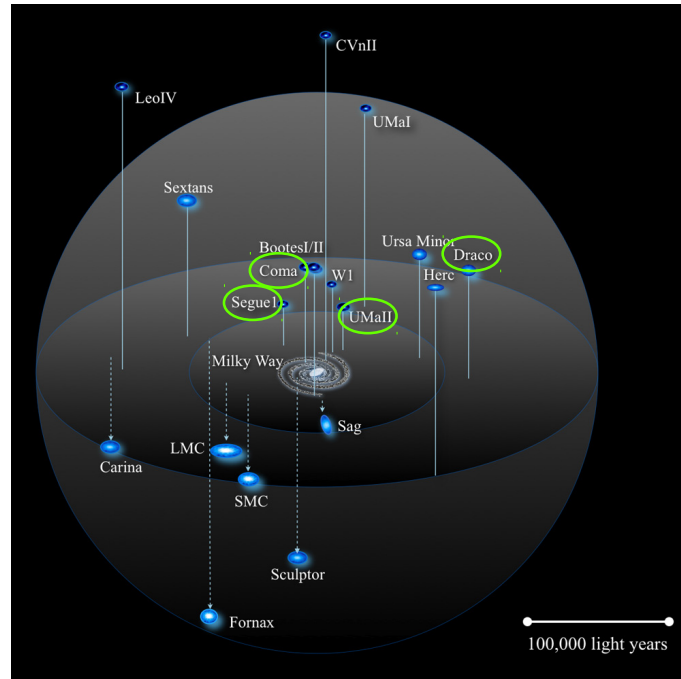


**Figure 9.1:** Map of dwarf spheroidal satellite galaxies, orbiting the Milky Way Galaxy, taken from [240]. The four dSphs considered for this combined analysis are marked with a green ellipse.

## 9.1 Dwarf spheroidal satellite galaxy data samples

The four dSphs observed with the MAGIC telescopes are shown in Fig. 9.1 (marked with a green circle) and listed in Tab. 9.1 (Triangulum II is not included here for the reasons explained previously), in which their respective total  $J$ -factors  $\log(J(\theta_{\max}))$ , outermost member star angle  $\theta_{\max}$ , the angle containing 50% of the dark matter signal emission  $\theta_{0.5}$  (i.e.  $J(\theta_{0.5}) = 0.5 \times J(\theta_{\max})$ ), and the MAGIC target observation time are reported. The values in the second, third and fourth columns of the table have been taken from Geringer-Sameth et al. [119], a common reference adopted for all the dSphs, and chosen at the moment of the latest proposals of observation, when the multi-year observational diversification strategy started.

Although for Segue 1 a different  $J$ -factor had been previously adopted in a paper published by the MAGIC collaboration [164], for the sake of uniformity, we decided to use the  $J$ -factor value taken from [119] for this work. The estimate of the Segue 1  $J$ -factor has been recently discussed in the literature (see Bonivard et al. [241, 242] and Hayashi et al. [243]), because of the variability obtained when applying different methods of estimation of the star sample, from which the velocity dispersion is evaluated. To support the choice made for our analysis, the works of Chiappo et al. [244] and the Fermi-LAT collaboration [245] and the same [164], present  $J$ -factor values compatible with the one of [119], whose  $J$ -factor estimate lies exactly in the middle of the range of variation discussed in [242]. The four dSphs present values of  $\log J \geq 19 \text{ GeV}^2\text{cm}^{-5}$ ,

**Table 9.1:** List of the candidates proposed for the dSphs multi-year DM project (first two lines, Draco and Coma Berenice dSphs) and previously observed (last two lines, Segue 1 [164] and Ursa Major II [157]). The  $J$ -factors are presented together with their asymmetric uncertainties. The third column shows the source extension, as described in section 6.2 of [119]. The maximum angle  $\theta_{\max}$  refers to the galactocentric distance of the outermost member star used to evaluate the velocity dispersion profile, whereas  $\theta_{0.5}$  refers to the angle containing 50% of the dark matter emission (i.e.  $J(\theta_{0.5}) = 0.5 \times J(\theta_{\max})$ ). The last column presents the total time of observation of the targets acquired with the MAGIC telescopes.

Target	$\log J(\theta_{\max})$ [ $\text{GeV}^2\text{cm}^{-5}$ ]	$\theta_{\max}$ [deg]	$\theta_{0.5}$ [deg]	$T_{\text{obs}}$ [h]
Coma Berenices	$19.02^{+0.37}_{-0.41}$	0.31	$0.16^{+0.02}_{-0.05}$	49.5
Draco	$19.05^{+0.22}_{-0.21}$	1.30	$0.40^{+0.16}_{-0.15}$	52.1
Segue 1	$19.36^{+0.32}_{-0.35}$	0.35	$0.13^{+0.05}_{-0.07}$	157.9
Ursa Major II	$19.42^{+0.44}_{-0.42}$	0.53	$0.24^{+0.06}_{-0.11}$	94.8

thus appearing as the most DM dominated in the northern hemisphere, and uncertainties of the order of few percents in  $\log J$ . This ensures the robustness of the  $J$ -factor estimates, without considering the target-related uncertainty that cannot be evaluated numerically.

The total sample available for the combined analysis results, then, to be composed of 354 h of data, about three times larger than the Segue 1 data sample. A huge data sample, together with the improved binned full-likelihood method

implemented in [161], leads to velocity-averaged cross-section ULs on WIMP annihilation at least twice better than the ones previously published for any single dSphs. In the same way, the combination of data that present ULs with lower constraints on  $\langle\sigma_{ann}v\rangle$ , such as, e.g., the case of Draco, with data providing better constraints on the WIMP characteristics, can reduce the possible improvement of the combined UL achieved, for example with respect of considering a larger data sample of an object with similarly high  $\log J$ .

The data needed as input for the combined likelihood are the IRF of each data sample and the event list, obtained from the data reduction applied in each analysis. In the case of Draco and Coma Berenices dSphs, information is obtained from the analyses reported in this thesis. The analysis of Ursa Major II used the same approach as the ones presented in the previous chapters, the same likelihood method and the use of the Donut Monte Carlo tool to take into account the extension of the target, therefore the data set from the original publication (with 94.8 h of good quality data) [157] could be used with no modification. In the case of Segue 1, we decided to also take into account its extension in the analysis, which was not considered for the ULs presented in previous publications, the one by the MAGIC collaboration [164] and of the joint analysis with Fermi-LAT [93].

### 9.1.1 Revised analysis of Segue 1

The Segue 1 data, taken with the MAGIC telescopes, were analysed in a slightly different way in the paper published by the MAGIC collaboration, with respect to the paper published together with the Fermi-LAT collaboration. The changes reported in the latter consist of a different  $J$ -factor assumed for the analysis (the value obtained by [245] was also used for the MAGIC analysis), the introduction of the statistical uncertainty of the  $J$ -factor as nuisance parameter in the likelihood function, and the use of the prescription limiting  $\langle\sigma_{ann}v\rangle$  to only positive values, as described in the appendix A of [93]. Despite that, the extension of the object was not taken into account, and Segue 1 was treated as a pointlike source. This was not a big problem, since its extension is not much larger (the angular galactocentric distance of the outermost member star is  $0.35^\circ$  in [119]) than the MAGIC Point Spread Function ( $< 0.1^\circ$ ). If computing the new ULs considering Segue 1's extension and applying the Donut Monte Carlo method, as done for the other dSphs observed with the MAGIC telescopes, the results differ by less than 10% compared to the ones previously published (as already pointed out in [164]), thus introducing a difference on the final limits smaller than the statistical uncertainty of the  $J$ -factor. Nevertheless, for the sake of homogeneity with the other data sets used for the data combination, the new reconstructed data set accounts for the extension. The curves obtained with this method are reported in Fig. 9.2 for the  $b\bar{b}$ ,  $W^+W^-$ ,  $\tau^+\tau^-$  and  $\mu^+\mu^-$  WIMP annihilation channels.

## 9.2 Results and discussion

All the dSph analyses for the limit combination have been performed following the MAGIC standard analysis procedure, using the software MARS [226], and the reduced data have been finally analysed with the gLike software [161], in

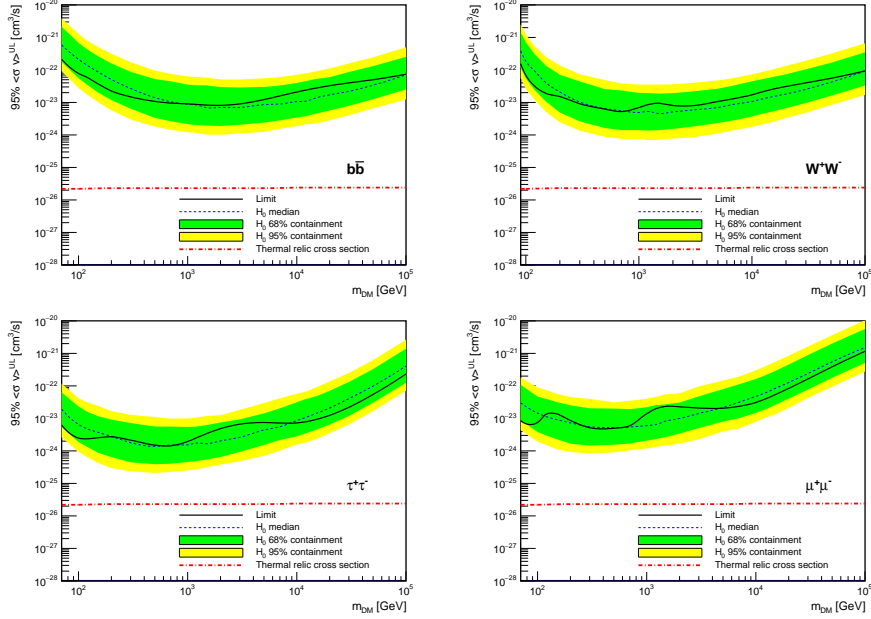


**Figure 9.2:** Segue 1  $\langle\sigma_{ann}v\rangle$  revised ULs for the annihilation channels  $b\bar{b}$ ,  $W^+W^-$ ,  $\tau^+\tau^-$  and  $\mu^+\mu^-$ . The limits presented in this figure (solid black lines), with the respective 68% (green) and 95% (yellow) containment bands, have been rescaled from the ones in [164] as described in the text. The red dashed line is present in all the plots for the comparison of the limits obtained with the thermal relic cross-section [51].

order to compute the results for the DM study. The binned full-likelihood function used to check for DM signals from the gamma-ray flux emitted by the targets, described in section 5.5, is written for the dSphs data combination as the product of the likelihoods of each target  $t$ :

$$\mathcal{L}(\langle\sigma_{ann}v\rangle; \nu | \mathcal{D}) = \prod_{t=1}^{N_{target}} \mathcal{L}_t(\langle\sigma_{ann}v\rangle; J_t, \mu_t | \mathcal{D}_t) \cdot \mathcal{J}(J_t | J_{obs,t}, \sigma_{J,t}). \quad (9.1)$$

This function is implemented in the gLike tool, where a NFW profile for the DM density of the source and the DM annihilation model of Cirelli et al. [162] have been adopted. The uncertainty in the ON/OFF normalization of 1.5%, that takes into account the limited acceptance of the telescopes' cameras, has been included as nuisance parameter in the likelihood, and the number of energy bins  $n$  has been left free to set.

For this analysis,  $n = 20$  bins were used for each data sample, and DM masses from 100 GeV to 100 TeV were chosen as interval to be tested for the annihilation study. Only positive values of the  $\langle\sigma_{ann}v\rangle$  estimator have been considered. The results in the velocity-averaged cross-section  $\langle\sigma_{ann}v\rangle$  of WIMP annihilation in the channels  $b\bar{b}$ ,  $t\bar{t}$ ,  $e^+e^-$ ,  $\mu^+\mu^-$ ,  $\tau^+\tau^-$ ,  $W^+W^-$ ,  $ZZ$ ,  $hh$  and  $\gamma\gamma$ , obtained from the combination of the data of the four dSphs presented in section 9.1, are presented in Figs. 9.3 to 9.7. For all the annihilation channels, no hints of DM signals have been found, and only ULs on  $\langle\sigma_{ann}v\rangle$  could be set. The 95% CL ULs are presented as a black solid line in the figures, together with the 68%

and 95% containment bands, obtained from 300 simulations. The median of the simulations is shown as a blue dashed line in the center of the bands. The thermal relic cross section has been plotted in all the figures, to allow comparing the limits obtained to the value of the cross-section that should be reached in order to exclude definitively WIMP DM at particular DM masses. Special considerations should be made for the case of the  $\gamma\gamma$  annihilation channel (see Fig. 9.7), for which the thermal relic cross-section is multiplied by a factor  $\alpha^2$  as described in [246], where  $\alpha$  is the fine structure constant, in order to consider the direct production of gamma-lines, without passing through intermediate sub-products.

The most constraining numerical values of the ULs on  $\langle\sigma_{ann}v\rangle$  for WIMP DM annihilation are reported in Tab. 9.2, together with the WIMP mass at which they apply.

**Table 9.2:** List of the most constraining ULs on  $\langle\sigma_{ann}v\rangle$  for the nine annihilation channels considered in this work. Each UL is associated with the respective WIMP mass.

Channel	DM particle mass [GeV]	$\langle\sigma_{ann}v\rangle_{UL}$ [ $\text{cm}^3/\text{s}$ ]
$b\bar{b}$	2000	$5.41 \times 10^{-24}$
$t\bar{t}$	2000	$7.91 \times 10^{-24}$
$e^+e^-$	500	$2.16 \times 10^{-24}$
$\mu^+\mu^-$	500	$3.46 \times 10^{-24}$
$\tau^+\tau^-$	700	$9.78 \times 10^{-25}$
$W^+W^-$	700	$3.72 \times 10^{-24}$
$ZZ$	1500	$5.04 \times 10^{-24}$
$hh$	2000	$6.73 \times 10^{-24}$
$\gamma\gamma$	200	$1.78 \times 10^{-26}$

Even if the limits are not shallow at these values, but rather present wide plane exclusion curves for all the DM masses considered, the table has been created to highlight the order of magnitude of the limits obtained. The annihilation channels which decay cascades present a majority of leptons, such as  $\tau^+\tau^-$  and  $e^+e^-$ , show more constraining ULs with respect to the ones with mostly hadronic decay cascades, like the  $b\bar{b}$  and  $t\bar{t}$  annihilation channels. This behaviour is well known for exclusion limits obtained with Cherenkov telescopes, because the flux of gamma photons is higher in the case of leptonic products, as visible in the spectra shown, e.g. in [247] and in [162].

The limits obtained from the combination of the four data samples described in section 9.1, as foreseen, improve the ULs obtained from the single dSphs, of a factor depending on the hours of observation available, on the  $J$ -factor and on its uncertainty. In the best case scenario, the Segue 1 limit, the combined limit is at least a factor 2 better around TeV DM masses, as shown in Figs. 9.8 to 9.12. This result is compatible with the predictions made regarding the improvement of the ULs with increasing the data sample.

The target-related uncertainties are also distributed. In fact, if adopting different  $J$ -factor values, that reflect those in an indirect way, the combined

ULs result to be compatible between each other, as visible in Fig. 9.13, where the  $J$ -factors taken from [119, 229, 230] and [244] have been considered.

As a final remark of this work, it is worth to compare the ULs on  $\langle\sigma_{ann}v\rangle$  for WIMPs, obtained in this analysis for the different annihilation channels, with the ULs obtained by other experiments testing similar ranges of WIMP DM masses. The results of Fermi-LAT analysing six years of data of 25 dSphs [245], of H.E.S.S. with 90 h of Sagittarius dSph [248], of VERITAS with 216 h of four dSph data [92] and of HAWC with 1038 d of 15 dSph data [249] are reported in Fig. 9.14, for the  $b\bar{b}$  and  $\tau^+\tau^-$  annihilation channels and as a function of the DM masses considered in this work, together with the MAGIC ULs on 354 h of dSph data of this work.

Being optimized for gamma ray energies in the range 20 MeV-300 GeV, thus more sensitive to low DM masses, Fermi-LAT dominates the limits, in both annihilation channels, up to TeV/tens of TeV DM masses. On the other hand, the HAWC limits dominate for masses above 100 GeV, or tens of TeV in the case of the  $\tau^+\tau^-$  annihilation channel. Between the two mass ranges, the MAGIC ULs obtained with dSphs data are the most constrainings, of a factor of a few better than the ones from other IACTs.

### 9.3 Conclusions and outlook

The MAGIC collaboration has performed indirect searches on WIMP DM since the first light of its telescopes, ranging over different types of DM dominated objects in the MW and outside. Among them, galaxy clusters [250], dark matter anisotropies, dwarf spheroidal satellite galaxies, the Galactic Center and the Galactic halo [251] can be named. Depending on the morphology of the target, searches for signals of DM from annihilation processes are more or less preferred with respect to studies of decay processes. Compact objects, like dSphs, have been investigated mainly to search for annihilating DM particles, given the quadratic dependence of the annihilation cross-section on the DM density. On the other hand, more extended objects, such as galaxy clusters, are preferred for decay studies, as in that case, the dependence on the density is linear.

The DM content of each target can be described by the multiplication of a particle physics factor and of an astrophysical (or  $J$ -) factor, as described in chapter 5. The former is completely defined by the theoretical model adopted to characterize the DM particle, while the latter depends on the density profile of the source and on its distance, thus changing for each source, on the contrary of the other factor. This dependence is of utmost importance, as it can give rise to unquantifiable target-related uncertainties, more than the statistical and systematic ones, coming from the density computation. The lack of knowledge of some binary star systems or, in general, massive objects, possibly modifying the star velocity dispersion profiles, from which the DM density is calculated, and the underestimated or overestimated distances of the targets are the main source of this systematic uncertainty.

The only possible way of, not avoiding but, distributing biases on the estimation of the DM profile is to carry on and combining an analysis on different targets of the same type or different types of targets.

Starting from 2011, the MAGIC collaboration performed observations of dSphs

in stereo mode, to look for DM annihilation signatures. These targets are very common among IACTs, given their vicinity (less than few tens of kpc away), their low, or null, astrophysical background, but, most of all, their highest M/L ratio (up to  $\sim 4000 M_{\odot}/L_{\odot}$ ) in the Universe. Given the possible target-related uncertainties, starting from the observation of UMaII in 2016, an observation diversification approach was adopted, even if, officially, the diversification strategy started in 2018 with a dSphs multi-year program.

On this ground, the dSphs with the highest  $J$ -factors in the northern hemisphere, following a ranking of dSphs on the base of [119], confirmed by the consistency of the uncertainties presented with the independent analyses of [229], [230] and [244], have been selected for the observations. After Segue 1 [164] and UMaII [157], Draco and Coma Berenices dSphs were observed. No hint of signals have been detected from these dSphs and only ULs at the 95% CL could be set, as reported in chapters 7 and 8. Despite the robustness of the  $J$ -factor estimate of these targets, and given the lower  $J$ -factor values with respect to the ones of Segue 1 and UMaII, no improvement of the previous limits could be achieved.

In the same way, the diversification of the observational targets, adopted to enlarge the pool of dSphs observed by MAGIC and to reduce systematics due to the uncertainties of the individual  $J$ -factors, achieved its goal with a joint analysis of the four dSphs mentioned, providing the best limits on DM models at TeV scales. The most constraining values on the velocity averaged cross-section from the annihilation of WIMP DM in the  $b\bar{b}$  and  $\tau^+\tau^-$  obtained are  $\langle\sigma_{ann}v\rangle_{b\bar{b}} = 5.41 \times 10^{-24} \text{ cm}^3/\text{s}$  and  $\langle\sigma_{ann}v\rangle_{\tau^+\tau^-} = 9.78 \times 10^{-25} \text{ cm}^3/\text{s}$ , for DM masses of 2 TeV and 0.7 TeV, respectively. These limits improve the ones obtained up to now by the MAGIC collaboration and are the most constraining among the other gamma-ray experiments in the range 10-100 TeV WIMP masses. The results obtained, soon published also in a paper of the collaboration, represents the MAGIC legacy for WIMP DM searches in dSphs.

The data collected within this diversification strategy, more than for the limits obtained by a single experiment, would also be of importance for the ongoing global effort [252] to produce the most sensitive results on DM searches in the range between  $\sim 10$  GeV and  $\sim 100$  TeV, through the combination of data acquired by gamma-ray instruments: the Cherenkov telescopes MAGIC, VERITAS and H.E.S.S., the Fermi-LAT satellite and HAWC water Cherenkov detector.

In addition, over the past years, several new suitable dSph candidates have been discovered (and will likely continue to appear in the near future) by means of deep on-going and future optical surveys, such as DES [253, 254], Pan-STARRS [255], GAIA [256, 257], and LSST [258], that will offer more margin to spread observations over more DM targets and enhance the pool of dSphs for data combination. This may give a chance of a positive detection, before CTA [259, 260] will be fully operating. The sensitivity of CTA will improve the measurements on the gamma-ray flux with respect to the MAGIC telescopes, and will be optimized for energies slightly higher than the ones of MAGIC. However, this will not bring a significant lowering on the WIMP velocity-averaged cross-section upper limits from dSphs, but will greatly improve the current results on DM studies in galaxy clusters and the Galactic Center [10], detecting or definitively ruling out WIMP DM.

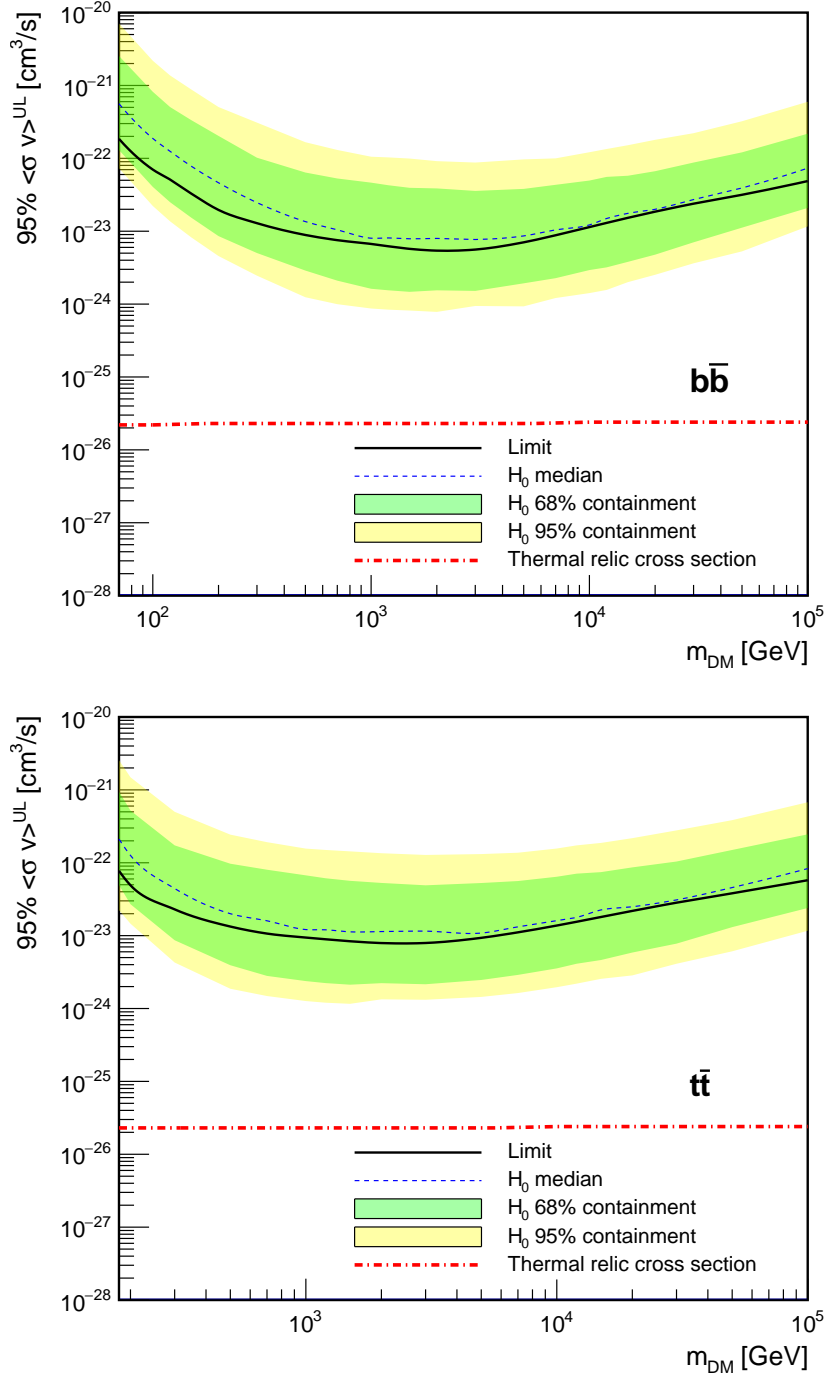


**Figure 9.3:** MAGIC ULs on  $\langle \sigma_{ann} v \rangle$  (solid black lines), for the  $b\bar{b}$  and  $t\bar{t}$  annihilation channels, obtained through the combination of the results of Draco, Coma Berenices, Ursa Major II [157] and Segue 1 [164]. The 68% (green) and 95% (yellow) containment bands and the median of the simulations (blue dashed line) are also shown. The comparison with the thermal relic cross-section [51] is reported in both plots (red dashed line).

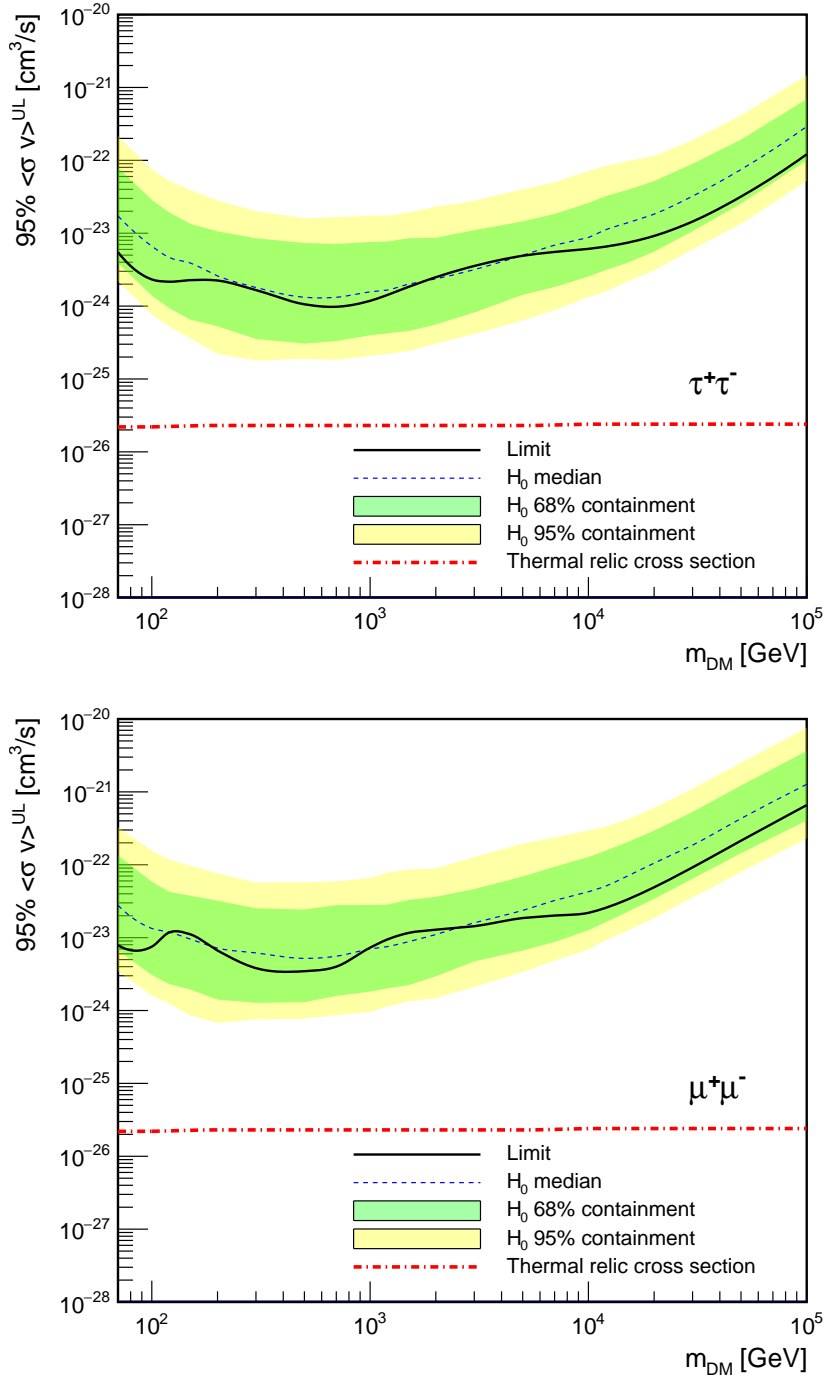


**Figure 9.4:** MAGIC ULs on  $\langle \sigma_{ann} v \rangle$  (solid black lines), for the  $\tau^+\tau^-$  and  $\mu^+\mu^-$  annihilation channels, obtained through the combination of the results of Draco, Coma Berenices, Ursa Major II [157] and Segue 1 [164]. The 68% (green) and 95% (yellow) containment bands and the median of the simulations (blue dashed line) are also shown. The comparison with the thermal relic cross-section [51] is reported in both plots (red dashed line).

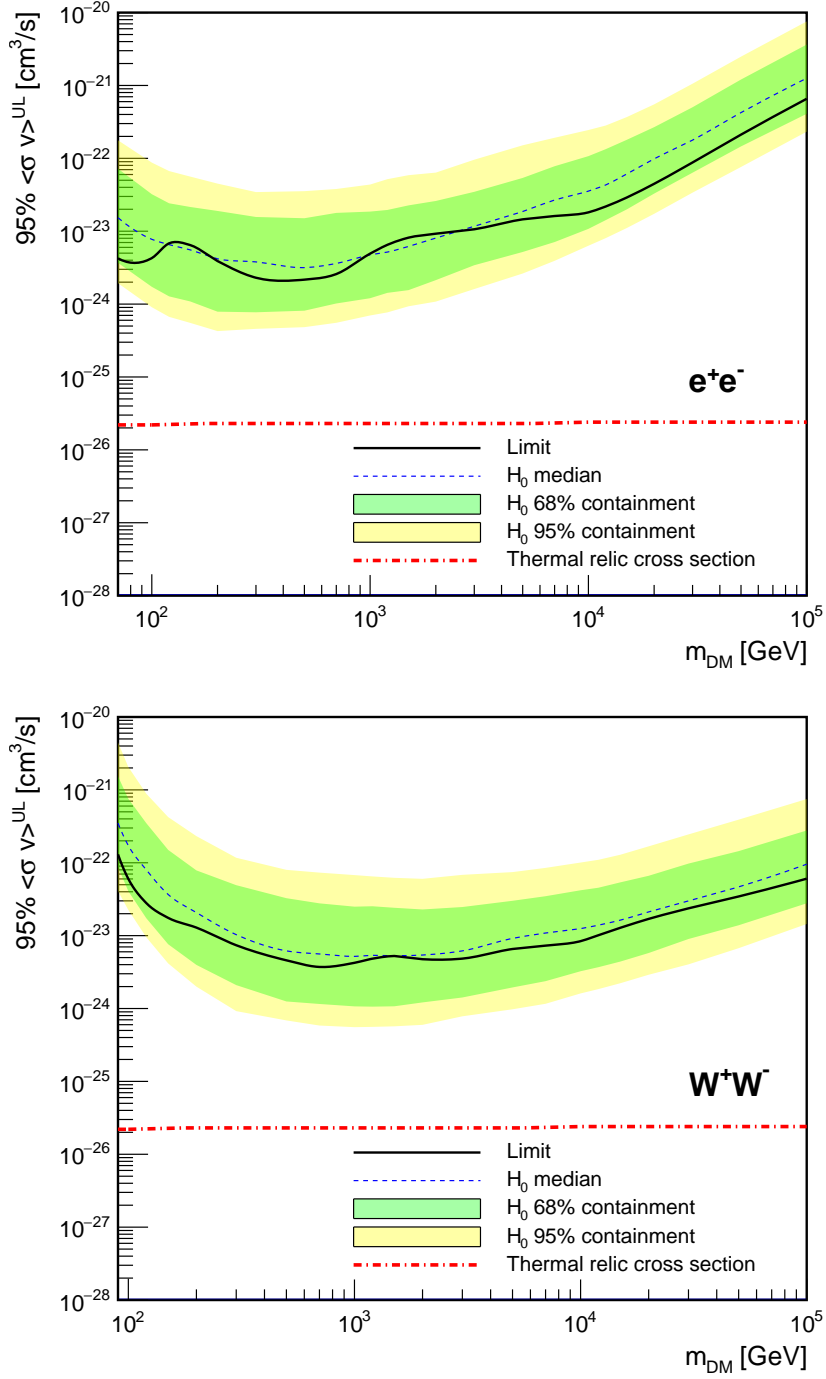


**Figure 9.5:** MAGIC ULs on  $\langle \sigma_{ann} v \rangle$  (solid black lines), for the  $e^+e^-$  and  $W^+W^-$  annihilation channels, obtained through the combination of the results of Draco, Coma Berenices, Ursa Major II [157] and Segue 1 [164]. The 68% (green) and 95% (yellow) containment bands and the median of the simulations (blue dashed line) are also shown. The comparison with the thermal relic cross-section [51] is reported in both plots (red dashed line).

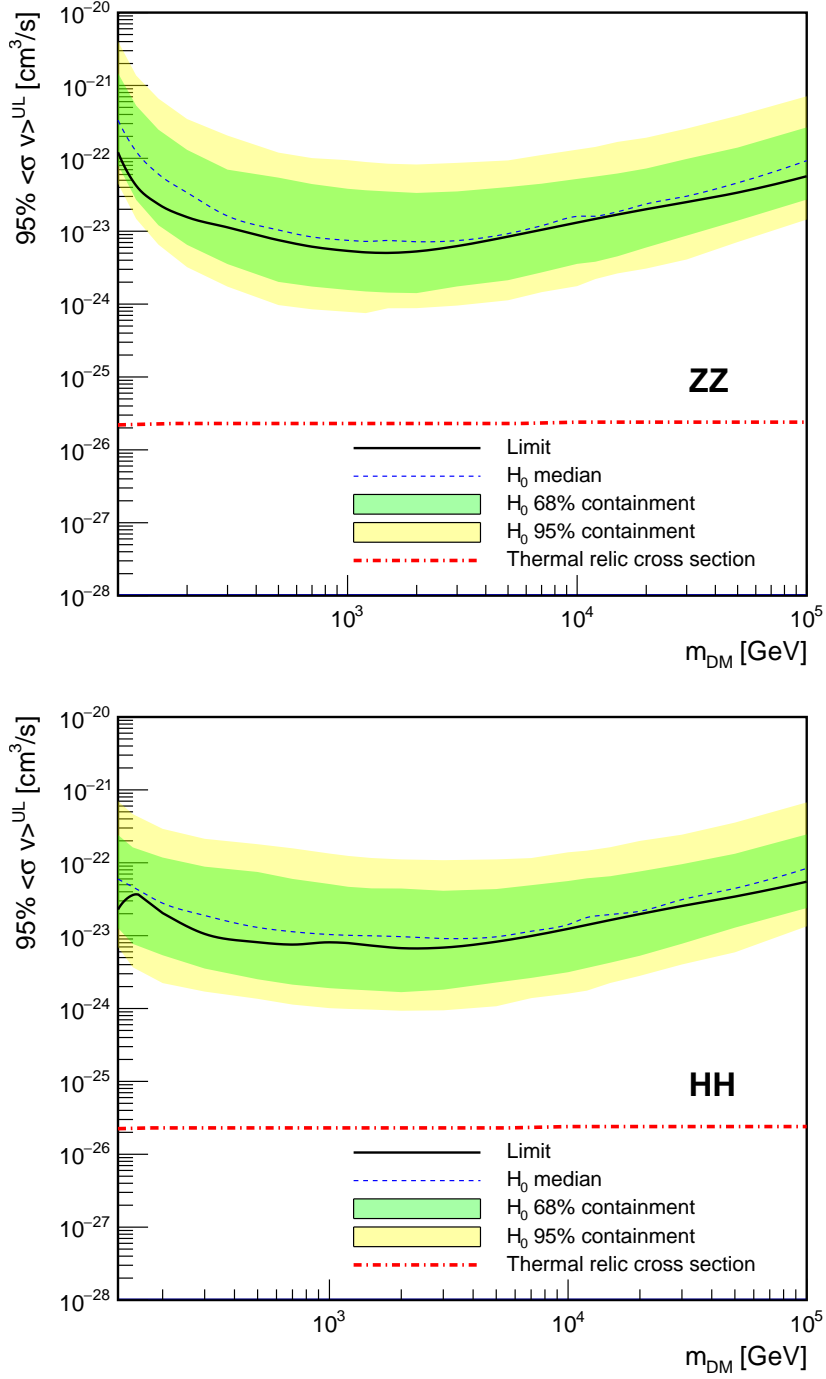


**Figure 9.6:** MAGIC ULs on  $\langle \sigma_{ann} v \rangle$  (solid black lines), for the  $ZZ$  and  $HH$  annihilation channels, obtained through the combination of the results of Draco, Coma Berenices, Ursa Major II [157] and Segue 1 [164]. The 68% (green) and 95% (yellow) containment bands and the median of the simulations (blue dashed line) are also shown. The comparison with the thermal relic cross-section [51] is reported in both plots (red dashed line).

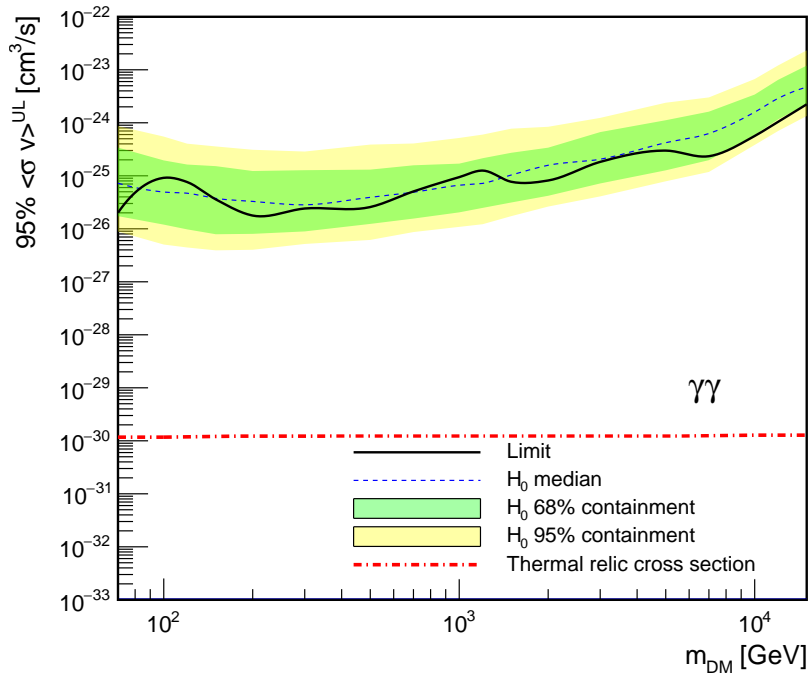


**Figure 9.7:** MAGIC ULs on  $\langle \sigma_{ann} v \rangle$  (solid black lines), for the  $\gamma\gamma$  annihilation channel, obtained through the combination of the results of Draco, Coma Berenices, Ursa Major II [157] and Segue 1 (see section 9.1.1). The 68% (green) and 95% (yellow) containment bands and the median of the simulations (blue dashed line) are also shown. The thermal relic cross-section [51] reported (red dashed line) for this annihilation channel has been multiplied by a factor  $\alpha^2$ , as described in [246], where  $\alpha$  is the fine structure constant.

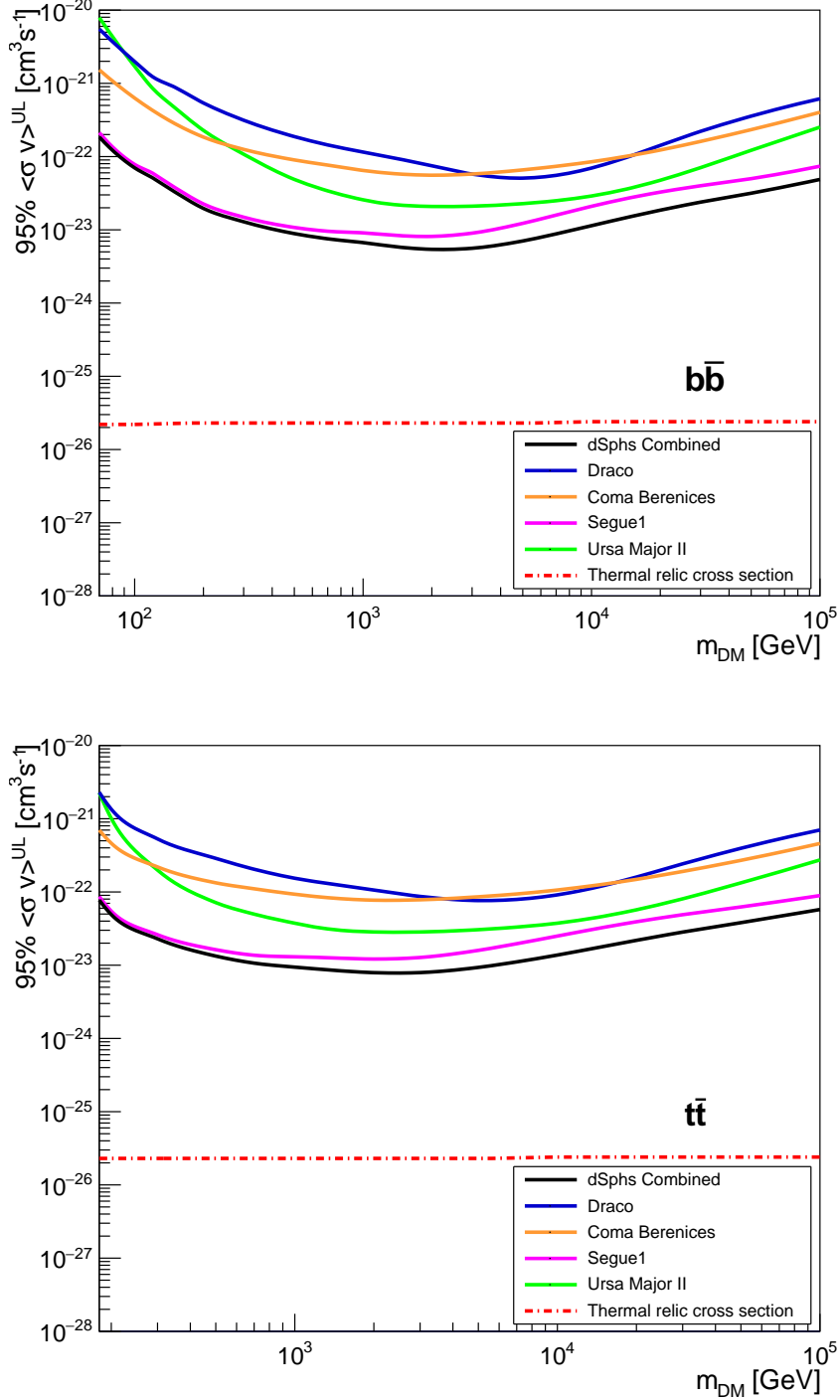


**Figure 9.8:** Velocity-averaged cross-section ULs, for the  $b\bar{b}$  (top) and  $t\bar{t}$  (bottom) annihilation channels, obtained by the MAGIC Collaboration for each single dSph taken into account in the present paper. The blue lines are the results of Draco dSph analysis, the orange lines of Coma Berenices dSph analysis, the magenta lines of Segue 1 (see section 9.1.1), the green lines of Ursa Major II [157] and the black line the combined limit of all four dSphs. The comparison with the thermal relic cross-section [51] is reported in both plots (red dashed line).

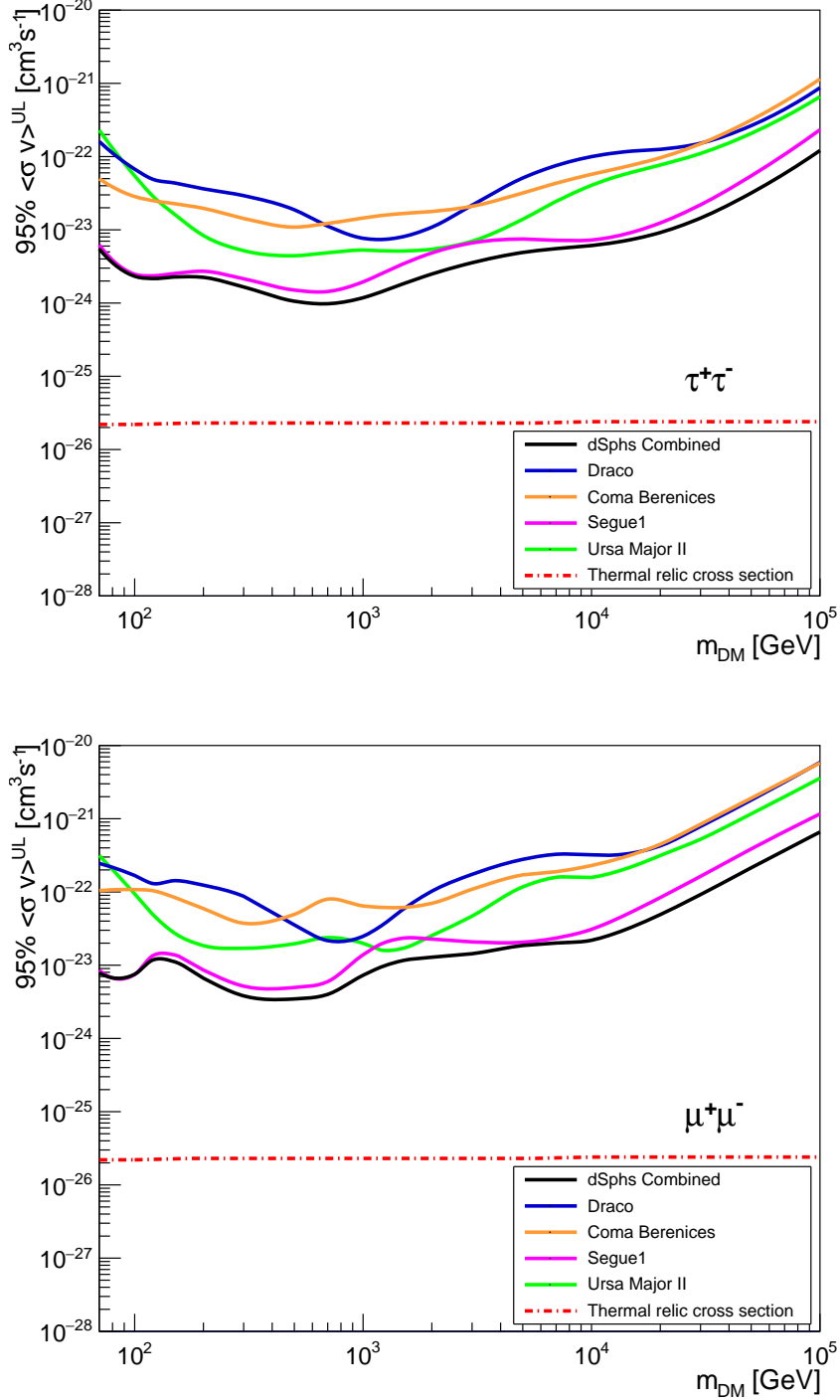


**Figure 9.9:** Velocity-averaged cross-section ULs, for the  $\tau^+\tau^-$  (top) and  $\mu^+\mu^-$  (bottom) annihilation channels, obtained by the MAGIC Collaboration for each single dSph taken into account in the present paper. The blue lines are the results of Draco dSph analysis, the orange lines of Coma Berenices dSph analysis, the magenta lines of Segue 1 (see section 9.1.1), the green lines of Ursa Major II [157] and the black line the combined limit of all four dSphs. The comparison with the thermal relic cross-section [51] is reported in both plots (red dashed line).

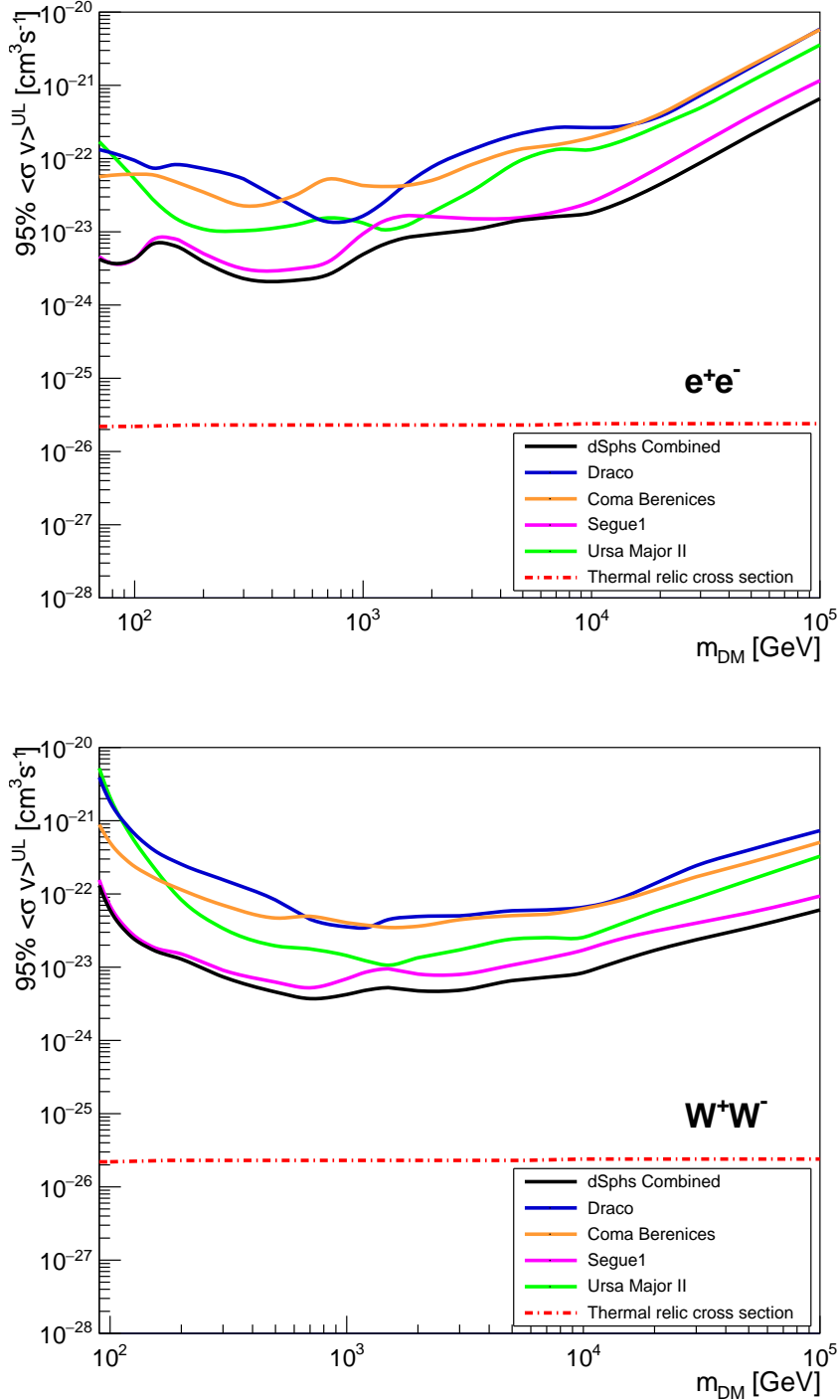


**Figure 9.10:** Velocity-averaged cross-section ULs, for the  $e^+e^-$  (top) and  $W^+W^-$  (bottom) annihilation channels, obtained by the MAGIC Collaboration for each single dSph taken into account in the present paper. The blue lines are the results of Draco dSph analysis, the orange lines of Coma Berenices dSph analysis, the magenta lines of Segue 1 (see section 9.1.1), the green lines of Ursa Major II [157] and the black line the combined limit of all four dSphs. The comparison with the thermal relic cross-section [51] is reported in both plots (red dashed line).

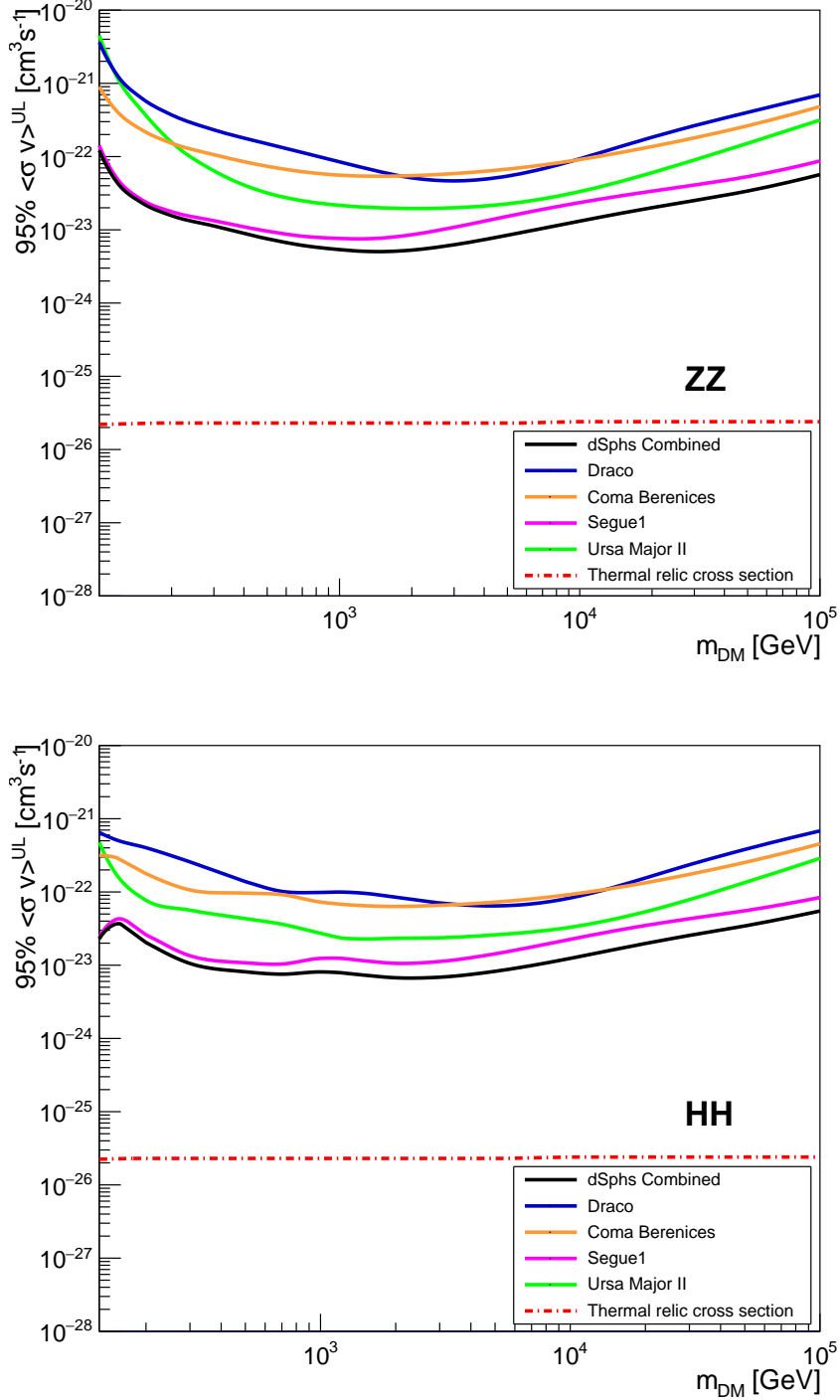


**Figure 9.11:** Velocity-averaged cross-section ULs, for the  $ZZ$  (top) and  $HH$  (bottom) annihilation channels, obtained by the MAGIC Collaboration for each single dSph taken into account in the present paper. The blue lines are the results of Draco dSph analysis, the orange lines of Coma Berenices dSph analysis, the magenta lines of Segue 1 (see section 9.1.1), the green lines of Ursa Major II [157] and the black line the combined limit of all four dSphs. The comparison with the thermal relic cross-section [51] is reported in both plots (red dashed line).

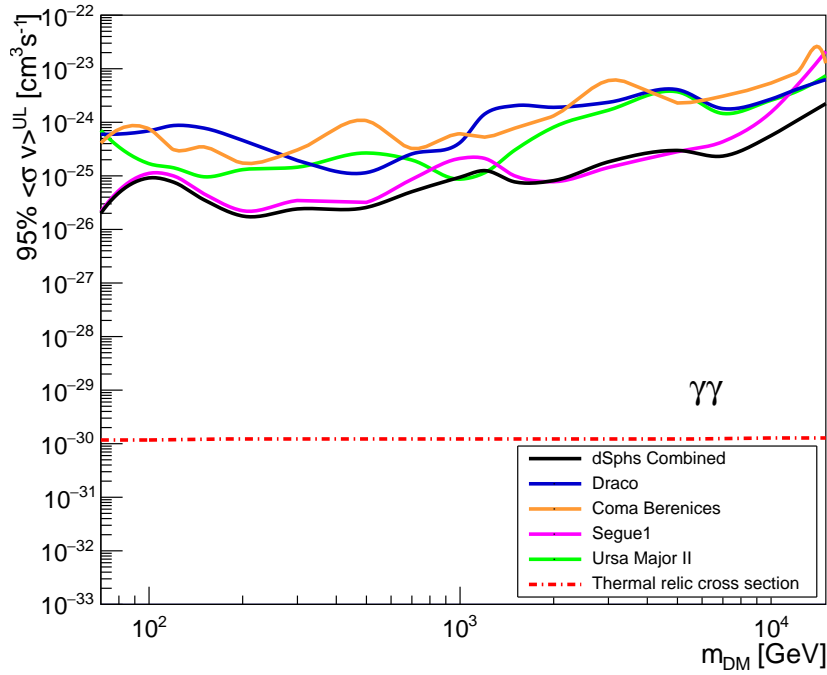


**Figure 9.12:** Velocity-averaged cross-section ULs, for the  $\gamma\gamma$  annihilation channel, obtained by the MAGIC Collaboration for each single dSph taken into account in the present paper. The blue lines are the results of Draco dSph analysis, the orange lines of Coma Berenices dSph analysis, the magenta lines of Segue 1 (see section 9.1.1), the green lines of Ursa Major II [157] and the black line the combined limit of all four dSphs. The thermal relic cross-section [51] reported (red dashed line) for this annihilation channel has been multiplied by a factor  $\alpha^2$ , as described in [246], where  $\alpha$  is the fine structure constant.

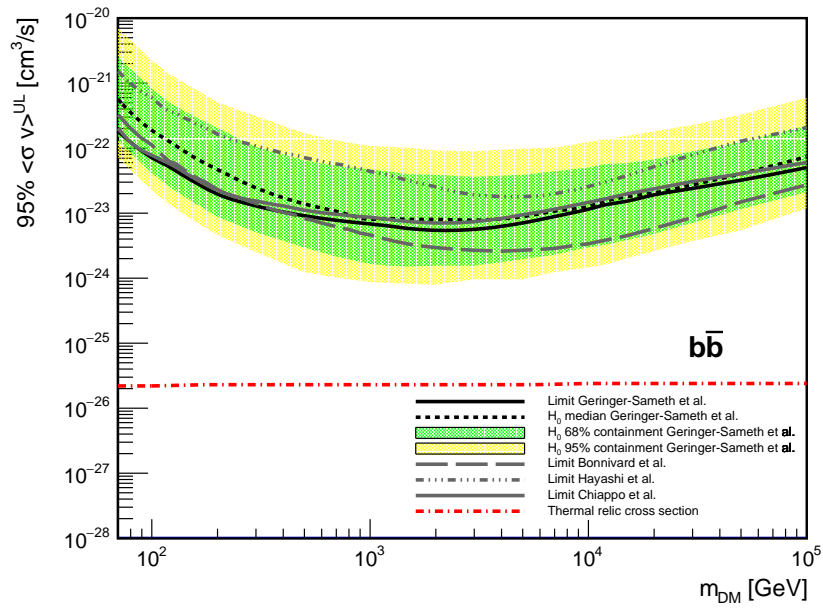


**Figure 9.13:** 95% CL combined ULs on the  $\langle \sigma_{ann} v \rangle$  of WIMP DM annihilating in the  $b\bar{b}$  annihilation channel calculated using the  $J$ -factors values presented in [229] (grey dashed line), in [230] (grey dash dot dot dot line), and in [244] (grey solid line) in comparison to the ULs estimated in this work and based on the Geringer-Sameth et al. [119]  $J$ -factors (black solid line). The thermal relic cross-section is also reported (dash dot red line).

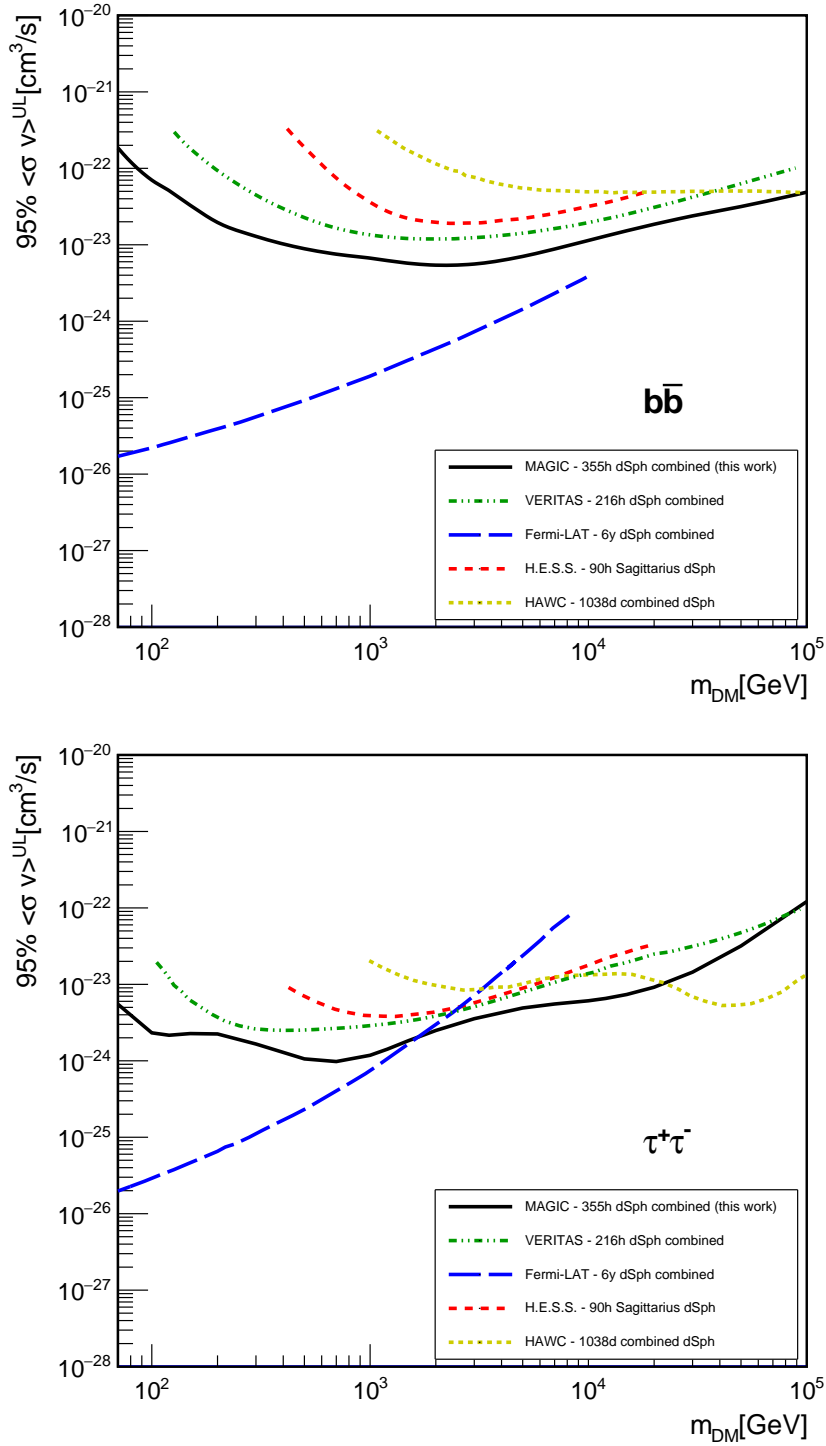


**Figure 9.14:** 95% CL combined UL on the  $\langle \sigma_{ann} v \rangle$  of WIMP DM annihilating in the  $b\bar{b}$  (top) and  $\tau^+\tau^-$  (bottom) annihilation channels by VERITAS (in green), Fermi-LAT (in blue), H.E.S.S. (in red) and HAWC (in yellow), in comparison to the UL estimated in this work (in black).

## Part II

# The Barcelona Raman LIDAR for the Cherenkov Telescope Array

## Chapter 10

# Atmospheric Characterization for the Cherenkov Telescope Array

The Earth's atmosphere is the fundamental medium that permits to detect gamma rays with Cherenkov telescopes. After having travelled to the Earth and interacted with the particles that compose the atmosphere, gamma rays create electromagnetic (EM) showers that can be detected by IACTs through the Cherenkov photons emitted. A reduced transmission of these photons, due to the presence of clouds or dust in the aerosol layer of the Earth's atmosphere, can worsen the signal that reaches the ground. This circumstance can affect the measurements in different ways [261]:

- due to a change of the refractive index of the air, it can alter the number of Cherenkov photons produced in the shower;
- it can dim the camera images because of *Rayleigh*, and rarely *Mie*, *scattering* of the Cherenkov photons, that are scattered out of the telescope Field-of-View (FoV);
- it can blur the image, or create a halo around it, as a consequence of a scattering of light enhanced in forward direction, dependent on the size of the aerosol particles.

Constant monitoring of the quality of the atmosphere is, hence, mandatory in order to obtain good quality data to analyse and reduce the atmosphere-related systematic uncertainty associated to the photon flux and reconstructed shower energies.

Characterization of the atmosphere at the altitude of interest for IACTs, i.e. in the *troposphere* and lower *stratosphere*, can be performed by different active remote sensing techniques. The instrument that fits best in this scenario is the **LIDAR (Light Imaging Detection and Ranging)**. Thanks to its pulsed laser, a reflective surface and a detection system to collect and characterize the signal, as a function of light travel time, it can accurately describe the structure, composition and dynamics of the atmosphere.

The evolution from an array of few Cherenkov telescopes, like MAGIC (mainly limited by statistics), to an observatory of Cherenkov telescopes such as the Cherenkov Telescope Array (CTA, primarily limited by systematics) have created the need for advanced instruments for atmospheric monitoring. The lower systematic uncertainties required for observations with the new array of telescopes lead to the need for accurate extinction profiles, best obtained with Raman LIDARs.

After an introduction to the fundamentals of the LIDAR technique, a description of the CTA atmospheric monitoring plan follows. The chapter will end with a description of the Barcelona Raman LIDAR prototype, accepted by CTA as a pathfinder project.

## 10.1 Light Detection And Remote sensing systems

LIDARs are widely used instruments in atmospheric research, as they can provide range-resolved measurements of the atmospheric constituents: molecules (air gases like oxygen and nitrogen) and aerosols (liquid and solid air pollution particles). They provide the possibility to derive optical characteristics of the particles. In the particular case of IACTs, of major interest is the extinction coefficient from which the transmission profile of the incoming Cherenkov light can be estimated.

LIDAR systems are composed of three main parts: a powerful pulsed laser, a mirror to recollect the back-scattered light and an acquisition system, as shown in Fig. 10.1 for the case of a generic coaxial LIDAR.

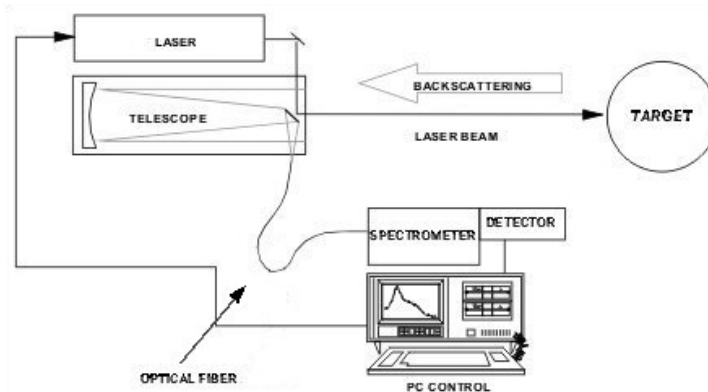


**Figure 10.1:** Scheme of a generic coaxial LIDAR system. Image taken from [262].

The light beam is emitted parallel to the telescope axis, recollected by the mirror and focused at the entrance of an optical fibre, which transfers the signal to a detection unit. A system of lenses, mirrors and filters select the different wavelengths and focus them to PMTs to transform the light pattern in electrical signals and to amplify them. The resulting signal, given by the initial laser light backscattered by air molecules and aerosols can be described

by Eq. 10.1, the so-called *LIDAR equation*:

$$P(R) = \frac{KO(R)}{R^2} \beta(R) T^2(R) . \quad (10.1)$$

The power  $P$  of the signal coming from a distance  $R$  is given by:

- the product of the LIDAR performance  $K$ , that encapsulates the telescope collection area, the receiver transmission and the detection efficiency;
- the geometry of the measurement  $O$ ;
- the backscatter coefficient  $\beta$ , for both air molecules and aerosols ( $\beta = \beta_{mol} + \beta_{aer}$ );
- the square of the transmission  $T$ , for both particles as in the previous case.

The last two factors contain all the information regarding the atmosphere. The last term is the one needed to understand the extinction of Cherenkov light. In the simplest case of an *elastic-backscatter* LIDAR, the power of the backscattered light can be written as [263]:

$$P(R) = \frac{E_0 A \eta_L}{R^2} O(R) \beta(R) \exp \left[ -2 \int_0^R \alpha(r) dr \right], \quad (10.2)$$

where  $E_0$  is the pulse energy of the laser,  $A$  is the effective mirror area and  $\eta_L$  the efficiency of the spectrometer and the detector. These three factors represent the LIDAR performance  $K$ . The factors  $O(R)$  and  $\beta(R)$  are the same of Eq. 10.1. The exponential indicates the transmission of the atmosphere, written as a function of the extinction coefficients,  $\alpha(R)$ .

In the case of an elastic-backscatter LIDAR, the particle extinction coefficient cannot be obtained from direct measurements, and only a combination of backscatter and extinction coefficient can be estimated (with an uncertainty of the order of 25% on the extinction coefficient). This comes from the fact that the system can measure only the combined atmospheric backscatter and extinction, without separating the different contributions of each. An example of an elastic-backscatter LIDAR is the one used by the MAGIC collaboration [155]. A more accurate type of LIDAR is the *Raman LIDAR*. Its principle of operation is based on the detection of the light that has suffered Raman scattering with molecules of the atmosphere (basically Nitrogen or Oxygen is used, but also water vapour) [264]. This light has suffered a wavelength shift that depends on the type of molecules.

Unlike the case of the elastic-backscatter LIDAR, this instrument presents an acquisition system of multiple detectors for the elastic and Raman lines, separately, allowing to take into account the wavelength-shifted Raman scattered return simultaneously with the elastic back-scattered one. Since the first depends only on the (known) backscatter efficiency abundance of  $N_2$  (or  $O_2$ ) as a function of altitude, the signal is only modified by the (molecular and particulate) extinction, which can be retrieved straightaway. This characteristic guarantees more precise information on the atmosphere with respect to the

elastic-only case and permits to evaluate accurately the extinction coefficient and its wavelength dependence, if several laser lines are used.

Eq. 10.2, for a Raman LIDAR channel, is now written as [265]:

$$P(R, \lambda_{Ra}) = \frac{E_0 \eta \lambda_{Ra}}{R^2} O(R) \beta_{Ra}(R, \lambda_0) \exp \left\{ - \int_0^R [\alpha(r, \lambda_0) + \alpha(r, \lambda_{Ra})] dr \right\}. \quad (10.3)$$

The power of the backscattered light presents now a dependence on the wavelength of the backscattered Raman line ( $\lambda_{Ra}$ ). The factor  $\eta$  is also written as a function of the Raman wavelength. The exponential factor now takes into account the extinction of light in the region between the LIDAR and the backscatter zone and on its way back, for the molecular and particulate extinction of light, after the Raman scattering has taken place. The backscatter coefficient  $\beta_{Ra}$  is the main difference with respect to the elastic LIDAR equation (Eq. 10.2). It represents only the Raman backscatter coefficient (of Nitrogen or Oxygen), that is known to great precision, if the density of Nitrogen/Oxygen molecules is well estimated. This is normally the case if standard radiosonde, or global data assimilation systems are employed.

The intensity of the Raman line is 3.5 – 4 orders of magnitude lower than the Rayleigh one [264]. It depends on the corresponding differential cross-section:

$$\beta_{Ra} = N_{Ra}(R) \frac{d\sigma_{Ra}}{d\Omega}(\pi, \lambda_0) \quad (10.4)$$

where  $N_{Ra}$  is the density number of molecules involved in the process and  $d\sigma_{Ra}(\pi, \lambda_0)/d\Omega$  the differential cross-section per integration angle  $\Omega$  as a function of the backscattering angle of  $180^\circ$  and the laser wavelength.

A Raman LIDAR with the characteristics described here is the one in construction for the CTA [266, 267], that will be presented in the following section.

Other types of LIDARs are available on the market and are mostly used for weather forecast purposes. An example is the high spectral resolution lidar (HSRL), that measures the differences present in the elastic-backscatter spectra of aerosol particles with respect to the air molecules due to Doppler shifts.

## 10.2 CTA atmospheric monitoring plans

The CTA observatory covers both hemispheres. The construction sites for the two arrays of telescopes have been fixed after accurate studies of the environmental and meteorological conditions (see [268]). The northern site, whose climatic and environmental characteristics were well known in advance as being the site of the MAGIC telescopes, offers an excellent area for CTA-N. Among the major advantages of the place, one can find low light pollution, restricted airspace (being inside the ORM), clean sky conditions and an optimal weather stability throughout the year. Moreover, the altitude of the site (at around 2200 m a.s.l.) ensures that the array is located well above the thermal inversion layer, leaving clouds and dust at lower heights. The southern array will also be located at one of the best places on Earth for ground based astronomy: the dry and isolated desert of Atacama, just 10 km from the Paranal Observatory.

Even being at the best sites on Earth for gamma-ray astrophysics, a continuous

characterization of the atmosphere is mandatory for IACTs.

The challenge undertaken by the CTA collaboration is to comply with a maximum systematic uncertainty on the reconstructed energy of 7-8% rms [269]. The latter is dominated by atmospheric uncertainties which alter the Cherenkov photon density at ground level. In addition to that, due to the short time-scale variations of the atmospheric conditions and in order not to affect the observations, a fast and frequent evaluation of the atmosphere is required. The regular monitoring of the status of the atmosphere will also be employed to select targets, increasing the efficiency of the use of the observation time thanks to online dynamic scheduling.

Different and complementary types of devices have been proposed, and some already installed, to fulfil with the prerequisites [270, 271]: a combination of a wide-angle optical telescope (FRAM [272]), to produce atmospheric extinction maps of the FoV using stellar photometry, and LIDARs characterize the observed FoV of CTA, both instruments being constantly cross-calibrated with a Sun/Moon photometer for each site and weather stations. To characterize the full sky, in turn, and take decisions about the viability of a next target observation, All-Sky Cameras (ASC) for stellar photometry and cloud detection, and ceilometers, detectors of night sky background are proposed in combination. Raman LIDARs are ideal to characterize the aerosol extinction profile along the line-of-sight of the observed target. The Barcelona Raman LIDAR [267], described in the next section, and the Raman LIDAR in construction at the Laboratoire Univers et Particules de Montpellier (LUPM) [266] are the ones proposed for the northern and southern site, respectively. In addition, aerosol climatology at both sites will be studied thanks to the ARCADE LIDAR [273]. Satellites and global data assimilation models (validated by a radiosonde campaign) will complement those measurements, in addition to information on the atmosphere obtained by the data using the Cherenkov Transparency Coefficient (CTC) method [274].

## 10.3 The Barcelona Raman LIDAR

### 10.3.1 The project and its design

Since the beginning of the CTA project, several institutes, part of the CTA Collaboration, started to design Raman LIDAR systems: the Institut de Física d'Altes Energies (IFAE), together with the Universitat Autònoma de Barcelona (Spain), the University of Padova (Italy) and, as new member, the University of Nova Gorica (Slovenia) have been developing the Barcelona Raman LIDAR, recently approved as pathfinder project for CTA-N; in parallel, the LUPM (Montpellier, France) is building a Raman LIDAR for CTA-S. Both Raman LIDARs were built in parallel and with the same starting point: the re-use of the previous CLUE experiment [275, 276] telescopes.

The Barcelona Raman LIDAR, that has been under construction for several years at the campus of the Universitat Autònoma de Barcelona, has been proposed in 2009 in order to fulfil the requirements imposed by CTA [277]:

- the aerosol transmission profile along the line-of-sight of CTA shall be monitored up to an altitude of 15 km a.s.l.;

- the profiling shall be possible for any direction within the Observable Sky of CTA, i.e. up to a range of 30 km at least;
- the aerosol transmission profile must have a range resolution of at least or better than 300 m;
- the aerosol transmission from any altitude (up to the maximum one) to ground shall be measured with an absolute accuracy better than 0.05;
- the wavelength dependency of aerosol transmission (Ångström exponent<sup>1</sup>) shall be monitored over the full altitude profile, for the wavelength range to which the CTA-N telescopes are sensitive;
- independent cross-checks for the measurement accuracy of the aerosol transmission profiles and maps must be made available to ensure a robust system;
- the Raman LIDAR shall be included in the Laser Traffic Control System operating at the ORM and always cede to the other telescopes in case of conflict.

Since the CTA telescopes will be blinded by a LIDAR producing laser pulses propagating into their FoV, the LIDAR shall permit to characterize one profile a few minutes before and after a CTA *observation block*, or during a change of wobble position. In the latter case, the LIDAR measurement must be accomplished after one minute of data taking. These characteristics cannot be found in a commercial LIDAR. Thus, the Barcelona Raman LIDAR is an innovation in the LIDAR field, optimized for Cherenkov telescopes' atmosphere monitoring.

A main ingredient of the Barcelona Raman LIDAR is the use of one of the previous Cherenkov Light Ultraviolet Experiment (CLUE) containers and telescopes and their adaptation to a performing LIDAR system. The CLUE experiment was an Italian cosmic-rays detector array installed at the ORM, composed of 8 Cherenkov telescopes in the UV energy band. After being dismantled 15 years ago, many of the containers were kept alive and three of them were purchased by the University of Pisa (Italy) and sold to IFAE (two of them) and LUPM in a second round. One main characteristic of CLUE telescopes is the container design: it permits the enclosure of a relatively large LIDAR system into a maritime container that can be opened sideways (thanks to motors and actuators, operating remotely or through a handheld control). The container doors do not shadow the telescopes Fov when opened at maximum. The second key characteristic is the telescope placed inside: a mechanized alt-azimuth mount telescope with a parabolic mirror of 1.8 m diameter and  $f/D = 1$ . Fig. 10.2 shows a current picture of the container with the complete Barcelona Raman LIDAR system installed.

In order to fulfil with all the requirements for CTA-N, the Barcelona Raman LIDAR followed particular design choices. A powerful laser emits the beam co-axially to the main mirror, thanks to two small dichroic guiding mirrors.

---

<sup>1</sup>This exponent is the parameter  $y$  appearing in the equation  $\alpha_1/\alpha_2 = (\lambda_1/\lambda_2)^{-y}$ , where  $\alpha_1$  and  $\alpha_2$  are the extinction coefficients respectively related to the wavelengths  $\lambda_1$  and  $\lambda_2$ .



**Figure 10.2:** Picture of the opened Barcelona Raman LIDAR container with the LIDAR system mounted.

The light, scattered by the atmospheric particles, is then collected by the main mirror and focused on the entrance of a 8 mm liquid light guide. The latter transmits the light to the back part of the telescope, where an in-house made polychromator selects the different wavelengths (elastic and Raman back-scattered) and acquires the signal through 4 PMTs connected to an external acquisition unit.

Fig. 10.3 reports a scheme of the Barcelona Raman LIDAR (in this case, only a pair of acquisition channels is shown).

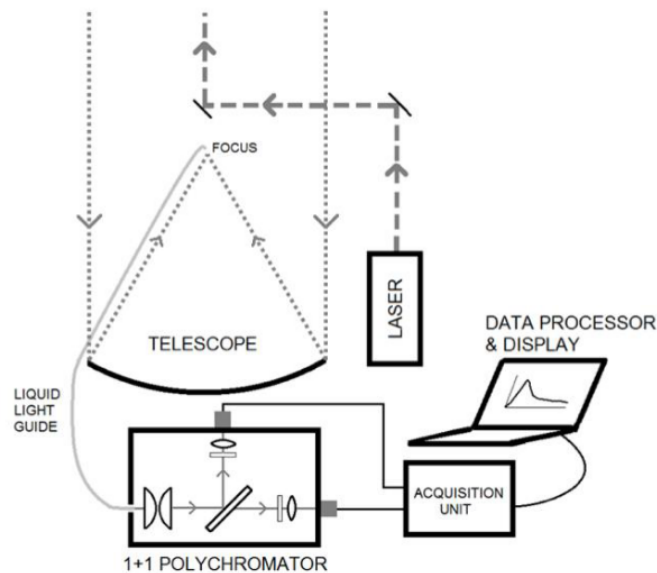


**Figure 10.3:** Sketch of the key design choices of the Barcelona Raman LIDAR.

All design choices and components will be described in detail in the next subsections.

### 10.3.2 The telescope structure

The former CLUE telescopes were built with a Cassegrain configuration, with a hole for the detector in the center of the primary mirror. For the case of the Barcelona Raman LIDAR, instead, a modified Newton solution<sup>2</sup> has been adopted for the telescope structure. The reason for this choice comes from the fact that with any kind of Cassegrain design the FoV would have been too small, and with problems of obscuration, caused by the secondary mirror. Limitations in the depth of field have been mitigated by installing the liquid light guide a bit farther than the focal distance (1806 mm instead of 1800 mm) where signals from 300 m and 20 km are contained in a circle smaller than 6 mm.

The Barcelona Raman LIDAR presents a co-axial structure, for which the laser beam is coincident with the telescope's optical axis. A bi-axial design could have also been possible. Even if easier to produce, without steering optics to guide the laser beam to the optical axis, it would have had the disadvantage of a higher range of full overlap distance.

The range of full overlap between the laser beam and the telescope's FoV determines the minimum range above which the atmosphere can be sensed. The minimum height at which the full overlap starts determines the lowest atmospheric layer that can be characterized. Below that distance, the measurement can still be done, but it has to be corrected [278]; however the correction becomes increasingly noisier at lower altitudes of full overlap.

The range of full overlap  $R$  can be approximated through the following equation [279, 280]:

$$R \approx \frac{2x + D + d}{p/f - \theta - 2\alpha} \quad (10.5)$$

where  $x$  is the distance between the laser and the telescope optical axis,  $D$  is the diameter of the mirror,  $d$  the receiver aperture (in our case, the size of the PSF at the focal plane),  $p/f$  the fraction of the pinhole diameter with respect to the focal length (the FoV of the telescope, that in our case is 4.4 mrad with a PSF of 6 mm),  $\theta$  the opening angle of the laser beam and  $\alpha$  is a possible angle of misalignment between the receiver and the transmitter optical axis. Substituting the parameters  $f = 1.8$  m,  $d = 6$  mm diameter,  $\theta = 0.5$  mrad and  $p = 8$  cm ( $\alpha$  has been considered 0), the range of full overlap becomes 400 m in the case of bi-axiality and 160 m in case of co-axiality. In both cases, it has to be taken into account that even with  $x = 0$  m,  $R$  can not be 0, due to the confusion circle of the source image, that becomes big at small distances if the telescope is focused at  $r$  close to infinity.

In order to increase sensitivity to even lower distances, the Raman LIDAR has been equipped with additional near-range optics that permit to determine the full ground layer transmission reliably.

As shown in Fig. 10.4, the near-range is a mini-telescope composed of a parabolic mirror used to focus the back-scattered light to an optical fibre, that transmits the signal to a PMT. With only the use of the elastic channel, the full overlap

<sup>2</sup>The secondary mirror is not used.

is already reached at 30 m, consistent with the theoretical expectation [279].



**Figure 10.4:** Components of the near-range system. (a) is the parabolic mirror, (b) the support to mount the mirror on the telescope structure and (c) the optic fibre. Credits to [281].

On the other side, with this LIDAR system the atmosphere can be monitored up to the end of the stratosphere, at least when pointing towards the zenith, reaching around 30 km distance.

### 10.3.3 The laser and used wavelengths



**Figure 10.5:** Picture of the Nd:YAG pulsed 1064 nm laser of type Brilliant showing the main laser body and the two harmonics dismountable generators. Image taken from [282].

A Nd:YAG pulsed 1064 nm laser of type Brilliant (Fig. 10.5), made by the company *Quantel*<sup>3</sup> (now discontinued) is mounted on a *XY*-motorized support (used for alignment) in parallel to the optical axis of the main mirror. Thanks to two harmonic dismountable generators, it can emit at three wavelengths: the base line at 1064 nm, its second harmonic at 532 nm and a third harmonic at 355 nm. The frequency of the emitted pulse is 10 Hz and its amplitude at the correct temperature of operation ( $\sim 34^\circ\text{C}$ ) is 6 mm, with a nominal beam divergence of 0.5 mrad.

A fundamental characteristic of the Barcelona Raman LIDAR is the choice of the wavelength of the signal emitted by the laser. The wavelength of major interest is the one that approximates most the wavelength interval in which the CTA telescopes are most sensitive to Cherenkov light, i.e. in the range

<sup>3</sup>[www.quantel-laser.com/home.html](http://www.quantel-laser.com/home.html)

300-400 nm. As scattering by Nitrogen molecules is the one considered for this LIDAR, the Raman back-scattered wavelength is 387 nm. Using exclusively these two wavelengths would be sufficient to evaluate the extinction coefficient as described in section 10.1. The addition of the 532 nm wavelength, with the Raman back-scattered one at 607 nm allows the reconstruction of the Å ngström exponent (giving the dependency of the extinction parameters on wavelength). The wavelength of 1064 nm is completely removed by the couple of dichroic mirrors, as described below.

The inclusion of further lines like CO<sub>2</sub>, water vapour, additional elastic and Raman channels would have improved the precision and accuracy of the results, but at the expense of an increased complexity of the system.

### 10.3.4 The mirrors

Two dichroic guiding mirrors are mounted on metallic supports and used to shift the laser beam to the optical axis of the telescope. An important aspect of these mirrors is their transmission. As visible in Fig. 10.6, wavelengths around 355 nm and 532 nm are completely reflected, whereas wavelengths in between and in the infrared band are mostly transmitted. This helps in the elimination of the 1064 nm signal, thanks to the absorption by the dichroic mirror system, and guarantees perfect reflection of the desired wavelengths. This measure is important to protect the liquid light guide against strong infrared light that can damage it.

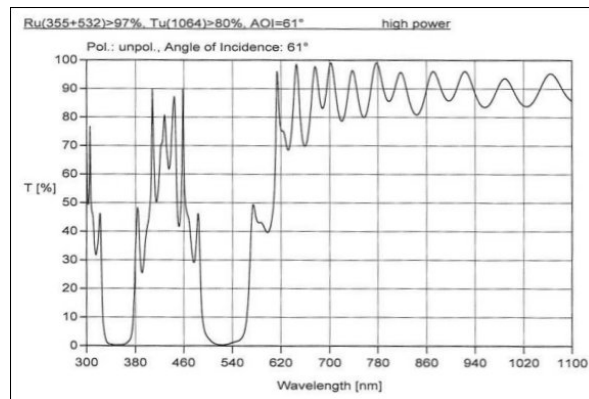


**Figure 10.6:** Transmission as a function of the wavelength of the dichroic guiding mirrors.

The main mirror, made of solid-glass, has been adopted from the former CLUE experiment. After numerous tests along the years, due to a degradation of the reflectivity, it has been found that 90% of the light at the focal plane falls into a circle of 8 mm diameter, that fits well with the entrance of the liquid light guide [283]. A complete re-aluminization and re-coating of the mirror was performed at the end of 2020 by the company ZAOT<sup>4</sup>, Italy, before sending the LIDAR to the CTA-N site.

In Fig. 10.7, all the components presented so far are recognizable, mounted on the telescope structure. In the image, the movable petals to protect the mirror

<sup>4</sup>[www.zaot.com/it/](http://www.zaot.com/it/)

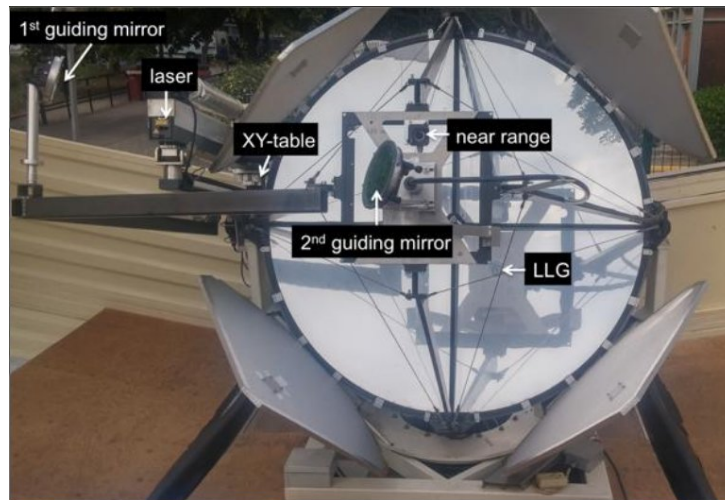


**Figure 10.7:** Picture of the telescope showing the main components of the Raman LIDAR system: the laser and the first guiding mirror on the left, the second guiding mirror, the near range system and the liquid light guide (LLG), respectively, at the center.

from dust are also visible.

### 10.3.5 The Liquid Light Guide

A 3.2 m long liquid light guide (LLG) of type Lumatec Series 300, of 8 mm diameter, is used to transport the recollected light at the focal plane to the optical readout system, the polychromator. The light transmission reaches values of up to 80% and is optimized for the spectral range from 330 nm to 650 nm.

The LLG was chosen, instead of the usual optical fibre, as a consequence of the relative large point spread of the main mirror. Thanks to its aperture of 8 mm, it can recollect all the signal reflected. However, the robustness of this system can not be guaranteed by the manufacturer for the particular use given to it in the Barcelona Raman LIDAR. Various tests have been performed to test the stability of the transmission characteristics of the LLG (temperature, vibration, humidity and so on) and no significant variations in transmission have been found. Furthermore, the reduction of the background light and the relation between the angle of incidence of the light and the output angle have to be taken into account. For the later case, a linear dependence has been observed. After testing the transmittivity of the LLG with respect to incident angle, it has been found that from  $15^\circ$  to  $30^\circ$  transmission decreases slightly and falls down by one order of magnitude from  $30^\circ$  to  $35^\circ$  [283]. This is exactly what is needed for the Barcelona Raman LIDAR, since the maximum incidence angle of light reflected by the mirror toward the LLG is exactly  $30^\circ$ .

### 10.3.6 The polychromator

The optical readout system of the Barcelona Raman LIDAR, the *polychromator* [284], has been designed by the University and INFN (Istituto Nazionale di Fisica Nucleare) of Padova in collaboration with the CNR (Consiglio Nazionale delle Ricerche) Padova [284] (see upper part of Fig. 10.8). The light rcollected

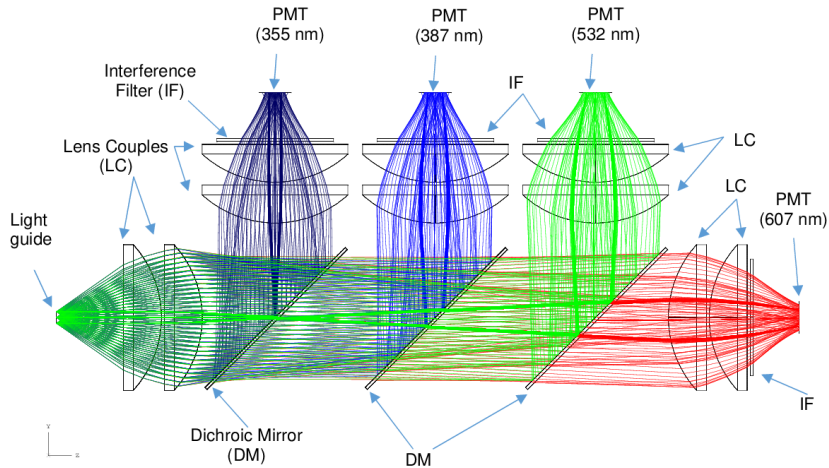


**Figure 10.8:** Polychromator design layout (*top*) and picture of the interior (*bottom*) for a 4-channel read-out unit.

by the main mirror and transmitted by the LLG (to the back part of the telescope, where the polychromator is installed) reaches the entrance of the polychromator on the left side. After getting collimated by two lenses, wavelengths smaller than or equal to 355 nm are reflected by a first dichroic mirror to a first PMT. The rest of the light is transmitted towards a second dichroic mirror that reflects wavelengths equal to and lower than the Raman line at 387 nm. After this second dichroic mirror, the remaining light passes through a third one that reflects light at 532 nm, and lower wavelengths, and transmits the 607 nm Raman wavelength to a fourth PMT, together with higher wavelengths. As the light reflected and transmitted is not monochromatic, narrow band filters<sup>5</sup> are installed in front of each detector for the final wavelength

<sup>5</sup>The pass-band of the filters adopted is 10 nm, larger than 1 nm pass-band filters commonly used in LIDARs, as the change of transmission due to wider incident angles on the filter is relatively large in case of the polychromator design adopted.

selection and are coupled with further collimating lenses. In the lower part of Fig. 10.8, the interior of the polychromator is shown. Four *Hamamatsu* R11920-100 high quantum efficiency PMTs are installed in the polychromator. In order to have the maximum efficiency for the wavelength of interest at each read-out channel, an efficiency test has been performed (see section 11.2). Given the fact that the Raman light is few orders of magnitude dimmer than the elastic line, care has to be taken for unwanted spurious light from reflections inside the instrument.

### 10.3.7 The acquisition system: Licel modules and software

The Licel Optical Transient Recorder (LOTR) is a powerful data acquisition system, especially designed for remote sensing applications. It combines analog detection of the PMTs current and single photon counting.

Five LOTR modules will be installed in the LIDAR container (four of them are already installed), one for each collected signal wavelength and one for the near-range system. The final data acquisition, as well as the overall LIDAR system, will be operated remotely through an in-house made control software, written in Java, as shown in Fig. 10.9.

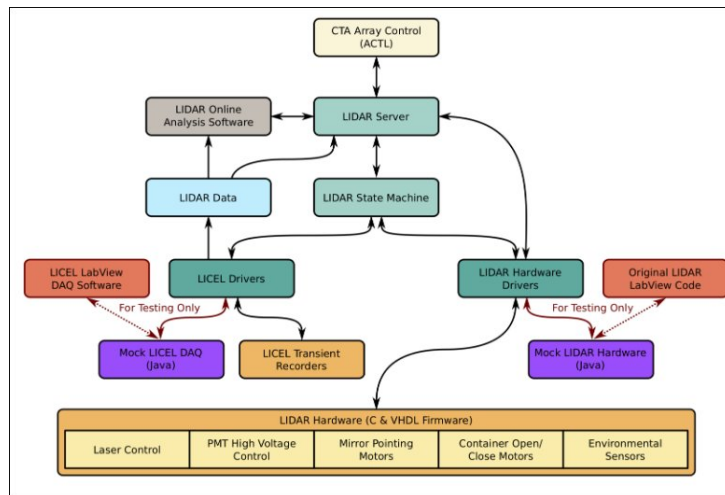


**Figure 10.9:** Block diagram of the control software of the Barcelona Raman LIDAR.

A python code is then used for the final analysis of the data. The results obtained from the a couple of data taking tests are presented at the end of the next chapter, together with future plans for the Barcelona Raman LIDAR.

Numerous tests of the components and data-taking tests have been performed along the years. In the following chapter, the laser beam divergence test and the PMT characterization will be described in more detail.

## Chapter 11

# Component Characterization of the Barcelona Raman LIDAR and Concluding Remarks

Since the beginning of the Barcelona Raman LIDAR project, various tests have been performed on its components, in order to characterize them. Several of them are reported in A. López-Oramas PhD thesis [283], but many others have been reported only in internal documents. In this chapter, I will describe two of the tests in which I collaborated, introducing the experimental setup, the analysis methods and providing results. At the end of the chapter, I will conclude presenting the results obtained with a full-operative Barcelona Raman LIDAR prototype.

### 11.1 Laser beam divergence test

The Quantel Brilliant laser, mounted on the Barcelona Raman LIDAR, broke in November 2015 after a failure of its internal flash lamp. The latter was replaced by a new one by an external company, and the laser came back to be operational in November 2016, even if presenting a slight misalignment of the internal mirrors. Because of this issue, a new set of measurements of its optical properties was performed.

A first test was carried out inside a dark room of  $\sim 2.5$  m length, but the results were inconclusive due to the large systematic uncertainty in converting the retrieved beam profiles into beam divergence. Afterwards, a second and a third tests were conducted, choosing a setup that permitted to have a larger distance ( $\sim 80$  m) from the laser spot, giving hence more robust values of the beam divergence.

#### 11.1.1 Theoretical background

Laser beams in optics and in laser physics are usually at first approximated as Gaussian beams, which means assuming exclusively operations in fundamental transverse, or  $TEM_{00}$ , mode (see Fig. 11.2). The intensity  $I$  of such a type of beam, as a function of its radius  $r$  and the axial distance  $z$ , can be written

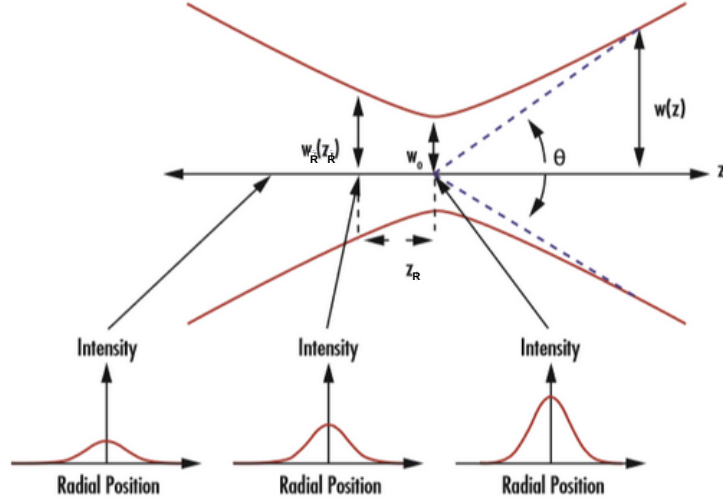


**Figure 11.1:** Scheme of a Gaussian beam, including the waist parameters and the intensity at different axial distances. Credits to: [286].

as [285]:

$$I(r, z) = I_0 \left( \frac{w_0}{w(z)} \right)^2 \exp \left( -\frac{2r^2}{w^2(z)} \right) \quad , \quad (11.1)$$

where  $I_0$  and  $w_0$  ( $\approx 3$  mm) are, respectively, the intensity and the waist radius<sup>1</sup> of the beam at the beam waist (usually coinciding with the beam exit point), and  $w(z)$  the beam radius, at an axial distance  $z$ , at which the intensity drops to  $1/e^2 \approx 0.135$  of its central axial value. A sketch of a Gaussian beam is presented in Fig. 11.1. In the figure, the Rayleigh length  $z_R$ <sup>2</sup> and the divergence angle  $\Theta$  are also presented.

The beam diameter  $d(z)$  is then defined as  $2 \cdot w(z)$ , and the divergence  $\Theta$  can be obtained, in the far-field (at a distance much larger than the Rayleigh radius, where the beam diameter increases mostly linearly with the distance from the focus [287]), as approximately [285]:

$$\Theta \approx \frac{d(z)}{z} \quad . \quad (11.2)$$

For a diffraction limited Gaussian beam, the divergence  $\Theta$ , also called *full-angle*

<sup>1</sup>Radius of the beam at the beam waist, i.e. location along the propagation path of the beam, where the beam radius presents a minimum.

<sup>2</sup>Defined as the distance from the beam waist where the beam radius increases by a factor of  $\sqrt{2}$ .

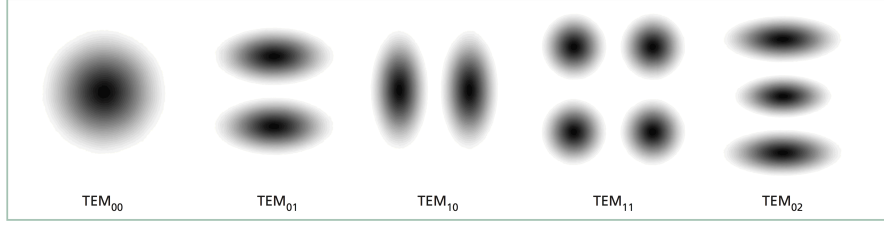


**Figure 11.2:** Low-order Hermite-Gaussian resonator modes (taken from [285])

*divergence*, can be predicted as:

$$\Theta = \frac{2\lambda}{\pi \cdot w_0} \approx 0.23 \text{ mrad} \quad , \quad (11.3)$$

where the last approximation has been obtained for the laser wavelength 1064 nm, and a beam waist of 3 mm, as provided by the Quantel company.

In the real world, pure Gaussian laser beams are practically impossible to find. Usually, the higher the output power, the more higher-order modes add to the fundamental one, creating a mixed mode beam. Such a beam can be characterized by a *beam quality factor*  $M^2$ :

$$M^2 = \frac{\pi \cdot w_0 \cdot \Theta}{2\lambda} \quad , \quad (11.4)$$

a measure of the quality of a laser beam. It is directly proportional to the beam divergence and its value ranges from 1, for a diffraction-limited beam (a perfect Gaussian beam), to higher values. Smaller values of  $M^2$  are not physical. Given the specifications from the manufacturer (see Appendix A), we would expect a beam divergence of twice the diffraction limited one, and hence a beam quality factor of about  $M^2 \approx 2.2$  for the original laser wavelength of  $\lambda = 1064 \text{ nm}$ .

Higher-order modes can introduce non-radially symmetric beam profiles (like all higher-order Hermite-Gaussian (HG) resonator modes, see Fig. 11.2). It is, however, important to realize that any family of HG modes propagates with distance as [288]:

$$w^2 = w_0^2 + \left( \frac{\lambda}{\pi w_0} \right)^2 (z - z_0)^2 \quad , \quad (11.5)$$

and beam sizes of any multi-mode real laser beam can be expressed as [288]:

$$w_{x,y}^2 = w_{0x,y}^2 + M_{x,y}^4 \left( \frac{\lambda}{\pi w_{0x,y}} \right)^2 (z - z_0)^2 = w_{0x,y}^2 + \left( \frac{\Theta_{x,y}}{2} \right)^2 (z - z_0)^2 \quad , \quad (11.6)$$

with the introduction of the beam quality factors  $M_x$  and  $M_y$  in the appropriate transverse directions, and correspondingly the beam waists  $w_{0x}$  and  $w_{0y}$  and the beam sizes  $w_x(z)$  and  $w_y(z)$ . If  $w_{0x} \neq w_{0y}$ , the beam is said to exhibit *waist asymmetry*, and *divergence asymmetry* if  $M_x^2/w_{0x} \neq M_y^2/w_{0y}$ .

### 11.1.2 The experimental setup and the data acquisition

As mentioned in the introduction of this section, different tests were carried out to describe the laser beam profile and its divergence. The first test was

performed in January 2017, mounting the experimental setup in a dark-room inside the IFAE workshop. The laser was aligned with a thin lead panel, first at a distance  $L = 2.4$  m, then moved to 1.8 m. Due to the short distance between the laser and the lead panel of this first setup, an improved setup was chosen for next tests. The campus bus terminal of UAB was chosen as location (see Fig. 11.3). Given the wide area available, it was possible to reach distances



**Figure 11.3:** Location and setup of the second and third beam divergence tests.

$L = 72.6$  m (in the setup of the test performed in April 2017) and 84.4 m (in the setup of the test performed in July 2017) between the laser and a sheet of graph paper mounted on a white panel (the target substituting the lead panel). With the latter experimental setup, various pictures (in raw-mode) of the laser signal reflected on the paper were taken using two digital cameras, namely a *Canon EOS 1000D* and a *Nikon D5000*. The beam spot was observed from very small angles with respect to the vertical distance, taking care of avoiding any shadowing of the very same laser beam.

Since a significant amount of the images was saturated in the first tests, most of the pictures of July 2017 were taken with *Neutral Density (ND) filters* to reduce the intensity of the laser light to acceptable values. As in January and April 2017 such filters had not been used, only the very lowest laser intensity could produce non-saturated images.

To summarize, four data sample were collected:

- *Sample 1* - images taken on January 2017 with a *Canon 1000D* camera and no filters;
- *Sample 2* - images taken on April 2017 with a *Canon 1000D* camera and no filters;
- *Sample 3* - images taken on July 2017 with a *Canon 1000D* camera with and without filters;
- *Sample 4* - images taken on July 2017 with a *Nikon D5000* camera with and without filters.

For each experimental setup, the parameters presented in Tab. 11.1 were retrieved from direct measurements. The parameters  $D_{\text{ext}}$  and  $D_{\text{int}}$  were mea-

**Table 11.1:** Basic parameters directly measured in the different experimental setups (see text). The entries marked with ‘-’ corresponds to the parameters not directly retrieved, but obtained, in a second moment, from the analysis presented in subsection 11.1.3.

Parameter	Jan. 2017	April 2017	July 2017	comments
$L$	2.4 m 1.80 m	(72.6±0.1) m	(84.4±0.1) m	measured with rulers
$\Theta_x$	1.3 mrad	-	-	from July 2017 analysis
$\Theta_y$	0.9 mrad	-	-	from July 2017 analysis
$1 - \Theta_x^2 L^2 / 2d_x^2$	0.88 0.90	-	-	see Eq. 11.9
$1 - \Theta_y^2 L^2 / 2d_y^2$	0.85 0.93	-	-	see Eq. 11.9
$w_{0x}$	-	2.7 mm	2.7 mm	from Jan. 2017 analysis
$w_{0y}$	-	1.7 mm	1.7 mm	from Jan. 2017 analysis
$1 - d_{0x}^2 / 2d_x^2$	-	0.999	0.999	see Eq. 11.9
$1 - d_{0y}^2 / 2d_y^2$	-	0.999	0.999	see Eq. 11.9
$D_{\text{ext}}$	not used	(1280±5) mm	(1280±5) mm	measured with ruler
$D_{\text{int}}$	not used	(1168±5) mm	(1168±5) mm	measured with ruler

sured only in the data acquisitions of summer 2017, and correspond to the sizes of the external and internal part of the white panel, respectively.

### 11.1.3 Data analysis

In the case of *Sample 2*, *Sample 3* and *Sample 4*, the pictures of the reflected laser beam (taken in raw-mode) were downloaded to disc and converted to FITS-format (using the code *cr2fits.py* [289] in the case of the pictures taken with *Canon EOS 1000D*). Only the *Bayer-Green* points have been extracted from the FITS-files. Subsequently, the non-saturated pictures have been analysed with a self-written code, called *LaserSpot*, whose underlying algorithm is described in the following lines. The resulting beam diameters  $d$ , also called *beam profiles*, were converted in physical units by comparing the distance in image pixels of the outer edges of the white panel with its measured real distance in millimetres.

If the beam in consideration is perfectly Gaussian, its irradiance decreases monotonically with radius. However, in the case of real laser beams, the irradiance might not be uniform around the center at all radii, introducing some arbitrariness in the definition of the beam profile. We used, therefore, a numerically more robust definition of the beam diameter, based on the concept of *encircled energy* (EE): the radius around a central point at which the relative image content contained within that radius has fallen to  $(1 - 1/e^2)$ . This definition turns out to be equivalent to the one based on irradiance in the case of Gaussian beams, since:

$$e^{-r^2} = \frac{\int_0^r e^{-r'^2} dr'}{\int_0^\infty e^{-r'^2} dr'} \quad (11.7)$$

The analysis method was further elaborated to fit ellipses, instead of circles, to the images, given the fact that all the samples showed images with rather

elliptic than circular shapes.

The normalized image content within ellipses of increasing half axes has been counted considering only ellipses of the same shape and centred at the same point. In this way, two beam radii are obtained: one corresponding to the major and the other to the minor axis of the ellipse, including  $(1 - e^{-2}) \approx 86.5\%$  of the laser image content.

Images were fitted with a two-dimensional asymmetric Gaussian of height  $I_0$ , with variable center coordinates  $x_0$  and  $y_0$ , major and minor axis widths  $\sigma_x$ ,  $\sigma_y$  and a rotation angle  $\alpha$ , plus an offset  $I_{\text{off}}$ :

$$I(x, y) = I_{\text{off}} + I_0 \exp\left(-\frac{a \cdot (x - x_0)^2 + c \cdot (y - y_0)^2 + 2b \cdot (x - x_0) \cdot (y - y_0)}{2}\right)$$

with:

$$\begin{aligned} a &= \frac{\cos(\alpha)^2}{\sigma_x^2} + \frac{\sin(\alpha)^2}{\sigma_y^2} \\ b &= -\frac{\sin(2\alpha)}{2\sigma_x^2} + \frac{\sin(2\alpha)}{2\sigma_y^2} \\ c &= \frac{\sin(\alpha)^2}{\sigma_x^2} + \frac{\cos(\alpha)^2}{\sigma_y^2} \end{aligned} \quad (11.8)$$

The background was evaluated considering the outside regions of the fitted ellipse, at  $5\sigma_{x,y}$  from the center, up to a suitably chosen cutout of the image. The cutout was chosen by eye on the basis of a constant number of entries, coinciding with a constant image color. After subtraction of the background, the image was normalized and, then, integrated in ellipses of equal axes ratio and rotation angle from  $x_0, y_0$  to the point where the integral reaches  $(1 - e^{-2})$ . At that point, the major and minor axis were evaluated and multiplied by a factor two to convert beam radii to beam diameters. Subsequently, these values were divided by the distance  $L$  to obtain the two de-rotated full-angle divergences  $\Theta_{x,y}$ .

The input parameters used in the code for the analysis of the *Sample 3* (for a more detailed description of the analysis and results of *Sample 4* see [290]) are reported in Tab. 11.2. *Sample 2* is composed of only one file (IMG\_0825), selected to have the lowest laser intensity, as filters were not used during data acquisition, but the input parameters of the analysis are not available.

The analysis of *Sample 1* data was performed together with the analysis of the other data sample, using a different method. The two de-rotated full-angle divergences  $\Theta_{x,y}$  have been taken into consideration, and the beam diameter at the beam waist retrieved, following:

$$d_{0,(x,y)} = \sqrt{d_{x,y}^2 - \Theta_{x,y}^2 \cdot L^2} \approx d_{x,y} \cdot \left(1 - \frac{\Theta_{x,y}^2 \cdot L^2}{2d_{x,y}^2}\right) \quad . \quad (11.9)$$

**Table 11.2:** Table of the parameters used as input for the script: name of the raw file, coordinates for the cutout and conversion factors. In the last column of the table, a distinction is made between saturated (Y), non-saturated (N) and lower intensity (low int.) images. The latter are all non-saturated.

<b>Image_file</b>	<b>x<sub>1</sub></b>	<b>x<sub>2</sub></b>	<b>y<sub>1</sub></b>	<b>y<sub>2</sub></b>	<b>conv.</b>	<b>sat.</b>
IMG_0894	1089	1375	1127	1358	0.68	Y
IMG_0895	918	1111	1518	1732	0.83	Y
IMG_0897	1001	1221	1276	1562	0.82	Y
IMG_0898	957	1177	1331	962	0.83	Y
IMG_0899	951	1199	1320	1562	0.83	Y
IMG_0906	1050	1248	1798	2029	0.89	Y
IMG_0907	1050	1248	1881	2084	0.89	Y
IMG_0909	1149	1397	852	1144	0.87	N
IMG_0912	1122	1369	1072	1369	0.90	N
IMG_0913	1160	1397	984	1254	0.90	N
IMG_0914	1039	1287	1006	1287	0.91	N
IMG_0920	1045	1298	1243	1589	0.82	Y
IMG_0922	1034	1276	984	1314	0.79	Y
IMG_0925	1045	1309	1028	1358	0.79	Y
IMG_0927	819	1072	1479	1809	0.77	Y
IMG_0929	874	1155	1446	1820	0.77	Y
IMG_0942	924	1111	1474	1006	1.26	Y
IMG_0945	836	1061	1353	1589	1.03	Y
IMG_0947	896	1105	1325	1573	0.64	Y
IMG_0948	913	1111	1215	1474	1.03	Y
IMG_0949	957	1166	1650	1903	1.03	Y
IMG_0960	1006	1270	2007	2337	0.76	N
IMG_0961	951	1259	2051	2387	0.77	N
IMG_0962	1006	1298	2106	2442	0.76	N
IMG_0965	737	1012	1815	2134	0.77	Y
IMG_0966	726	1012	1864	2167	0.77	Y
IMG_0967	753	1039	1859	2172	0.78	Y
IMG_0968	1122	1386	1584	1859	0.79	N
IMG_0978_1	979	1204	1441	1688	0.78	low int./N
IMG_0979	990	1210	1474	1771	0.78	low int./N
IMG_0982	786	1039	1479	1732	0.78	low int./N

#### 11.1.4 Results and discussion

In the following lines I will present the results obtained by the analyses of the first three data samples.

##### Sample 3 detailed results

*Sample 3* is formed by saturated and non-saturated pictures, whose difference is clearly visible by eye (see Fig. 11.4).

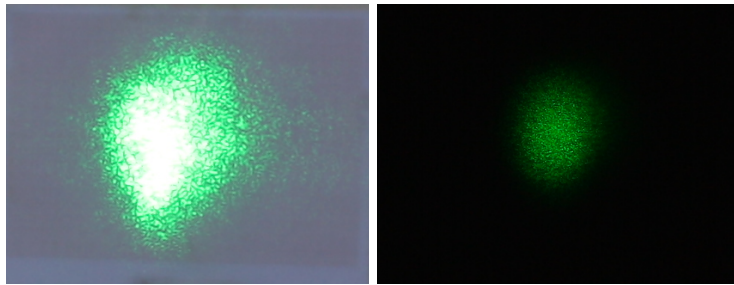


**Figure 11.4:** Comparison between saturated and non-saturated images from raw camera pictures.

Running the analysis code on both type of pictures, differences can be observed also in the results. Figs. 11.5 and 11.8 show an example of the output of the script for the case of saturated images, while Figs. 11.6 and 11.9 display the case of non-saturated ones, and Figs. 11.7 and 11.10 present low intensity non-saturated pictures.

Each image type presents peculiar characteristics. In the case of saturated pictures (Figs. 11.5 and 11.8), the laser spot appears a bit more extended than in the other two cases, and more symmetric. This is due to a distorted 2D-Gaussian fit, and a consequently wrong calculation of the integrated image content, because of a missing central image content. The behaviour of the reconstructed ellipses is different in the case of non-saturated images (Figs. 11.6 and 11.9 and Figs. 11.7 and 11.10): the diameter of the minor axis is smaller in the low intensity case with respect to the case of high intensity laser beam.

The results obtained for all the pictures are summarized in Tab. 11.3.

Tables 11.4 and 11.5 report the average results and standard deviation values obtained from the analysis of *Sample 3*. In order to get these values, the overall sample has been divided in a low intensity (last three images of Tab. 11.3) and high intensity laser beam cases (first eight images of Tab. 11.3). It is worth notice that the full-divergence angles appear to be smaller in the case of low intensity laser beams. This is due to the fact that the pictures taken with a low laser intensity were taken under a different angle in both axes (sitting on ground), while the others were taken in upright position. Thus, care has to be taken when considering the low laser intensity images, since correction for the inclination angle may be needed.

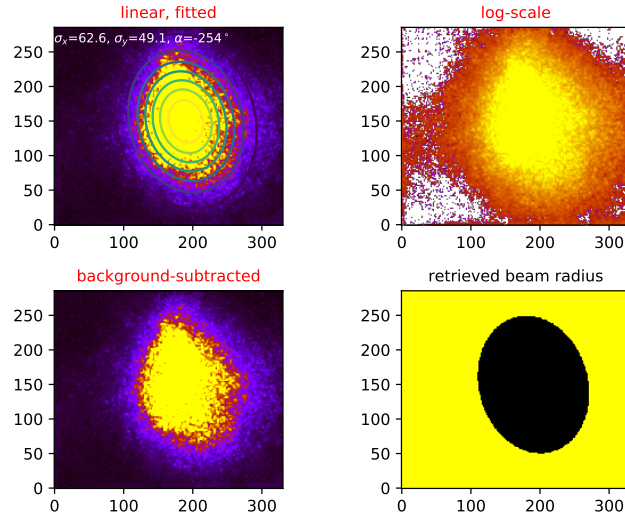


**Figure 11.5:** Plots obtained from the analysis of a saturated image file. The upper left part shows the laser spot image in linear scale, fitted with the 2D-elliptic gaussian. The upper right picture presents the same plot in logarithmic scale and without the retrieved concentric ellipses. The lower left panel shows the background-subtracted image, and the lower right displays the ellipse that contains  $(1 - 1/e^2)$  of the total normalized distribution.

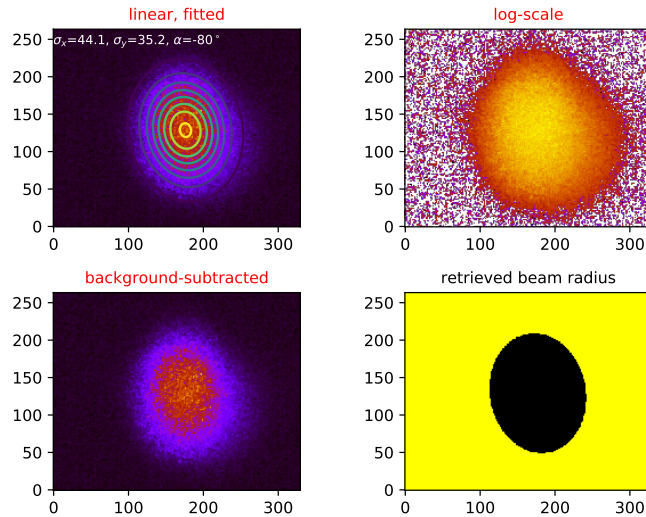


**Figure 11.6:** Plots obtained from the analysis of a medium-intensity non-saturated image. See Fig. 11.5.

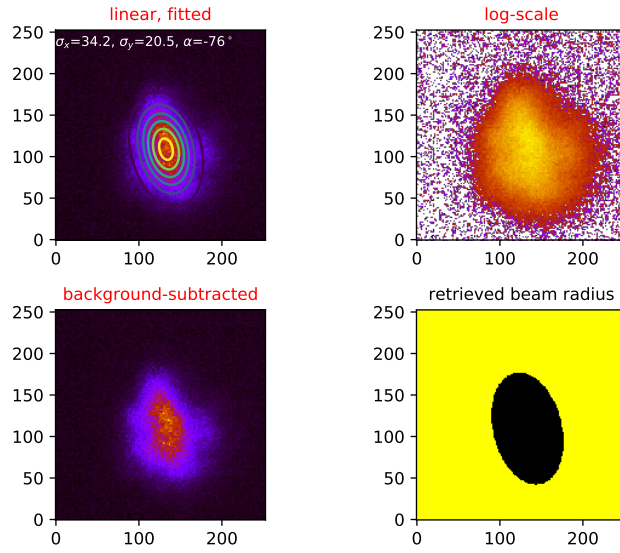


Figure 11.7: Plots obtained from the analysis of a low intensity image. See Fig. 11.5.

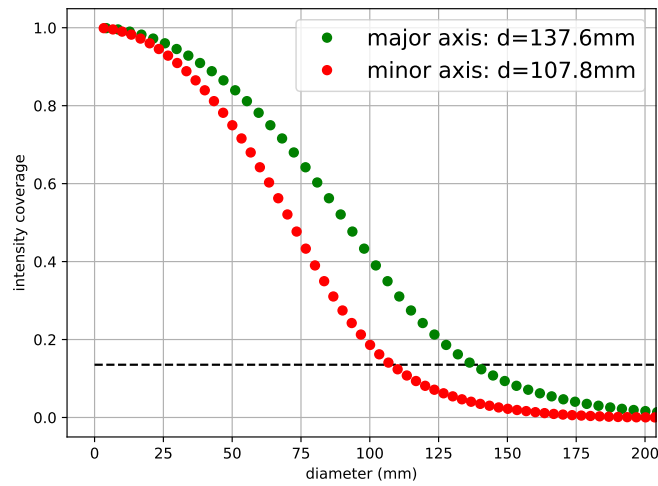
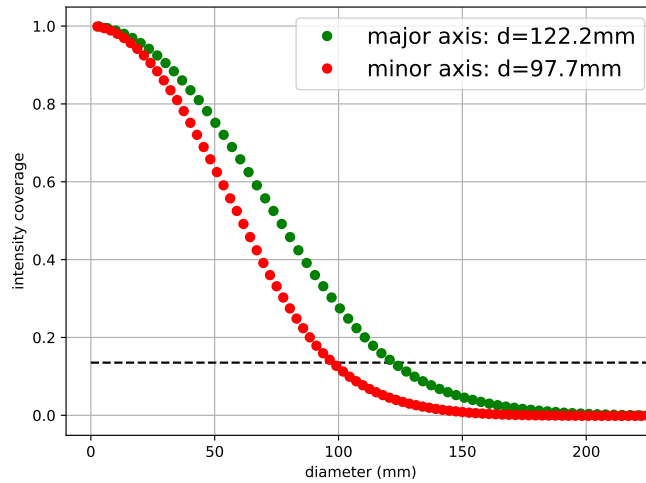
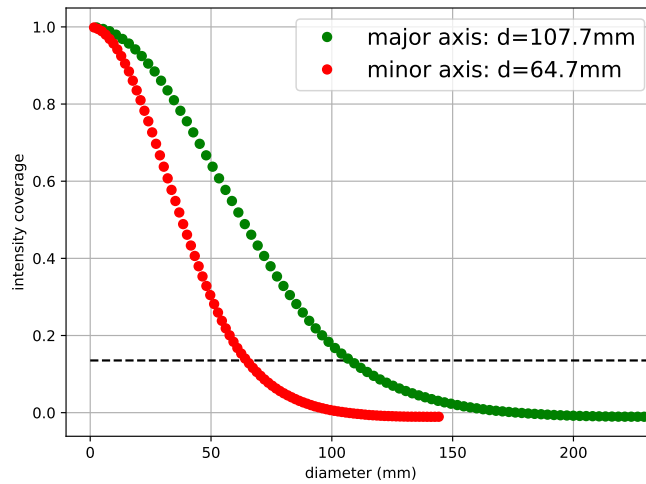


Figure 11.8: Intensity coverage of the background subtracted and normalized saturated image, as a function of the fitted ellipse's major and minor axes.



**Figure 11.9:** Intensity coverage of the background subtracted and normalized medium-intensity non-saturated image, as a function of the fitted ellipse's major and minor axes.



**Figure 11.10:** Intensity coverage of the background subtracted and normalized low intensity image, as a function of the fitted ellipse's major and minor axes.

**Table 11.3:** Results of the image fits: name of the raw file, value of the major axis of the ellipse ( $d_{maj}$ ), value of the beam divergence along the major axis ( $\Theta_{maj}$ ), value of the minor axis of the ellipse ( $d_{min}$ ), value of the beam divergence along the minor axis ( $\Theta_{min}$ ), rotation angle of the beam profile ( $\alpha$ ).

Image_file	$d_{maj}$ (mm)	$\Theta_{maj}$ (mrad)	$d_{min}$ (mm)	$\Theta_{min}$ (mrad)	$\alpha$ (deg)
IMG_0909	119.5	1.42	83.5	0.99	101
IMG_0912	118.3	1.40	86.0	1.02	109
IMG_0913	118.7	1.41	80.9	0.96	100
IMG_0914	122.6	1.45	79.0	0.94	107
IMG_0960	122.8	1.45	98.2	1.16	100
IMG_0961	124.8	1.49	99.3	1.18	92
IMG_0962	120.4	1.43	96.6	1.14	102
IMG_0968	112.8	1.27	90.4	1.07	105
IMG_0978_1	106.1	1.26	66.7	0.79	94
IMG_0979	108.0	1.28	68.8	0.82	103
IMG_0982	110.0	1.30	66.1	0.78	104

**Table 11.4:** Average and standard deviation of the results obtained for the high intensity laser beam: major axis of the ellipse ( $d_{maj}$ ), beam divergence along the major axis ( $\Theta_{maj}$ ), minor axis of the ellipse ( $d_{min}$ ), beam divergence along the minor axis ( $\Theta_{min}$ ), rotation angle of the ellipse ( $\alpha$ ).

$d_{maj}$ [mm]	$\Theta_{maj}$ [mrad]	$d_{min}$ [mm]	$\Theta_{min}$ [mrad]	$\alpha$ [deg]
(120±3)	(1.39±0.04)	(90±8)	(1.06±0.09)	(102±5)

**Table 11.5:** Average and standard deviation of the results obtained for the low intensity laser beam: major axis of the ellipse ( $d_{maj}$ ), beam divergence along the major axis ( $\Theta_{maj}$ ), minor axis of the ellipse ( $d_{min}$ ), beam divergence along the minor axis ( $\Theta_{min}$ ), rotation angle of the ellipse ( $\alpha$ ).

$d_{maj}$ [mm]	$\Theta_{maj}$ [mrad]	$d_{min}$ [mm]	$\Theta_{min}$ [mrad]	$\alpha$ [deg]
(108±2)	(1.28±0.02)	(67±1)	(0.80±0.02)	(100±5)

### Sample 2 detailed results

*Sample 2* pictures were taken without the use of filters. Given this fact, only one image could be considered for the analysis. The results obtained from this picture are presented in Table 11.6, and the plots retrieved in the analysis are shown in Figs. 11.11 and 11.12.

### Sample 1 detailed results

Similarly to the case of *Sample 2*, all the images of the data sample, except for one, were saturated. For this reason, upper limits, presented in Tab. 11.7, had to be retrieved. The results obtained by the analyses of the four data samples

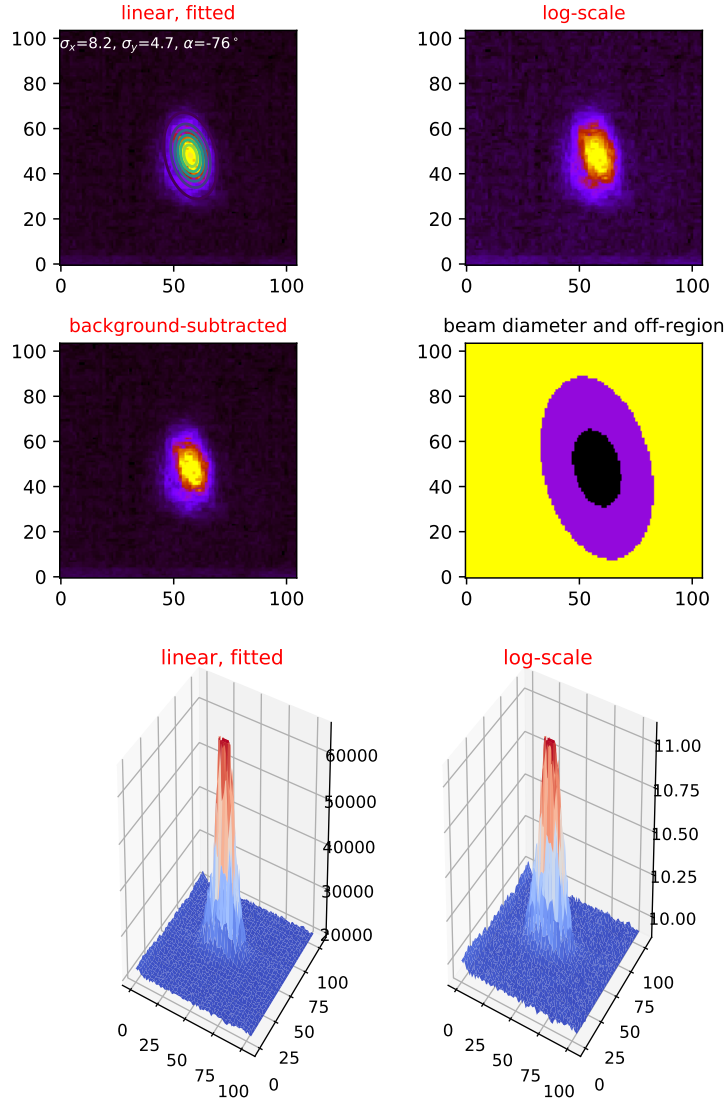


**Figure 11.11:** Plots obtained from the analysis of the photo “IMG\_0825”. The upper left part shows the laser spot image in linear scale, fitted with the 2D-elliptic Gaussian. The upper right picture presents the same plot in logarithmic scale and without the retrieved concentric ellipses. The lower left panel shows the background-subtracted image, and the lower right displays the ellipse that contains  $(1 - e^{-2})$  of the total normalized distribution (black), and region used for the determination of the background (yellow). The lower images show the raw image in 3d, in linear (left) and logarithmic (right) scale.

**Table 11.6:** Results of the image analysis 3 for the data from April 2017.

file name	beam diameter major axis [mm]	beam diameter minor axis [mm]	beam rotation angle $\alpha$ [deg]	beam intensity
IMG_0825	63.5	36.8	104	lowest possible

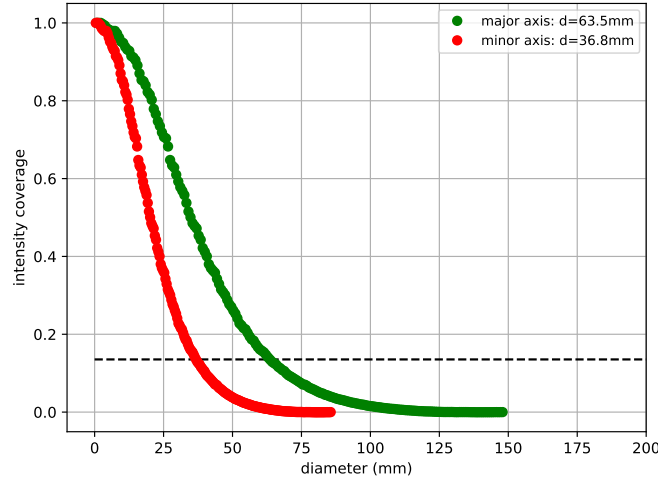


**Figure 11.12:** Intensity coverage (enclosed energy) of the background subtracted and normalized image “IMG\_0825”, as a function of the fitted ellipse major and minor axes.

are summarized in Tab. 11.8. Using Eq. 11.4, the beam quality factors result to be  $M_x^2 \approx 6.1$  and  $M_y^2 \approx 4.2$ .

The beam divergences obtained are significantly larger (at least a factor 2.6 wider along the major axis, and at least a factor 1.7 wider along the minor axis) than the one presented by the manufacturer (Appendix A), unless the absolutely lowest laser intensity is used, and, in addition, they are asymmetric. The asymmetry is more than 35% and increases as intensity gets lower. Moreover, the beam appears rotated by about  $10^\circ$  with respect to the vertical axis, although the form of the laser spot shows often further substructures, additionally to its elliptic shape.

On the other hand, the waist diameters at 1064 nm result to be smaller than those provided in the data sheet. This could be due to the fact that our data had been taken using the frequency-doubling non-linear crystal, that produces some beam narrowing, while the results in the data sheet have been given without the use of that laser module. Nevertheless, the diameter waist obtained are in agreement with the results obtained in [283].

In order to understand better the results we retrieved from our analyses, different systematic effect have been investigated. The quadratic sum of all the uncertainties considered is 2-3% for the major axis of the beam and of  $\sim 6\%$  for the minor axis. A list of the systematic effects considered is reported below:

- **Residual backgrounds:** a variation on the cutoff distance for the back-

**Table 11.7:** Results of the image analysis 3 for the near-range data from January 2017. The upper set of lines were obtained with a laser distance of 2402 mm, while the two lower images were taken at an even closer distance of 1798 mm. Only the upper set of pictures contains one without any saturation. All beam sizes obtained from the saturated pictures are therefore given as upper limits.

file name	major axis [mm]	minor axis [mm]	angle $\alpha$ [deg]	intensity	saturation
IMG_0358	6.3	4.0	96	lowest possible	no
IMG_0395	<7.2	<5.3	101	low	yes
IMG_0396	<7.2	<5.2	102	low	yes
IMG_0398	<6.6	<4.5	99	low	yes
IMG_0399	<6.8	<5.0	104	low	yes
IMG_0400	<6.8	<4.8	103	low	yes
IMG_0401	<7.1	<5.2	100	low	yes
IMG_0402	<7.0	<5.0	102	low	yes
IMG_0403	<7.0	<5.0	102	low	yes
<b>average</b>	6.3	4.0	101±2		
IMG_0443	<5.3	<4.2	96	low	yes
IMG_0474	≲5.5	≲4.5	99	low	slight
<b>average</b>	≲5.3	≲4.2	98±2		

**Table 11.8:** Summary of the retrieved beam characteristics from the different analysis. Both the beam divergences  $\Theta_{x,y}$  cover the full angle, and the beam waists  $d_{0,(x,y)}$  show the full radius, as provided in the data sheet of the laser (Appendix A). Those numbers given uncertainties are the result of several measurements of the same parameter, while those without uncertainty have been obtained from one measurement only. The expected uncertainty of these numbers may be estimated roughly as 10%. The numbers marked with a star \* might be affected by systematics due to a larger viewing angle and should be treated with caution.

intensity	month	distance [m]	$\Theta_x$ [mrad]	$\Theta_y$ [mrad]	asymmetry	$\alpha$ [deg]	comments
high	July	(84.4±0.1)	1.42±0.04	1.06±0.09	1.34±0.13	102±5	Sample3
high	July	(84.4±0.1)	1.39±0.05	0.98±0.04	1.43±0.08	100±4	Sample4
medium	July	(84.4±0.1)	1.28±0.02*	0.80±0.02*	1.61±0.06*	100±5	Sample3
medium	July	(84.4±0.1)	1.41±0.05	0.93±0.03	1.50±0.08	99±3	Sample4
lowest	April	(72.6±0.1)	0.87	0.51	1.71	104	Sample2
intensity	month	distance [m]	$d_{0x}$ [mm]	$d_{0y}$ [mm]	asymmetry	$\alpha$ [deg]	comments
lowest	Jan.	(2.40±0.05)	5.5	3.5	1.6	101±2	Sample1
low	Jan.	(1.80±0.05)	≲4.9	≲3.9	1.2	98±2	Sample1

ground estimation produces an alteration on the reconstructed beam profiles of less than 1%;

- **Camera viewing angle:** the average horizontal offset of  $\approx 20^\circ$  in taking the pictures of the laser spot in upright position (pictures taken into account for the analyses, except for the case of *Sample 1* analysis) introduces a systematic uncertainty of less than few percents in the major axis of the beam, and of about 5% in the minor axis;

- **Camera rotation:** again because of the data-taking method, since the camera and the ND filters were held by hand, possible rotations could have been of  $3^\circ$  max, thus negligible for the systematic uncertainty evaluation. This value has been retrieved from measurements of the rotation of the graph paper, stuck to the white panel;
- **Non-diffuse reflection:** this effect, due to the presence of the graph paper, is negligible at the moment of evaluating the beam diameter;
- **Binning used in the analysis:** this can affect the results of 1-2%, as the integrals of the ellipses from the central point were made with bins of about 2% of the obtained ellipse length (3% of its width);
- **Errors in the analysis code:** the method used for evaluating the beam diameter are commonly used in the field, thus, believing in the goodness of the fit, the only possible error could have been done in the conversion factor. However, the good agreement between the analysis of *Sample 3* and the one of *Sample 4* excludes this error.

To conclude, even if summing or subtracting the systematic error from the final results, our conclusions are not altered.

#### 11.1.5 Conclusions

The laser beam divergence retrieved from the analyses has a value larger than the one presented in the data sheet provided by the manufacturer. This fact implies a direct effect on the range of full overlap achievable with the Barcelona Raman LIDAR, passing from  $\sim 450$  m (without the use of the near-range system) to  $\sim 600$  m from ground. Nevertheless, the laser used for the tests will just be used for the Barcelona Raman LIDAR commissioning phase, and a new laser will be purchased for the final LIDAR. Thus, the observed beam degradation will affect only the first-light tests, and the long-term testing at La Palma. This study has been, in any case, of great importance for future laser tests, particularly if doubts arise about the quality of a new laser, as it has been established a protocol to assess laser characteristics with relatively small investment of time and material.

## 11.2 PMT characterization

Four PMTs of type Hamamatsu R11920-100 (the same model used for the LST1 prototype) were available to be mounted in the polychromator. Given their sensitivity curve, peaked at precise wavelength, a matching of each PMT with a corresponding acquisition channel, fitting in the wavelength range of the best PMT sensitivity, was required. For this reason, and to check the correct operation of the PMTs, a characterization of them before the installation has been performed.

As reported in the description of the Barcelona Raman LIDAR (see chapter 10), the four high quantum efficiency PMTs (with serial number ZQ6623, ZQ5819, ZQ6627 and ZQ6622) are the ones used as detectors in the polychromator. A full characterization of the them would require separately characterizing the quantum efficiency (QE) and high-voltage-dependent gain (HVDG). For a matter of time and missing instrumentation, it has been chosen to investigate the total current power ( $CP = QE \times HVDG$ ) as a response of the PMTs to a Xenon light source for different wavelengths. The following experiment description has been modified from an internal document written by S. Griffiths.

### 11.2.1 Experimental setup

For the experimental setup, a monochromator of 2 nm bandpass, a Xenon lamp and the liquid light guide (the same installed in the LIDAR) were installed on an optic table in a dark room, as showed in Fig. 11.13.

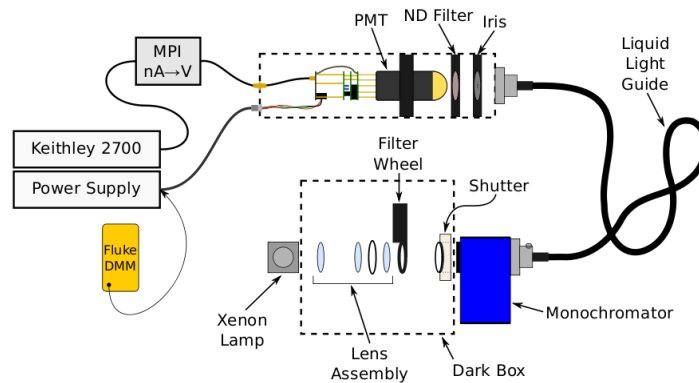


**Figure 11.13:** Schematic setup used for the PMT characterization. Credits to S. Griffiths.

A dark box, containing a lens assembly, a filter wheel and a shutter, was installed between the lamp and the monochromator. This last one was connected with the PMT aluminium dark-box by the LLG. Inside the PMT box, between the LLG and the PMT, an iris and an aluminium ND filter, with optical depth of 2.0, were installed. These two components were used to strengthen even more the wavelength pass-band of the monochromator.

Two of the four PMTs to be tested were configured with printed circuit boards (PCBs) using long cables. These procedure required the top of the aluminium box to be open in the back, so that the cables could be routed outside. For

this reason, a black cloth was used to cover the PMT box, to further improve the light-tightness.

The PMTs were placed one at a time in the box in the following order:

1. ZQ6623
2. ZQ5819
3. ZQ6627
4. ZQ6622

In order to obtain the total current in response of the different wavelength, a single operating voltage has been set (at an arbitrary value of 1200 V).

The measurements were performed for each PMT in different phases. Starting from 300 nm, the wavelength was incremented by 10 nm ( $\pm 2$  nm) up to 600 nm. At each step, measures of the PMT current with the shutter open (*on data*) and closed (*off data*) were taken.

To provide some insight on the intrinsic spectrum of the Xenon light source, some data were also collected using a calibrated Newport 818-UV PIN photodiode (showed in Fig. 11.14).

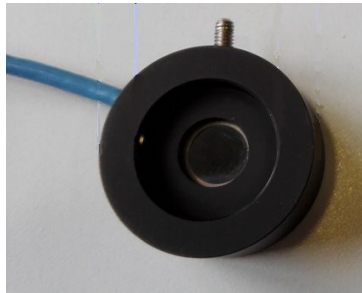


**Figure 11.14:** Newport 818-UV PIN photodiode used for the cross-check measurements.

### 11.2.2 Data analysis

For each measurement of the PMT current, 10 *off data* samples have been taken and subtracted from the *on data*. These has been done because a dependence of the background data on time was noticed, as shown in in Fig. 11.15 for the 4 PMTs.

The comparison with the PIN-diode subtracted-background data (PIN-diode data multiplied by the PMT QE and ND filter transmission) was also performed.

In Tab. 11.9 the final data obtained by averaging each single measurement are presented. The comparison of the results obtained for the four PMTs and for the photodiode (normalized, so that the value of its maxima matches the PMT data) is presented in Fig. 11.16.

As expected, the response of the PMTs is pretty the same for all the wavelengths. In order to optimize the coupling of each PMT with the particular readout channel of the polychromator, the percent deviation of the normalized PMT data with respect to the mean of the normalized PMT data has been estimated (Fig. 11.17).

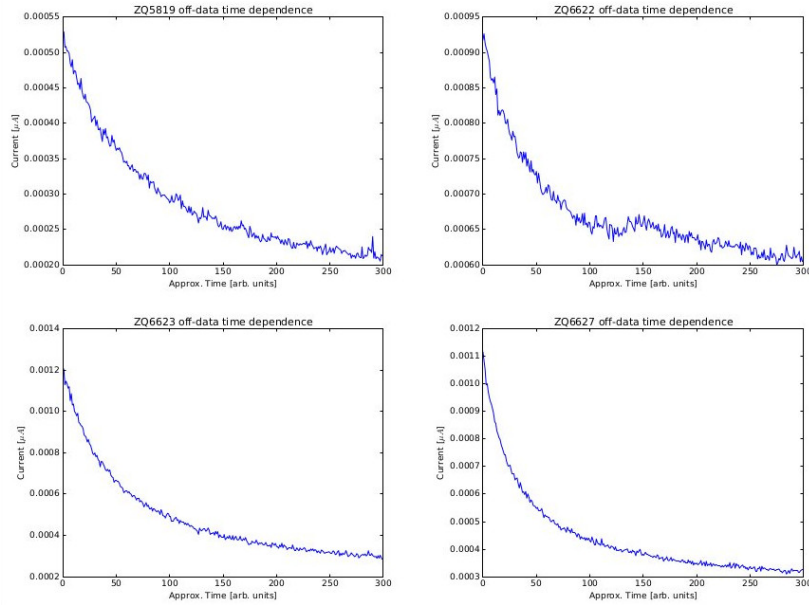


**Figure 11.15:** Response of the PMTs with the shutter close as a function of time. As the time intervals were not with the same time-stamp, arbitrary units have been used.

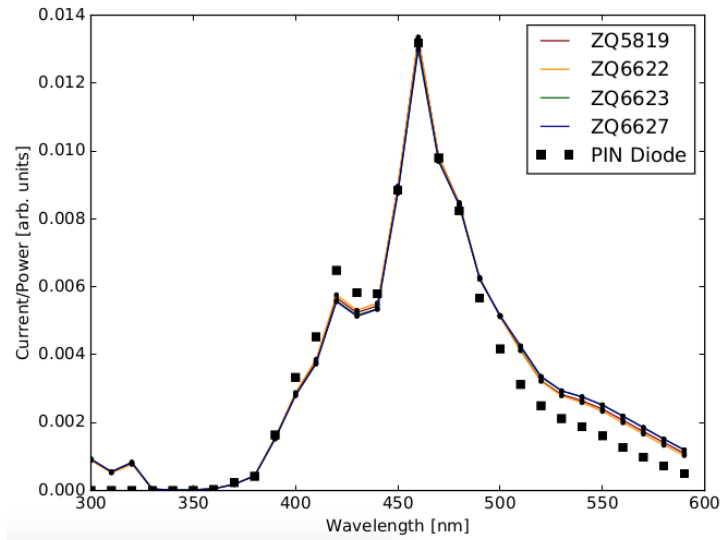


**Figure 11.16:** PMTs normalized current power data as a function of the wavelength. The results of each PMT are represented with a solid line, the one of the photodiode is showed with black squares.

### 11.2.3 Results and conclusions

Looking at Fig. 11.17 one can select the PMT to couple with each of the readout channels (for the wavelengths at: 355 nm, 387 nm, 532 nm and 607 nm). For

**Table 11.9:** Table of the mean values of the current power, with associated standard deviation, as a function of the wavelength ( $\lambda$ ).

$\lambda$ [nm]	ZQ5819		ZQ6622		ZQ6623		ZQ6627	
	Mean [ $\mu$ A]	Std. Dev.						
300.0	0.010079	0.000046	0.013596	0.000070	0.016739	0.000052	0.012717	0.000069
310.0	0.006004	0.000028	0.008002	0.000054	0.010007	0.000040	0.007587	0.000034
320.0	0.008956	0.000034	0.011840	0.000066	0.015080	0.000055	0.011351	0.000037
330.0	0.000473	0.000011	0.000619	0.000011	0.000781	0.000014	0.000587	0.000018
340.0	0.000220	0.000008	0.000303	0.000011	0.000362	0.000017	0.000270	0.000011
350.0	0.000215	0.000004	0.000300	0.000011	0.000357	0.000010	0.000260	0.000008
360.0	0.000625	0.000014	0.000850	0.000010	0.001004	0.000011	0.000752	0.000013
370.0	0.002062	0.000013	0.002835	0.000027	0.003331	0.000048	0.002488	0.000017
380.0	0.004925	0.000020	0.006796	0.000033	0.007871	0.000036	0.005911	0.000020
390.0	0.017332	0.000061	0.023991	0.000121	0.027764	0.000167	0.020752	0.000099
400.0	0.031969	0.000151	0.044137	0.000165	0.051038	0.000182	0.038183	0.000098
410.0	0.042668	0.000138	0.059029	0.000156	0.067902	0.000278	0.050931	0.000132
420.0	0.063734	0.000202	0.088176	0.000294	0.101254	0.000277	0.076005	0.000136
430.0	0.058813	0.000150	0.081174	0.000199	0.093451	0.000341	0.070111	0.000198
440.0	0.061104	0.000126	0.084441	0.000285	0.096939	0.000323	0.072875	0.000175
450.0	0.100327	0.000383	0.137106	0.000351	0.159061	0.000464	0.119604	0.000272
460.0	0.149442	0.000337	0.204303	0.000522	0.234931	0.000652	0.178611	0.000197
470.0	0.110330	0.000277	0.150126	0.000499	0.175540	0.000564	0.132446	0.000476
480.0	0.095118	0.000329	0.129648	0.000372	0.152148	0.000401	0.114860	0.000247
490.0	0.070011	0.000217	0.095997	0.000232	0.112667	0.000357	0.085199	0.000194
500.0	0.057485	0.000187	0.078454	0.000239	0.093301	0.000279	0.070352	0.000145
510.0	0.046348	0.000149	0.063061	0.000178	0.076425	0.000211	0.058222	0.000146
520.0	0.036314	0.000109	0.049218	0.000167	0.060418	0.000156	0.045936	0.000145
530.0	0.031767	0.000123	0.042701	0.000121	0.053153	0.000134	0.040149	0.000082
540.0	0.029689	0.000124	0.039645	0.000097	0.050016	0.000163	0.037682	0.000093
550.0	0.026921	0.000063	0.035676	0.000093	0.045652	0.000123	0.034379	0.000119
560.0	0.023255	0.000069	0.030560	0.000083	0.039726	0.000094	0.029918	0.000054
570.0	0.019501	0.000088	0.025483	0.000074	0.033646	0.000115	0.025326	0.000080
580.0	0.015862	0.000107	0.020437	0.000092	0.027482	0.000082	0.020713	0.000073
590.0	0.012296	0.000087	0.015800	0.000055	0.021707	0.000087	0.016360	0.000066

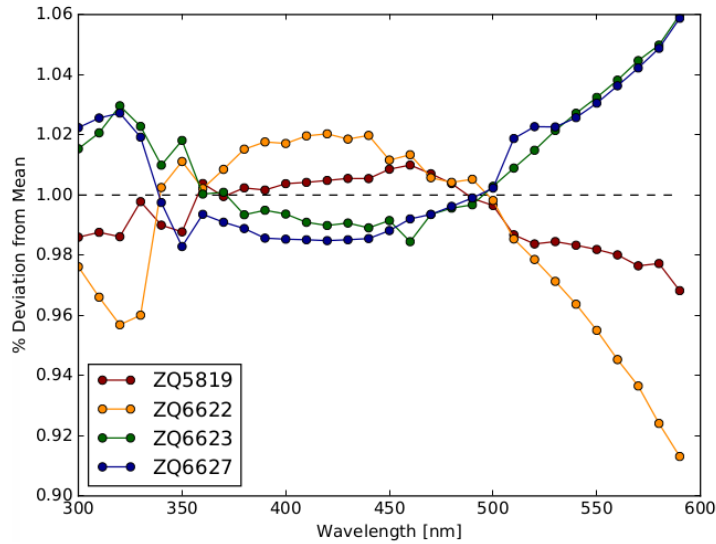


**Figure 11.17:** Percent deviation of the normalized PMT data (dotted coloured lines) with respect to the mean of the normalized PMT data (dashed line).

the elastic channels (355 nm and 532 nm), the PMTs with serial numbers ZQ5819 and ZQ6623 have been mounted on the polychromator, respectively, and the PMTs with serial numbers ZQ6622 and ZQ6627 have been used for the 387 nm and 607 nm readout channel, respectively.

The criterion used for the PMT selection, based on the total current power response, had been sufficient for the polychromator prototype, as we were in an early stage of the commissioning phase. In the case of a change of any of the PMTs, a new characterization would be needed, maybe improved with distinguishing QE and gain of the PMTs.

### 11.3 Barcelona Raman LIDAR results of the commissioning phase

The early operations of the Raman LIDAR started in 2018 [267], and several minor optimizations and modifications have been performed up to now.

First results of the finalized Barcelona Raman LIDAR prototype system were presented at the International Cosmic Ray Conference (ICRC) in 2019 [266]. As showed there, and reported in Fig. 11.18, both the analog and photon counting signals for the two elastic lines and the 387 nm Raman line have been detected and analysed. The results reported on the plot comes from data samples of

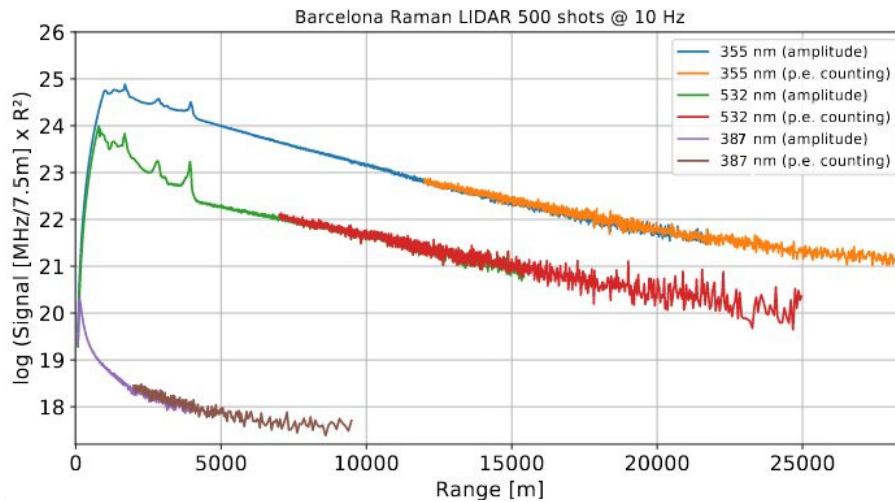


**Figure 11.18:** Logarithm of range-corrected signals from three colour lines of the Barcelona Raman LIDAR based on 500 laser shots. The analog (amplitude) and photo-electron (p.e.) counting parts are shown where applicable. The features visible in the elastic lines below 4 km correspond to aerosol layers and clouds.

500 laser shots in average, each within 50 s total duration. As can be seen, the reconstructed signal (after background subtraction) goes up to 25 km for the elastic channels and only to  $\sim 10$  km for the Raman channel. The maximum altitude reached is lower than expected. This is due to the fact that the gain of the PMTs was reduced because of a saturation of the elastic channels in the near range (at less than  $\sim 1.5$  km). Given this issue, filter methods [291] and Raman inversion [292] have been tested, only in the range of good signal-to-

noise ratio of the analog readout chain. In addition, data were affected by a loss of about 50% of the emitted laser signal, due to the primary mirror low reflectivity. Even with this issue, if testing the LIDAR with the laser at the maximum power, the maximum height reachable goes up to 30 – 40 km at the zenith.

Other performance tests of all the LIDAR components have been performed until nowadays, and the commissioning phase has been carried on until December 2020, when the Barcelona Raman LIDAR was shipped to La Palma for the final part of the commissioning. The last data taken in Barcelona are reported in Fig. 11.19.

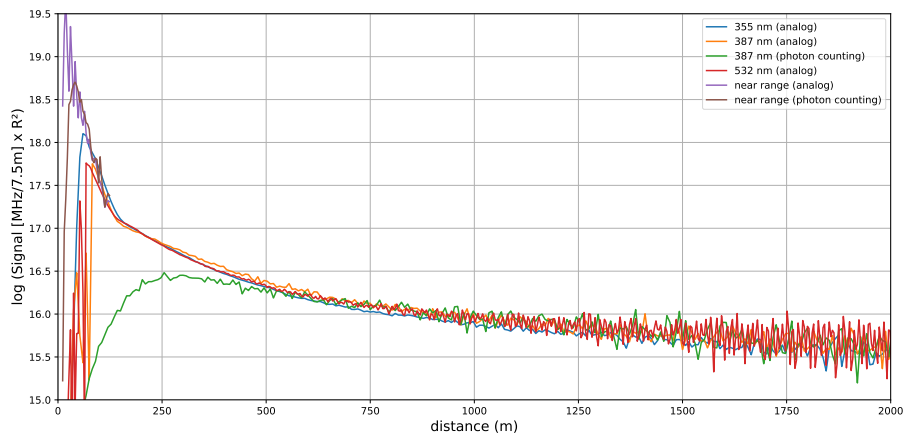


**Figure 11.19:** Logarithm of range-corrected signals from three colour lines of the Barcelona Raman LIDAR and the near-range receiver. All lines, except for the Raman wavelength, have been scaled to the photo-electron (p.e.) counting signal at 387 nm. Data were taken with 500 laser shots.

Since the reflectivity of the primary mirror had come back to its initial value of close to 100%, after the re-coating performed a couple of months ago, the laser power had to be reduced for the data-taken. Additionally, the High Voltage (HV) of the elastic channel PMTs were greatly reduced, in order not to overdrive the respective trans-impedance amplifiers. For this reason, the maximum altitude reached here is about 8 km. To reduce the near-range intensity of the signal received by the PMTs corresponding to the two elastic acquisition channels, a gating system is currently under construction. Once mounted on the receivers, both the laser power and the HVs applied can return to their maximum values and the monitoring of the atmosphere will reach again  $\approx 15$  km a.s.l.

## 11.4 Conclusions and future plans

As showed in the ICRC presentation, the Barcelona Raman LIDAR is an advanced and powerful tool to calibrate the atmosphere for IACTs. Most of the requirements imposed by the CTA collaboration have been fulfilled up to now, and only a few of them are waiting to be satisfied. All the readout channels have been tested, together with the near-range one, and additional Licel mod-

ules have been installed.

In December 2020, the Barcelona Raman LIDAR was moved to La Palma for the commissioning phase in-situ. At the moment the LIDAR container is still waiting to be placed in LST1 area, but it will be done in the next weeks.

The Barcelona Raman LIDAR is foreseen to be fully operational for spring 2021, but this date could have some delay because of a worldwide state alarm due to the pandemic of the new virus SARS-COVID-19.

## Chapter 12

# Conclusions

Indirect dark matter (DM) observations with Imaging Atmospheric Cherenkov Telescopes are carried out by searching for Very High Energy (50 GeV to 100 TeV) photons produced in DM annihilation/decay processes. The Weakly Interacting Massive Particle (WIMP) is the preferred DM candidate for this type of experiments, since its mass fits perfectly in the energy range to which IACTs are most sensitive. Following the  $\Lambda$ -Cold Dark Matter (CDM) scenario, WIMPs, and in general CDM, are expected to be gravitationally bound in halos, in the potential wells of which baryonic structures formed in the early Universe. In the vicinity of our Galaxy, such DM overdensities are expected to be found in dwarf spheroidal satellite galaxies (dSphs), the Galactic Center and Halo and as non-luminous DM subhaloes.

In this thesis, after an introduction to the main concepts, I focused first on the globular cluster M15. This target, in the same way as other globular clusters found in our Galaxy, is not considered a promising DM observation candidate, given its very low mass-to-light (M/L) ratio presented in the literature. Despite moderate to low DM over-densities in the cores of globular clusters have not been excluded so far by observations, high baryonic densities at their centres impede, there, accurate measurements of the velocity dispersion of stars and, thus, experimental validation of models describing the formation and evolution of these objects. Within these limitations, I tried to derive possible sensitivities for WIMP DM annihilation searches from data already acquired with the MAGIC telescopes during a key-science project campaign for the search of millisecond pulsars in M15. I took into account four different possible realizations of the DM density profile. To start, I followed the works of the Whipple and H.E.S.S. collaborations, that attempted to model the M15 DM density profile from its cosmological evolution, and used their density profile estimates for my analysis. Given the absence of a signal in the MAGIC data, I derived statistical upper limits on the velocity-averaged cross-section of WIMP annihilating totally into the  $b\bar{b}$  or  $\tau^+\tau^-$  channels for different DM masses. The results obtained are compatible with the ones of Whipple and H.E.S.S., once rescaled for the MAGIC respective target observation time. To deal with the large systematic uncertainties, due to the many unknowns in a (so far necessary) theoretical modelling of the DM profile of M15 and, in particular, the lack of knowledge on the density profile of the cluster's center,

I considered the density and M/L profiles presented in the work of [198], estimated from N-body simulations. I convoluted the two profiles, taking into account the most optimistic scenario for DM, in which the missing mass is exclusively attributed to WIMP DM, neglecting possible baryonic dark objects, such as neutron stars or black holes. To cross-check the values obtained, I considered also a different sample of N-body simulations [183] for the M/L profile. No major differences in the two DM density profile estimates were found.

Using these estimates, deviating considerably from the Whipple and H.E.S.S. theoretical models towards the core of M15, statistical upper limits (ULs) on  $\langle\sigma_{ann}v\rangle$  reach values down to the order of  $\approx 10^{-29}$  cm<sup>3</sup>s<sup>-1</sup>, better than the limits obtained from the most promising dSphs, but at the same time systematically unreliable, given the optimistic assumption made on the nature of the dark mass. Such toy ULs are useful as rough estimates of the minimum values achievable, awaiting more precise models on the formation and evolution of globular clusters, and particularly new kinematic measurements at their cores.

Further indirect WIMP DM searches presented in this thesis have been performed on dSphs, considered the most promising targets for DM observations with IACTs. The MAGIC Collaboration started a multi-year observational campaign on dSphs in 2011, during which five dSphs were observed, ranked among the ones with the highest expected DM content. I was the main analyst of the last two observed, Draco and Coma Berenices dSphs, and Principal Investigator of the proposal of observation of Coma Berenices dSph. In this thesis, I have presented the analysis and results of WIMP annihilation searches in these two dSphs. No signal from WIMP annihilation was found, and 95% CL ULs on  $\langle\sigma_{ann}v\rangle$  have been set on the  $b\bar{b}$ ,  $\tau^+\tau^-$ ,  $\mu^+\mu^-$  and  $W^+W^-$  annihilation channels, considering 100% branching ratios for each of them.

In addition to this outcome, I presented the MAGIC legacy results on WIMP DM annihilation searches in dSphs, which will soon be published in a dedicated paper, of which I am corresponding author. The legacy results have been obtained from a combination of data of four of the five dSphs observed with the MAGIC telescopes, namely Segue 1, Ursa Major II, Draco and Coma Berenices dSphs (the fifth one, Triangulum II, has been excluded because of still unresolved controversies on its DM content). A revision of Segue 1's analysis was required, as to unify the methodology adopted for the analysis of the different data sets, taking into account the DM morphology of the targets and the same DM density profile estimation approach (with values taken from [119]). With a total amount of 354.3 hours of observational data, the most constraining MAGIC ULs on  $\langle\sigma_{ann}v\rangle$  for WIMP DM, annihilating with 100% branching ratios into the  $b\bar{b}$ ,  $t\bar{t}$ ,  $e^+e^-$ ,  $\mu^+\mu^-$ ,  $\tau^+\tau^-$ ,  $W^+W^-$ ,  $ZZ$ ,  $hh$  and  $\gamma\gamma$  channels, have been obtained. These results set also the most constraining ULs between few TeV and 100 TeV WIMP DM masses among all gamma-ray experiments. The window for possible velocity-averaged annihilation cross-sections for WIMPs has now been narrowed down further, taking advantage of different analysis approaches developed and the wealth of data provided by astronomical installations and experiments. With future results on DM annihilation searches provided by CTA, WIMP DM will be detected or definitively rejected, thus closing completely the WIMP observational window.

The last part of the thesis is devoted to the Barcelona Raman LIDAR, an instrumental development in which I worked in parallel to the DM searches with the MAGIC telescopes. The system, which is based on a previous CLUE telescope system, has been built to monitor the atmosphere above CTA, for its northern array on La Palma. It is based on the Raman LIDAR technique, and can measure atmospheric extinction through four acquisition channels, two devoted to elastically backscattered light (emitted by a powerful pulsed laser mounted on the telescope structure) and two further channels dedicated to capture laser light after Raman backscattering. In addition, a near-range system, with its respective acquisition channel, has been added, in order to enlarge the LIDAR's sensing range.

Several tests were carried out during the years to characterize the components mounted on the Raman LIDAR. I reported on a couple of them in the last chapter of this thesis.

My manuscript ends with the latest results obtained with the Barcelona Raman LIDAR, looking at the sky above the Universitat Autònoma de Barcelona, a place where it was located before being shipped to La Palma for the final part of its commissioning phase.

# Acknowledgements

First of all, I would like to thank my supervisors Markus Gaug and Lluís Font Guiteras, without whom I would not have reached this step. They helped me since the first day I came to Barcelona, when I was speaking very little Spanish and nothing of Catalan, and they have been like a family for me in these four years. I would thank them for making me grow up from a scientific and a human point of view, supporting me and trusting in my capabilities. At last, but not least, I would thank them very much for revising my manuscript and helping me to improve it.

I would like also to thank all the people with whom I collaborate and that gave their contribution to this work. Following the order of the thesis chapters, I want to thank Justin Read and Miguel Ángel Sanchez Conde for their suggestions on how to proceed with the M15 study, and Julian Sitarek for sharing with me the event reconstructed files. I want also to thank Lorenzo Bellizzi for his cross-check analysis and also for trusting in my work.

For the dwarf spheroidal satellite galaxies analyses, I would like to thank Daniel Kerzberg, Daniele Ninci and Vincenzo Vitale for their contribution to the work, their cross-check analyses and for being co-author of the paper that will be published soon. I want to thank also Michele Doro and David Paneque that suggested me the analysis combination, and the MAGIC collaboration in totality for supporting my work.

A big thank to Javier Rico Castro, that introduced me to the dwarf spheroidal satellite galaxies project and that let me continue with the M15 work, already started by Joaquim Palacio Navarro.

I want to thank also Oscar Blanch Bigas for letting me join, and enjoy, the LST1 camera project.

A thank also to my office-mate Miguel Ángel Caballero Pacheco, and the new entry Santi Ubach Ramirez, that supported me during these last years. And a thank to all the people of the C3 flat 3, especially to Maite Romero.

To conclude, I would like to thank a lot my boyfriend, who was at my side during these years, helped me when I was getting crazy in coding or analysing data, and during all the manuscript process. I want to thank also my friends, and, last but not least, I want to say a big "thank you" to my mother, who has always been present when I needed, and trusted in me, also when I was not doing it.

And to the people not directly mentioned here, thank you for being part of this process, called life.

# Bibliography

- [1] Longair M.S. (1992). *High-energy astrophysics*
- [2] Moralejo Olaizola A. (2000). *Búsqueda de fuentes cósmicas de radiación gamma de muy alta energía con el detector AIROBICC*. Ph.D. thesis, Universidad Complutense de Madrid
- [3] Wagner R.M. (2006). *Measurement of Very High Energy Gamma-Ray Emission from Four Blazars Using the MAGIC Telescope and a Comparative Blazar Study*. Ph.D. thesis, Munich, Tech. U.
- [4] Grieder P.K. (2010). *Atmospheric Cherenkov Radiation*, pp. 835–878. Springer Berlin Heidelberg, Berlin, Heidelberg
- [5] Observatory C.T.A. (2016). *cta24*. <https://www.cta-observatory.org/project/technology/cta24/>
- [6] Benbow W. (2006). *The H.E.S.S. experiment*. AIP Conf. Proc., volume 842, pp. 998–1000
- [7] Park N. & VERITAS Collaboration (2015). *Performance of the VERITAS experiment*. In *Proceedings, 34th International Cosmic Ray Conference (ICRC 2015): The Hague, The Netherlands, July 30-August 6, 2015*, volume 34 of *International Cosmic Ray Conference*, p. 771
- [8] Atwood W.B. *et al.* (2009). *The Large Area Telescope on the Fermi Gamma-ray Space Telescope Mission*. *Astrophys. J.*, volume 697, pp. 1071–1102
- [9] Mostafá M.A. (2014). *The High-Altitude Water Cherenkov Observatory*. *Braz. J. Phys.*, volume 44, pp. 571–580. [0933(2013)]
- [10] Acharya B.S. *et al.* (2018). *Science with the Cherenkov Telescope Array*. WSP
- [11] Zwicky F. (1933). *Die Rotverschiebung von extragalaktischen Nebeln*. *Helv. Phys. Acta*, volume 6, pp. 110–127. [Gen. Rel. Grav.41,207(2009)]
- [12] Smith S. (1936). *The Mass of the Virgo Cluster*. *Astrophys. J.*, volume 83, pp. 23–30
- [13] Rubin V.C., Ford W. Kent J. & Thonnard N. (1978). *Extended rotation curves of high-luminosity spiral galaxies. IV. Systematic dynamical properties, Sa through Sc*. *Astrophys. J.*, volume 225, pp. L107–L111

- [14] Smoot G.F. *et al.* (1992). *Structure in the COBE differential microwave radiometer first year maps*. *Astrophys. J.*, volume 396, pp. L1–L5
- [15] Squires G., Kaiser N., Babul A. *et al.* (1996). *The Dark matter, gas and galaxy distributions in Abell-2218: A Weak gravitational lensing and x-ray analysis*. *Astrophys. J.*, volume 461, p. 572
- [16] Markevitch M., Gonzalez A.H., Clowe D. *et al.* (2004). *Direct constraints on the dark matter self-interaction cross-section from the merging galaxy cluster 1E0657-56*. *Astrophys. J.*, volume 606, pp. 819–824
- [17] Clowe D., Bradač M., Gonzalez A.H. *et al.* (2006). *A direct empirical proof of the existence of dark matter*. *The Astrophysical Journal*, volume 648, p. L109–L113
- [18] Carlstrom J.E., Holder G.P. & Reese E.D. (2002). *Cosmology with the Sunyaev-Zel'dovich effect*. *Ann. Rev. Astron. Astrophys.*, volume 40, pp. 643–680
- [19] Milgrom M. (1983). *A Modification of the Newtonian dynamics as a possible alternative to the hidden mass hypothesis*. *Astrophys. J.*, volume 270, pp. 365–370
- [20] — (1983). *A Modification of the Newtonian dynamics: Implications for galaxies*. *Astrophys. J.*, volume 270, pp. 371–383
- [21] — (1983). *A modification of the Newtonian dynamics: implications for galaxy systems*. *Astrophys. J.*, volume 270, pp. 384–389
- [22] Blumenthal G.R., Faber S.M., Primack J.R. *et al.* (1984). *Formation of Galaxies and Large Scale Structure with Cold Dark Matter*. *Nature*, volume 311, pp. 517–525. [96(1984)]
- [23] Laletin M. & Cudell J.R. (2019). *Strongly interacting dark matter and the DAMA signal*. *Journal of Cosmology and Astroparticle Physics*, volume 2019, pp. 010–010
- [24] Beylin V., Khlopov M., Kuksa V. *et al.* (2020). *New physics of strong interaction and Dark Universe*. *Universe*, volume 6, p. 196
- [25] Smirnov J. & Beacom J.F. (2020). *New freezeout mechanism for strongly interacting dark matter*. *Phys. Rev. Lett.*, volume 125, p. 131301
- [26] Aghanim N., Akrami Y., Ashdown M. *et al.* (2020). *Planck 2018 results. vi. cosmological parameters*. *Astronomy & Astrophysics*, volume 641, p. A6
- [27] Einstein A. (1916). *The Foundation of the General Theory of Relativity*. *Annalen Phys.*, volume 49, pp. 769–822
- [28] Fixsen D.J. (2009). *The temperature of the cosmic microwave background*. *The Astrophysical Journal*, volume 707, pp. 916–920
- [29] Akrami Y., Ashdown M., Aumont J. *et al.* (2020). *Planck 2018 results. iv. diffuse component separation*. *Astronomy & Astrophysics*, volume 641, p. A4

- [30] Dhawan S., Jha S.W. & Leibundgut B. (2018). *Measuring the hubble constant with type ia supernovae as near-infrared standard candles*. *Astronomy & Astrophysics*, volume 609, p. A72
- [31] Ibarra A. (2015). *Neutrinos and dark matter*. AIP Conference Proceedings, volume 1666, p. 140004
- [32] Baumann D., Beutler F., Flauger R. *et al.* (2019). *First constraint on the neutrino-induced phase shift in the spectrum of baryon acoustic oscillations*. *Nature Physics*, volume 15, p. 465–469
- [33] Bond J., Efstathiou G. & Silk J. (1980). *Massive Neutrinos and the Large Scale Structure of the Universe*. *Phys. Rev. Lett.*, volume 45, pp. 1980–1984
- [34] Bond J.R. & Szalay A.S. (1983). *The collisionless damping of density fluctuations in an expanding universe*. *The Astrophysical Journal*, volume 274, pp. 443–468
- [35] Blanton M.R., Bershadsky M.A., Abolfathi B. *et al.* (2017). *Sloan Digital Sky Survey IV: Mapping the Milky Way, Nearby Galaxies, and the Distant Universe*. *Astronomical Journal*, volume 154, p. 28
- [36] Bennett C.L., Larson D., Weiland J.L. *et al.* (2013). *Nine-year wilkinson microwave anisotropy probe (wmap) observations: Final maps and results*. *The Astrophysical Journal Supplement Series*, volume 208, p. 20
- [37] Colless M., Dalton G., Maddox S. *et al.* (2001). *The 2dF Galaxy Redshift Survey: spectra and redshifts*. *Monthly Notices of the Royal Astronomical Society*, volume 328, pp. 1039–1063
- [38] Springel V., White S.D.M., Jenkins A. *et al.* (2005). *Simulations of the formation, evolution and clustering of galaxies and quasars*. *Nature*, volume 435, pp. 629–636
- [39] Springel V., Frenk C.S. & White S.D.M. (2006). *The large-scale structure of the universe*. *Nature*, volume 440, p. 1137–1144
- [40] Peebles P.J.E. (1982). *Primeval adiabatic perturbations - Effect of massive neutrinos*. *The Astrophysical Journal*, volume 258, pp. 415–424
- [41] Schramm D.N. & Steigman G. (1981). *Relic Neutrinos and the Density of the Universe*. *Astrophys. J.*, volume 243, p. 1
- [42] Bullock J.S. & Boylan-Kolchin M. (2017). *Small-scale challenges to the  $\lambda$ cdm paradigm*. *Annual Review of Astronomy and Astrophysics*, volume 55, pp. 343–387
- [43] Moore B., Ghigna S., Governato F. *et al.* (1999). *Dark Matter Substructure within Galactic Halos*. *The Astrophysical Journal Letters*, volume 524, pp. L19–L22
- [44] Swaters R.A., Madore B.F., van den Bosch F.C. *et al.* (2003). *The central mass distribution in dwarf and low surface brightness galaxies*. *The Astrophysical Journal*, volume 583, p. 732–751

- [45] Boylan-Kolchin M., Bullock J.S. & Kaplinghat M. (2011). *Too big to fail? the puzzling darkness of massive milky way subhaloes*. Monthly Notices of the Royal Astronomical Society: Letters, volume 415, p. L40–L44
- [46] Lisanti M. (2016). *Lectures on dark matter physics*. New Frontiers in Fields and Strings
- [47] Gilman D., Birrer S., Nierenberg A. *et al.* (2019). *Warm dark matter chills out: constraints on the halo mass function and the free-streaming length of dark matter with eight quadruple-image strong gravitational lenses*. Monthly Notices of the Royal Astronomical Society, volume 491, p. 6077–6101
- [48] Kim S.Y., Peter A.H. & Hargis J.R. (2018). *Missing satellites problem: Completeness corrections to the number of satellite galaxies in the milky way are consistent with cold dark matter predictions*. Physical Review Letters, volume 121
- [49] Tulin S. & Yu H.B. (2018). *Dark matter self-interactions and small scale structure*. Physics Reports, volume 730, p. 1–57
- [50] Bertone G. & Tait Tim M.P. (2018). *A new era in the search for dark matter*. Nature, volume 562, pp. 51–56
- [51] Steigman G., Dasgupta B. & Beacom J.F. (2012). *Precise Relic WIMP Abundance and its Impact on Searches for Dark Matter Annihilation*. Phys. Rev., volume D86, p. 023506
- [52] Feng J.L. (2010). *Dark matter candidates from particle physics and methods of detection*. Annual Review of Astronomy and Astrophysics, volume 48, p. 495–545
- [53] Gondolo P. & Gelmini G. (1991). *Cosmic abundances of stable particles: improved analysis*. Nuclear Physics B - NUCL PHYS B, volume 360, pp. 145–179
- [54] Bauer M. & Plehn T. (2019). *Yet Another Introduction to Dark Matter: The Particle Physics Approach*, volume 959 of *Lecture Notes in Physics*. Springer
- [55] Boehm C., Ensslin T.A. & Silk J. (2004). *Can Annihilating dark matter be lighter than a few GeVs?*. J. Phys., volume G30, pp. 279–286
- [56] Witten E. (1981). *Mass Hierarchies in Supersymmetric Theories*. Phys. Lett. B, volume 105, p. 267
- [57] Datta A. (2002). *R-parity-violating susy and cp violation in  $b \rightarrow \varphi ks$* . Physical Review D, volume 66
- [58] Ellis J.R., Kelley S. & Nanopoulos D.V. (1992). *Constraints from gauge coupling unification on the scale of supersymmetry breaking*. Phys. Lett. B, volume 287, pp. 95–100
- [59] Fayet P. (1976). *Supersymmetry and weak, electromagnetic and strong interactions*. Physics Letters B, volume 64, pp. 159–162

- [60] Ellis J.R., Hagelin J., Nanopoulos D.V. *et al.* (1984). *Supersymmetric Relics from the Big Bang*. Nucl. Phys. B, volume 238, pp. 453–476
- [61] Chamseddine A.H., Arnowitt R.L. & Nath P. (1982). *Locally Supersymmetric Grand Unification*. Phys. Rev. Lett., volume 49, p. 970
- [62] Benakli K., Chen Y., Dudas E. *et al.* (2017). *Minimal model of gravitino dark matter*. Physical Review D, volume 95
- [63] Bringmann T., Bergström L. & Edsjö J. (2008). *New gamma-ray contributions to supersymmetric dark matter annihilation*. Journal of High Energy Physics, volume 2008, p. 049–049
- [64] McGaugh S.S. (2012). *The baryonic tully-fisher relation of gas-rich galaxies as a test of  $\lambda$ CDM and mond*. The Astronomical Journal, volume 143, p. 40
- [65] Watkins R., Feldman H.A. & Hudson M.J. (2009). *Consistently large cosmic flows on scales of 100  $h^{-1}$  mpc: a challenge for the standard  $\lambda$ cdm cosmology*. Monthly Notices of the Royal Astronomical Society, volume 392, p. 743–756
- [66] Feldman H.A., Watkins R. & Hudson M.J. (2010). *Cosmic flows on 100  $h^{-1}$  mpc scales: standardized minimum variance bulk flow, shear and octupole moments*. Monthly Notices of the Royal Astronomical Society, volume 407, p. 2328–2338
- [67] Copi C.J., Huterer D., Schwarz D.J. *et al.* (2007). *Uncorrelated universe: Statistical anisotropy and the vanishing angular correlation function in wmap years 1-3*. Physical Review D, volume 75
- [68] — (2009). *No large-angle correlations on the non-Galactic microwave sky*. Monthly Notices of the Royal Astronomical Society, volume 399, pp. 295–303
- [69] Moffat J.W. (2006). *Scalar–tensor–vector gravity theory*. Journal of Cosmology and Astroparticle Physics, volume 2006, pp. 004–004
- [70] Aalseth C.E., Barbeau P.S., Colaresi J. *et al.* (2014). *Search for An Annual Modulation in Three Years of CoGeNT Dark Matter Detector Data*. arXiv e-prints, p. arXiv:1401.3295
- [71] Bernabei R. *et al.* (2020). *The DAMA project: Achievements, implications and perspectives*. Prog. Part. Nucl. Phys., volume 114, p. 103810
- [72] Aprile E., Aalbers J., Agostini F. *et al.* (2018). *Dark matter search results from a one ton-year exposure of xenon1t*. Phys. Rev. Lett., volume 121, p. 111302
- [73] — (2020). *Excess electronic recoil events in xenon1t*. Physical Review D, volume 102
- [74] Xia J. *et al.* (2019). *PandaX-II Constraints on Spin-Dependent WIMP-Nucleon Effective Interactions*. Phys. Lett. B, volume 792, pp. 193–198

- [75] Akerib D., Araújo H., Bai X. *et al.* (2016). *Results on the spin-dependent scattering of weakly interacting massive particles on nucleons from the run 3 data of the lux experiment.* Physical Review Letters, volume 116
- [76] Amole C., Ardid M., Arnquist I. *et al.* (2019). *Dark matter search results from the complete exposure of the pico-60 c3f8 bubble chamber.* Physical Review D, volume 100
- [77] Bernabei R. *et al.* (2003). *Further results on the WIMP annual modulation signature by DAMA/NaI.* PoS, volume AHEP2003, p. 063
- [78] — (2014). *The Annual Modulation Signature for Dark Matter: DAMA/LIBRA-Phase1 Results and Perspectives.* Adv. High Energy Phys., volume 2014, p. 605659
- [79] Akerib D.S., Alsum S., Araújo H.M. *et al.* (2017). *Limits on spin-dependent wimp-nucleon cross section obtained from the complete lux exposure.* Phys. Rev. Lett., volume 118, p. 251302
- [80] Aprile E., Alfonsi M., Arisaka K. *et al.* (2013). *Limits on spin-dependent wimp-nucleon cross sections from 225 live days of xenon100 data.* Phys. Rev. Lett., volume 111, p. 021301
- [81] Aprile E. *et al.* (2019). *Constraining the spin-dependent WIMP-nucleon cross sections with XENON1T.* Phys. Rev. Lett., volume 122, p. 141301
- [82] Evans L. (2007). *The large hadron collider.* New Journal of Physics, volume 9, pp. 335–335
- [83] Collaboration T.A., Aad G., Abat E. *et al.* (2008). *The ATLAS experiment at the CERN large hadron collider.* Journal of Instrumentation, volume 3, pp. S08003–S08003
- [84] Bayatian G.L. *et al.* (2006). *CMS Physics: Technical Design Report Volume 1: Detector Performance and Software*
- [85] Giagu S. (2019). *WIMP Dark Matter Searches With the ATLAS Detector at the LHC.* Front. in Phys., volume 7, p. 75
- [86] Orsi S. (2007). *PAMELA: A payload for antimatter matter exploration and light nuclei astrophysics.* Nucl. Instrum. Meth. A, volume 580, pp. 880–883
- [87] Bindi V. *et al.* (2014). *Calibration and performance of the AMS-02 time of flight detector in space.* Nucl. Instrum. Meth. A, volume 743, pp. 22–29
- [88] Vannuccini E., Aramaki T., Bird R. *et al.* (2018). *GAPS, low-energy antimatter for indirect dark-matter search.* arXiv e-prints, p. arXiv:1812.06691
- [89] Reed C. (2009). *Measuring neutrinos with the antares telescope.* AIP Conference Proceedings, volume 1182
- [90] Aartsen M., Ackermann M., Adams J. *et al.* (2017). *The icecube neutrino observatory: instrumentation and online systems.* Journal of Instrumentation, volume 12, p. P03012–P03012

- [91] Aartsen M.G., Ackermann M., Adams J. *et al.* (2017). *Search for neutrinos from dark matter self-annihilations in the center of the milky way with 3 years of icecube/deeppcore*. The European Physical Journal C, volume 77
- [92] Archambault S. *et al.* (2017). *Dark Matter Constraints from a Joint Analysis of Dwarf Spheroidal Galaxy Observations with VERITAS*. Phys. Rev., volume D95, p. 082001
- [93] Ahnen M.L. *et al.* (2016). *Limits to Dark Matter Annihilation Cross-Section from a Combined Analysis of MAGIC and Fermi-LAT Observations of Dwarf Satellite Galaxies*. JCAP, volume 1602, p. 039
- [94] Abdallah H. *et al.* (2016). *Search for dark matter annihilations towards the inner Galactic halo from 10 years of observations with H.E.S.S.* Phys. Rev. Lett., volume 117, p. 111301
- [95] Albert A. *et al.* (2020). *Search for dark matter towards the Galactic Centre with 11 years of ANTARES data*. Phys. Lett. B, volume 805, p. 135439
- [96] Wood C. (2020). *The search for dark matter is dramatically expanding*. Last access: 2021/01/28
- [97] Rott C. (2018). *Status of Dark Matter Searches (Rapporteur Talk)*. PoS, volume ICRC2017, p. 1119
- [98] Merritt D., Milosavljevic M., Verde L. *et al.* (2002). *Dark matter spikes and annihilation radiation from the galactic center*. Phys. Rev. Lett., volume 88, p. 191301
- [99] Ackermann M., Ajello M., Albert A. *et al.* (2017). *The fermi galactic center gev excess and implications for dark matter*. The Astrophysical Journal, volume 840, p. 43
- [100] Yuan Q. & Zhang B. (2014). *Millisecond pulsar interpretation of the galactic center gamma-ray excess*. Journal of High Energy Astrophysics, volume 3-4
- [101] Strigari L.E., Koushiappas S.M., Bullock J.S. *et al.* (2008). *The Most Dark Matter Dominated Galaxies: Predicted Gamma-ray Signals from the Faintest Milky Way Dwarfs*. Astrophys. J., volume 678, p. 614
- [102] Collaboration T.F.L. (2010). *Constraints on dark matter annihilation in clusters of galaxies with the fermi large area telescope*
- [103] Boyarsky A., Neronov A., Ruchayskiy O. *et al.* (2006). *Restrictions on parameters of sterile neutrino dark matter from observations of galaxy clusters*. Phys. Rev. D, volume 74, p. 103506
- [104] Acciari V.A. *et al.* (2018). *Constraining Dark Matter lifetime with a deep gamma-ray survey of the Perseus Galaxy Cluster with MAGIC*. Phys. Dark Univ., volume 22, pp. 38–47

- [105] Nieto D., Aleksić J., Barrio J.A. *et al.* (2011). *The search for galactic dark matter clump candidates with fermi and magic*. Proceedings of the 32nd International Cosmic Ray Conference, ICRC 2011, volume 5
- [106] Palacio Navarro J. (2018). *Indirect dark matter searches on the Triangulum II dwarf spheroidal galaxy and the Perseus galaxy cluster with the MAGIC telescopes*. Ph.D. thesis, Barcelona, Autònoma U.
- [107] Navarro J.F., Frenk C.S. & White S.D.M. (1996). *The structure of cold dark matter halos*. The Astrophysical Journal, volume 462, p. 563
- [108] Einasto J. (1965). *On the Construction of a Composite Model for the Galaxy and on the Determination of the System of Galactic Parameters*. Trudy Astrofizicheskogo Instituta Alma-Ata, volume 5, pp. 87–100
- [109] Iocco F., Pato M., Bertone G. *et al.* (2011). *Dark matter distribution in the milky way: microlensing and dynamical constraints*. Journal of Cosmology and Astroparticle Physics, volume 2011, p. 029–029
- [110] Read J.I. (2014). *The local dark matter density*. Journal of Physics G: Nuclear and Particle Physics, volume 41, p. 063101
- [111] Gaskins J.M. (2016). *A review of indirect searches for particle dark matter*. Contemporary Physics, volume 57, p. 496–525
- [112] Burkert A. (1995). *The structure of dark matter halos in dwarf galaxies*. The Astrophysical Journal, volume 447
- [113] Fornasa M. & Green A.M. (2014). *Self-consistent phase-space distribution function for the anisotropic dark matter halo of the milky way*. Physical Review D, volume 89
- [114] Walker M.G. & Peñarrubia J. (2011). *A method for measuring (slopes of) the mass profiles of dwarf spheroidal galaxies*. The Astrophysical Journal, volume 742, p. 20
- [115] Read J.I., Walker M.G. & Steger P. (2018). *The case for a cold dark matter cusp in Draco*. Monthly Notices of the Royal Astronomical Society, volume 481, pp. 860–877
- [116] Charbonnier A., Combet C., Daniel M. *et al.* (2011). *Dark matter profiles and annihilation in dwarf spheroidal galaxies: perspectives for present and future  $\gamma$ -ray observatories - i. the classical dwarf spheroidal galaxies*. Monthly Notices of the Royal Astronomical Society, volume 418, p. 1526–1556
- [117] Zhao H. (1996). *Analytical models for galactic nuclei*. Monthly Notices of the Royal Astronomical Society, volume 278, p. 488–496
- [118] Hernquist L. (1990). *An Analytical Model for Spherical Galaxies and Bulges*. The Astrophysical Journal, volume 356, p. 359
- [119] Geringer-Sameth A., Koushiappas S.M. & Walker M. (2015). *Dwarf galaxy annihilation and decay emission profiles for dark matter experiments*. The Astrophysical Journal, volume 801, p. 74

- [120] Strigari L.E., Koushiappas S.M., Bullock J.S. *et al.* (2007). *Precise constraints on the dark matter content of milky way dwarf galaxies for gamma-ray experiments*. Phys. Rev. D, volume 75, p. 083526
- [121] Martinez G.D., Bullock J.S., Kaplinghat M. *et al.* (2009). *Indirect Dark Matter detection from Dwarf satellites: joint expectations from astrophysics and supersymmetry*. JCAP, volume 2009, p. 014
- [122] Aleksić J., Ansoldi S., Antonelli L. *et al.* (2016). *The major upgrade of the magic telescopes, part ii: A performance study using observations of the crab nebula*. Astroparticle Physics, volume 72, p. 76–94
- [123] Strom D. (2020). *The MAGIC Sum-Trigger-II System*. PoS, volume ICRC2019, p. 802
- [124] Acciari V.A., Ansoldi S., Antonelli L.A. *et al.* (2020). *Magic very large zenith angle observations of the crab nebula up to 100 tev*. Astronomy & Astrophysics, volume 635, p. A158
- [125] Manganaro M., Becerra J., Nievas M. *et al.* (2016). *Latest magic discoveries pushing redshift boundaries in the astrophysics*. Journal of Physics: Conference Series, volume 718, p. 052022
- [126] MAGIC Collaboration, Acciari V.A., Ansoldi S. *et al.* (2019). *Teraelectronvolt emission from the  $\gamma$ -ray burst grb 190114c*. Nature, volume 575, p. 455–458
- [127] Acciari V., Ansoldi S., Antonelli L. *et al.* (2020). *MAGIC observations of the nearby short gamma-ray burst GRB 160821B*. Technical Report arXiv:2012.07193. 13 pages, 4 figures, Accepted for publication in ApJ. Corresponding authors: K. Noda, L. Nava, and S. Inoue
- [128] Aartsen M., Ackermann M., Adams J. *et al.* (2018). *Multimessenger observations of a flaring blazar coincident with high-energy neutrino icecube-170922a*. Science, volume 361, p. eaat1378
- [129] De Lotto B., Ansoldi S., Antonelli A. *et al.* (2016). *MAGIC electromagnetic follow-up of gravitational wave alerts*. IAU Symp., volume 324, pp. 287–290
- [130] Berti A., Antonelli L.A., Bosnjak Z. *et al.* (2019). *Searching for GRBs at VHE with MAGIC: the status before CTA*. In *36th International Cosmic Ray Conference (ICRC2019)*, volume 36 of *International Cosmic Ray Conference*, p. 634
- [131] Aartsen M.G. *et al.* (2016). *Very High-Energy Gamma-Ray Follow-Up Program Using Neutrino Triggers from IceCube*. JINST, volume 11, p. P11009
- [132] Ahnen M., Ansoldi S., Antonelli L. *et al.* (2017). *Performance of the magic telescopes under moonlight*. Astroparticle Physics, volume 94, pp. 29 – 41

- [133] Guberman D.A. (2018). *MAGIC observations with bright Moon and their application to measuring the VHE gamma-ray spectral cut-off of the PeVatron candidate Cassiopeia A*. Ph.D. thesis, Barcelona, Autònoma U.
- [134] Clarke A. (1984). *Profiles of the Future: An Inquiry Into the Limits of the Possible*. Holt, Rinehart, and Winston
- [135] Collaboration T.M. (2014). *Facebook profile picture*. <https://www.facebook.com/MAGICtelescopes/photos/a.349960845151612/349960851818278>
- [136] Zanin R. & Cortina J. (2009). *The Central Control of the MAGIC telescopes*
- [137] Mirzoyan R. & Lorentz E. (1997). *On the Calibration Accuracy of Light Sensors in Atmospheric Cherenkov Fluorescence and Neutrino Experiments*. In *International Cosmic Ray Conference*, volume 7 of *International Cosmic Ray Conference*, pp. 265–268
- [138] Gaug M. (2006). *Calibration of the MAGIC telescope and observation of  $\gamma$ -ray bursts*. Ph.D. thesis, Barcelona, Autònoma U.
- [139] Sitarek J., Gaug M., Mazin D. *et al.* (2013). *Analysis techniques and performance of the domino ring sampler version 4 based readout for the magic telescopes*. Nuclear Instruments and Methods in Physics Research Section A: Accelerators, Spectrometers, Detectors and Associated Equipment, volume 723
- [140] López-Coto R., Mazin D., Paoletti R. *et al.* (2016). *The topo-trigger: a new concept of stereo trigger system for imaging atmospheric cherenkov telescopes*. Journal of Instrumentation, volume 11, p. P04005–P04005
- [141] Fruck C., Gaug M., Zanin R. *et al.* (2014). *A novel LIDAR-based Atmospheric Calibration Method for Improving the Data Analysis of MAGIC*. In *Proceedings, 33rd International Cosmic Ray Conference (ICRC2013): Rio de Janeiro, Brazil, July 2-9, 2013*, p. 1054
- [142] Albert J., Aliu E., Anderhub H. *et al.* (2008). *Fadc signal reconstruction for the magic telescope*. Nuclear Instruments and Methods in Physics Research Section A: Accelerators, Spectrometers, Detectors and Associated Equipment, volume 594, pp. 407 – 419
- [143] Aleksić J., Ansoldi S., Antonelli L. *et al.* (2016). *The major upgrade of the magic telescopes, part i: The hardware improvements and the commissioning of the system*. Astroparticle Physics, volume 72, p. 61–75
- [144] Hillas A.M. (1985). *Cerenkov Light Images of EAS Produced by Primary Gamma Rays and by Nuclei*. In *19th International Cosmic Ray Conference (ICRC19), Volume 3*, volume 3 of *International Cosmic Ray Conference*, p. 445
- [145] Ninci D. (2020). *Search for gamma-ray signals from dark matter annihilation or decay at the Draco dwarf galaxy and the Galactic Halo with MAGIC*. Ph.D. thesis, Barcelona, Autònoma U.

- [146] (1994). *Muon ring images with an atmospheric Čerenkov telescope*. Astroparticle Physics, volume 2, pp. 1 – 11
- [147] Albert J., Aliu E., Anderhub H. *et al.* (2008). *Implementation of the random forest method for the imaging atmospheric cherenkov telescope magic*. Nuclear Instruments and Methods in Physics Research Section A: Accelerators, Spectrometers, Detectors and Associated Equipment, volume 588, p. 424–432
- [148] Brun R. & Rademakers F. (1997). *ROOT: An object oriented data analysis framework*. Nucl. Instrum. Meth. A, volume 389, pp. 81–86
- [149] Zanin R. (2013). *MARS, the MAGIC analysis and reconstruction software*. In *33rd International Cosmic Ray Conference*, p. 0773
- [150] Fruck C., Gaug M., Zanin R. *et al.* (2014). *A novel LIDAR-based Atmospheric Calibration Method for Improving the Data Analysis of MAGIC*. arXiv e-prints, p. arXiv:1403.3591
- [151] Fruck C. (2015). *The Galactic Center resolved with MAGIC and a new technique for Atmospheric Calibration*. Dissertation, Technische Universität München, München
- [152] Pardo S., Nieto D., Oya I. *et al.* (2011). *Onsite analysis of the MAGIC telescopes*. In M.R. Zapatero Osorio, J. Gorgas, J. Maíz Apellániz, J.R. Pardo & A. Gil de Paz (editors), *Highlights of Spanish Astrophysics VI*, pp. 779–779
- [153] Ahnen M., Ansoldi S., Antonelli L. *et al.* (2017). *Performance of the magic telescopes under moonlight*. Astroparticle Physics, volume 94, p. 29–41
- [154] McCarthy D. (1998). *The julian and modified julian dates*. Journal for the History of Astronomy, volume 29, p. 327
- [155] Fruck C. & Gaug M. (2015). *Atmospheric monitoring in MAGIC and data corrections*. In *European Physical Journal Web of Conferences*, volume 89 of *AtmoHEAD 2014: Atmospheric Monitoring for High Energy AstroParticle Detectors*, p. 02003
- [156] López Coto R. (2017). *The Imaging Atmospheric Cherenkov Technique and the IACTs MAGIC and CTA*, pp. 15–64. Springer International Publishing, Cham
- [157] Ahnen M.L. *et al.* (2018). *Indirect dark matter searches in the dwarf satellite galaxy Ursa Major II with the MAGIC Telescopes*. JCAP, volume 1803, p. 009
- [158] Li T.P. & Ma Y.Q. (1983). *Analysis methods for results in gamma-ray astronomy*. The Astrophysical Journal, volume 272, pp. 317–324
- [159] Rolke W.A., López A.M. & Conrad J. (2005). *Limits and confidence intervals in the presence of nuisance parameters*. Nuclear Instruments and Methods in Physics Research Section A: Accelerators, Spectrometers, Detectors and Associated Equipment, volume 551, p. 493–503

- [160] Aleksic J., Rico J. & Martinez M. (2012). *Optimized analysis method for indirect dark matter searches with Imaging Air Cherenkov Telescopes*. JCAP, volume 1210, p. 032
- [161] Rico J., Nigro C., Kerszberg D. *et al.* (2020). *glike: numerical maximization of heterogeneous joint likelihood functions of a common free parameter plus nuisance parameters*. Zenodo, volume <https://doi.org/10.5281/zenodo.3967385>
- [162] Cirelli M., Corcella G., Hektor A. *et al.* (2011). *PPPC 4 DM ID: A Poor Particle Physicist Cookbook for Dark Matter Indirect Detection*. JCAP, volume 1103, p. 051. [Erratum: JCAP1210,E01(2012)]
- [163] Wilks S.S. (1938). *The large-sample distribution of the likelihood ratio for testing composite hypotheses*. Ann. Math. Statist., volume 9, pp. 60–62
- [164] Aleksic J. *et al.* (2014). *Optimized dark matter searches in deep observations of Segue 1 with MAGIC*. JCAP, volume 1402, p. 008
- [165] Acciari V. *et al.* (2019). *Deep observations of the globular cluster M15 with the MAGIC telescopes*. Mon. Not. Roy. Astron. Soc., volume 484, pp. 2876–2885
- [166] Banerjee S. & Kroupa P. (2011). *A new type of compact stellar population: Dark star clusters*. The Astrophysical Journal, volume 741, p. L12
- [167] (MTU) R.N. & (USRA) J.B. (2004). *M39: Open cluster in cygnus*
- [168] of Physics D. & Astronomy U.o.I. *Exploring the night sky:star wheels and star walk*
- [169] Richmond M. (2014). *Interpreting the hr diagram of stellar clusters*
- [170] Meylan G. & Heggie D. (1997). *Internal dynamics of globular clusters*. Astronomy and Astrophysics Review, volume 8, p. 1–143
- [171] Shu F.H. (1985). *The physical universe. An introduction to astronomy*. Mill Valley
- [172] Harris W.E. (2001). *Globular Cluster Systems*. Springer-Verlag Berlin Heidelberg
- [173] Surdin V.G. (1994). *How many globular clusters exist in the galaxy?*. Astronomy Letters, volume 20, pp. 398–402
- [174] Gnedin O.Y. & Ostriker J.P. (1997). *Destruction of the galactic globular cluster system*. The Astrophysical Journal, volume 474, pp. 223–255
- [175] Renaud F., Agertz O. & Gieles M. (2016). *The origin of the milky way globular clusters*. Monthly Notices of the Royal Astronomical Society, volume 465, p. 3622–3636
- [176] Tonini C. (2012). *The metallicity bimodality of globular cluster systems: A test of galaxy assembly and of the evolution of the galaxy mass-metallicity relation*. The Astrophysical Journal, volume 762

- [177] Forbes D., Bastian N., Gieles M. *et al.* (2018). *Globular cluster formation and evolution in the context of cosmological galaxy assembly: Open questions*. Proceedings of the Royal Society A: Mathematical, Physical and Engineering Science, volume 474
- [178] Peebles P.J.E. (1984). *Dark matter and the origin of galaxies and globular star clusters*. The Astrophysical Journal, volume 277, pp. 470–477
- [179] Ramos F., Coenda V., Muriel H. *et al.* (2015). *Tidal stripping of globular clusters in a simulated galaxy cluster*. The Astrophysical Journal, volume 806
- [180] Baumgardt H. & Makino J. (2003). *Dynamical evolution of star clusters in tidal fields*. Monthly Notices of the Royal Astronomical Society, volume 340, pp. 227–246
- [181] Moore B. (1996). *Constraints on the global mass-to-light ratios and on the extent of dark matter halos in globular clusters and dwarf spheroidals*. The Astrophysical Journal, volume 461
- [182] Mashchenko S. & Sills A. (2005). *Globular clusters with dark matter halos. II. evolution in a tidal field*. The Astrophysical Journal, volume 619, pp. 258–269
- [183] Baumgardt H. (2016). *N-body modelling of globular clusters: masses, mass-to-light ratios and intermediate-mass black holes*. Monthly Notices of the Royal Astronomical Society, volume 464, p. 2174–2202
- [184] Bahcall J.N., Piran T. & Weinberg S. (2004). *Dark matter in the universe (2nd ed.)*. World Scientific
- [185] Gnedin O.Y., Kravtsov A.V., Klypin A.A. *et al.* (2004). *Response of dark matter halos to condensation of baryons: Cosmological simulations and improved adiabatic contraction model*. The Astrophysical Journal, volume 616, p. 16–26
- [186] Merritt D. (2004). *Evolution of the dark matter distribution at the galactic center*. Phys. Rev. Lett., volume 92, p. 201304
- [187] Messier C. (1774). *Catalogue des Nébuleuses & des amas d'Étoiles, que l'on découvre parmi les Étoiles fixes sur l'horizon de Paris; observées à l'Observatoire de la Marine, avec differens instruments.*, pp. 435–461
- [188] Frommert H. & Kronberg C. (2011). *Charles Messier's Catalog of Nebulae and Star Clusters*. <https://www.messier.seds.org/xtra/history/m-cat.html>
- [189] Tapley B., Schutz B. & Born G. (2004). *Preface*. pp. xi – xv
- [190] Durrell P.R. & Harris W.E. (1993). *A Color-Magnitude Study of the Globular Cluster M15*. Astronomical Journal, volume 105, p. 1420
- [191] Harris W.E. (1996). *A Catalog of Parameters for Globular Clusters in the Milky Way*. Astronomical Journal, volume 112, p. 1487

- [192] Salaris M., Degl'Innocenti S. & Weiss A. (1997). *The age of the oldest globular clusters*. The Astrophysical Journal, volume 479, pp. 665–672
- [193] Marks M. & Kroupa P. (2010). *Initial conditions for globular clusters and assembly of the old globular cluster population of the Milky Way*. Monthly Notices of the Royal Astronomical Society, volume 406, pp. 2000–2012
- [194] Dull J.D., Cohn H.N., Lugger P.M. *et al.* (1997). *The Dynamics of M15: Observations of the Velocity Dispersion Profile and Fokker-Planck Models*. The Astrophysical Journal, volume 481, pp. 267–281
- [195] Phinney E. (1993). *Structure and Dynamics of Globular Clusters*. In S.D..G.M.S. Francisco:ASP) (editor), *Astronomical Society of the Pacific Conference Series*, volume 50, p. 141
- [196] Abbott R., Abbott T.D., Abraham S. *et al.* (2020). *Gw190521: A binary black hole merger with a total mass of  $150 M_{\odot}$* . Phys. Rev. Lett., volume 125, p. 101102
- [197] Baumgardt H., Hut P., Makino J. *et al.* (2003). *On the Central Structure of M15*. The Astrophysical Journal Letters, volume 582, pp. L21–L24
- [198] den Brok M., van de Ven G., van den Bosch R. *et al.* (2013). *The central mass and mass-to-light profile of the Galactic globular cluster M15*. Monthly Notices of the Royal Astronomical Society, volume 438, pp. 487–493
- [199] Boyles J., Lorimer D.R., Turk P.J. *et al.* (2011). *YOUNG RADIO PULSARS IN GALACTIC GLOBULAR CLUSTERS*. The Astrophysical Journal, volume 742, p. 51
- [200] Wood M., Blaylock G., Bradbury S.M. *et al.* (2008). *A search for dark matter annihilation with the whipple 10 m telescope*. The Astrophysical Journal, volume 678, p. 594–605
- [201] van den Bosch R., de Zeeuw T., Gebhardt K. *et al.* (2006). *The dynamical mass-to-light ratio profile and distance of the globular cluster m15*. The Astrophysical Journal, volume 641, p. 852–861
- [202] Blumenthal G.R., Faber S.M., Flores R. *et al.* (1986). *Contraction of Dark Matter Galactic Halos Due to Baryonic Infall*. The Astrophysical Journal, volume 301, p. 27
- [203] Abramowski A., Acero F., Aharonian F. *et al.* (2011). *H.e.s.s. observations of the globular clusters ngc 6388 and m15 and search for a dark matter signal*. The Astrophysical Journal, volume 735, p. 12
- [204] Fomin V., Stepanian A., Lamb R. *et al.* (1994). *New methods of atmospheric Cherenkov imaging for gamma-ray astronomy. 1: The False source method*. Astropart. Phys., volume 2, pp. 137–150
- [205] Chevalley, Patrick. *Skychart*. <https://www.ap-i.net/skychart/start?id=en/start>

- [206] Read J.I., Agertz O. & Collins M.L.M. (2016). *Dark matter cores all the way down*. Monthly Notices of the Royal Astronomical Society, volume 459, pp. 2573–2590
- [207] Pasquali A., De Marchi G., Pulone L. *et al.* (2004). *The global mass function of  $m15$* . Astronomy & Astrophysics, volume 428, p. 469–478
- [208] Charbonnier A., Combet C. & Maurin D. (2012). *clumpy: A code for  $\gamma$ -ray signals from dark matter structures*. Computer Physics Communications, volume 183, p. 656–668
- [209] ESO (2011). *The E-ELT construction proposal*. ESO
- [210] de Zeeuw T. (2017). *Reaching new heights in astronomy - eso long term perspectives*
- [211] Skidmore W. (2015). *Thirty meter telescope detailed science case: 2015*. Research in Astronomy and Astrophysics, volume 15, p. 1945–2140
- [212] Hickson P. (2010). *A technical comparison of the tmt and the e-elt*
- [213] Young P. (1980). *Numerical models of star clusters with a central black hole. I - Adiabatic models.*. The Astrophysical Journal, volume 242, pp. 1232–1237
- [214] Sellwood J.A. & McGaugh S.S. (2005). *The Compression of Dark Matter Halos by Baryonic Infall*. The Astrophysical Journal, volume 634, pp. 70–76
- [215] Moliné A., Sánchez-Conde M.A., Palomares-Ruiz S. *et al.* (2017). *Characterization of subhalo structural properties and implications for dark matter annihilation signals*. Mon. Not. Roy. Astron. Soc., volume 466, pp. 4974–4990
- [216] Acciari V., Ansoldi S., Antonelli L. *et al.* (2020). *A search for dark matter in triangulum ii with the magic telescopes*. Physics of the Dark Universe, volume 28, p. 100529
- [217] Genina A. & Fairbairn M. (2016). *The potential of the dwarf galaxy triangulum ii for dark matter indirect detection*. Monthly Notices of the Royal Astronomical Society, volume 463, p. 3630–3636
- [218] Kirby E.N., Cohen J.G., Simon J.D. *et al.* (2015). *Triangulum ii: Possibly a very dense ultra-faint dwarf galaxy*. The Astrophysical Journal, volume 814, p. L7
- [219] — (2017). *Triangulum II. not especially dense after all*. The Astrophysical Journal, volume 838, p. 83
- [220] Moitinho A., Barros M. & Mignard F.o.b.o.D. (2016). *Gaia's first sky map, annotated*. Last access: 2020/11/17
- [221] Aaronson M. (1983). *Accurate radial velocities for carbon stars in Draco and Ursa Minor :the first hint of a dwarf spheroidal mass-to-light ratio.*. The Astrophysical Journal Letters, volume 266, pp. L11–L15

- [222] Wilson A.G. (1955). *Sculptor-Type Systems in the Local Group of Galaxies*. Publications of the Astronomical Society of the Pacific, volume 67, pp. 27–29
- [223] McConnachie A.W. (2012). *The Observed Properties of Dwarf Galaxies in and around the Local Group*. *Astronomical Journal*, volume 144, p. 4
- [224] Aparicio A., Carrera R. & Martínez-Delgado D. (2001). *The star formation history and morphological evolution of the draco dwarf spheroidal galaxy*. *The Astronomical Journal*, volume 122, pp. 2524–2537
- [225] Kleyna J., Wilkinson M., Evans N. *et al.* (2003). *First evidence for an extended dark halo in the draco dwarf spheroidal*
- [226] Zanin R., Carmona E., Sitarek J. *et al.* (2013). *MARS, the MAGIC analysis and reconstruction software*. In *Proceedings of the 33rd International Cosmic Ray Conference (ICRC2013): Rio de Janeiro, Brazil, July 2-9, 2013*, p. 0773
- [227] Ahnen M., Ansoldi S., Antonelli L. *et al.* (2017). *Performance of the magic telescopes under moonlight*. *Astroparticle Physics*, volume 94, p. 29–41
- [228] Albert J. *et al.* (2008). *Implementation of the Random Forest Method for the Imaging Atmospheric Cherenkov Telescope MAGIC*. *Nucl. Instrum. Meth.*, volume A588, pp. 424–432
- [229] Bonnavard V., Combet C., Maurin D. *et al.* (2015). *Spherical Jeans analysis for dark matter indirect detection in dwarf spheroidal galaxies - impact of physical parameters and triaxiality*. *Monthly Notices of the Royal Astronomical Society*, volume 446, pp. 3002–3021
- [230] Hayashi K., Ichikawa K., Matsumoto S. *et al.* (2016). *Dark matter annihilation and decay from non-spherical dark halos in galactic dwarf satellites*. *Monthly Notices of the Royal Astronomical Society*, volume 461, pp. 2914–2928
- [231] Ackermann M., Albert A., Anderson B. *et al.* (2013). *Dark matter constraints from observations of 25 milky way satellite galaxies with the fermi large area telescope*. *Physical Review D*, volume 89
- [232] Belokurov V. *et al.* (2007). *Cats and Dogs, Hair and A Hero: A Quintet of New Milky Way Companions*. *Astrophys. J.*, volume 654, pp. 897–906
- [233] Martin N.F., de Jong J.T.A. & Rix H. (2008). *A comprehensive maximum likelihood analysis of the structural properties of faint milky way satellites*. *The Astrophysical Journal*, volume 684, p. 1075–1092
- [234] Kirby E.N., Simon J.D., Geha M. *et al.* (2008). *Uncovering Extremely Metal-Poor Stars in the Milky Way's Ultrafaint Dwarf Spheroidal Satellite Galaxies*. *The Astrophysical Journal Letters*, volume 685, p. L43
- [235] Gaug M. *et al.* (2014). *Atmospheric Monitoring for the MAGIC Telescopes*. In *International Workshop on Atmospheric Monitoring for High-Energy Astroparticle Detectors*

- [236] Betorz Llobet J. (2015). *Search for correlations of atmospheric transmission obtained from the MAGIC LIDAR and the Pyrometer and Characterization of ASICs for the CTA*
- [237] Strigari L.E. (2013). *Galactic searches for dark matter*. Physics Reports, volume 531, pp. 1 – 88. Galactic searches for dark matter
- [238] Zyla P. *et al.* (2020). *Review of Particle Physics*. PTEP, volume 2020, p. 083C01
- [239] Acciari V.A., Arlen T., Aune T. *et al.* (2010). *Veritas search for the gamma-ray emission from dwarf spheroidal galaxies*. The Astrophysical Journal, volume 720, p. 1174–1180
- [240] Wolchover N. (2014). *Dwarf galaxies dim hopes of dark matter*. Last access: 2020/11/23
- [241] Bonnivard V., Combet C., Daniel M. *et al.* (2015). *Dark matter annihilation and decay in dwarf spheroidal galaxies: the classical and ultrafaint dSphs*. Monthly Notices of the Royal Astronomical Society, volume 453, pp. 849–867
- [242] Bonnivard V., Maurin D. & Walker M.G. (2016). *Contamination of stellar-kinematic samples and uncertainty about dark matter annihilation profiles in ultrafaint dwarf galaxies: the example of segue i*. Monthly Notices of the Royal Astronomical Society, volume 462, p. 223–234
- [243] Hayashi K., Ichikawa K., Matsumoto S. *et al.* (2016). *Dark matter annihilation and decay from non-spherical dark halos in galactic dwarf satellites*. Monthly Notices of the Royal Astronomical Society, volume 461, pp. 2914–2928
- [244] Chiappo A., Cohen-Tanugi J., Conrad J. *et al.* (2016). *Dwarf spheroidal j-factors without priors: A likelihood-based analysis for indirect dark matter searches*. Monthly Notices of the Royal Astronomical Society, volume 466, p. 669–676
- [245] Ackermann M. *et al.* (2015). *Searching for Dark Matter Annihilation from Milky Way Dwarf Spheroidal Galaxies with Six Years of Fermi Large Area Telescope Data*. Phys. Rev. Lett., volume 115, p. 231301
- [246] Arina C., Hambye T., Ibarra A. *et al.* (2010). *Intense Gamma-Ray Lines from Hidden Vector Dark Matter Decay*. JCAP, volume 1003, p. 024
- [247] Rico J. (2020). *Gamma-ray dark matter searches in milky way satellites—a comparative review of data analysis methods and current results*. Galaxies, volume 8, p. 25
- [248] Abramowski A. *et al.* (2014). *Search for dark matter annihilation signatures in H.E.S.S. observations of Dwarf Spheroidal Galaxies*. Phys. Rev., volume D90, p. 112012

- [249] Albert A., Alfaro R., Alvarez C. *et al.* (2020). *Search for gamma-ray spectral lines from dark matter annihilation in dwarf galaxies with the high-altitude water cherenkov observatory*. *Phys. Rev. D*, volume 101, p. 103001
- [250] Acciari V., Ansoldi S., Antonelli L. *et al.* (2018). *Constraining dark matter lifetime with a deep gamma-ray survey of the perseus galaxy cluster with magic*. *Physics of the Dark Universe*, volume 22, p. 38–47
- [251] Ninci D., Inada T., Rico J. *et al.* (2020). *Search for Dark Matter decay signals in the Galactic Halo with the MAGIC telescopes*. volume ICRC2019, p. 538
- [252] Oakes L. (2019). *Combined Dark Matter Searches Towards Dwarf Spheroidal Galaxies with Fermi-LAT, HAWC, HESS, MAGIC and VERITAS*. In *36th International Cosmic Ray Conference (ICRC2019)*, volume 36 of *International Cosmic Ray Conference*, p. 539
- [253] Sevilla-Noarbe I., Bechtol K., Kind M.C. *et al.* (2020). *Dark energy survey year 3 results: Photometric data set for cosmology*
- [254] Gatti M., Sheldon E., Amon A. *et al.* (2020). *Dark Energy Survey Year 3 Results: Weak Lensing Shape Catalogue*. arXiv e-prints, p. arXiv:2011.03408
- [255] Laevens B., Martin N., Ibata R. *et al.* (2015). *A new faint milky way satellite discovered in the pan-starrs1  $3\pi$  survey*. *The Astrophysical Journal*, volume 802
- [256] Collaboration G., Brown A.G.A., Vallenari A. *et al.* (2020). *Gaia early data release 3: Summary of the contents and survey properties*
- [257] Collaboration G., Smart R.L., Sarro L.M. *et al.* (2020). *Gaia early data release 3: The gaia catalogue of nearby stars*
- [258] Ivezić Ž., Kahn S.M., Tyson J.A. *et al.* (2019). *LSST: From Science Drivers to Reference Design and Anticipated Data Products*. *The Astrophysical Journal*, volume 873, p. 111
- [259] Balázs C., Conrad J., Farmer B. *et al.* (2017). *Sensitivity of the cherenkov telescope array to the detection of a dark matter signal in comparison to direct detection and collider experiments*. *Phys. Rev. D*, volume 96, p. 083002
- [260] Hiroshima N., Hayashida M. & Kohri K. (2019). *Dependence of accessible dark matter annihilation cross sections on the density profiles of dwarf spheroidal galaxies with the cherenkov telescope array*. *Phys. Rev. D*, volume 99, p. 123017
- [261] Bernlohr K. (2000). *Impact of atmospheric parameters on the atmospheric Cherenkov technique*. *Astropart. Phys.*, volume 12, pp. 255–268
- [262] Siano S. (2006). *Handbook on the Use of Laser in Conservation and Conservation Science*

- [263] Fernald F.G., Herman B.M. & Reagan J.A. (1972). *Determination of aerosol height distributions by lidar*. Journal of Applied Meteorology, volume 11, pp. 482–489
- [264] Wandinger U. (2005). *Raman lidar*. pp. 241–271
- [265] Ansmann A. & Müller D. (2005). *Lidar and atmospheric aerosol particles*. pp. 105–141
- [266] Ballester O. *et al.* (2020). *Raman LIDARs for the atmospheric calibration along the line-of-sight of CTA*. PoS, volume ICRC2019, p. 814
- [267] Gaug M. *et al.* (2019). *The IFAE/UAB Raman LIDAR for the CTA-North*. EPJ Web Conf., volume 197, p. 02005
- [268] Ebr J. *et al.* (2020). *Characterization of atmospheric properties at the future sites of the Cherenkov Telescope Array*. PoS, volume ICRC2019, p. 667
- [269] Gaug M. (2017). *Cta atmospheric calibration*. EPJ Web of Conferences, volume 144, p. 01003
- [270] Ebr J., Bulik T., Font L. *et al.* (2018). *Atmospheric calibration of the Cherenkov Telescope Array*. PoS, volume ICRC2017, p. 833
- [271] Ebr J. *et al.* (2020). *Characterization of atmospheric properties at the future sites of the Cherenkov Telescope Array*. PoS, volume ICRC2019, p. 667
- [272] Janežek P. *et al.* (2019). *FRAM telescopes and their measurements of aerosol content at the Pierre Auger Observatory and at future sites of the Cherenkov Telescope Array*. EPJ Web Conf., volume 197, p. 02008
- [273] Valore L. *et al.* (2018). *The ARCADE Raman Lidar and atmospheric simulations for the Cherenkov Telescope Array*. PoS, volume ICRC2017, p. 763
- [274] Stefanik S. & Nosek D. (2019). *Atmospheric monitoring using the cherenkov transparency coefficient for the cherenkov telescope array*. EPJ Web of Conferences, volume 197, p. 02010
- [275] ALEXANDREAS D., Bartoli B., Bastieri D. *et al.* (1995). *Status report on clue*. Nuclear Instruments and Methods in Physics Research Section A: Accelerators, Spectrometers, Detectors and Associated Equipment, volume 360, pp. 385–389
- [276] Peruzzo L. *et al.* (1991). *CLUE: Cherenkov light ultraviolet experiment: Preliminary results and future plans*. Italian Phys. Soc. Proc., volume 28, pp. 423–430
- [277] Doro M., Gaug M., Pallotta J. *et al.* (2014). *Status and motivation of raman lidars development for the cta observatory*
- [278] Wandinger U. & Ansmann A. (2002). *Experimental determination of the lidar overlap profile with raman lidar*. Appl. Opt., volume 41, pp. 511–514

- [279] Biavati G., Di Donfrancesco G., Cairo F. *et al.* (2011). *Correction scheme for close-range lidar returns*. Appl. Opt., volume 50, pp. 5872–5882
- [280] Kumar D. (2012). *Concept design, analysis, and integration of the new UPC multispectral lidar system*. Ph.D. thesis, Universitat Politècnica de Catalunya. Departament de Teoria del Senyal i Comunicacions
- [281] Calpe Blanch O. (2017). *Cta, lidar i near range*. Bachelor’s Thesis
- [282] Lab L.T.G.B. *Pulsed laser systems*. <https://laser-research.lbl.gov/pulsed-laser-systems/>. Last visit on 24-01-2021
- [283] López-Oramas A. (2014). *Multi-year campaign of the gamma-ray binary LS I +61<sup>o</sup> 303 and search for VHE emission from gamma-ray binary candidates with the MAGIC telescopes*. Ph.D. thesis, Barcelona, Autònoma U.
- [284] Deppo V.D., Doro M., Blanch O. *et al.* (2012). *Preliminary optical design of a polychromator for a Raman LIDAR for atmospheric calibration of the Cherenkov Telescope Array*. In L. Mazuray, R. Wartmann, A.P. Wood, M.C. de la Fuente, J.L.M. Tissot, J.M. Raynor, D.G. Smith, F. Wyrowski, A. Erdmann, T.E. Kidger, S. David & P. Benítez (editors), *Optical Systems Design 2012*, volume 8550, pp. 537 – 543. International Society for Optics and Photonics, SPIE
- [285] Griot M. (2000). *Introduction to Laser Technology, Melles Griot Technical Guide*, chapter 10. CVI Melles Griot
- [286] optics E. (2020). *Gaussian beam propagation*. <https://www.edmundoptics.com/knowledge-center/application-notes/lasers/gaussian-beam-propagation/>
- [287] Paschotta R. (2017). *Encyclopedia of laser physics and technology*. <https://www.rp-photonics.com/encyclopedia.html>
- [288] Siegman A.E. (1993). *High-power laser beams: defining, measuring and optimizing transverse beam quality*. In C. Fotakis, C. Kalpouzos & T.G. Papazoglou (editors), *9th International Symposium on Gas Flow and Chemical Lasers*, volume 1810, pp. 758 – 765. International Society for Optics and Photonics, SPIE
- [289] K. J. (2012). *cr2fits*. <https://github.com/kjordahl/cr2fits>
- [290] Çolak S.M. Ph.D. thesis, Institut de Física d’Altes Energies. Foreseen to be discussed in April 2021.
- [291] Iarlori M., Madonna F., Rizi V. *et al.* (2015). *Effective resolution concepts for lidar observations*. Atmospheric Measurement Techniques, volume 8
- [292] Ansmann A., Wandinger U., Riebesell M. *et al.* (1992). *Independent measurement of extinction and backscatter profiles in cirrus clouds by using a combined raman elastic-backscatter lidar*. Applied optics, volume 31, p. 7113

## List of Figures

2.1	Electromagnetic spectrum associated to the instruments that can detect photons in a precise energy interval. Credits to [1–3]. . . . .	4
2.2	Comparison of the development of an EM shower ( <i>left</i> ) w.r.t. a hadronic shower ( <i>right</i> ). Image taken from [3]. . . . .	5
2.3	Schematic view of the Cherenkov radiation emitted by a charged particle when travelling in a medium. Credits to [4]. . . . .	5
2.4	Representation of the IACT technique. The Cherenkov cascade is reflected by the telescopes' mirror to the camera, where the signal is collected. Image taken from CTA website [5]. . . . .	7
2.5	In order, a picture of the H.E.S.S. experiment ( <i>top left</i> ) [Credits to: H.E.S.S. Collaboration, Clementina Medina], a picture of the VERITAS experiment ( <i>top right</i> ) [Credits to: K. Gibbs & N. Galante, Whipple Observatory], an artistic representation of the Fermi-LAT experiment ( <i>bottom left</i> ) [Credits to: NASA E/PO, Sonoma State University, Aurore Simonnet] and a picture of the HAWC experiment ( <i>bottom right</i> ) [Credits to: Jordana Goodman]. . . . .	8
2.6	Location of the MAGIC telescopes. In the map on the background, some of the countries part of the MAGIC Collaboration are marked in light blue. Other member countries are not visible, because of the zoom into only a part of the world. . . . .	9
2.7	Artistic representations of the northern (CTA-N) and southern (CTA-S) sites approved for the construction of the Cherenkov Telescope Array. Credits to Gabriel Pérez Díaz and Marc-André Besel (Cherenkov Telescope Array Observatory, CTAO) for the two representations. . . . .	10
2.8	CTA sensitivity, for each construction site, w.r.t. the sensitivity of other gamma experiments operative at the current days. . . . .	11
3.1	Planck satellite map of the temperature anisotropies of the CMB, retrieved using the SMICA method [29] ( <i>top</i> ) and the retrieved temperature power spectrum [26] ( <i>bottom</i> ). In the graphics on the bottom, the temperature power spectrum points have been fitted with a base- $\Lambda$ CDM theoretical spectrum ( <i>light blue line</i> ). In the bottom part of the plot, the residuals are shown. Credits to ESA and the Planck Collaboration. . . . .	16

3.2	Large scale structure of the Universe mapped by the 2dF Galaxy Redshift Survey [37] ( <i>left panel</i> ) and by the Sloan Digital Sky-Survey [35] ( <i>top panel</i> ), and obtained with the <i>Millennium simulations</i> [38] for the corresponding portions of the sky (right and bottom panels, respectively). Figure taken from [39]. . . . .	18
3.3	Comoving number density (left axis) and thermal relic density (right axis) of an annihilating DM particle of mass $m_\chi = 100$ GeV, as a function of the inverse temperature of the Universe $T$ and the time $t$ . The solid black line corresponds to the annihilation cross-section that yields the correct relic density. The yellow, orange and violet regions correspond to cross-sections that differ from the central value for a factor 10, 100 and 1000, respectively. The dashed black line depicts the number density $N_{\text{EQ}}$ of a particle that remains in thermal equilibrium. Image adapted from [52]. . . . .	19
3.4	XENON1T upper limits on WIMP-nucleon cross section in comparison to the LUX [79] and PandaX-II [74] results for the case of spin-independent interactions ( <i>left</i> ), and to XENON100 [80], LUX [79], PandaX-II [74] and PICO-60 [76] for the case of spin-dependent interactions ( <i>left</i> ). Figures taken from [72] and [81]. . . . .	24
3.5	Fits to the data of the XENON1T experiment (black data points) under various hypotheses: tritium (a), solar axions (b), and a neutrino magnetic moment (c). The null and alternative hypotheses in each scenario, respectively, are denoted by gray (solid) and red (solid) lines. Panel (d) shows the best fits for an additional statistical test on the solar axion hypothesis, in which an unconstrained tritium component is included. Image taken from [73]. . . . .	25
3.6	ATLAS results on the WIMP-nucleon cross-section compared with limits from direct detection experiments, in the case of spin-independent ( <i>top</i> ) and spin-dependent ( <i>bottom</i> ) interactions, respectively. Image taken from [85]. . . . .	27
3.7	Schematic view of WIMPs annihilation into heavy SM particles ( <i>left</i> ) or directly into gamma-photons ( <i>right</i> ). . . . .	28
3.8	Limits on the velocity-averaged cross-section of WIMP DM annihilation, in the $\tau^+\tau^-$ channel, obtained with 11 years of ANTARES data, compared with current similar searches from IceCube [91] and from the gamma-ray telescopes VERITAS [92], Fermi-LAT + MAGIC [93] and H.E.S.S. [94], for different targets of observation and different DM density profile models. Image taken from [95]. . . . .	29
3.9	Scheme of the current DM candidates taken into consideration, associated to the detection systems that can observe them. Image taken from [96]. . . . .	31
3.10	Representation of the targets of indirect DM searches with gamma rays. Each candidate is presented with its respective characteristics and the associated detection instrument. For the latter, the Fermi-LAT satellite and IceCube images have been used as reference for gamma-ray satellite detectors and neutrino detectors, respectively. The third type of instrument is a general IACT. Image taken from [97]. . . . .	32
3.11	Differential energy spectrum of WIMP particles of mass 300 GeV ( <i>left</i> ) and $10^4$ GeV ( <i>right</i> ) self-annihilating in the $b\bar{b}$ , $\tau^+\tau^-$ , $\mu^+\mu^-$ and $W^+W^-$ channels. Image taken from [106]. . . . .	34

3.12	NFW, Einasto and Burkert profiles retrieved with Milky Way parameters. Image taken from [111]. . . . .	35
4.1	Evolution of the sensitivity of the MAGIC telescopes with the different upgrades. Image taken from [122]. . . . .	37
4.2	MAGIC telescope details of the structure frame ( <i>left</i> ) and of the movement system ( <i>right</i> ). . . . .	39
4.3	Reflective plane of the M1 telescope. Image taken from the MAGIC Facebook page [135]. . . . .	40
4.4	Pictures of the MAGIC telescope camera from the front ( <i>left</i> ) and from the back ( <i>right</i> ). . . . .	40
4.5	Detail of the front part of the camera, showing the PMTs and the Winstone cones. Credits to C. Righi. . . . .	41
4.6	Scheme of the different <i>wobble</i> pointings of the MAGIC telescopes. OFF regions are marked in red, while the ON ones in green. Image taken from [133]. . . . .	44
4.7	Scheme of the trigger regions in the MAGIC camera. The L0 trigger region is marked with a green line, the L1 trigger regions as grey areas. Image taken from [106]. . . . .	45
5.1	Image of an electromagnetic shower signal in the camera before (top left) and after (bottom) the image cleaning procedure. The image of the signal arrival times is also shown (top right). . . . .	50
5.2	View of an electromagnetic shower in camera coordinates, marked with the respective Hillas parameters. Image taken from [145]. . . . .	52
5.3	Excess events in the M1 camera. The image on the top left shows a hadronic-initiated shower, while the one on the top right a gamma-initiated one. On the bottom part, the NSB (on the left) and a muon ring (on the right), created by a high-energy muon [146], are presented. . . . .	53
5.4	Simulated distributions of <i>Width</i> and <i>Length</i> Hillas parameters as a function of the shower <i>size</i> for gamma-initiated (left) and hadrons-initiated (right) showers [147]. . . . .	53
5.5	View of the stereo parameters reconstruction starting from a gamma-initiated shower. On the top right side of the figure, the <i>shower core impact on ground</i> evaluation, starting from the shower image of each telescope, is shown. Modified figure from [151]. . . . .	54
5.6	Overview panel of the quality cut procedure. See the main text for the explanation of each single plot. . . . .	55
5.7	Schematic view of the MC simulations in the MAGIC camera, marked in green, for the case of pointlike targets (a) and extended targets (b). Image taken from [156]. . . . .	58
5.8	Probability density function simulations of true directions of gamma-events for 1 source center/pointing direction orientation ( <i>top left</i> ), and 4 ( <i>top right</i> ), 10 ( <i>bottom left</i> ) and 100 ( <i>bottom right</i> ) source center/pointing direction orientations. The last plot is the convoluted one used for the <i>Donut MC</i> method, as explained in the text. Credits [106]. . . . .	60

5.9	Example of the convolution of events' PDF for the case of MC simulated diffuse events considered in the analysis of Coma Berenices dSph in 2 dimensions ( <i>left</i> ) and 1 dimension ( <i>right</i> ). In this case, the maximum event true direction considered if found at a smaller angular distance with respect to Fig. 5.8, as in this case the extension of the source is smaller. . . . .	61
5.10	Source brightness profile, in the case of Coma Berenices dSph analysis, convoluted with the <i>Donut</i> ring obtained in the first step of the <i>Donut MC</i> procedure. . . . .	61
5.11	$\theta^2$ plot of 2.64 h of Crab Nebula data. The signal excess is visible at the center of the source, around $\theta^2 = 0$ . The data of the OFF region are marked with a grey area. All numerical and statistical details about the data are presented in the upper right corner. . .	62
5.12	Example of a (smoothed) significance skymap. The excess events are marked following the color code presented in the vertical band on the right side of the figure. . . . .	63
5.13	Migration matrix obtained for the Draco dSph data analysis. . . .	65
6.1	Schematic painting of the location of star clusters in the MW, together with the image of an open star cluster (M39) on the upper left corner, and of a globular cluster (M10) on the bottom right corner. The M39 image has been taken from APOD website [167], the central image from The University of Iowa website [168], and the bottom right one from Michael Richmond's classes [169]. . . .	69
6.2	HR diagram of apparent magnitudes of the Pleiades open star cluster (in red) in comparison with the one of M53 globular cluster (in green), taken from [169] (the V-band magnitudes of the stars in M53 have been shifted upwards by 8 in order to fit nicely on the same graph with the Pleiades). The stars belonging to the Pleiades are reported in dark red, the ones belonging to M53 are in dark green. The turn-off point of the GC is also indicated. . . . .	70
6.3	M15 GC captured by the Hubble telescope. Credits: ESA/Hubble & NASA . . . . .	72
6.4	Schematic view of the four MAGIC wobble pointings for the case of M15 observation during the data-taking night of 2015-09-25 at 5 a.m. The image was produced using the SkyChart software [205] and setting a threshold of 10 for the apparent magnitude of the sky objects. . . . .	76
6.5	The aerosol transmission as a function of time at different altitudes for the data-taking cycle ST.03.06. In semi-transparent green the area that marks the data kept for the analysis is shown. . . . .	77
6.6	The aerosol transmission as a function of time at different altitudes for the data-taking cycle ST.03.07. In semi-transparent green the area that marks the data kept for the analysis is shown. . . . .	77
6.7	$\theta^2$ plot representing the excess events with respect to the background in the signal region, delimited by a dashed vertical line. The significance obtained is reported in the upper right corner of the figure. . . . .	78

6.8	Smoothed significance skymap of M15 FoV for an extension of $2.4^\circ$ . The white cross indicates the center of M15, the white solid circle the extension of MAGIC telescopes point spread function (PDF). . . . .	79
6.9	<i>Left</i> : Mass-to-light profile (deprojected-squares and projected-circles) of M15 from the fitting of discrete velocity data as a function of the radial distance from the center. The $1\sigma$ band for the deprojected profile (in red) and the earlier measurements of [207] (dashed line) are also presented. <i>Right</i> : M15 inferred mass-density profile, with $1 - \sigma$ error band (red region), as a function of the radius. The expected power-law mass-density profile for dark remnants from [197] is also presented. Both plots have been adopted from [198]. . . . .	80
6.10	DM density profile (light-blue circles) in comparison to the total density profile (orange circles) as a function of the radial distance from the cluster center. . . . .	81
6.11	DM density profiles retrieved from Whipple (in red and violet), H.E.S.S. (in orange and green) and this work (in light-blue). . . . .	82
6.12	Geometry of the integral used to calculate the $J$ -factor. $D$ is the distance of the target from the observer $obs$ , $\theta$ the direction angle of observation, $R$ the maximum radius of integration, $r$ the variable radius of integration and $s$ the l.o.s. at the lower ( $s_1$ ) and higher ( $s_2$ ) extremes of integration. . . . .	82
6.13	M15 M/L profile obtained by rescaling the averaged M/L profile of [183]. . . . .	83
6.14	Cumulative $J$ -factors with respect to the angular distance from the cluster center in the case of the estimation from [198] (in light-blue) and from [183] (in dark-blue). . . . .	83
6.15	95% CL ULs on $\langle\sigma_{ann}v\rangle$ for the annihilation of WIMP DM in the $b\bar{b}$ ( <i>left</i> ) and $\tau^+\tau^-$ channels ( <i>right</i> ) using MAGIC M15 data and Whipple's $J$ -factor. . . . .	84
6.16	95% CL ULs on $\langle\sigma_{ann}v\rangle$ for the annihilation of WIMP DM in the $b\bar{b}$ ( <i>left</i> ) and $\tau^+\tau^-$ channels ( <i>right</i> ) using MAGIC M15 data and H.E.S.S.'s $J$ -factor. . . . .	84
6.17	Toy ULs on $\langle\sigma_{ann}v\rangle$ for the annihilation of WIMP DM in the $b\bar{b}$ ( <i>left</i> ) and $\tau^+\tau^-$ channels ( <i>right</i> ) using MAGIC M15 data and the optimistic $J$ -factor calculated in this work. . . . .	85
6.18	ULs on $\langle\sigma_{ann}v\rangle$ of WIMPs annihilation in the $b\bar{b}$ channel for M15 compared to the limits obtained by the combination of the single ULs, in the $b\bar{b}$ channel, of the dSphs observed by the MAGIC collaboration (dotted black line). The ULs obtained considering the most optimistic DM scenario for M15 are showed as a solid grey line. The 95% CL limits obtained using Whipple and H.E.S.S. estimated $J$ -factors are showed in green and blue, as a dotted line for the analyses done by the respective collaborations (extracted from [200] and [203]) and as a solid line for the analyses performed in this work. The thermal relic cross section is presented as a red dashed line. . . . .	86
7.1	Position of Draco dSph in the MW (red circle). Image taken from the ESA website [220]. . . . .	90

7.2	Distribution of the observations as a function of the azimuth telescope pointing angles for the two wobbles. <i>W1</i> observations are presented in red, while <i>W3</i> ones in blue. . . . .	92
7.3	Source brightness profile of Draco dSph taken from the DM profile in [119] and normalized. . . . .	94
7.4	Source brightness profile of Draco dSph simulated as probability density functions around the camera center, in the case of 100 simulations. . . . .	95
7.5	Example of transformation from MC simulations of diffuse $\gamma$ -rays around the center of the camera up to an angle of $1.5^\circ$ ( <i>left</i> plot) to Donut MC simulations around the center of the camera, re-weighted for the source brightness profile of Draco dSph ( <i>right</i> plot), for the case of the MCs associated to the data subsample S09. . . . .	95
7.6	Geometry of the OffFromWobblePartner background estimation method. The red ellipses indicate the wobble positions, with the respective ON and OFF positions, considered in this analysis. . . . .	96
7.7	Normalized sensitivity of the analysis performed with respect to different $\theta^2$ cuts. Each sensitivity curve is associated to a DM mass. The black vertical line indicates the chosen $\theta^2$ cut value. . . . .	97
7.8	Sensitivities of the analysis for the different hadronness cuts (fixed for each energy bin or depending on the cut efficiency) at different DM masses. The black rectangle on the legend indicates the chosen hadronness cut value. The curves inside the rectangle, on the bottom central part of the figure, have been zoomed in, in order to let the reader appreciate the trends of the sensitivities in the central part of the covered energy range. . . . .	98
7.9	Significance skymap of Draco dSph for a FoV of $2.4^\circ$ . The position of the source, in equatorial coordinates, is marked as a white cross. The orange dashed circle delimits the expected signal region. For comparing the extension of the optimized emission region of the source (defined by the square root of the $\theta^2$ cut value), the PSF reached by the MAGIC telescope is also shown as a white solid circle. . . . .	99
7.10	Squared distances of reconstructed shower directions w.r.t. source ( $\theta^2$ plot) of Draco dSph. The black vertical dashed line delimits the signal region at $\theta^2 = 0.05 \text{ deg}^2$ . . . . .	99
7.11	Draco $\langle\sigma v\rangle$ ULs for the annihilation channels $b\bar{b}$ , $W^+W^-$ , $\tau^+\tau^-$ and $\mu^+\mu^-$ . The black line indicates the evaluated limit, with the respective 68% (green) and 95% (yellow) containment bands, while the dashed line is the median of the simulations. The red dashed line is present in all the plots for the comparison of the limits obtained with the thermal relic cross-section [51]. . . . .	100
7.12	95% CL ULs on the $\langle\sigma v\rangle$ for WIMP annihilation, as a function of the DM mass, in the $b\bar{b}$ ( <i>up</i> ) and $\tau^+\tau^-$ ( <i>down</i> ) channels. Draco dSph ULs have been compared to the ULs obtained by the MAGIC collaboration analysing other dSphs. The limits obtained in this work are presented in black, the ones obtained from 157.9 h of Segue 1 data, in orange, the ones obtained from 94.8 h of UMaII data, in blue, and the ones obtained from 62.4 h of TriII data, in purple. For the ULs, only DM masses in the range $10^2 - 10^5 \text{ GeV}$ have been considered. . . . .	101

8.1	Position of Coma Berenices dSph in galactic coordinates. Image taken from [231]. The difference between filled and unfilled circles is given by the dSphs respectively considered or not for the analysis in [231]. . . . .	103
8.2	Distribution of the observations as a function of the azimuth telescope pointing angles for the two wobbles. <i>W1</i> observations are presented in red, while <i>W3</i> ones in blue. . . . .	104
8.3	Source brightness profile of Coma Berenices dSph taken from the DM profile in [119] and normalized. . . . .	106
8.4	Example of transformation from MC simulations of diffuse $\gamma$ -rays around the center of the camera up to an angle of $2.5^\circ$ ( <i>left</i> plot) to Donut MC simulations around the center of the camera, re-weighted for the source brightness profile of Coma Berenices dSph ( <i>right</i> plot). . . . .	106
8.5	Significance skymap of Coma Berenices dSph for a FoV of $2.4^\circ$ . The position of the source, in equatorial coordinates, is marked as a white cross. The orange dashed circle delimits the expected signal region. For comparing the extension of the optimized emission region of the source (defined by the square root of the $\theta^2$ cut value), the PSF reached by the MAGIC telescope is also shown as a white solid circle. . . . .	107
8.6	Normalized sensitivity of the analysis performed with respect to different $\theta^2$ cuts. Each sensitivity curve is associated to a DM mass. The black vertical line indicates the chosen $\theta^2$ cut value. . . . .	108
8.7	Normalized sensitivities of the analysis performed with respect to different hadronness cuts, per each WIMP DM mass considered. The black vertical line indicates the chosen hadronness cut value. . . . .	108
8.8	Normalized sensitivities of the analysis performed with respect to different hadronness cuts in efficiency, per each WIMP DM mass considered. The black vertical line indicates the chosen hadronness cut value. . . . .	109
8.9	Sensitivities of the analysis for the different hadronness cuts, fixed for each energy bin ( <i>had</i> in the legend) or depending on the cut efficiency ( <i>eff</i> in the legend), at different DM masses. The black rectangle on the legend indicates the chosen hadronness cut value. The curves inside the rectangle, on the bottom central part of the figure, have been zoomed in, in order to let the reader appreciate the trends of the sensitivities in the central part of the covered energy range. . . . .	110
8.10	Squared distances of reconstructed shower directions w.r.t. source ( $\theta^2$ plot) of Coma Berenices dSph. The black vertical dashed line delimits the signal region at $\theta^2 = 0.03 \text{ deg}^2$ . . . . .	110
8.11	Coma Berenices $\langle \sigma_{ann} v \rangle$ 95% CL ULs for the annihilation channels $b\bar{b}$ , $W^+W^-$ , $\tau^+\tau^-$ and $\mu^+\mu^-$ . The black line indicates the evaluated limit, with the respective 68% (green) and 95% (yellow) containment bands, while the dashed line is the median of the simulations. The red dashed line is present in all the figures, for comparison, and indicates the thermal relic cross-section [51]. . . . .	111

8.12	95% CL ULs on the $\langle\sigma_{ann}v\rangle$ for WIMP annihilation, as a function of the DM mass, in the $b\bar{b}$ ( <i>top</i> ) and $\tau^+\tau^-$ ( <i>bottom</i> ) channels. Coma Berenices dSph ULs have been compared to the ULs obtained by the MAGIC collaboration analysing other dSphs. The limits obtained in this work are presented in black, the ones obtained from the Draco dSphs analysis, presented in the previous chapter, in pink, the ones obtained from 157.9 h of Segue 1 data, in orange, the ones obtained from 94.8 h of UMaII data, in blue, and the ones obtained from 62.4 h of TriII data, in purple. For the ULs, only DM masses in the range $10^2 - 10^5$ GeV have been considered. . . . .	113
9.1	Map of dwarf spheroidal satellite galaxies, orbiting the Milky Way Galaxy, taken from [240]. The four dSphs considered for this combined analysis are marked with a green ellipse. . . . .	115
9.2	Segue 1 $\langle\sigma_{ann}v\rangle$ revised ULs for the annihilation channels $b\bar{b}$ , $W^+W^-$ , $\tau^+\tau^-$ and $\mu^+\mu^-$ . The limits presented in this figure (solid black lines), with the respective 68% (green) and 95% (yellow) containment bands, have been rescaled from the ones in [164] as described in the text. The red dashed line is present in all the plots for the comparison of the limits obtained with the thermal relic cross-section [51].	118
9.3	MAGIC ULs on $\langle\sigma_{ann}v\rangle$ (solid black lines), for the $b\bar{b}$ and $t\bar{t}$ annihilation channels, obtained through the combination of the results of Draco, Coma Berenices, Ursa Major II [157] and Segue 1 [164]. The 68% (green) and 95% (yellow) containment bands and the median of the simulations (blue dashed line) are also shown. The comparison with the thermal relic cross-section [51] is reported in both plots (red dashed line). . . . .	122
9.4	MAGIC ULs on $\langle\sigma_{ann}v\rangle$ (solid black lines), for the $\tau^+\tau^-$ and $\mu^+\mu^-$ annihilation channels, obtained through the combination of the results of Draco, Coma Berenices, Ursa Major II [157] and Segue 1 [164]. The 68% (green) and 95% (yellow) containment bands and the median of the simulations (blue dashed line) are also shown. The comparison with the thermal relic cross-section [51] is reported in both plots (red dashed line). . . . .	123
9.5	MAGIC ULs on $\langle\sigma_{ann}v\rangle$ (solid black lines), for the $e^+e^-$ and $W^+W^-$ annihilation channels, obtained through the combination of the results of Draco, Coma Berenices, Ursa Major II [157] and Segue 1 [164]. The 68% (green) and 95% (yellow) containment bands and the median of the simulations (blue dashed line) are also shown. The comparison with the thermal relic cross-section [51] is reported in both plots (red dashed line). . . . .	124
9.6	MAGIC ULs on $\langle\sigma_{ann}v\rangle$ (solid black lines), for the $ZZ$ and $HH$ annihilation channels, obtained through the combination of the results of Draco, Coma Berenices, Ursa Major II [157] and Segue 1 [164]. The 68% (green) and 95% (yellow) containment bands and the median of the simulations (blue dashed line) are also shown. The comparison with the thermal relic cross-section [51] is reported in both plots (red dashed line). . . . .	125

- 9.7 MAGIC ULs on  $\langle\sigma_{ann}v\rangle$  (solid black lines), for the  $\gamma\gamma$  annihilation channel, obtained through the combination of the results of Draco, Coma Berenices, Ursa Major II [157] and Segue 1 (see section 9.1.1). The 68% (green) and 95% (yellow) containment bands and the median of the simulations (blue dashed line) are also shown. The thermal relic cross-section [51] reported (red dashed line) for this annihilation channel has been multiplied by a factor  $\alpha^2$ , as described in [246], where  $\alpha$  is the fine structure constant. . . . . 126
- 9.8 Velocity-averaged cross-section ULs, for the  $b\bar{b}$  (top) and  $t\bar{t}$  (bottom) annihilation channels, obtained by the MAGIC Collaboration for each single dSph taken into account in the present paper. The blue lines are the results of Draco dSph analysis, the orange lines of Coma Berenices dSph analysis, the magenta lines of Segue 1 (see section 9.1.1), the green lines of Ursa Major II [157] and the black line the combined limit of all four dSphs. The comparison with the thermal relic cross-section [51] is reported in both plots (red dashed line). . . . . 127
- 9.9 Velocity-averaged cross-section ULs, for the  $\tau^+\tau^-$  (top) and  $\mu^+\mu^-$  (bottom) annihilation channels, obtained by the MAGIC Collaboration for each single dSph taken into account in the present paper. The blue lines are the results of Draco dSph analysis, the orange lines of Coma Berenices dSph analysis, the magenta lines of Segue 1 (see section 9.1.1), the green lines of Ursa Major II [157] and the black line the combined limit of all four dSphs. The comparison with the thermal relic cross-section [51] is reported in both plots (red dashed line). . . . . 128
- 9.10 Velocity-averaged cross-section ULs, for the  $e^+e^-$  (top) and  $W^+W^-$  (bottom) annihilation channels, obtained by the MAGIC Collaboration for each single dSph taken into account in the present paper. The blue lines are the results of Draco dSph analysis, the orange lines of Coma Berenices dSph analysis, the magenta lines of Segue 1 (see section 9.1.1), the green lines of Ursa Major II [157] and the black line the combined limit of all four dSphs. The comparison with the thermal relic cross-section [51] is reported in both plots (red dashed line). . . . . 129
- 9.11 Velocity-averaged cross-section ULs, for the  $ZZ$  (top) and  $HH$  (bottom) annihilation channels, obtained by the MAGIC Collaboration for each single dSph taken into account in the present paper. The blue lines are the results of Draco dSph analysis, the orange lines of Coma Berenices dSph analysis, the magenta lines of Segue 1 (see section 9.1.1), the green lines of Ursa Major II [157] and the black line the combined limit of all four dSphs. The comparison with the thermal relic cross-section [51] is reported in both plots (red dashed line). . . . . 130

9.12	Velocity-averaged cross-section ULs, for the $\gamma\gamma$ annihilation channel, obtained by the MAGIC Collaboration for each single dSph taken into account in the present paper. The blue lines are the results of Draco dSph analysis, the orange lines of Coma Berenices dSph analysis, the magenta lines of Segue 1 (see section 9.1.1), the green lines of Ursa Major II [157] and the black line the combined limit of all four dSphs. The thermal relic cross-section [51] reported (red dashed line) for this annihilation channel has been multiplied by a factor $\alpha^2$ , as described in [246], where $\alpha$ is the fine structure constant. . . . .	131
9.13	95% CL combined ULs on the $\langle\sigma_{ann}v\rangle$ of WIMP DM annihilating in the $b\bar{b}$ annihilation channel calculated using the $J$ -factors values presented in [229] (grey dashed line), in [230] (grey dash dot dot line), and in [244] (grey solid line) in comparison to the ULs estimated in this work and based on the Geringer-Sameth et al. [119] $J$ -factors (black solid line). The thermal relic cross-section is also reported (dash dot red line). . . . .	132
9.14	95% CL combined UL on the $\langle\sigma_{ann}v\rangle$ of WIMP DM annihilating in the $b\bar{b}$ ( <i>top</i> ) and $\tau^+\tau^-$ ( <i>bottom</i> ) annihilation channels by VERITAS (in green), Fermi-LAT (in blue), H.E.S.S. (in red) and HAWC (in yellow), in comparison to the UL estimated in this work (in black). . . . .	133
10.1	Scheme of a generic coaxial LIDAR system. Image taken from [262].	136
10.2	Picture of the opened Barcelona Raman LIDAR container with the LIDAR system mounted. . . . .	141
10.3	Sketch of the key design choices of the Barcelona Raman LIDAR. . . . .	141
10.4	Components of the near-range system. (a) is the parabolic mirror, (b) the support to mount the mirror on the telescope structure and (c) the optic fibre. Credits to [281]. . . . .	143
10.5	Picture of the Nd:YAG pulsed 1064 nm laser of type Brilliant showing the main laser body and the two harmonics dismountable generators. Image taken from [282]. . . . .	143
10.6	Transmission as a function of the wavelength of the dichroic guiding mirrors. . . . .	144
10.7	Picture of the telescope showing the main components of the Raman LIDAR system: the laser and the first guiding mirror on the left, the second guiding mirror, the near range system and the liquid light guide (LLG), respectively, at the center. . . . .	145
10.8	Polychromator design layout ( <i>top</i> ) and picture of the interior ( <i>bottom</i> ) for a 4-channel read-out unit. . . . .	146
10.9	Block diagram of the control software of the Barcelona Raman LIDAR.	147
11.1	Scheme of a Gaussian beam, including the waist parameters and the intensity at different axial distances. Credits to: [286]. . . . .	149
11.2	Low-order Hermite-Gaussian resonator modes (taken from [285]) . . . . .	150
11.3	Location and setup of the second and third beam divergence tests. . . . .	151
11.4	Comparison between saturated and non-saturated images from raw camera pictures. . . . .	155

11.5	Plots obtained from the analysis of a saturated image file. The upper left part shows the laser spot image in linear scale, fitted with the 2D-elliptic gaussian. The upper right picture presents the same plot in logarithmic scale and without the retrieved concentric ellipses. The lower left panel shows the background-subtracted image, and the lower right displays the ellipse that contains $(1 - 1/e^2)$ of the total normalized distribution. . . . .	156
11.6	Plots obtained from the analysis of a medium-intensity non-saturated image. See Fig. 11.5. . . . .	156
11.7	Plots obtained from the analysis of a low intensity image. See Fig. 11.5. . . . .	157
11.8	Intensity coverage of the background subtracted and normalized saturated image, as a function of the fitted ellipse's major and minor axes. . . . .	157
11.9	Intensity coverage of the background subtracted and normalized medium-intensity non-saturated image, as a function of the fitted ellipse's major and minor axes. . . . .	158
11.10	Intensity coverage of the background subtracted and normalized low intensity image, as a function of the fitted ellipse's major and minor axes. . . . .	158
11.11	Plots obtained from the analysis of the photo "IMG_0825". The upper left part shows the laser spot image in linear scale, fitted with the 2D-elliptic Gaussian. The upper right picture presents the same plot in logarithmic scale and without the retrieved concentric ellipses. The lower left panel shows the background-subtracted image, and the lower right displays the ellipse that contains $(1 - e^{-2})$ of the total normalized distribution (black), and region used for the determination of the background (yellow). The lower images show the raw image in 3d, in linear (left) and logarithmic (right) scale. . . . .	160
11.12	Intensity coverage (enclosed energy) of the background subtracted and normalized image "IMG_0825", as a function of the fitted ellipse major and minor axes. . . . .	161
11.13	Schematic setup used for the PMT characterization. Credits to S. Griffiths. . . . .	164
11.14	Newport 818-UV PIN photodiode used for the cross-check measurements. . . . .	165
11.15	Response of the PMTs with the shutter close as a function of time. As the time intervals were not with the same time-stamp, arbitrary units have been used. . . . .	166
11.16	PMTs normalized current power data as a function of the wavelength. The results of each PMT are represented with a solid line, the one of the photodiode is showed with black squares. . . . .	166
11.17	Percent deviation of the normalized PMT data (dotted coloured lines) with respect to the mean of the normalized PMT data (dashed line). . . . .	167
11.18	Logarithm of range-corrected signals from three colour lines of the Barcelona Raman LIDAR based on 500 laser shots. The analog (amplitude) and photo-electron (p.e.) counting parts are shown where applicable. The features visible in the elastic lines below 4 km correspond to aerosol layers and clouds. . . . .	168

11.19	Logarithm of range-corrected signals from three colour lines of the Barcelona Raman LIDAR and the near-range receiver. All lines, except for the Raman wavelength, have been scaled to the photoelectron (p.e.) counting signal at 387 nm. Data were taken with 500 laser shots. . . . .	169
A.1	Technical specifications of the Quantel Brilliant laser . . . . .	213

# List of Tables

6.1	M15 $J$ -factor values used by the Whipple collaboration for the indirect detection of self-annihilating DM [200]. Both their minimum and maximum values of the $J$ -factor are reported for the NFW and AC NFW models. . . . .	74
6.2	M15 $J$ -factor values used by the H.E.S.S. collaboration for the indirect detection of self-annihilating DM [203]. The values reported for each model are averaged over the solid angle of integration. The $J$ -factor estimate for the IMBH model is missing, because it was not considered in the H.E.S.S. analysis. The other $J$ -factors are estimated, in order, for a generic NFW profile (Initial NFW), for a NFW profile affected by AC (AC NFW) and for a AC NFW profile affected also by the kinetic heating by baryons (Final NFW). The latter has been used by the H.E.S.S. collaboration to calculate the upper limits on the $\langle\sigma_{ann}v\rangle$ for WIMP DM annihilation. . . . .	74
6.3	95% CL ULs on the $\langle\sigma_{ann}v\rangle$ of WIMP DM candidate of $m_\chi = 1$ TeV in the case of Whipple [200] and of $m_\chi = 2$ TeV in the case of H.E.S.S. [203], associated to the $J$ -factors used for the estimation of the limits. The average $J$ -factor values of H.E.S.S., presented in Tab. 6.2, have been multiplied for the solid angle $5 \times 10^{-6}$ sr in order to get the cumulative $J$ -factors presented in this table. . . . .	75
6.4	95% CL ULs on the $\langle\sigma_{ann}v\rangle$ of WIMP DM candidate obtained by using Whipple and H.E.S.S. $J$ -factors in association to a MAGIC data sample and toy ULs estimated using the $J$ -factor evaluated in this work, with the respective DM masses for the most constraining limit. . . . .	85
7.1	The details of the Draco observation and the data selection parameters are reported in the table. In order, the time intervals, the observation conditions, the wobble pointings and the cuts applied (in percentage) are shown for each subsample. The effective times before and after the cuts (indicated with an arrow) are also presented. The total time of observation after cuts is reported at the end of the table. . . . .	93
7.2	List of the most constraining ULs on $\langle\sigma_{ann}v\rangle$ for the four annihilation channels considered in the work. Each UL is associated to the respective WIMP mass. . . . .	98

8.1	List of the most constraining ULs on $\langle\sigma_{ann}v\rangle$ for the four annihilation channels considered in the work. Each UL is associated to the respective WIMP mass. . . . .	109
9.1	List of the candidates proposed for the dSphs multi-year DM project (first two lines, Draco and Coma Berenice dSphs) and previously observed (last two lines, Segue 1 [164] and Ursa Major II [157]). The $J$ -factors are presented together with their asymmetric uncertainties. The third column shows the source extension, as described in section 6.2 of [119]. The maximum angle $\theta_{\max}$ refers to the galactocentric distance of the outermost member star used to evaluate the velocity dispersion profile, whereas $\theta_{0.5}$ refers to the angle containing 50% of the dark matter emission (i.e. $J(\theta_{0.5}) = 0.5 \times J(\theta_{\max})$ ). The last column presents the total time of observation of the targets acquired with the MAGIC telescopes. . . . .	116
9.2	List of the most constraining ULs on $\langle\sigma_{ann}v\rangle$ for the nine annihilation channels considered in this work. Each UL is associated with the respective WIMP mass. . . . .	119
11.1	Basic parameters directly measured in the different experimental setups (see text). The entries marked with ‘-’ corresponds to the parameters not directly retrieved, but obtained, in a second moment, from the analysis presented in subsection 11.1.3. . . . .	152
11.2	Table of the parameters used as input for the script: name of the raw file, coordinates for the cutout and conversion factors. In the last column of the table, a distinction is made between saturated (Y), non-saturated (N) and lower intensity (low int.) images. The latter are all non-saturated. . . . .	154
11.3	Results of the image fits: name of the raw file, value of the major axis of the ellipse ( $d_{maj}$ ), value of the beam divergence along the major axis ( $\Theta_{maj}$ ), value of the minor axis of the ellipse ( $d_{min}$ ), value of the beam divergence along the minor axis ( $\Theta_{min}$ ), rotation angle of the beam profile ( $\alpha$ ). . . . .	159
11.4	Average and standard deviation of the results obtained for the high intensity laser beam: major axis of the ellipse ( $d_{maj}$ ), beam divergence along the major axis ( $\Theta_{maj}$ ), minor axis of the ellipse ( $d_{min}$ ), beam divergence along the minor axis ( $\Theta_{min}$ ), rotation angle of the ellipse ( $\alpha$ ). . . . .	159
11.5	Average and standard deviation of the results obtained for the low intensity laser beam: major axis of the ellipse ( $d_{maj}$ ), beam divergence along the major axis ( $\Theta_{maj}$ ), minor axis of the ellipse ( $d_{min}$ ), beam divergence along the minor axis ( $\Theta_{min}$ ), rotation angle of the ellipse ( $\alpha$ ). . . . .	159
11.6	Results of the image analysis 3 for the data from April 2017. . . . .	161
11.7	Results of the image analysis 3 for the near-range data from January 2017. The upper set of lines were obtained with a laser distance of 2402 mm, while the two lower images were taken at an even closer distance of 1798 mm. Only the upper set of pictures contains one without any saturation. All beam sizes obtained from the saturated pictures are therefore given as upper limits. . . . .	162

11.8 Summary of the retrieved beam characteristics from the different analysis. Both the beam divergences  $\Theta_{x,y}$  cover the full angle, and the beam waists  $d_{0,(x,y)}$  show the full radius, as provided in the data sheet of the laser (Appendix A). Those numbers given uncertainties are the result of several measurements of the same parameter, while those without uncertainty have been obtained from one measurement only. The expected uncertainty of these numbers may be estimated roughly as 10%. The numbers marked with a star \* might be affected by systematics due to a larger viewing angle and should be treated with caution. . . . . 162

11.9 Table of the mean values of the current power, with associated standard deviation, as a function of the wavelength ( $\lambda$ ). . . . . 167

# Acronyms

AAS	Automatic Alert System
AC	Adiabatic Contraction
AMC	Active Mirror Control
ASC	All-Sky Camera
BAO	Baryonic Acoustic Oscillation
BH	Black Hole
CC	Central Control
CCD	Charged-Coupled Device
CDM	Cold Dark Matter
CFRP	Carbon Fibre Reinforce Plastic
CH	Counting House
CL	Confidence Level
CLUE	Cherenkov Light Ultraviolet Experiment
CMB	Cosmic Microwave Background
CNR	Consiglio Nazionale delle Ricerche
CoG	Center of Gravity
CP	Charge-Parity
CR	Cosmic Ray
CTA	Cherenkov Telescope Array
CTA-N	CTA-Nord
CTA-S	CTA-Sud
CTC	Cherenkov Transparency Coefficient
D-MC	Donut MC
DAQ	Data Acquisition
DC	Direct Current
DEC	Declination
DISP	Distance between the Image centroid and the Source Position
DM	Dark Matter
DRS4	Domino Ring Sampler 4
dSph	dwarf Spheroidal satellite galaxy
DT (or TH)	Discriminator Threshold
EAS	Extensive Air Shower
EBL	Extragalactic Background Light
EE	Encircled Energy
EHE	Extremely High Energy
ELT	Extremely Large Telescope

EM	ElectroMagnetic
FADC	Flash Analog-to-Digital Converter
FoV	Field of View
FWHM	Full Width Half Maximum
GC	Globular Cluster
GCN	Gamma-ray Coordinate Network
GH	Galactic Halo
GRB	Gamma Ray Burst
GW	Gravitational Wave
HDM	Hot Dark Matter
HG	Hermite-Gaussian
HR	Hertzsprung-Russel
HST	Hubble Space Telescope
HV	High Voltage
HVDOG	High Voltage Dependent Gain
IAC	Imaging Atmospheric Cherenkov Telescope
ICRC	International Cosmic Ray Conference
IFAE	Institut de Fisica d'Altes Energies
IMBH	Intermediate Mass Black Hole
INFN	Istituto Nazionale di Fisica Nucleare
IPRC	Individual Pixel Rate Control
IRF	Instrument Response Function
KK	Kaluza-Klein
KSP	Key Science Project/Program
L0	Level 0
L1	Level 1
L3	Level 3
LCDM	Lambda Cold Dark Matter
LIDAR	Light Detection And Ranging
LLG	Liquid Light Guide
l.o.s.	line-of-sight
LOTR	Licel Optical Transient Recorder
LSP	Lightest SUSY Particle
LST	Large Size Telescope
LUPM	Laboratoire Universe et Particules de Montpellier
LZA	Large Zenith Angle
M/L	Mass-to-Light ratio
M1	MAGIC 1
M15	Messier 15
M2	MAGIC 2
MAGIC	Major Atmospheric Gamma Imaging Cherenkov
MARS	MAGIC Analysis and Reconstruction Software
MC	Monte Carlo
MET	Missing Transverse Energy
MIR	Magic Integrated Read-out
MJD	Modified Julian Date
MOND	Modified Newtonian Dynamics
MONSTER	MAGIC Optical Nano-Second Trigger and Event Receiver

MP	Metal-Poor
MR	Metal-Rich
MSP	Milli-Second Pulsar
MSSM	Minimal SUSY Model
MST	Medium Size Telescope
MW	Milky Way
ND	Neutral Density
NFW	Navarro-Frenk-White
NN	Next-Neighbour
NSB	Night Sky Background
NumIsland	Number Of Island
ORM	Observatorio del Roque de los Muchachos
OSA	On-Site Analysis
PCB	Printed Circuit Board
PDF	Probability Density Function
PI	Principal Investigator
PIC	Port d'Informació Científica
PMT	PhotoMultiplier Tube
POSS	Palomar Observatory Sky Survey
PP	Particle Physics
PSF	Point Spread Function
QE	Quantum Efficiency
RA	Right Ascension
RF	Random Forest
RMS	Root Mean Square
SD	Spin Dependent
SI	Spin Independent
SiPM	Silicon Photo-Multiplier
SM	Standard Model
SST	Small Size Telescope
SUSY	SUPERSYMMETRY
TEM	Transverse Mode
TeV <sub>S</sub>	Tensor-Vector-Scalar
TMT	Thirty Meter Telescope
TriII	Triangulum II
TS	Test Statistics
UAB	Universitat Autònoma de Barcelona
UED	Universal Extra Dimensions
UFD	Ultra Faint Dwarf
UFO	Unidentified Fermi Object
UHE	Ultra High Energy
UL	Upper Limit
UMaII	Ursa Major II
UV	Ultra Violet
VCSEL	Vertical Cavity Surface Emitting Laser
VHE	Very High Energy
WDM	Warm Dark Matter
WIMP	Weakly Interacting Massive Particle

## Appendix A

# Specifications Quantel Brilliant

## Brilliant Specifications

Repetition rate (Hz)	10	20	50			
Energy per pulse (mJ)	1064 nm	360	350	150	Measured with a calibrated wattmeter	
	532 nm	180	160	65		
	355 nm	65/100*	60/70*	20		*High energy UV option
	266 nm	40	30	12		
	213 nm	8	6	2		
Energy stability - shot to shot (%)	1064 nm	±2 (0.6)	±2 (0.6)	±3 (1)	Peak to peak, 100% of the shots (RMS)	
	532 nm	±4 (1.3)	±4 (1.3)	±7 (2.3)		
	355 nm	±6 (2)	±6 (2)	±9 (3)		
	266 nm	±8 (2.6)	±8 (2.6)	±12 (4)		
	213 nm	±12 (4)	±12 (4)	±16 (5.3)		
Power drift (%)	1064 nm	±3	±3	±3	Over 8 hours, without readjustment of phase-matching, 18°C<T<28°C (10Hz/20Hz) 18°C<T<25°C (50Hz) W/W exchanger or chiller options available	
	532 nm	±3	±3	±3		
	355 nm	±3	±3	±3		
	266 nm	±6	±6	±6		
	213 nm	±10	±10	±10		
Pulse duration (ns)	1064 nm	≈5	≈5	≈6	FWHM, fast photodiode and 1GHz scope	
	532 nm	≈4	≈4	≈5		
	355 nm	≈4	≈4	≈5		
	266 nm	≈4	≈4	≈5		
	213 nm	≈4	≈4	≈5		
Linewidth (cm <sup>-1</sup> )	1064 nm	0.7	0.7	0.7	FWHM, measured by a grating spectrometer with a 0,045 cm <sup>-1</sup> resolution	
	532 nm	1.4	1.4	1.4		
Jitter (ns)	1064 nm	±0.5	±0.5	±0.5	With respect to Q-switch trigger, measured at half-width of 500 accumulated shots	
Pointing stability (μrad)	1064 nm	<50	<75	<75	Measured by SPIRICON LBA-100, RMS, on 200 pulses at the focal plane of a 2m focus lens	
	532 nm	<50	<75	<75		
	355 nm	<50	<75	<75		
	266 nm	<50	<75	<75		
Divergence (mrad)	1064 nm	0.5	0.5	0.7	Full angle, at 1/e <sup>2</sup> of the peak, 85 % of total energy	
Polarization ratio (%)	1064 nm	>90	>90	>80	Horizontal polarization	
Beam diameter (mm)	1064 nm	6	6	6	At the output of the laser	
Focusability (times Diffraction Limit)	1064 nm	<2	<2	<3	At 1/e <sup>2</sup> of the peak, by SPIRICON LBA-100	
Spatial profile (fit to gaussian)	Near field	1064 nm	0.70	0.70	0.70	At 1m from the laser output At focal plane of a 2m focus lens Least square fit to gaussian (perfect fit=1)
	Far field	1064 nm	0.95	0.95	0.90	

Figure A.1: Technical specifications of the Quantel Brilliant laser